

# For Reference

NOT TO BE TAKEN FROM THIS ROOM

Ex LIBRIS  
UNIVERSITATIS  
ALBERTAENSIS









THE UNIVERSITY OF ALBERTA

RELEASE FORM

NAME OF AUTHOR	Michael Blades
TITLE OF THESIS	Spatial Emission Characteristics of an Inductively Coupled Plasma
DEGREE FOR WHICH THIS THESIS WAS PRESENTED	Ph.D.
YEAR THIS DEGREE GRANTED	1981

Permission is hereby granted to THE UNIVERSITY OF ALBERTA LIBRARY to reproduce single copies of this thesis and to lend or sell such copies for private, scholarly or scientific research purposes only.

The author reserves other publication rights, and neither the thesis nor extensive extracts from it may be printed or otherwise reproduced without the author's written permission.



THE UNIVERSITY OF ALBERTA

SPATIAL EMISSION CHARACTERISTICS OF AN  
INDUCTIVELY COUPLED PLASMA

by



MICHAEL W. BLADES

A THESIS

SUBMITTED TO THE FACULTY OF GRADUATE STUDIES AND RESEARCH  
IN PARTIAL FULFILMENT OF THE REQUIREMENTS FOR THE DEGREE  
OF DOCTOR OF PHILOSOPHY

DEPARTMENT    CHEMISTRY  
.....

EDMONTON, ALBERTA

SPRING 1981





THE UNIVERSITY OF ALBERTA  
FACULTY OF GRADUATE STUDIES AND RESEARCH

The undersigned certify that they have read, and  
recommend to the Faculty of Graduate Studies and Research,  
for acceptance, a thesis entitled SPATIAL EMISSION CHARAC-  
.....  
TERISTICS OF AN INDUCTIVELY COUPLED PLASMA  
.....  
submitted by MICHAEL BLADES  
.....  
in partial fulfilment of the requirements for the degree of  
Doctor of Philosophy in Analytical Chemistry.



## ABSTRACT

As the inductively coupled plasma (ICP) becomes increasingly more popular as a spectrochemical source, the need to understand analyte emission characteristics at a fundamental level becomes more urgent. A detailed knowledge of the emission characteristics as a function of spatial position is an important part of this characterization. A self-scanning linear photodiode array measurement system has been used to obtain vertical and horizontal spatial profiles of emission intensity.

Vertical spatial profiles are normally bell-shaped, with the position of maximum intensity above the load coil varying, depending on ICP instrumental parameters and analyte excitation characteristics. This dependence has been investigated. It has been found that the spatial structure of many atom lines can be predicted theoretically. This involves the calculation of emission intensity for a particular atom line as a function of the excitation and ionization potential of that line, and source "temperature" gradients. The spatial dependence of ion emission on these parameters has also been investigated.

The photodiode array provides an almost ideal sensor for the acquisition of lateral intensity data (horizontal profiles) exactly in a format for input to an Abel inversion





computer program. This program converts spatially integrated, lateral profiles to spatially resolved radial profiles. A group of lateral profiles taken at different heights above the load coil can provide a complete 3 dimensional radial map of analyte emission in the ICP. These detailed maps provide information about the excitation environment experienced by analyte species.

A spatial study of the effect of an excess of an easily ionizable element (EIE), such as Na, has been undertaken, using both vertical and radial emission profiles. This study has clarified the observations of other ICP spectroscopists studying this complex system. The spatial data has provided sufficient information to postulate several possible mechanisms for the effect.



## ACKNOWLEDGEMENTS

I would like to thank several people who contributed significantly to the writing of this thesis. First and foremost, thank you Gary Horlick for your guidance and constructive criticism, and for creating an atmosphere in which learning new things was a pleasure. Thanks, Annabelle Wiseman for typing above and beyond the call of duty (and for your editorial prowess). Also thanks Faye Nagle for sweating over a draughting table to reproduce many of the figures contained in this thesis.

Finally I would like to thank the National Sciences and Engineering Research Council for financial support during my last year.





## TABLE OF CONTENTS

CHAPTER		PAGE
I	Introduction	1
	What is a Plasma	3
	The Inductively Coupled Plasma	4
	Generating and Sustaining the Plasma	6
	Plasma Physical Properties and Spectral Features	8
	Plasma Temperature	14
	Excitation Mechanisms in the ICP	19
	Spatially Resolved Measurements	26
II	Experimental	30
	Plasma Generation	30
	Aerosol Generation	35
	Nebulizer Construction	35
	Nebulizer Performance	37
	Spatial Profiles with a Photodiode Array	39
	Computer Coupled Photodiode Array	41
	Chemicals	47
III	Vertical Spatial Features of Analyte Emission	48
IV	Spatial Behaviour and Analyte Excitation Characteristics	71
	Introduction	71
	Soft Lines	71



CHAPTER		PAGE
	Theoretical Treatment of Analyte Emission Intensity	77
	Hard Lines	91
	Discussion	95
V	Implementing Abel Inversions Using a Photodiode Array Measurement System	104
	Introduction	104
	Experimental	106
	Abel Inversion of Lateral Data	108
	Results and Discussion	113
	Spatial Distribution of Excitation Temperatures	121
	Conclusion	125
VI	Interference from Easily Ionizable Element Matrices	126
	Introduction	126
	Survey of the EIE Effect in Plasmas	127
	Possible Mechanisms of EIE Interference	136
	Experimental	143
	Effect of EIE's on Vertical Profiles	144
	Effect of Varying Interferent	159
	Effect of Power on Matrix Effect	167
	Horizontal Spatial Profiles of the Matrix Effect	174
	Nebulizer Effects	184
	Ionization Equilibrium Shifts	185





CHAPTER	PAGE
Summary and Conclusions	186
VII Conclusions	191
Bibliography	196
Appendix A	206
Appendix B	229
Appendix C	235



# LIST OF TABLES

<u>Table</u>	<u>Description</u>	<u>Page</u>
I	Survey of plasma temperature.	18
II	Comparison of crossflow, Meinhard, and fixed tip crossflow nebulizers.	40
III	Excitation potentials and peak maximum position for analyte lines in Figure 23.	74
IV	Atom and ion partition function constants.	81
V	Normal temperature for several analyte lines.	88
VI	Wavelengths, excitation potentials, and sum of excitation potential and ionization potential for Cd.	98
VII	Wavelengths, excitation potentials and sum of excitation potentials and ionization potentials for BaII.	99
VIII	Wavelengths, transition probabilities, and excitation energies for PbI used for temperature determination.	123
IX	Emission intensity and absorbance of MgI 285.3 nm for various molar ratios of Na to Mg.	187
X	AM9511 command summary.	221



## LIST OF FIGURES

<u>Figure</u>	<u>Description</u>	<u>Page</u>
1.	Main features of the ICP discharge.	7
2.	Iso-intensity profile of emission from ArI 415.8 nm (heavy lines mark torch edge).	11
3.	Block diagram of ICP instrumentation.	31
4.	ICP torch (dimensions in mm).	33
5.	ICP torch, spray chamber assembly.	34
6.	Schematic diagram of fixed tip crossflow nebulizer (dimensions in mm).	36
7.	Nebulizer and Teflon carrying block (dimensions in mm).	36
8.	Photodiode array profiling concept.	42
9.	Block diagram of computer controlled photodiode array profiling system.	44
10.	Signal conditioning electronics for photodiode array.	46
11.	Vertical spatial profiles for CaI 422.7 nm. Aerosol flow rates; (a) 0.7 lpm, (b) 0.8 lpm, (c) 0.9 lpm. RF power; (1) 1.0 kw, (2) 1.25 kw, (3) 1.50 kw, (4) 1.75 kw, and (5) 2.0 kw.	52
12.	Vertical spatial profiles for CaII 393.3 nm. Aerosol flow rates; (a) 0.7 lpm, (b) 0.8 lpm, (c) 0.9 lpm. RF power; (1) 1.0 kw, (2) 1.25 kw, (3) 1.50 kw, (4) 1.75 kw, and (5) 2.0 kw.	53
13.	Emission intensity of CaI and CaII as a function of RF power at an observation height of 14 mm.	55
14.	Vertical spatial profiles for LiI 670.3 nm. RF power; (1) 1.25 kw, (2) 1.50 kw, (3) 1.75 kw, and (4) 2.0 kw.	58





<u>Figure</u>	<u>Description</u>	<u>Page</u>
15.	Vertical spatial profiles for CdI 228.8 nm. Aerosol flow rates; (a) 0.9 lpm, (b) 1.0 lpm, and (c) 1.1 lpm. RF power; (1) 1.25 kw, (2) 1.50 kw, (3) 1.75 kw, (4) 2.0 kw, and (5) 2.25 kw.	59
16.	Vertical spatial profiles for ZnI 213.9 nm. Aerosol flow rates; (a) 0.9 lpm, (b) 1.0 lpm, and (c) 1.1 lpm. RF power; (1) 1.25 kw, (2) 1.50 kw, (3) 1.75 kw, (4) 2.0 kw, and (5) 2.25 kw.	60
17.	Vertical spatial profiles for MnII 403.1 nm. Aerosol flow rates; (a) 0.9 lpm, (b) 1.0 lpm, and (c) 1.1 lpm. RF power; (1) 1.25 kw, (2) 1.50 kw, (3) 1.75 kw, (4) 2.0 kw, and (5) 2.25 kw.	61
18.	Vertical spatial profiles for CdII 226.5 nm. Aerosol flow rates; (a) 0.1 lpm, (b) 1.0 lpm, and (c) 1.1 lpm. RF power; (1) 1.25 kw, (2) 1.50 kw, (3) 1.75 kw, (4) 2.0 kw, and (5) 2.25 kw.	62
19.	Vertical spatial profiles for ZnII 202.5 nm. Aerosol flow rates; (a) 0.1 lpm, (b) 1.0 lpm, and (c) 1.1 lpm. RF power; (1) 1.25 kw, (2) 1.50 kw, (3) 1.75 kw, (4) 2.0 kw, and (5) 2.25 kw.	63
20.	Vertical spatial profiles for NaI 588.9 nm. Aerosol flow rates; (a) 0.8 lpm, (b) 0.9 lpm. RF power; (1) 1.25 kw, (2) 1.50 kw, (3) 1.75 kw, and (4) 2.0 kw.	65
21.	Emission intensity as a function of power for NaI 588.9 nm, at observation heights of 13 mm, 19 mm, and 25 mm above the load coil.	66
22.	Vertical spatial profiles for ArI 418.2 nm. Aerosol flow rate; (a) 0.9 lpm and (b) 1.0 lpm. RF power; (1) 1.0 kw, (2) 1.25 kw, (3) 1.50 kw, (4) 1.75 kw, (5) 2.0 kw.	67
23.	Vertical spatial emission profiles for; (a) NaI 588.9 nm, (b) LiI 610.4 nm, (c) LiI 670.8 nm, (d) CrI 357.8 nm, (e) KI 766.5 nm, (f) CaI 422.7 nm, (g) MgI 285.3 nm.	73



<u>Figure</u>	<u>Description</u>	<u>Page</u>
24.	Position of peak maximum for lines listed in Table III, as a function of excitation potential of the line.	75
25.	Theoretically generated profiles of emission intensity as a function of height above the load coil for MgI 285.3 nm and KI 766.5 nm.	82
26.	Vertical spatial profiles for MgI 285.3 nm and KI 766.5 nm.	83
27.	Plot of normal temperature versus excitation potential for lines listed in Table III.	85
28.	Normal temperature for MgI 283.3 nm, CrI 425.4 nm, BaI 553.4 nm, and KI 766.5 nm, as a function of electron density.	87
29.	Position of vertical profile peak as a function of normal temperature (in K).	89
30.	Vertical spatial profiles for ZnI 213.8 nm and ZnII 202.5 nm. RF power; (1) 2.0 kw, (2) 1.75 kw, (3) 1.5 kw, (4) 1.25 kw.	92
31.	Vertical spatial profiles for CdI 228.8 nm and CdII 226.5 nm. RF power; (1) 2.0 kw, (2) 1.75 kw, (3) 1.5 kw, (4) 1.25 kw.	93
32.	Superimposed vertical spatial profiles of CdI and CdII at 2.0 kw RF power.	94
33.	Vertical spatial profiles for BaII lines; (a) 455.4 nm, (b) 493.4 nm, (c) 413.1 nm, (d) 489.2 nm, and (3) 233.5 nm.	96
34.	Vertical spatial profiles for CaII lines; (a) 393.3 nm, (b) 373.6 nm, and (c) 315.9 nm.	97
35.	Horizontal profiling system.	107
36.	Schematic representation of the lateral and radial variables involved with Abel inversion.	110
37.	(A) Radial test data. (B) Lateral intensities calculated from radial test data.	112



<u>Figure</u>	<u>Description</u>	<u>Page</u>
	(C) Radial intensities calculated from lateral data via Abel inversion.	
38.	(A) Lateral intensity data measured for MgII 279.5 nm. (B) Average one-sided lateral data. (C) Calculated radial intensities.	114
39.	Complete radial emission map of the ICP discharge for CaI 422.7 nm.	116
40.	Complete radial emission map of the ICP discharge for CaII 393.3 nm.	117
41.	Complete radial emission map of the ICP discharge for MgI 285.3 nm.	118
42.	Complete radial emission map of the ICP discharge for MgII 279.5 nm.	119
43.	Radial temperature profiles for the ICP discharge.	124
44.	Vertical spatial profiles for Ca; (a) CaI 422.7 nm, (b) CaII 393.3 nm. Molar ratio of Na to Ca; (1) 0:1, (2) 10:1, (3) 30:1, (4) 100:1, (5) 300:1.	145
45.	Vertical spatial profiles for Mg; (a) MgI 285.3 nm, (b) MgII 279.5 nm. Molar ratio of Na to Mg; (1) 0:1, (2) 10:1, (3) 30:1, (4) 300:1.	146
46.	Vertical spatial profiles for Cd; (a) CdI 228.8 nm, (b) CdII 214.4 nm. Molar ratio of Na to Cd; (1) 0:1, (2) 10:1, (3) 30:1, (4) 100:1, (5) 300:1.	147
47.	Matrix effect of 100:1 molar ratio Na to Ca as a function of height above the load coil.	149
48.	Matrix effect of 100:1 molar ratio Na to Mg as a function of height above the load coil.	150





<u>Figure</u>	<u>Description</u>	<u>Page</u>
49.	Matrix effect of 100:1 molar ratio Na to Cd as a function of height above the load coil.	151
50.	Spatial position where enhancements change to depressions as a function of ionization potential for Ca, Mg, and Cd.	154
51.	Ratio of emission intensities (I) for CaII 393.3 nm and CaI 422.7 nm. Molar ratio of Na to Ca; (a) 0:1, (b) 100:1.	155
52.	Ratio of emission intensities (I) for MgII 279.5 nm and MgI 285.3 nm. Molar ratio of Na to Mg; (a) 0:1, (b) 100:1.	156
53.	Ratio of emission intensities (I) for CdII 214.4 nm and CdI 228.8 nm. Molar ratio of Na to Cd; (a) 0:1, (b) 100:1.	156
54.	Vertical spatial profiles for CaI 422.7 nm. Molar ratio of Li to Ca; (a) 0:1, (b) 10:1, (c) 30:1, (d) 100:1, (e) 300:1.	160
55.	Vertical spatial profiles for CaII 393.3 nm. Molar ratio of Li to Ca; (a) 0:1, (b) 10:1, (c) 30:1, (d) 100:1, (e) 300:1.	161
56.	Vertical spatial profiles for; (1) CrI 357.8 nm, and (2) CrII 283.5 nm. Molar ratio of Li to Cr; (a) 0:1, (b) 10:1, (c) 30:1, (d) 100:1, (e) 300:1.	162
57.	Vertical spatial profiles for; (1) CaI 422.7 nm, and (2) CaII 393.3 nm. Concomitant present in 100:1 molar ratio; (a) none, (b) Li, (c) Na, (d) K.	164
58.	Vertical spatial profiles for; (1) MgI 285.3 nm, and (2) MgII 279.5 nm. Concomitant present in 100:1 molar ratio; (a) none, (b) Li, (c) Na, (d) K.	165
59.	Vertical spatial profiles for; (1) CdI 228.8 nm, and (2) CdII 214.4 nm. Concomitant present in 100:1 molar ratio; (a) none, (b) Li, (c) Na, (d) K.	166





<u>Figure</u>	<u>Description</u>	<u>Page</u>
60.	( i) Vertical spatial profiles for CaI 422.7 nm. RF power; (a) 2.0 kw, (b) 1.75 kw, (c) 1.50 kw. (1) No Na, (2) 100:1 molar ratio at Na to Ca.	169
60.	(ii) Vertical spatial profiles for CaI 422.7 nm. RF power; (d) 1.25 kw, (e) 1.0 kw. (1) No Na, (2) 100:1 molar ratio of Na to Ca.	170
61.	( i) Vertical spatial profiles for CaII 393.3 nm. RF power; (a) 2.0 kw, (b) 1.75 kw, (c) 1.50 kw. (1) No Na, (2) 100:1 molar ratio of Na to Ca.	171
61.	(ii) Vertical spatial profiles for CaII 393.3 nm. RF power; (a) 2.0 kw, (b) 1.75 kw, (c) 1.50 kw. (1) No Na, (2) 100:1 molar ratio of Na to Ca.	172
62.	Matrix effect as a function of RF power input at (a) 12 mm, (b) 14.5 mm, and (c) 16.5 mm above the load coil for CaI 422.7 nm.	173
63.	Matrix effect as a function of RF power input at (a) 12 mm, (b) 14.5 mm, (c) 16.5 mm, and (d) 21 mm above the load coil for CaII 393.3 nm.	173
64.	Radial spatial profiles of Ca emission at, (i) 0 mm and (ii) 2 mm above the load coil. (a) No Na added, (b) 100:1 molar ratio of Na to Ca.	175
65.	Radial spatial profiles of Ca emission at, (i) 4 mm and (ii) 6 mm above the load coil. (a) No Na added, (b) 100:1 molar ratio of Na to Ca.	176
66.	Radial spatial profiles of Ca emission at, (i) 8 mm and (ii) 10 mm above the load coil. (a) No Na added, (b) 100:1 molar ratio of Na to Ca.	177
67.	Radial spatial profiles of Ca emission at, (i) 12 mm and (ii) 14 mm above the load coil. (a) No Na added, (b) 100:1 molar ratio of Na to Ca.	178



<u>Figure</u>	<u>Description</u>	<u>Page</u>
68.	Radial spatial profiles of Ca emission at, (i) 16 mm and (ii) 18 mm above the load coil. (a) No Na added, (b) 100:1 molar ratio of Na to Ca.	179
69.	Radial spatial profiles of Ca emission at, (i) 20 mm and (ii) 22 mm above the load coil. (a) No Na added, (b) 100:1 molar ratio of Na to Ca.	180
70.	Block diagram of the voltage-to-frequency converter and analog-to-digital converter based measurement systems.	208
71.	Block diagram of the 8253 programmable interval timer.	211
72.	Schematic representations of the 8253 modes.	212
73.	Circuit diagram of the complete program- mable frequency meter as interfaced to the SDK-80.	214
74.	Simplified block diagrams of the integration timer and the counter.	215
75.	Circuit diagram of the analog-to-digital converter based system as interfaced to the SDK-80.	218
76.	Interface circuit for the AM9511 to the SDK-80.	222
77.	Typical TTY dialogue and output for a run with the v-to-f converter based measure- ment system.	224
78.	Proposed approach for a multichannel meas- urement system based on the v-to-f con- verter-counter integration system.	227



## CHAPTER I

### INTRODUCTION

In the evolution of any analytical technique there are, in general, two complementary activities which contribute to its development. These are an investigation of the fundamental properties or characteristics of the technique, and application of the technique to routine and specialized problem solving. The success of a particular method must be evaluated in terms of the latter activity, the "ideal" being the analysis of all substances at all concentration levels, in any sample matrix without interferences. The value of the former activity is in suggesting ways in achieving this "ideal", through an understanding of the mechanisms of operation of the method. It is often the case, that the fundamental and practical pursuits do not progress at the same rate; such is the case with Inductively Coupled Plasma-Optical Emission Spectroscopy (ICP-OES). As a method for multielement atomic analyses, it has been used for a wide variety of analysis and is becoming firmly established in the analytical chemists arsenal as a result of its early successes. An understanding of its fundamental characteristics, in particular the mechanism of energy transfer to analyte species, has been slower in coming, in large part due to the complex nature of the "plasma state". Of course the





practical application of plasma spectroscopy can and will progress quite nicely on empirical data but the mechanistic understanding is important for the technique to reach its full potential. What is required is a description of the interactions between analyte species injected into the plasma gas and the plasma gas itself, as well as inter-analyte interactions in the plasma gas environment. Such a description should be capable of rationalizing the experimental data available about analytical plasmas.

Spatial studies are considered an important aspect in the characterization of emission sources [1-3]. The acquisition of spatial information involves the observation of some measurable quantity, such as emission intensity from an analyte line, as a function of a distance coordinate related to the source. Scheeline and Walters [2] have summarized the importance of such spatial studies;

"Spatial resolution of the numerous properties of spectral light sources may give insight into the mechanisms of operation of these sources and thence improved analytical procedures."

The rationalization for this statement is the fact that the spatial distribution of some measurable physical property is a reflection of the environment which caused the appearance of that property.

The general theme of this thesis is, as suggested by the title, a study of the spatial distribution of analyte species in a Radio Frequency Inductively Coupled Argon





Plasma (RF-ICAP). The investigations carried out are fundamental in nature and the data presented are used to rationalize or clarify the observations of other researchers, and to support the author's own speculations about physical processes in ICAP's. Before proceeding, a brief introduction to the ICAP is warranted.

### What is a Plasma?

Martin Umen, in his book, "An Introduction to Plasma Physics" [4] defines a plasma as a "conglomeration of mobile positively and negatively charged particles, there being approximately the same density of positive charges as negative". In argon, the ionization process:



creates mobile argon ions and electrons which are the predominant charged particles at low temperatures (<15,000 K). The analytical RF-ICAP is generally a weakly ionized plasma, the degree of ionization at 10,000 K being 9% at 1.1 atm [5] at equilibrium.

There are a variety of methods used for producing plasmas for analytical spectroscopy [6]. These include: D.C. plasma jets, microwave induced plasmas, capacitively coupled plasmas, and RF-ICAP's. The type of plasma under study in this work is the RF-ICAP or ICP for short.



## The Inductively Coupled Plasma

The first mention in the literature of an inductively coupled plasma was by Babat [7] in 1947. The area lay fallow until in 1961 Reed [8] published an article describing an ICP operating at atmospheric pressure supported by flowing argon gas. The plasma torch consisted of a quartz tube, open at one end supplied with flowing argon gas at the other. A five turn copper coil was wrapped around the quartz tube near its outlet and RF power to a maximum of 10 KW at 4 MHz was delivered to the coil. The plasma was initiated by inserting a graphite rod into the RF field which when heated inductively initiated breakdown of the argon gas in its vicinity after which the plasma became self-supporting. Reed also introduced the idea of vortex stabilization whereby the argon gas is introduced into the torch tangentially causing it to flow in a spiral motion up along the walls of the quartz tube. This centres the plasma, recirculates some of the plasma gas between the coils, and cools the quartz tube to prevent melting. This proved to be an important concept and has been widely employed for analytical plasmas.

It was quickly recognized that the ICP could be a useful tool for spectroscopic analysis and two groups independently published their application of the Reed type torch. Greenfield et al. [9] described a torch



which is very close to that utilized in present commercially available plasma systems. It consisted of two concentric glass tubes with tangential gas inlets on each and a central gas tube for injecting sample into the plasma. Emission from the elements injected was observed in the tailflame region of the plasma. This paper was followed by a description by Wendt and Fassel [10] of a laminar flow ICP torch. However Fassel's group eventually converted to tangential gas inlets favouring Reed's approach of vortex stabilization [11,12]. From these beginnings the use of plasmas, the ICP in particular, as a source for spectrochemical analysis has blossomed to the extent that a journal has been initiated which is devoted entirely to the source [13].

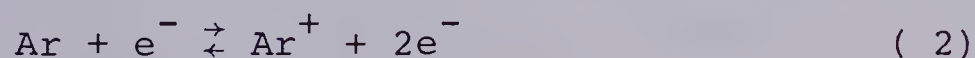
Some popular areas of application for the ICP have been in the analysis of rocks [14] and soils [15,16], in the metals industry [17] for the analysis of trace elements in steels, trace elements in biological materials [16,18] and natural waters [19], and in forensic science [20]. The ICP has also proven to be useful for the analysis of elements in oils [21] and organic compounds [22]. For good historical and application reviews of plasmas as spectrochemical sources the reader is referred to Greenfield et al. [23-25], Barnes [26], and Dahlquist and Knoll [16].





## Generating and Sustaining the Plasma

A schematic diagram outlining the main features of the ICP discharge is provided in Figure 1. This general approach has become one of the most popular and is that used for all the measurements described in this thesis. The plasma torch itself is described in detail in Chapter II. It generally consists of two concentric glass tubes with a smaller aerosol tube up the centre. Argon gas is introduced tangentially at the base of the torch and spirals up through the load coil. Power is fed into the coil from an RF generator operating at 27.18 MHz in the range of 1 to 3 Kw. A tesla coil is used to "seed" the incoming gas with electrons by ionizing a portion of the argon. The electrons produced are accelerated in the magnetic field produced as a result of the RF power applied to the coil and these accelerated electrons collide with neutral argon atoms causing further ionization. This can be represented as:



At some point in time the rate of production of argon atoms by the forward process in equation 2 will be balanced by the reverse process, and by the two body process:







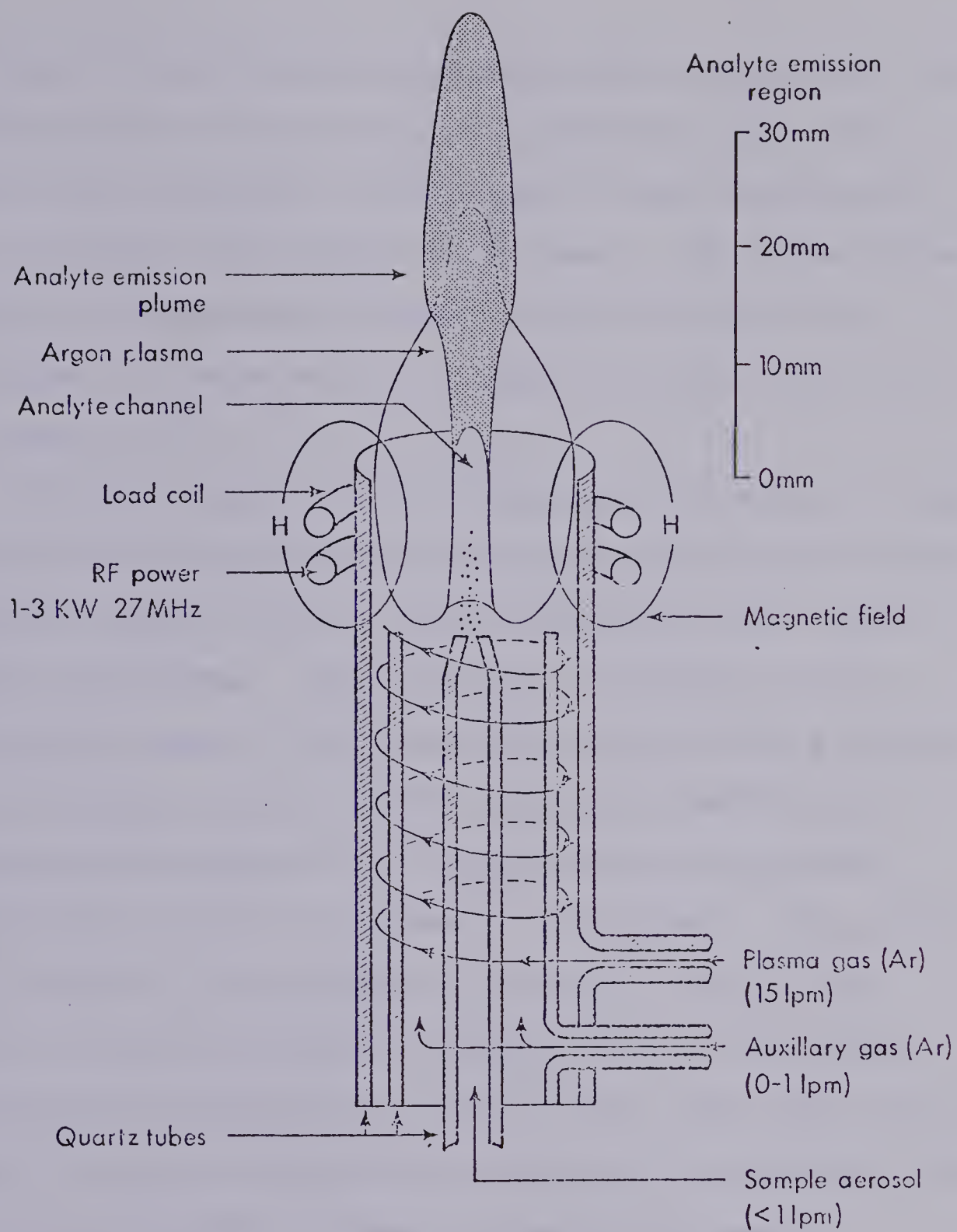


Figure 1. Main features of the ICP discharge.



such that an equilibrium is established in which the rate of production of argon ions is balanced by the rate of argon ion consumption. The plasma is thus sustained by the continuous application of RF power. The plasma forms a toroidal shape at a frequency of 27 MHz which facilitates the introduction of sample into the base of the hot gases [11].

Normally sample is introduced into the plasma in the form of an aerosol gas, although powdered samples [27,28] or solid samples [29-31] may be introduced using appropriate techniques. The aerosol gas "punches a hole" through the base of the plasma forming an analyte channel. The processes of desolvation, molecular dissociation, ionization equilibration, and excitation take place during the analyte's progress up the channel. The process of excitation and subsequent radiative emission creates a "plume" of analyte emission within the analyte channel approximately 30 mm high in the area above the load coil. It is the delineation of the spatial structure of this plume as a function of analyte species and sample matrix that is one of the major goals of the study contained in this thesis.

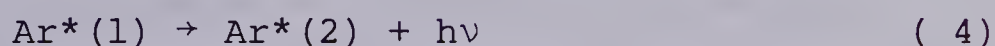
### Plasma Physical Properties and Spectral Features

The physical environment of the RF plasma is not characterized by combustion processes such as those found



in flames and very few analogies may be drawn between the two. Rather the energy contained in, and dissipated by, the plasma is the result of energy transferred from the power applied to the load coil to the argon species present. The energy thus absorbed is dissipated in three main ways [8]: by conduction to the walls of the quartz tube, by flow of hot gases away from the load coil, and by the emission of radiation.

Radiative emission from the plasma is the result of two main processes and yields the characteristic spectrum of an argon plasma. An argon line spectrum is produced by the emission of light as a result of transitions from upper excited states of argon neutral atoms ( $\text{Ar}^*(1)$ ) to lower excited states ( $\text{Ar}^*(2)$ ) or to ground state argon atom ( $\text{Ar}^\circ$ ) through the processes:



where  $\nu$  is the transition frequency. In addition a spectral continuum or background is produced as a result of the radiative recombination process given in equation (3). This recombination of a free electron produces a continuum which is characteristic of argon [32]. Emission from argon ions has not been observed in the ICP. The entrainment of air into the tailflame produces emission from NO molecular



species in the spectral region 200-300 nm [33]. Molecular emission from OH is observed in the region around 306 nm, and hydrogen atomic lines are observed when aqueous aerosols are introduced into the plasma. Some spectra of the argon ICP have been published demonstrating these features [33,34].

The continuum and argon line intensity is greatest in the spatial region within the load coils and drops quickly with increasing distance away from the load coils. The iso-intensity plot of the emission from Ar I at 415.8 nm provided in Figure 2 demonstrates this. This figure is a plot of the radial (from the centre of the plasma to the edge) intensity distribution of Ar I emission; the numbers on the lines representing the relative intensities. It can be seen that the intensity is significantly reduced in the centre of the plasma as a result of the aerosol channel. It can also be noticed that the argon line and continuum intensity will be relatively low in the region 15-20 mm above the load coil where analytical observations are usually made. This is good from the standpoint of maximum signal to background ratios.

One of the most striking features of the ICP and one which makes it particularly suitable for emission spectroscopy is its relatively high temperature. Values for the measured temperature vary depending on the measurement





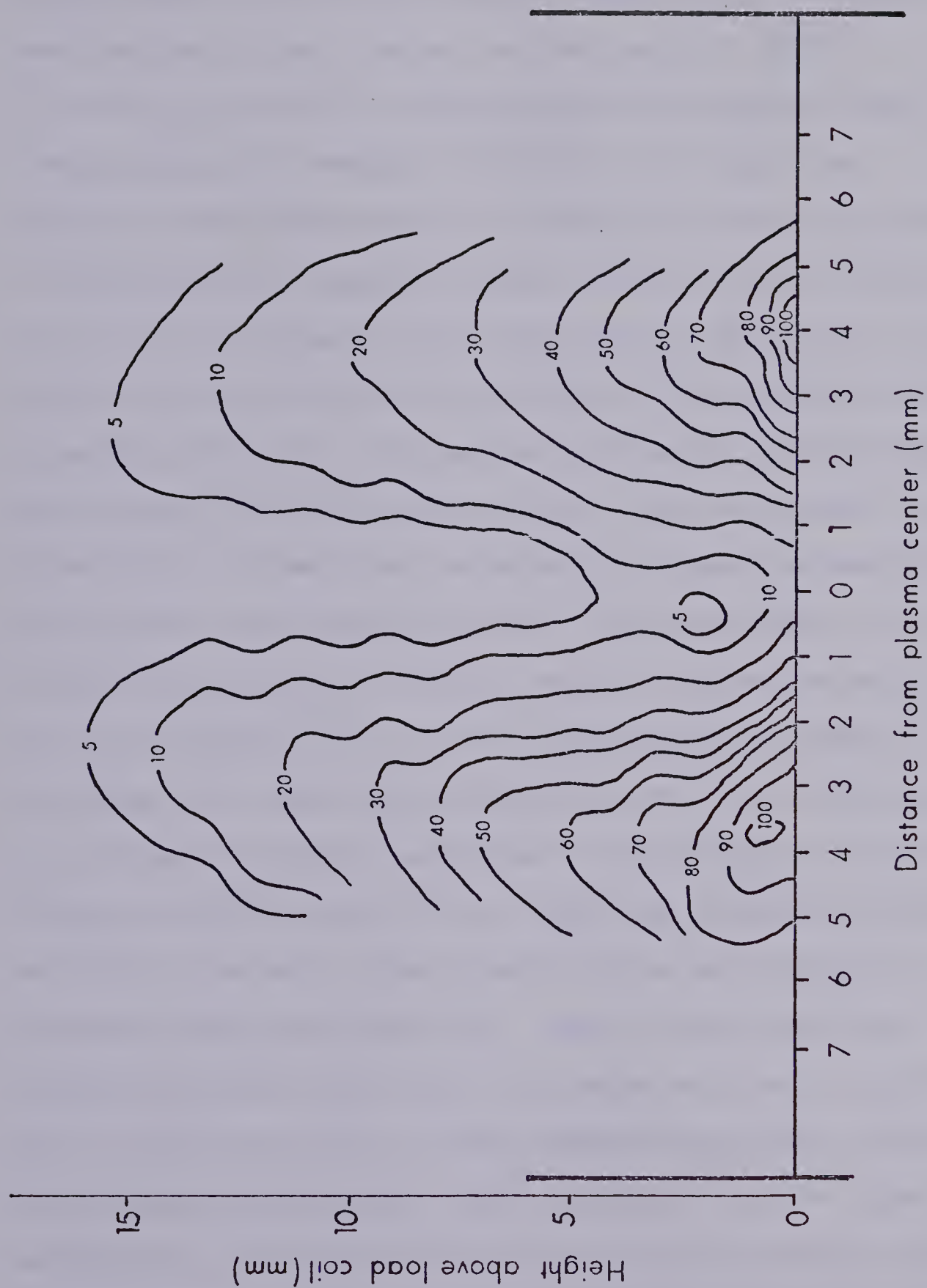


Figure 2. Iso-intensity profile of emission from ArI 415.8 nm (heavy lines mark torch edge).



method employed and the type of temperature measured, but most workers report values in the range of 4000 K to 8000 K [7,35-38]. The practical outcomes of these high temperatures are several. Firstly, the high temperatures mean that there is sufficient energy available to significantly populate upper levels of atoms leading to an analyte emission spectrum rich in analytical lines, some with high excitation energies. Even elements which have been difficult to analyze by emission spectroscopy due to high excitation potentials, such as sulphur, iodine, phosphorus, arsenic and selenium have been successfully determined using the ICP [39-40]. Of course one of the complications associated with an emission spectrum which is rich in analysis lines is the possibility of spectral overlaps [16] which may turn out to be one of the most significant problems associated with simultaneous multi-element analysis with ICP's. Even the high resolution afforded by echelle spectrometers does not completely overcome these problems [41]. Many of the most sensitive analysis lines are ionic emission lines, partially due to the fact that at these temperatures many species are highly ionized, but also resulting from an "ion line advantage". The possible source of this advantage will be discussed in a subsequent section but basically it means the population of many emitting ion energy levels



are one to three orders of magnitude higher than that predicted for the observed excitation temperature [42].

The analyte channel is a narrow emitting core surrounded by hot optically thin gases. This structure leads to very low levels of self absorption [43], which in turn provides analytical curves with a very large linear working range; about 4 to 5 orders of magnitude [44]. From an analytical standpoint this means that samples of widely varying composition can be analyzed without the need for dilution.

A further benefit of the high temperatures is that many of the classical vaporization interferences associated with emission and absorption flame spectroscopy are reduced or eliminated. For example, the suppression of emission due to the presence of phosphate or aluminium concomitants has been shown to be negligible in the ICP [45-48]. Presumably the plasma is sufficiently energetic to dissociate any compounds which may form before or after the nebulization stage. It has been reported that the effect of the presence of easily ionizable elements (EIE's) such as Na may be reduced to a negligible level under suitable operating conditions [47]. There is, however, much confusion in the literature about this effect and the exact nature of the influence of EIE's on analyte emission. The classical interpretation in flames of a



shift in the ionization equilibrium between analyte ion and neutral atom species does not seem to apply in the ICP. This is rationalized on the basis that the already high density of electrons in the plasma is not changed by addition of EIE's. Nevertheless, there is an effect on net analyte emission intensity due to these elements (Na, Li, K, Rb, Cs) and this area has been singled out as one in which a detailed spatial study is warranted. This study, presented in a later chapter, has led to a clarification of the "effect", showing that the variability in the influence of EIE's reported by different workers is probably spatial in origin.

### Plasma Temperature

Temperature has been mentioned several times throughout the preceding section on plasma properties. The interpretation of what is meant by temperature and its measurement is the subject of a massive body of plasma literature and will be considered only briefly in this thesis. A discussion of temperature is integrally bound with a discussion of equilibrium in the ICP.

Thermodynamic equilibrium is a state in which detailed energy balance applies, that is, "every process of energy transfer is perfectly balanced by the reverse process" [21]. This is not achievable in an emission







source since the loss of energy from the system by emission of radiation is not compensated for. For this reason the concept of local thermodynamic equilibrium (LTE) is introduced, whereby all energy transfer processes except emission of radiation are in thermodynamic equilibrium.

Under the condition that LTE applies, a single system temperature defines the following distributions.

- (1) The velocity of particles should be given by Maxwell's equation,

$$f(v) = \left(\frac{m}{2\pi kT_g}\right)^{3/2} \exp(-mv^2/2kT_g) 4\pi v^2 dv$$

where,

$f(v)$  = the probability function that a particle has velocity in the region  $v$  and  $v + dv$ .

$m$  = mass of the particle

$k$  = Boltzmann constant

$T_g$  = gas kinetic temperature.

For the velocity distribution of electrons, this temperature is called  $T_e$ , the electron temperature.

- (2) The population of excited states should be given by the Boltzmann equation,

$$\frac{n_g}{n_p} = \left(\frac{g_g}{g_p}\right) \exp[-(E_g - E_p)/kT_{exc}]$$

where,

$n_g$  and  $n_p$  = population of excited states  $g$  and  $p$



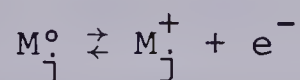
$g_g$  and  $g_p$  = degeneracies of states  $g$  and  $p$

$E_g$  and  $E_p$  = excitation energies of states  $g$  and  $p$

$T_{exc}$  = excitation temperature

(3) The distribution of molecules and their dissociation products should follow the mass action law of Guldberg and Waage.

(4) The distribution of atoms and ionization products should be described by the Saha equation; for



the equilibrium constant is:

$$K_{nj} = \frac{n_{ij} n_e}{n_{aj}} = S_{nj}(T)$$

where  $S_{nj}$  is the Saha equilibrium constant expressed in terms of number density ( $n$ ) of species. The equilibrium constant may also be expressed in terms of partial pressures,

$$S_{pj} \equiv \frac{p_{ij} p_e}{p_{aj}} = \frac{(2\pi m)^{3/2} (kT_i)^{5/2}}{h^3} \frac{2Z_{ij}}{Z_{aj}} \exp[-E_{ij}/kT_i]$$

where  $p_{ij}$ ,  $p_e$ ,  $p_{aj}$  = the partial pressures of ion, electron and atom species of element  $j$ ;

$m$  = electron mass;

$h$  = Planck's constant;

$Z_{ij}$ ,  $Z_{aj}$  = ion and atom partition function;



$E_{ij}$  = ionization energy of the atom;

$T_i$  = ionization temperature.

These definitions lead to the possibility of several different kinds of temperatures which are commonly specified for a particular source. These are the electron temperature ( $T_e$ ) defining free electron energies (velocities), gas dynamic temperature ( $T_g$ ) defining the gas particle energies (velocities), excitation temperature ( $T_{exc}$ ) defining atom excited state populations, rotational temperature ( $T_{rot}$ ) defining populations of excited rotational states of molecules, and ion temperature ( $T_i$ ) defining the distribution of atom and ion populations. Each type of temperature may be measured by spectroscopic means by observing the particular system with which it is associated. For a system which is in LTE the condition

$$T_g = T_e = T_{exc} = T_{rot} = T_i$$

will apply. The ICP is generally considered not to be in LTE [35-38,42,49,50]. The results of Kornblum and deGalen [35] obtained for an ICP operating at 50 MHz indicated that  $T_g < T_{exc} < T_i$  at both low and high aerosol flow rates.

The temperatures which have been reported in the literature vary widely but a summary of representative values is provided in Table I. It should be borne in mind



TABLE I

## SURVEY OF PLASMA TEMPERATURES

Worker	$T_{\text{exc}}$ (K)	$T_i$ (K)	$T_{\text{rot}}$ (K)
Alder et al. [38]	5230-8510	6320-8440	-
Kornblum, deGalan [35]	2800-8600	8000-9000	1700-3800
Kalnicky, et al. [36]	4100-6100	-	-
Jarosz, Mermet [50]	5500-6600	9200	-
Alder, Mermet [51]	5000-7000	-	6100
Jarosz, et al. [37]	4800	6700-7400	-





that the ICP is not spatially homogeneous so that different regions will exhibit different values for temperature. Also there is significant variation in the operating parameters used in the different studies including RF power level and frequency, aerosol flow rate, and spatial region observed. For these reasons it is probably not valid to intercompare the various values given in Table I, and the publications should be consulted for specific measurement details. It will, however, give the reader some feel for the relative magnitude of the various temperatures. Specific methods for the measurement and interpretation of source temperatures have not been included in this discussion although results of the measurement of excitation temperatures will be included in a latter chapter. Reif et al. [52-55] and Boumans [56] discuss these matters in some detail.

#### Excitation Mechanisms in the ICP

Elementary particles interact by virtue of gravitational, nuclear, and electromagnetic forces. The sum total of these interactions is termed a collision. These collisions may be either elastic in which the total kinetic energy of the colliding particles is conserved, or inelastic, in which the total energy is conserved but kinetic energy is not. In the latter case kinetic energy

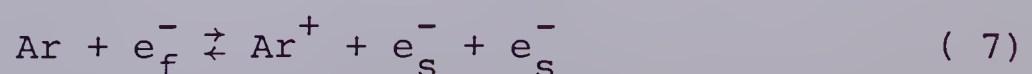


may be converted to excitation energy, eventually being lost radiatively. This type of collision is termed a "collision of the first kind". An example in which kinetic energy of colliding partners A and B is converted to excitation energy in B is provided by:



The reverse of this process in which stored excitation energy is partially converted to kinetic energy of the colliding partners is termed a "collision of the second kind". Both of these types of inelastic collisions are likely to be significant in the ICP.

The very existence of the plasma state in the argon ICP implies the presence of three elementary particles. These are argon neutral atoms (Ar), argon ions ( $\text{Ar}^+$ ) and electrons ( $e^-$ ). Initially the mode of production of argon ions is probably due to impact with "fast" electrons which have been accelerated in the magnetic field produced in the region of the load coil. The ionization energy of Ar is 15.75 eV so the electron must possess at least this energy to ionize the argon atom. Any energy in excess of 15.75 eV is carried away by "slow" electrons involved in the collision. This process is illustrated in Equation 7.



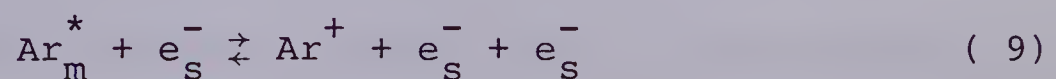


where  $e_f^-$  is a fast electron and  $e_s^-$  is a slow electron, fast and slow being terms which describe the relative amount of kinetic energy possessed by the electrons. The collision of fast electrons with energy greater than about 11.5 eV produces excited states of the argon atom ( $Ar^*$ ). This process is illustrated in Equation 8. The radiative



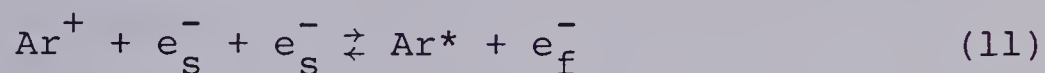
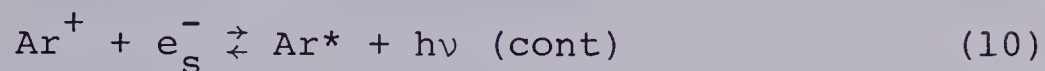
decay of argon excited in this manner, and argon excited by ion-electron recombination (Equation 3) gives rise to the Ar line spectrum.

The  $^3P_2$  and  $^3P_0$  states of the argon atom are "metastable" levels [57] and as such have relatively long lifetimes compared to radiating states. The relatively long lifetimes of these atoms means that they can play a role in the collision processes in the ICP. Thus production of argon ions in the less energetic regions of the plasma could be the result of the collision of argon metastable species ( $Ar_m^*$ ) with relatively slow electrons [42]. The energies of the metastable levels are 11.55 and 11.71 eV. Thus the electrons need only possess energy in the range of 4 eV to 4.2 eV to initiate this process. This process is illustrated in Equation 9.





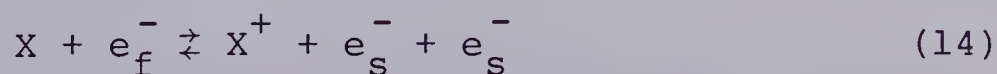
In this way the plasma state can exist above the energy addition region. Decay of the plasma state is the result of the radiative recombination and radiative de-excitation processes shown in Equations 10, 11, and 12.



When analyte species are introduced into the plasma gas these argon species and electrons give up at least part of their energy to these analyte atoms. Analyte atoms (X) may be excited by electron impact [58].



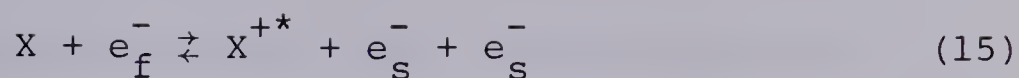
where the energy of the fast electron must be greater than the excitation potential of  $X^*$ . The probability of the forward process is greatest when the energy of the fast electron just exceeds the excitation potential of  $X^*$ . Analyte ions may also be produced by electron-atom collisions [58],



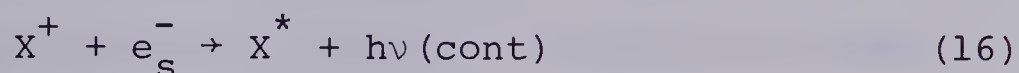
where the energy of the fast electron must exceed the ionization potential of the analyte atom. More energetic electrons can produce excited state ions



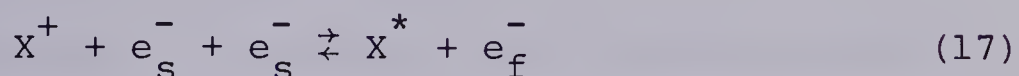




Analyte ions can recombine with slow electrons into excited states [59], in two body:

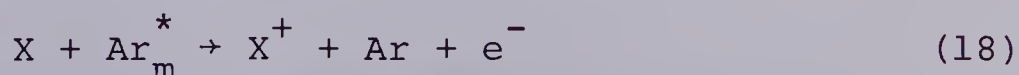


or three body recombination,

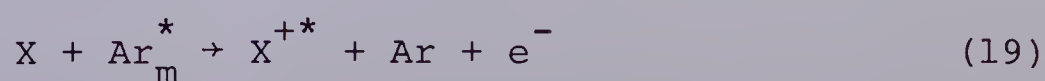


resulting in the production of excited state analyte atom species.

Alternate mechanisms for the generation of emitting species may involve argon species. Metastable argon has been implicated in ionization and excitation process through Penning ionization reactions [59-61]. In a scheme in which this type of reaction is present, analyte atoms are ionized, and/or ionized and excited depending on the energies involved with excess energy being carried away in the form of kinetic energy of the free electron. Thus the reaction [42]



will produce analyte ions for any species whose ionization potential is less than the metastable values of 11.55 and 11.71 eV. Similarly the reaction





will produce excited analyte ions. Brockaert et al. [62] have provided indirect evidence that this reaction may be important in the ICP. They have shown that emission from yttrium ion levels whose sum of ionization and excitation energies is in the range of 10-12 eV are most affected by the addition of an argon metastable quencher ( $\text{H}_3\text{BO}_3$ , or  $\text{Na}_2\text{B}_4\text{O}_7$  as a concomitant).

Direct excitation of atoms or ions is also possible through collisions of the second kind with argon metastable species. Thus atoms can be excited by,



and analogously for ions



The energy restrictions on these two reactions are quite critical, in that the excitation energy and argon metastable energy should match closely for highest probability of energy transfer. Beenekker [63] observed for argon and helium microwave induced plasmas,

"The ions of analyte atoms produced by Penning ionization are excited by metastable species of the plasma support gas, giving rise to the ion line emission observed. When this process is not possible for reasons of energy, these ions recombine with an electron to yield excited neutral atoms giving rise to the observed atom line emission."

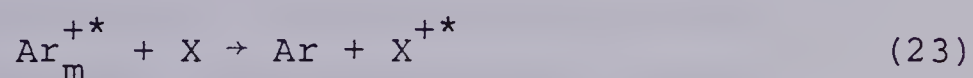


Beenakker also suggested the possibility of charge transfer reactions of the type;



which also has the energy constraint that the analyte ionization plus excitation energy should closely match the argon ionization energy. This type of charge transfer reaction is considered to be important in the energy region 15-16 eV [64], the ionization energy of the argon atom being 15.75 eV.

Jarosz and Mermet [50] also note the presence of some lines of sulphur ions for which the excitation energy is in the region of 30 eV and suggests that argon ion metastables ( $\text{Ar}_m^{+*}$ ) play a role through the mechanism;



the  $\text{Ar}_m^{+*}$  species having energies in the range 32.13 to 33.45 eV.

It is unlikely that any one of these mechanisms is the sole means of excitation in the ICP. Instead, depending on the energy requirements of the analyte species, the mechanism which leads to the most favourable probability of energy transfer must be considered. Additionally several of the mechanisms may be acting simultaneously to produce excited states, further complicating the inter-



pretation of plasma phenomena. A study of the spatial structure of emission in the plasma will certainly aid in delineating which of the mechanisms should be considered most important in the analytical ICP.

### Spatially Resolved Measurements

The well known adage, "a picture is worth a thousand words", is particularly applicable to scientific investigation. However, often it is not sufficient to simply present a photograph or an artistic sketch of an emission source, because many of the physical parameters which characterize the source cannot be directly observed, or often a parameter of interest is obscured by another. In these cases the investigator must use scientific instrumentation to isolate the parameter of interest and devise some system whereby the spatial variation of this parameter may be mapped. In this way the physical dependence of one parameter upon another can be accessed by a comparison of the spatial similarities. An example of this is found in a study of free-atom formation processes in flames undertaken by Cowley et al. [65]. They were able to correlate the spatial characteristics of metal oxide and free atom species with the spatial characteristics of flame produced molecular species such as CN, CH, C<sub>2</sub> and OH to account for the favourable





characteristics of the oxy-acetylene flame.

In a similar manner, Walters [66] was able to correlate the spatial dependence of emission intensity from metals in a spark discharge with the energy characteristics of the line being observed [66], the less ionized, less excited species being observed further from the spark channel. On the other hand continuum intensities peaked within the channel. Armed with this information he was able to postulate possible excitation mechanisms in the spark source. Also he suggested making use of this spatial separation to improve signal to noise, and signal to background ratios by observing emission from off the channel axis.

Most workers in the field of plasma spectroscopy recognize the utility of spatial profiling and have made use of the technique to augment their studies. The spatial distribution of temperature and electron number densities in the ICP have been studied by a number of workers [3,35-37,67], leading to the suggestion of a non-LTE plasma. Also the spatial effect of plasma operating conditions on emission intensities has been investigated [68-71]. These studies show a spatial structure which is highly dependent upon RF power and aerosol flow rate. Also the spatial effects of interferences have been studied in microwave plasmas [72-74],



DC plasmas [75] and ICPs [48,71,76,77]. The results of these studies will be discussed in greater detail in a subsequent chapter.

The usual modes of acquisition of spatial information from the ICP are vertical, that is parallel to the plasma axis, or horizontal, that is at right angles to the plasma axis. The spatial information thus gathered is the integral of emission from all depths from within the source. From a fundamental standpoint it is desirable to deconvolute these lateral emission intensities such that radial distributions can be obtained. The radial information provides emission intensity information as a function of distance from the central axis of the discharge. The transformation from lateral to radial information is usually performed using a mathematical technique called an "Abel inversion" [78]. There are a variety of methods for implementing this for horizontal profiles and it has been used extensively for the study of spectroscopic sources. Much of the early work in this area was in the domain of the plasma physicist [79,80], but more recently the method has been applied to spark discharges [1,81,82] and ICPs [3,36,37,67,76,83].

Traditionally the acquisition of detailed spatial profiles has involved the translation of monochromator and detection system, a data point being acquired



for each translation increment. Such a process is time consuming and may lead to inaccuracies due to source changes during the measurement process. Franklin et al. [85] introduced the idea of using photodiode arrays mounted vertically in the exit focal plane of the monochromator to dispense with the need to translate the measurement system to obtain detailed spatial profiles. This system has been used successfully in several studies involving measurement of emission intensity information from the ICP. Edmonds and Horlick [69] investigated the effects of aerosol flow rate and power on spatial profiles of emission, and Horlick and Blades [77] and Kawaguiki et al. [71] studied the effect of EIE's on analyte emission intensities. Blades and Horlick [83] have also described a photodiode array profiling system for implementing Abel inversions on emission from an ICP.

This approach has been used to acquire all of the spatial data presented in this thesis. The measurement system will be described in detail in the following chapter. The data gathered will be discussed in subsequent chapters.



## CHAPTER II

### EXPERIMENTAL

#### Plasma Generation

The instrumentation used for generating and sustaining the plasma is outlined in Figure 3. The system consists of a high power radio frequency (RF) generator, an automatic tuning and impedance matching network, a plasma torch assembly, a nebulizer and spray chamber for sample introduction, and a source of argon gas with associated gas pressure and gas flow controllers.

The RF generator (Model HFS 3000D), automatic power control (Model ADC5-3), automatic matching network (Model AMN-2500E), and plasma torch assembly (Model PT-2500), were purchased from Plasma-Therm Inc., Kresson. N.J.

The RF generator is of the crystal-controlled type operating at 27.12 MHz with variable power output from 0 to 3.0 kw. The tuning network allows the plasma to be ignited at the proper impedance point, with automatic returning by two variable vacuum capacitors, when the plasma is established. The three turn RF coil is constructed from 1/3" copper tubing and is connected to water cooled copper blocks inside the plasma housing. The coil is wound with a 26 mm inside diameter and 1 mm spacing between turns.







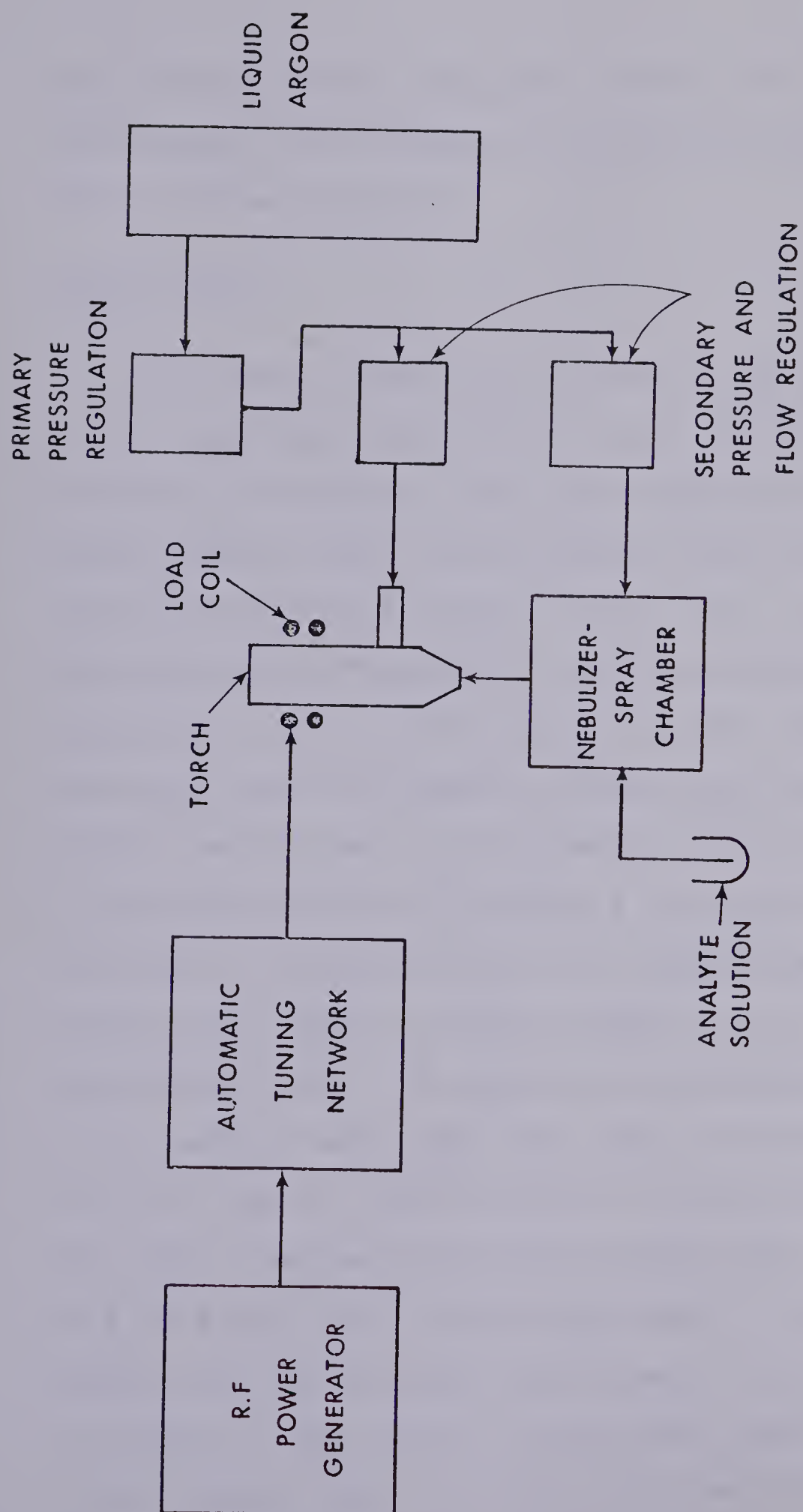


Figure 3. Block diagram of ICP instrumentation.



The distance between the torch and coil is 3 mm. Water is continuously fed through the load coil to keep it cool during plasma operation.

### Plasma Torch

The plasma torches used in this study were constructed at the Department of Chemistry glass blowing shop at the University of Alberta. The torch consists of three concentric quartz glass tubes fused to form a single unit of the type described by Fassel et al. [11]. A diagram of the torch and its dimensions is given in Figure 4. The outer quartz tube, 20 mm od and 18 mm id, serves to confine the argon gas during passage through the load coils. The middle quartz tube is tulip shaped, 12 mm id and 14 mm od at its exit and serves to direct a low flow of argon gas at the base of the plasma once it is established. This positions the plasma so that its base is 1 to 2 mm above the inner quartz tube. The argon gas is introduced tangentially at the base of each tube. The inner or aerosol tube is 5 mm od, 3 mm id, constricted to 1.5 mm id at its exit. This tube traverses the length of the torch and is joined to a 5/12 ball joint at the torch base. This ball joint couples with the aerosol spray chamber in the manner shown in Figure 5. The torch is positioned such that the exit of the aerosol tube is 2-3 mm below the bottom of the load



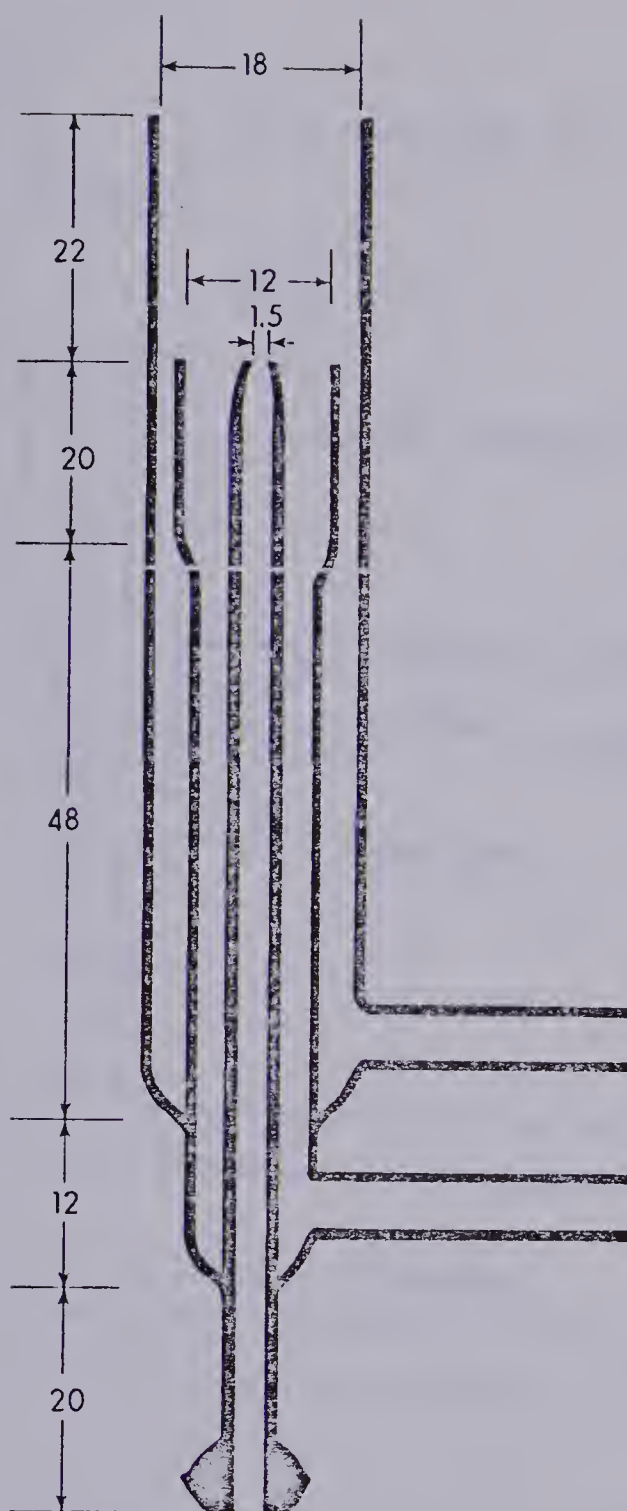


Figure 4. ICD torch (dimensions in in).



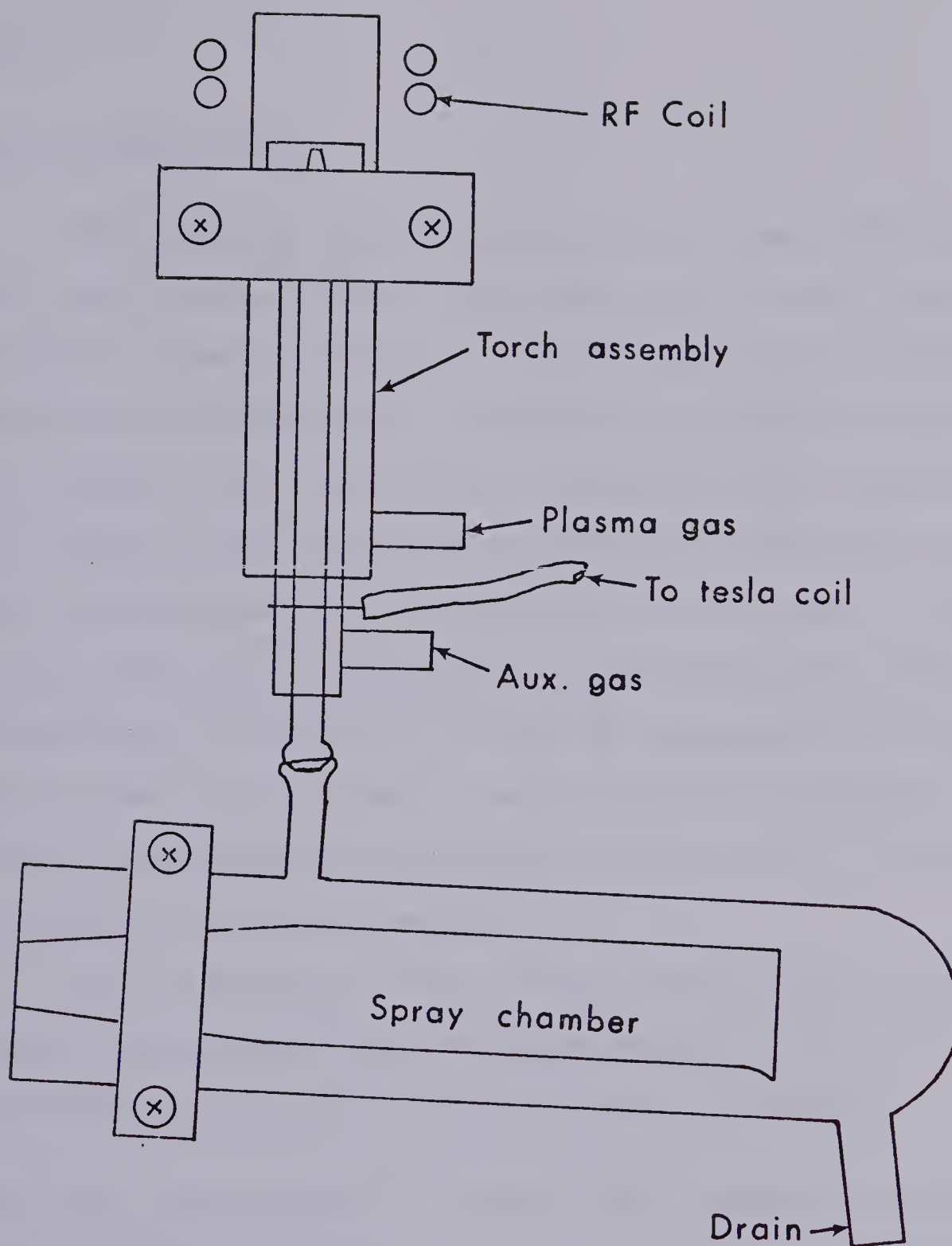


Figure 5. ICF torch, spray chamber assembly.





coil.

### Aerosol Generation

One advantage that concentric type glass nebulizers [86] have over crossflow nebulizers [84] is that the tip alignment remains fixed for the lifetime of the nebulizer, whereas the alignment of a crossflow may change during hookup or cleaning. The operation of concentric type nebulizers is, however, more sensitive to solutions containing high salt concentrations or suspended particles, such as dust. If the operating reliability of crossflows under high salt conditions is required, it would be advantageous to have one with "fixed tip alignment", which could be withdrawn, cleaned, and re-inserted into the carrier with no change in operating characteristics.

For the purpose of the studies carried out in this thesis, such a nebulizer was constructed, tested, and used successfully for all of the experiments described.

Nebulizer construction. Figure 6 is a schematic diagram of the fixed tip crossflow nebulizer. The crossflow tips, A and B are made of 1 mm id, 2 mm od quartz capillaries, 7-8 cm long, which have been drawn out in a flame; tip A at a right angle. The two capillaries are inserted into a small Teflon jig with two holes drilled in it to fix



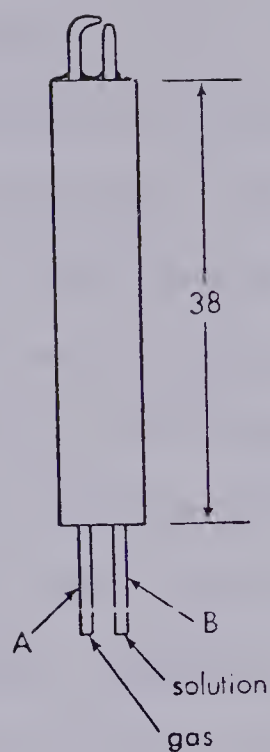


Figure 6. Schematic diagram of fixed tip crossflow nebulizer (dimensions in mm).

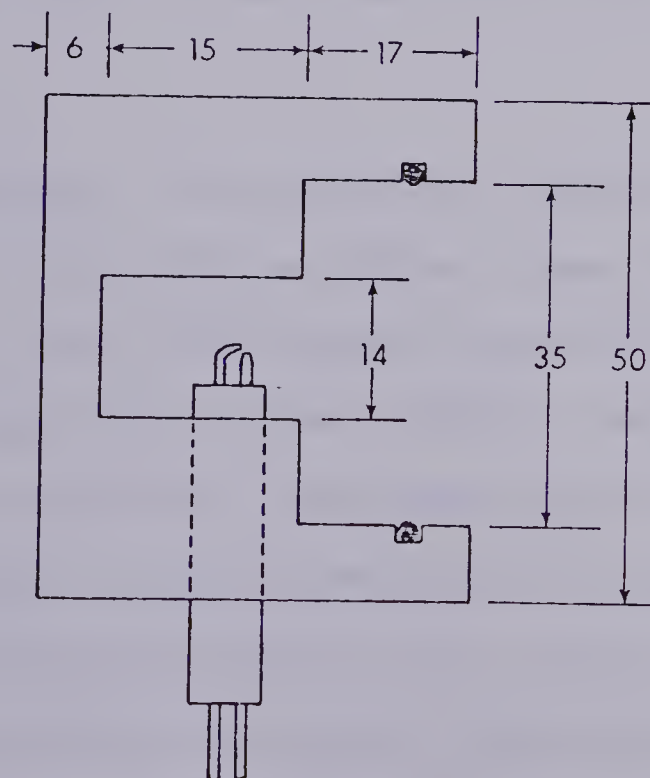


Figure 7. Nebulizer and Teflon carrying block (dimensions in mm).



the centre-to-centre separation at 3 mm. The tips are then "ground down" using a diamond saw until "proper" tip overlap and separation are achieved. Tip A is fire polished to close its tip diameter so that the gas flow rate through it is less than 1 lpm at 20 psig pressure. While still in the jig the capillaries A and B are connected to argon gas and sample tubes respectively and the tips aligned to give maximum aerosol production. They are then bonded together using E-63 Epoxy (Techkits, Demarust, New Jersey). The tips are subsequently sealed into an 8 mm od glass tube 38 mm long using RTV sealant (Silastic 732 RTV Adhesive/Sealant, Dow Corning, Midland, Mich.) with 4 to 5 mm of the tips exposed. The nebulizer may then be inserted into a standard Teflon carrying block with an 8 mm hole in the side as shown in Figure 7.

Nebulizer performance. The nebulizer performance was tested using a 5 kw Argon ICP obtained from Plasma Therm Inc. consisting of a 27.12 MHz RF generator (Model HFS-5000 D) with automatic power control box (ATPAC), automatic matching network (AMN for HFS-5000), and plasma torch assembly (PT-1).

The measurement system consisted of a Heath 1/3 meter monochromator (GCA/MacPherson EV-700) coupled to a Heath P.M.T. module (EV-701-30) with 1P28 photomultiplier tube. Emission intensity measurements were taken using a microprocessor-based system, constructed concurrent to this study



for the purpose of making such measurements. Details of the data acquisition system are included in Appendix A.

These results describe one of five nebulizers the author has constructed using the procedure outlined. The efficiency of the fixed tip crossflow nebulizer was calculated by aspirating a known amount of distilled water through the nebulizer with spray chamber and torch attached and collecting the drain-off liquid. The efficiency measured was 3.2% for a sample uptake rate of 8 ml per minute, when run at 0.85 lpm aerosol flow rate corresponding to a pressure of 20 psi. The fluid uptake rate of the nebulizer can be controlled at assembly time by adjusting the size of sample tip B. In general, the larger the tip diameter, the higher the sample uptake rate (this also degrades efficiency of the nebulizer due to leakage of the sample at the tip edges). One of the results of a sample uptake rate of 8 ml per minute has been that the nebulizer can be effectively used for high salt solutions. To show this, a 1 ppm Ca solution containing 2% NaCl was nebulized continuously for 1/2 hour. The emission intensity of Ca(II) measured at 393.3 nm varied no more than 6.8% from the average over this period of time. The variation in signal appeared random, and the intensity at the end of the 1/2 hour period was within 1% of the intensity at the beginning.

Analytical performance of the nebulizer was compared





to a conventional crossflow nebulizer of the type described by Kniseley [84], and a concentric glass nebulizer (Meinhard Model TR-30-A1), by aspirating a 1.0 ppm solution of Ca and integrating the emission intensity at 393.3 nm. The average, standard deviation, and signal to noise ratio were calculated on 16 consecutive 1 second integrations. The results are given in Table II.

The emission intensity was optimized for the particular nebulizer by adjusting the aerosol flow rate but otherwise all conditions were the same. The relative intensity and its standard deviation are shown in column 1 and the signal to noise ratio and its standard deviation in column 2. These figures were arrived at by averaging 10 sets of 16, 1 second integrations.

The fixed tip crossflow nebulizer constructed by the author compares favourably with the other two and can be used in any application where the other two might be used. The nebulizer can be constructed quickly and easily and once made retains its operating characteristics for its lifetime.

#### Spatial Profiles With A Photodiode Array

The measurement system employed for emission profile measurements consists of a Heath (GCA/MacPherson EV-700) 0.35 meter monochromator with a 256 element self-scanning photodiode array (Reticon Model RL-256/128). The photo-



TABLE II

COMPARISON OF CONVENTIONAL CROSSFLOW, MEINHARD,  
AND FIXED TIP CROSSFLOW NEBULIZERS

<u>Nebulizer Type</u>	<u>Relative Intensity (<math>\sigma</math>)</u>	<u>S/N (<math>\sigma</math>)</u>
Fixed Tip	65.4 (1.52)	95.5 (25.8)
Conventional	70.0 (1.16)	98.2 (13.9)
Meinhard Concentric	47.1 (1.29)	79.4 (26.0)



diode array is mounted vertically in the exit focal plane of the monochromator. The concept of spectral source profiling using a photodiode array has been described and implemented by Franklin et al. [85], and Edmonds and Horlick [69]. The method is outlined in Figure 8. An image of the source (the plasma in this case) is formed on the entrance slit of the monochromator using a 10 cm focal length bi-convex quartz lens. The entrance slit passes a thin vertical slice of the source image into the monochromator. The grating disperses the source light into its spectral components which fall on the exit focal plane of the monochromator. If one of the spectral components is allowed to fall on the vertical photodiode array, a readout of the array provides a quantitative measurement, at the wavelength selected, of the image formed at the entrance slit of the monochromator. The dimension of the image formed is altered by adjusting the distances between the source and lens, and the lens and monochromator, according to the magnification formulae for bi-convex lenses.

#### Computer Coupled Photodiode Array

All studies were carried out using a Reticon RL-256/128, 256 element photodiode array. The individual photodiodes are 25.4  $\mu\text{m}$  wide and are placed on 25.4  $\mu\text{m}$  centres; thus the light sensitive area of the array is 6.5 mm in length, and



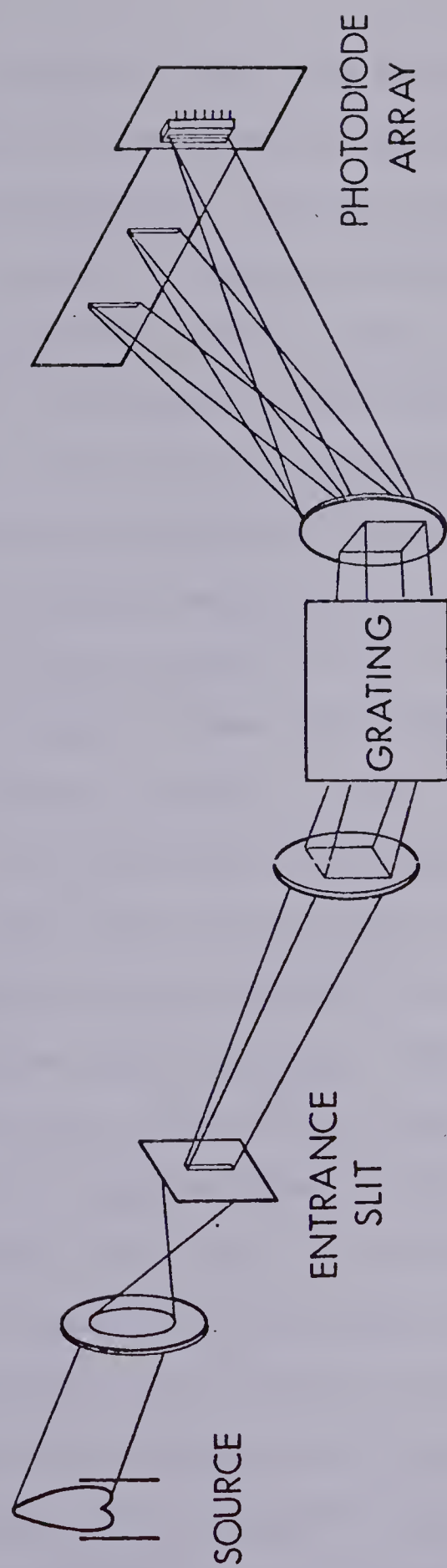


Figure 8. Photodiode array profiling concept.





25.4  $\mu\text{m}$  wide. The array and associated electronics are housed in a small metal cabinet. The front face plate of the monochromator has been removed and the cabinet mounted in its place. The exit folding mirror must be removed to allow spectral lines to fall on the array. The array, when mounted vertically in the exit focal plane, in a sense, acts as the exit slit of the monochromator. The characteristics of photodiode arrays and some examples of their implementation have been reviewed [87-89].

A block diagram of the computer controlled photodiode array readout system is provided in Figure 9. The array provides two control lines, a start, and a clock, which are used for timing and sequencing array signal acquisition. The start pulse signals the computer that the array has completed its integration and initiates readout of information from the array. The time between start pulses controls the integration time and is switch selectable in a binary sequence from 0.0128 to 26.43 sec when operating at 50 MHz clock rate. The clock controls the rate at which data is read from the array and is also used to control digitization and storage of the array output signal. The clock rate normally used is 50 KHz; thus a single scan of the array can be acquired and stored in about 5 msec. The array is cooled to  $-10^{\circ}\text{C}$  using a Peltier type cooler mounted on its back face. The monochromator is purged with nitrogen



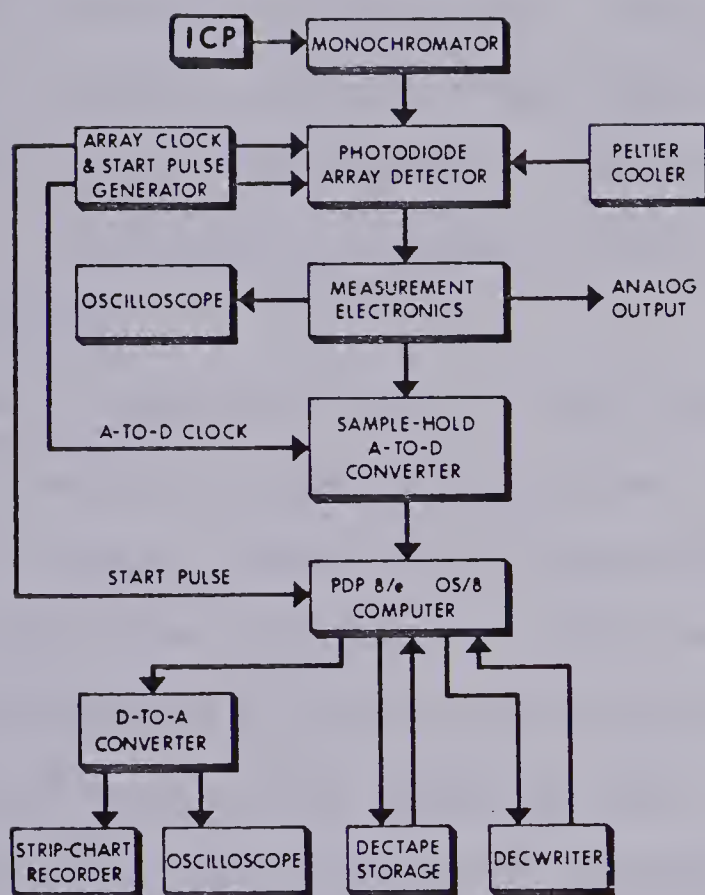


Figure 9. Block diagram of computer controlled photodiode array profiling system.



gas to prevent icing of the array.

The measurement system consists of a notch filter (PAR Model 210 selective amplifier) which is set at  $1/4$  the clock rate to remove the fixed pattern signal associated with clocking out the array information. The output from this is fed into a series of operational amplifiers which serve to amplify, filter, and provide a voltage offset for the array signal. A schematic diagram of this circuit is provided in Figure 10.

Analog outputs from the array are digitized using a high-speed 12 bit analog to digital converter (Model 600-8E, ADAC Corporation, Woburn, Mass.) which interfaces to the PDP8/e computer mainframe and operates under software control. The computer is a Digital Equipment Corporation PDP8/e computer with 16 k of core memory operating OS/8 from a DEC tape-based system. The FORTRAN/machine language program used to acquire and manipulate data from the diode array is provided in Appendix B. The acquired signal may be stored on DEC tape, displayed on an oscilloscope, plotted on an XY recorder (Hewlett-Packard Model 7045A), or output to a Decwriter.

The plasma torch assembly, lens, and monochromator-photodiode combination are mounted on an instrument rail bed analogous to the system designed and developed by Walters [90,91]. This system provides precise, stable



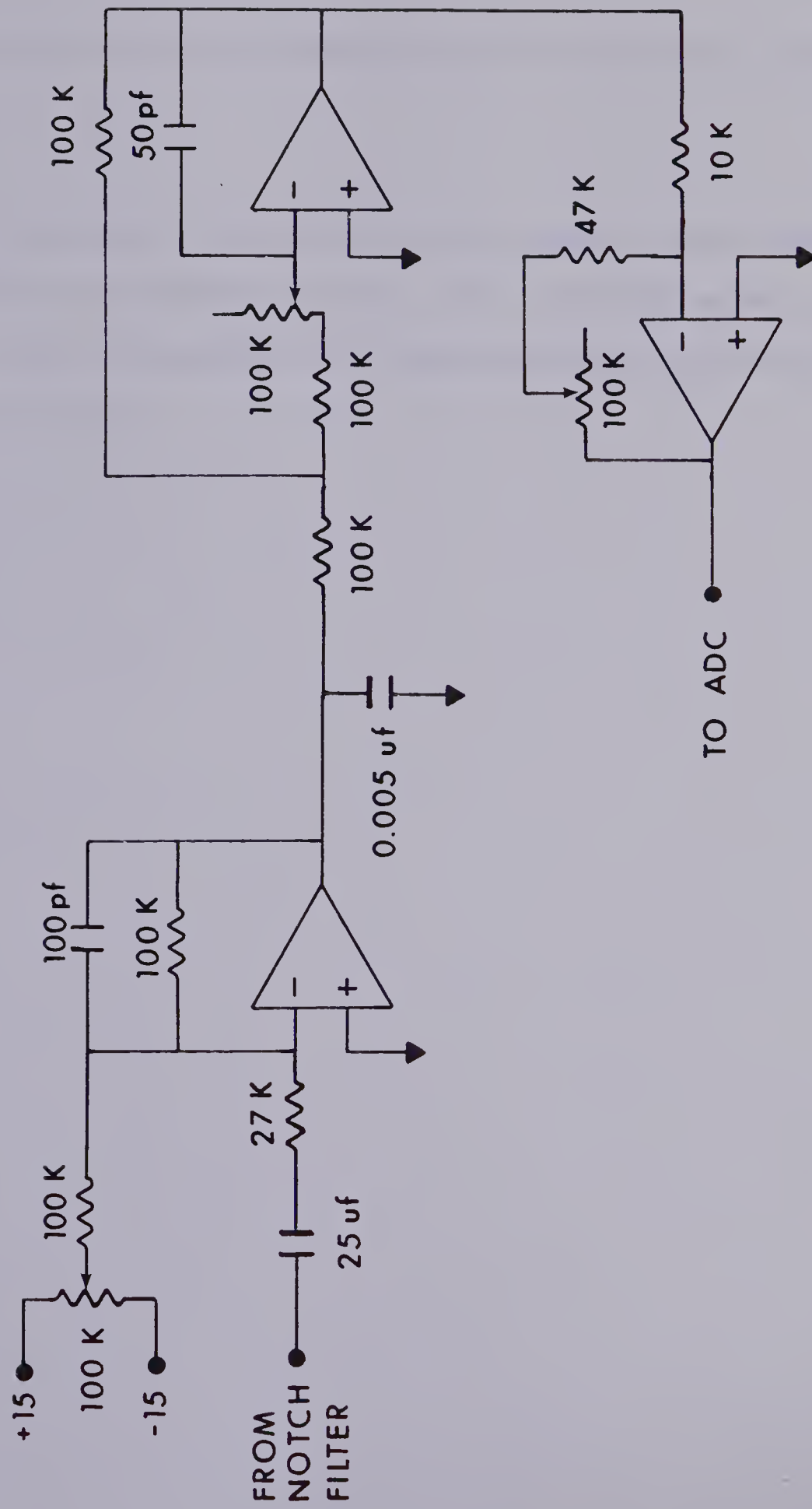


Figure 10. Signal conditioning electronics for photodiode array.





alignment while allowing flexibility of experimental design.

### Chemicals

All solutions were made up using reagent grade chemicals (Fisher Scientific Company) and distilled water. All dilutions were performed using laboratory pipettes and volumetric flasks.



## CHAPTER III

### VERTICAL SPATIAL FEATURES OF ANALYTE EMISSION

The establishment of ICP-OES as a simultaneous multi-element analysis method has meant finding a set of compromise conditions for operation of the associated instrumentation [46,47,92,93]. Apart from fixed parameters such as RF frequency, method of power coupling, and instrumental dispersion and detection system, there are three major variable parameters. When analyte is introduced into the plasma the observed emission intensities are subject to the following parameters:

- (1) RF power coupled into the plasma.
- (2) Aerosol carrier gas flow.
- (3) Observation height and zone above the load coil.

These parameters also affect the argon continuum and line emission intensity.

The way in which the variation of these parameters affects net emission intensity was investigated by Boumans and DeBoer [46,92], for the purpose of establishing compromise conditions for simultaneous multielement analysis. In these early investigations they found, in general, that emission intensity "...increases with power,...decreases with increasing observation height,...depends to only a small extent on carrier gas flow", and, "...is not appreciably



affected by the addition of an easily ionizable element." They also observed that spectral line intensities pass through a maximum when the carrier gas flow rate is increased. This effect was also observed by Berman and McLaren [93], who noted that as the aerosol flow rate is increased, the line to background ratio increases, reaches a maximum, and then decreases over the range 0.7 to 1.0 liters per minute (lpm). They also observed that for both Cr atom and Cr ion emission, net line intensity passed through a maximum as power was varied from 1.0 to 1.8 kw, although atom lines peaked at a lower power than ion lines.

In a later more complete study Boumans and DeBoer [42] observed the variation of continuum background intensity, net line emission intensity, and signal to background ratio as a function of power input for MnI, BaI, LiI, BaII, CdI, ZnI, MnII, and CdII species. They found that the net line signal increased rapidly initially and then plateaued for CdII, MnII, ZnI, and CdI as the power was varied from 0.8 to 2.2 kw, whereas the net line signal decreased for LiI, BaI, and MnI over the same power range. Emission intensity for BaII increased initially, then remained unchanged after 1.2 kw. These observations were for a 5 mm high observation window centered at 15 mm above the load coil. They related this behaviour to the "normal temperature" of the lines, which is in turn related to the



ionization and excitation potentials of the species involved. Boumans later termed lines which showed an increase in intensity with an increase in power as "hard" lines and those which showed a decrease in intensity with an increase in power as "soft" lines [94]. A full treatment and discussion of the importance of "normal temperature" to spatial structure of analyte emission will be given in the following chapter.

An interpretation of the response of line intensity to changes in RF power and aerosol flow rate is provided in spatial studies carried out by Edmonds and Horlick [69] and Dube and Boulos [68]. Both groups acquired analyte emission intensity information as a function of vertical height above the load coil. Both groups found that the emission intensity profiles for analyte species were in the general shape of a "camel's hump". That is, as one observes emission intensity up the analyte channel it initially increases, reaches a maximum and then decreases forming an emission intensity peak or maximum. The position of this peak maximum was found to shift upward as aerosol flow rate was increased. This suggests that the emission intensity maximum observed by Boumans and DeBoer as a function of aerosol flow rate is the result of an upward shift in the spatial profile across the spatial observation window. Edmonds and Horlick further found that analyte spatial em-





ission profiles fell into two distinct categories based on their response to applied power at a fixed aerosol flow rate. The intensity maximum of the atom lines of Ca, Ba, Sr, Cr, and Ti shifted to a lower position in the plasma as power was increased from 1.25 kw to 2 kw, whereas the intensity maximum of the ion lines of Ba, Sr, Ti, and Ca did not shift as power was varied over the same range. They concluded that atom lines exhibited one type of spatial dependence on power and ion lines a different type of spatial dependence. The atom lines of Cu and Ag, however, were observed to behave like "ion" lines.

A correlation between the observations of Boumans and DeBoer and Edmonds and Horlick can be made by examining the contents of Figures 11, 12, and 13. Figures 11 and 12 are similar to the type of data published previously [69]. The plots given in Figure 11 are vertical spatial profiles of Ca emission from the 422.7 nm atom line. The frames (a), (b) and, (c) relate to aerosol flow rates of 0.7, 0.8, and 0.9 lpm respectively. The numbers from 1 through 5 on each frame represent applied powers; these are : (1) 1.0 kw, (2) 1.25 kw, (3) 1.50 kw, (4) 1.75 kw, and (5) 2.0 kw. The emission intensity is plotted from 0 mm to 16 mm above the load coil, centered on the analyte channel. In agreement with the observations of Edmonds and Horlick, as the RF power is increased, the position of the maximum in em-



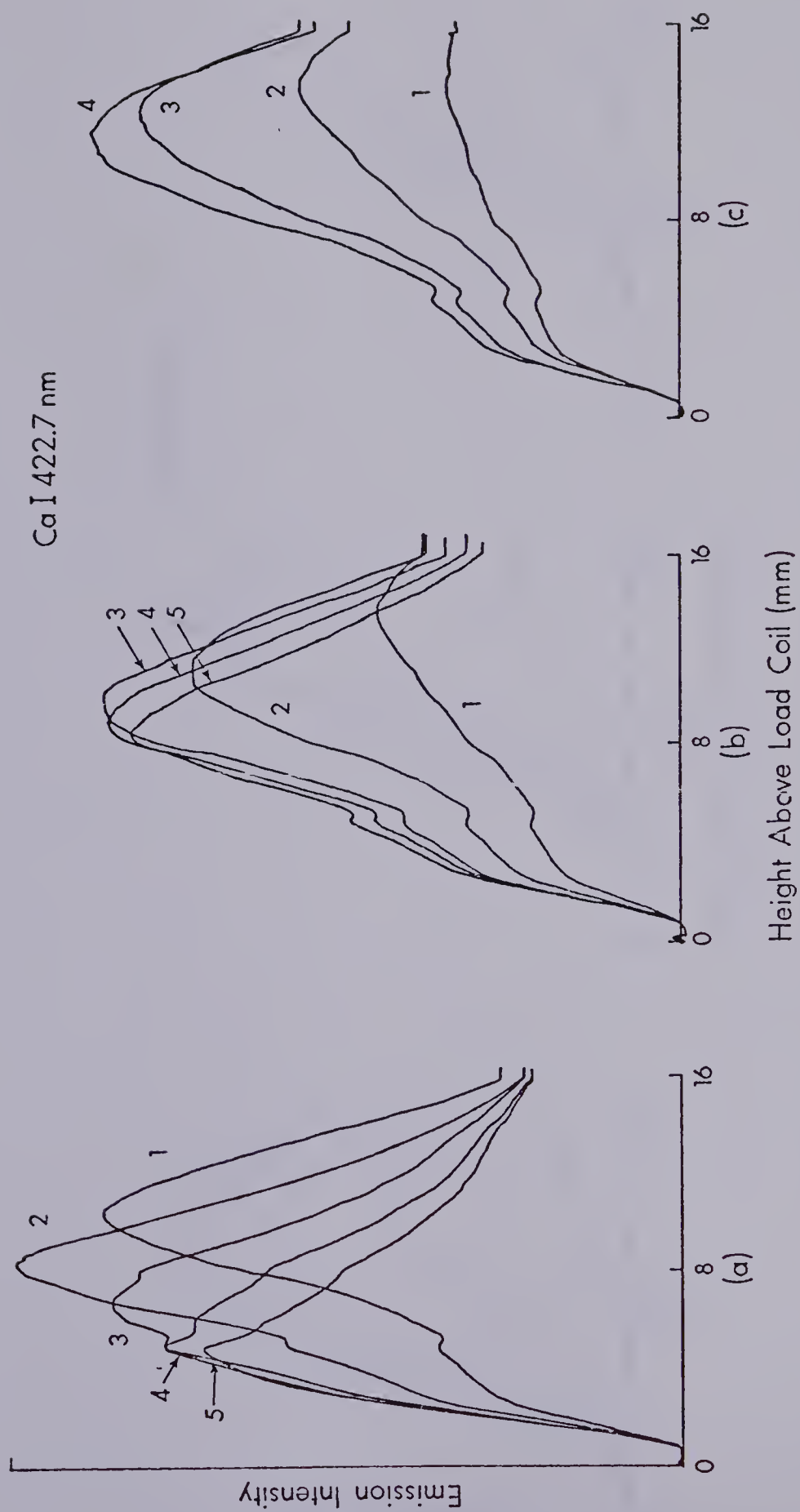


Figure 11. Vertical spatial profiles for Ca I 422.7 nm. Acetone flow rates; (a) 0.7 lpm, (b) 0.9 lpm, (c) 0.9 lpm RF power; (1) 1.0 kw, (2) 1.25 kw, (3) 1.50 kw, (4) 1.75 kw, and (5) 2.0 kw.



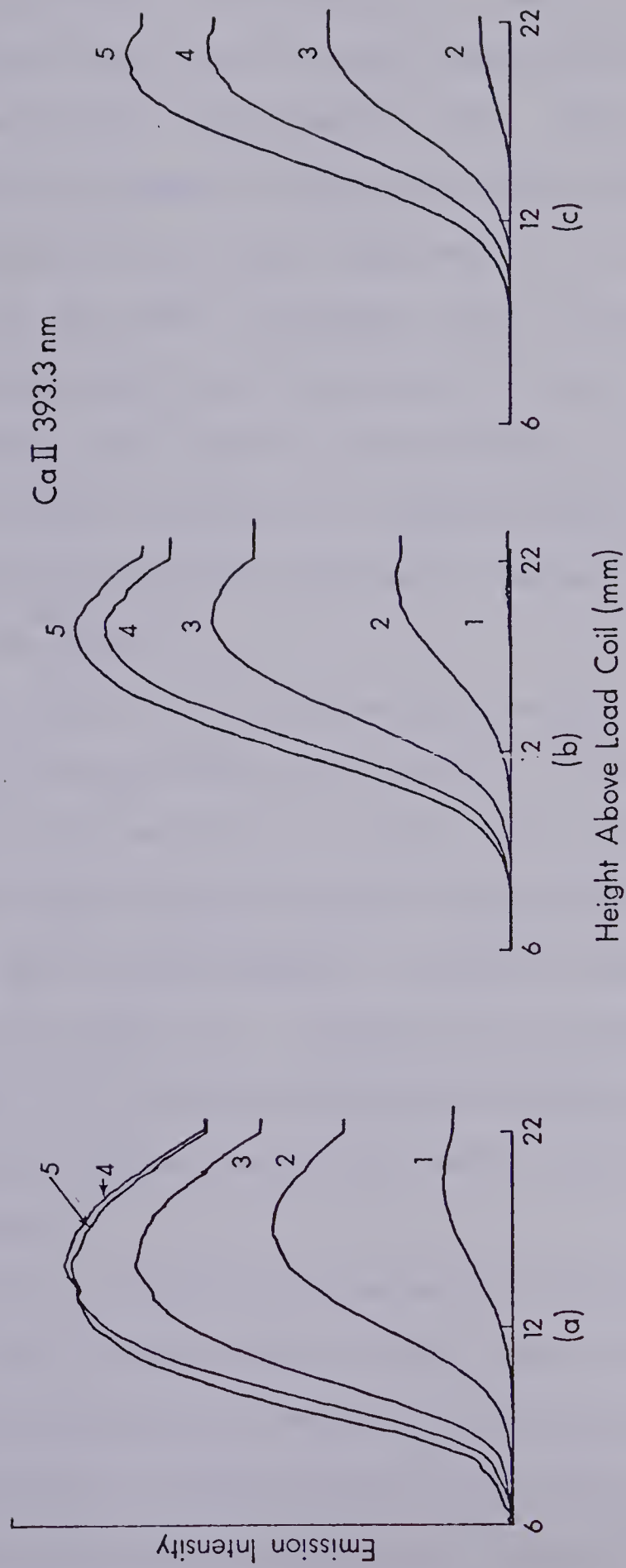


Figure 12. Vertical spatial profiles for Ca II 393.3 nm. Aerosol flow rates; (a) 0.7 lpm, (b) 0.8 lpm, (c) 0.9 lpm, RF power; (1) 1.0 kw, (2) 1.25 kw, (3) 1.50 kw, (4) 1.75 kw, and (5) 2.0 kw.



ission intensity shifts from higher to lower in the aerosol channel. Similar behaviour has been observed by Kawaguchi et al. [71], and Savage and Hieftje [96]. This is demonstrated in the sequence in frame (a) going from the plot labelled 1 through to the plot labelled 5. In addition, the net intensity of the peak increases from 1.0 to 1.25 kw, and then decreases from 1.25 kw up to 2.0 kw. At a fixed power (for example for curve 2) an increase in aerosol flow rate shifts the peak maximum to a higher position above the load coil and simultaneously decreases the net emission intensity of the peak.

Analogous plots for the emission from the ion line of Ca at 393.3 nm are provided in Figure 12, in the region 6 to 22 mm above the load coil. The ion line peaks at higher positions above the load coil and the maximum does not show the same shift with changes in applied power that is observed for the atom line. Instead, as the RF power is increased from 1.0 to 2.0 kw, the net intensity increases, while maintaining approximately the same spatial profile height dependence.

If one were to observe the emission intensity from CaI and CaII with an instrument with a fixed observation height and relatively small vertical entrance slit (such that a narrow spatial region of the plasma was observed) we would observe the data presented in Figure 13. This





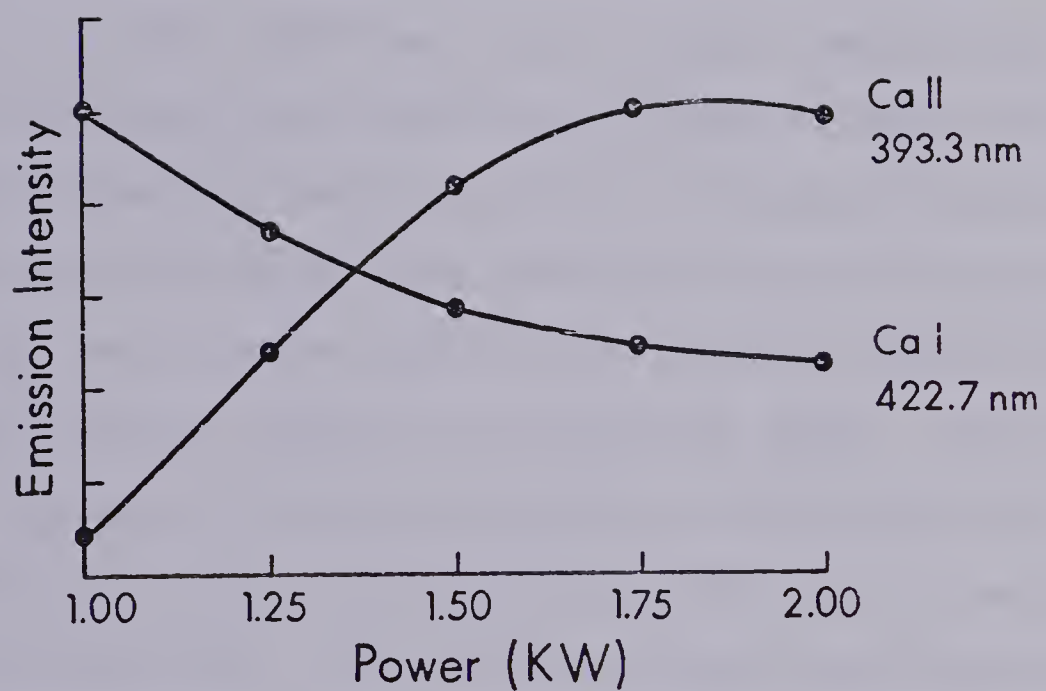


Figure 13. Emission intensity of CaI and CaII as a function of RF Power at an observation height of 14 mm.



figure provides a plot of emission intensity at a height of 14 mm above the load coil for CaI and CaII obtained from Figures 11 and 12 for various RF powers. It can be seen that the intensity of CaI decreases with applied power, and the intensity of CaII increases with applied power plateauing at higher levels of power. This is precisely the type of differing behaviour described by Boumans and DeBoer for the "soft" and "hard" lines respectively. In all likelihood their observations were probably the result of the differing spatial behaviour of the different species. Thus the division of line behaviour into the classes of hard and soft can be based on the spatial profile behaviour in response to changes in the applied power. Soft lines show the type of spatial behaviour exhibited by CaI, whereas hard lines are typified by the type of spatial behaviour of CaII. It should be noted that the relative intensities of the two lines are not the same and vary with observation height. This information is not apparent from the plots provided. For example, at a height of 6 mm the ratio of CaII emission to CaI emission is 1.54; at 20 mm this ratio is 15.5, at 0.85 lpm aerosol flow rate and 1.5 kw RF power.

On the basis of the previous discussion we can refer back to the plots of Boumans and DeBoer[42] and predict that the 670.8 nm Li atom line will show marked spatial variation



with power, whereas CdI (228.8 nm), ZnI (213.9 nm), MnII (403.1 nm) and CdII (226.5 nm) will not. The accuracy of this prediction is reflected in the spatial profiles provided in Figures 14, 15, 16, 17, and 18 for the above lines. LiI plotted in Figure 14 shows spatial variation in the region 4 to 18 mm above the load coil as power is changed from 1.25 kw to 2.0 in 0.25 kw increments corresponding to plots 2 to 4. These were taken at 0.85 lpm aerosol flow rate. On the other hand, CdI, CdII, MnII and ZnI do not show spatial shifts with changes in RF power. For the sake of completeness the spatial variation of emission intensity with power and flow rate have been included for CdI, CdII, MnII, and ZnI. Also, in the plot for ZnII provided in Figure 19, ZnII is seen to behave like a hard line. For the plots given in Figures 15 to 19, the frames (a), (b), and (c) represent aerosol flow rates of 0.9, 1.0, and 1.1 lpm respectively. The numbers on each frame represent the power applied in the following manner: (1) 1.25 kw, (2) 1.50 kw, (3) 1.75 kw, (4) 2.0 kw, and (5) 2.25 kw.

In all cases, the "hard" lines are seen to peak at about 18-20 mm above the load coil, and to decrease in net intensity with a decrease in applied RF power, but not shift in spatial position. The effect of an increase in aerosol flow rate is to shift the emission intensity peak only slightly higher in spatial position, while simul-



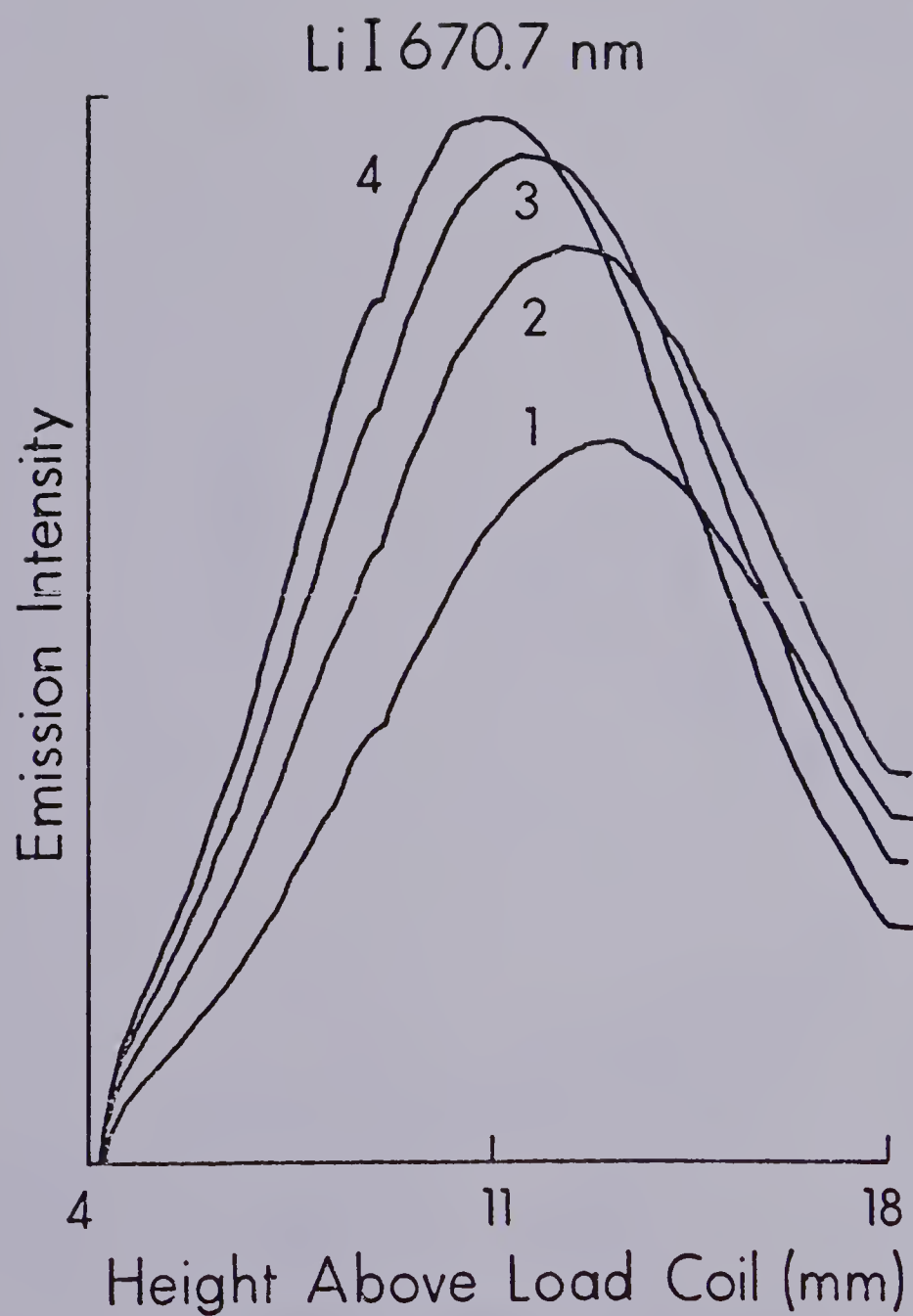


Figure 14. Vertical spatial profiles for Li I 670.8 nm. RF power; (1) 1.25 kw, (2) 1.50 kw, (3) 1.75 kw, and (4) 2.0 kw.





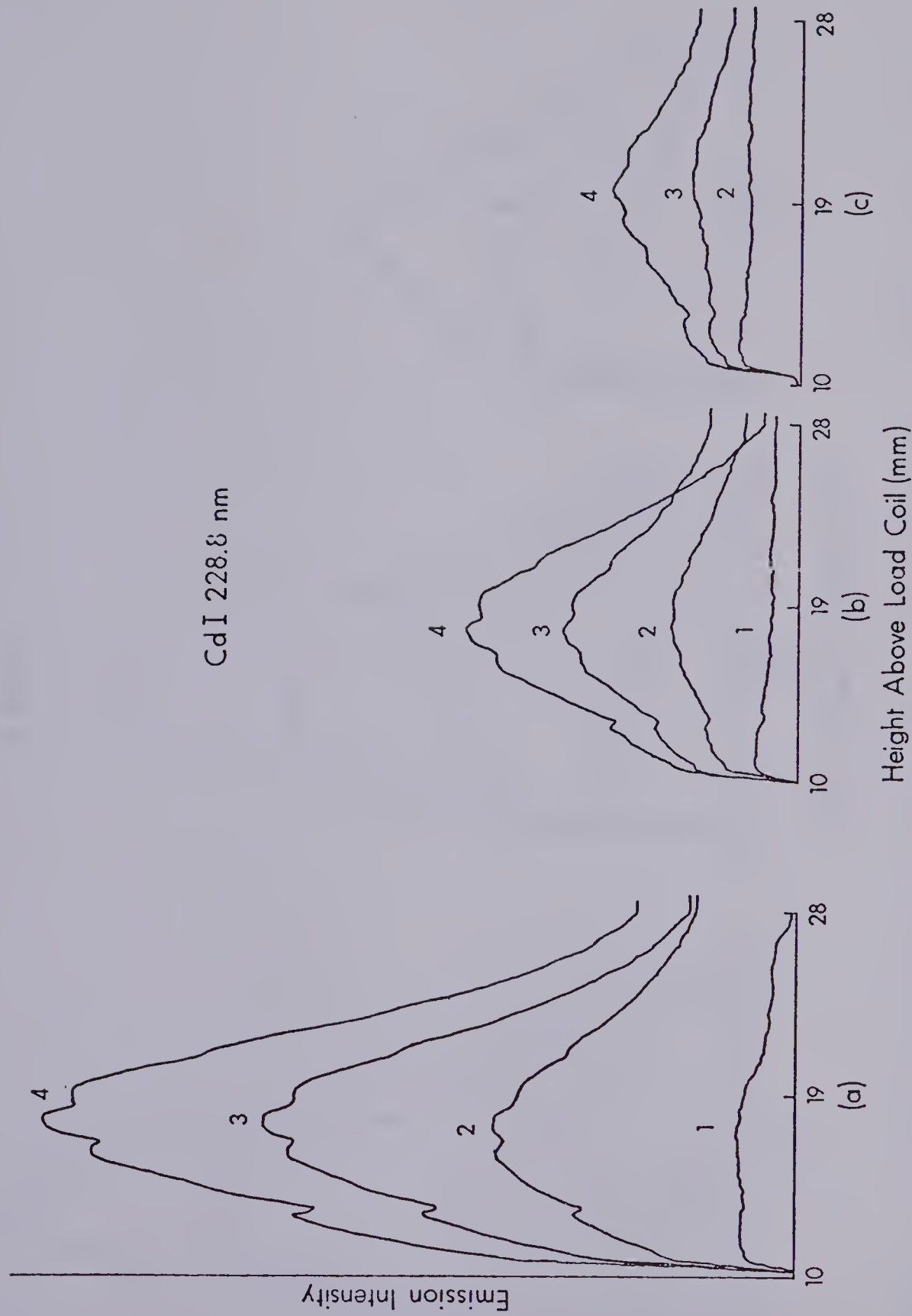


Figure 15. Vertical spatial profiles for CdI 228.8 nm. Aerosol flow rates; (a) 0.9 lpm, (b) 1.0 lpm, and (c) 1.1 lpm. RF power; (1) 1.25 kw, (2) 1.50 kw, (3) 1.75 kw, (4) 2.0 kw, and (5) 2.25 kw.



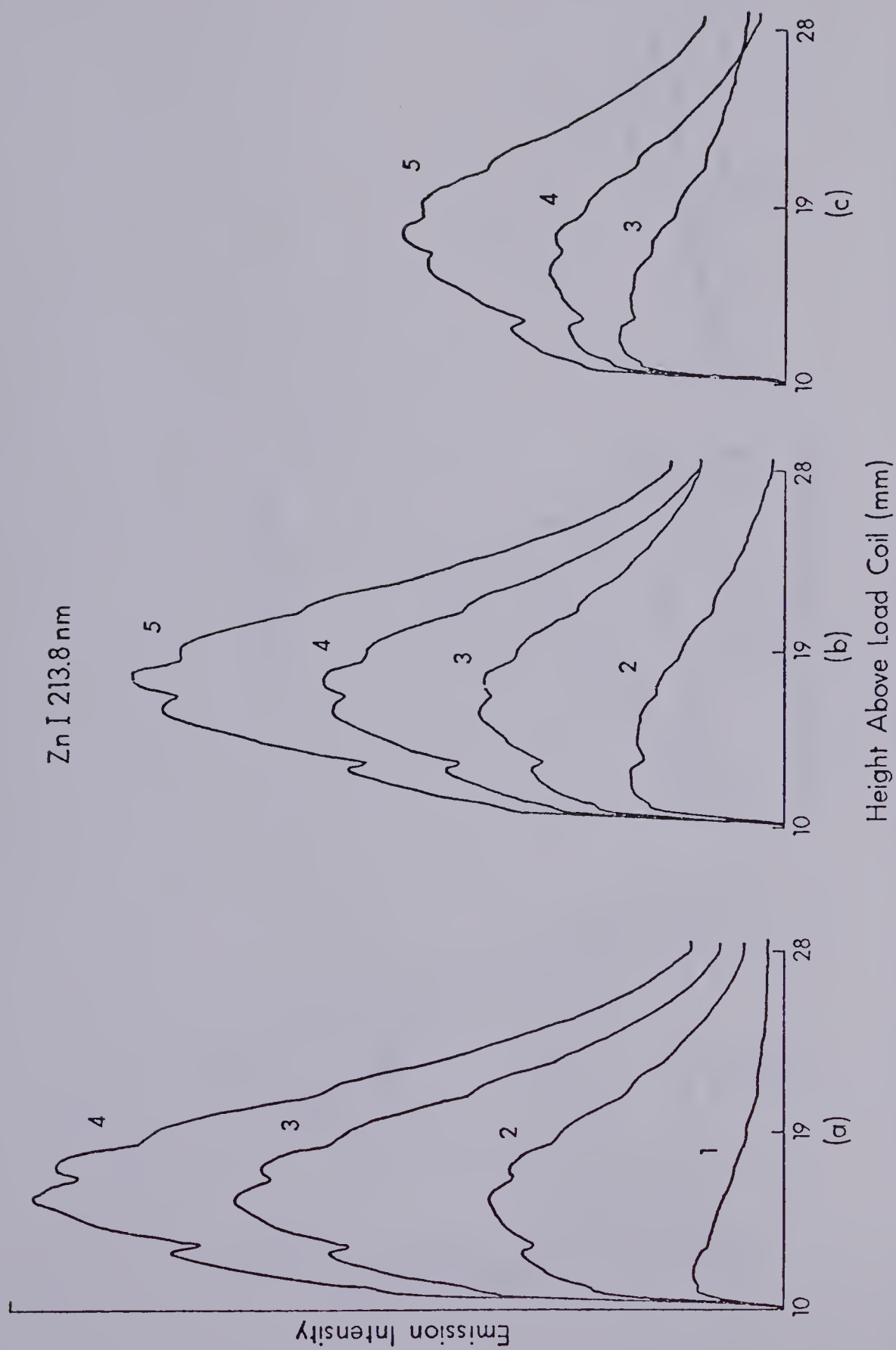


Figure 16. Vertical spatial profiles for Zn I 213.8 nm. Aerosol flow rates; (a) 0.9 lpm, (b) 1.0 lpm, and (c) 1.1 lpm. RF power; (1) 1.25 kw, (2) 1.50 kw, (3) 1.75 kw, (4) 2.0 kw, and (5) 2.25 kw.



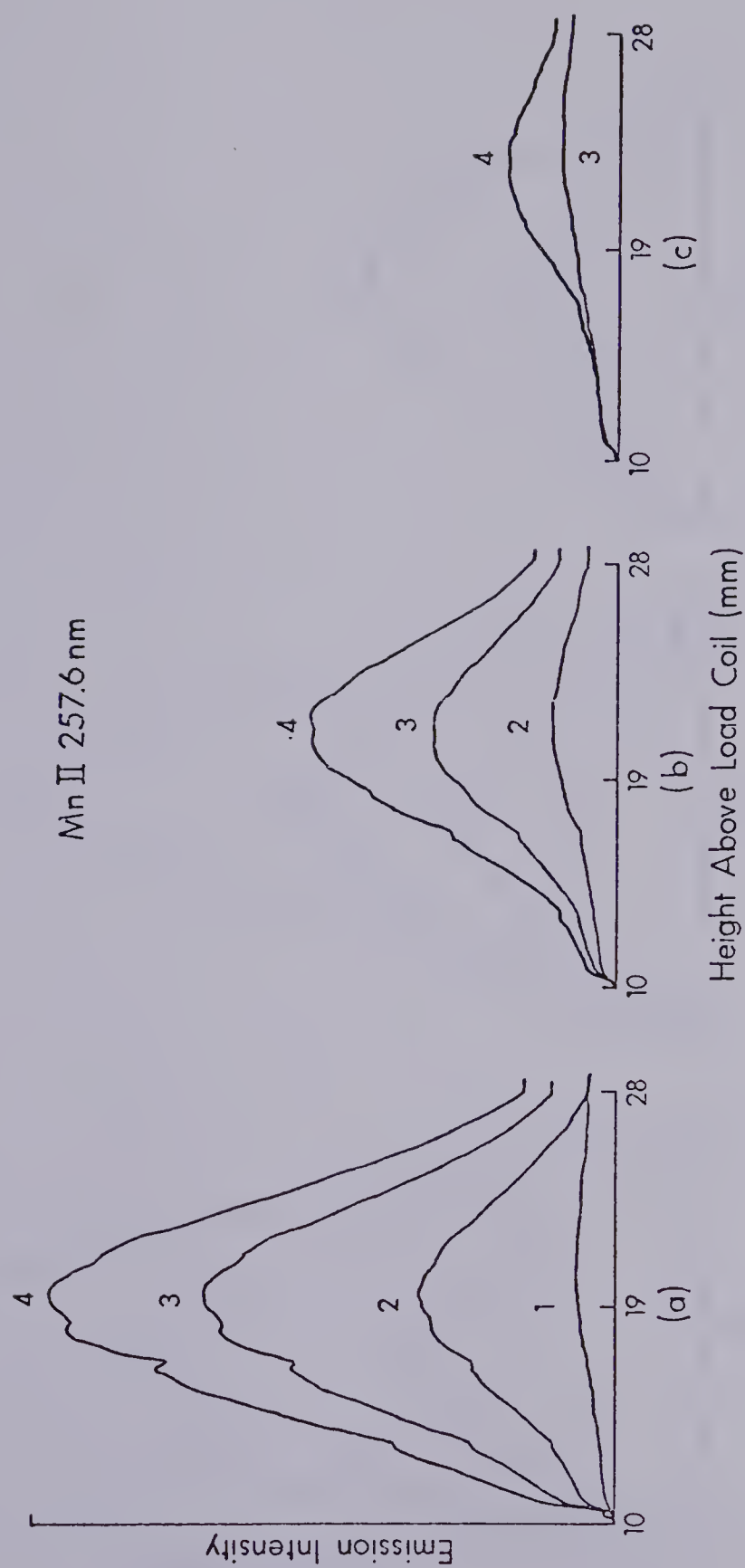


Figure 17. Vertical spatial profiles for MnII 403.1 nm. Aerosol flow rates; (a) 0.9 lpm, (b) 1.0 lpm, and (c) 1.1 lpm. RF power; (1) 1.25 kw, (2) 1.50 kw, (3) 1.75 kw, (4) 2.0 kw, and (5) 2.25 kw.



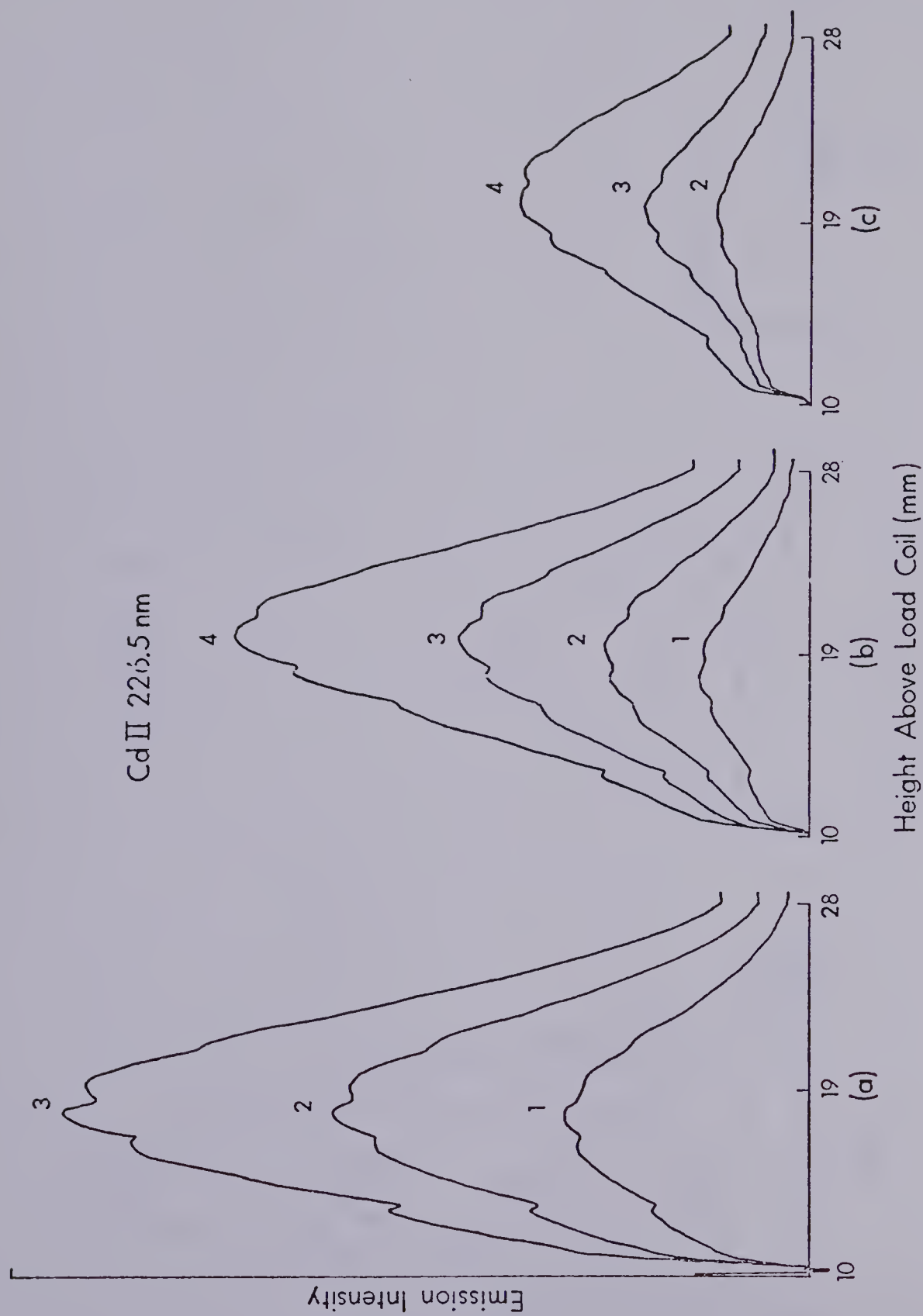


Figure 18. Vertical spatial profiles for CdII 226.5 nm. Aerosol flow rates; (a) 0.9 lpm, (b) 1.0 lpm, and (c) 1.1 lpm. RF power; (1) 1.25 kw, (2) 1.50 kw, (3) 1.75 kw, (4) 2.0 kw, and (5) 2.25 kw.





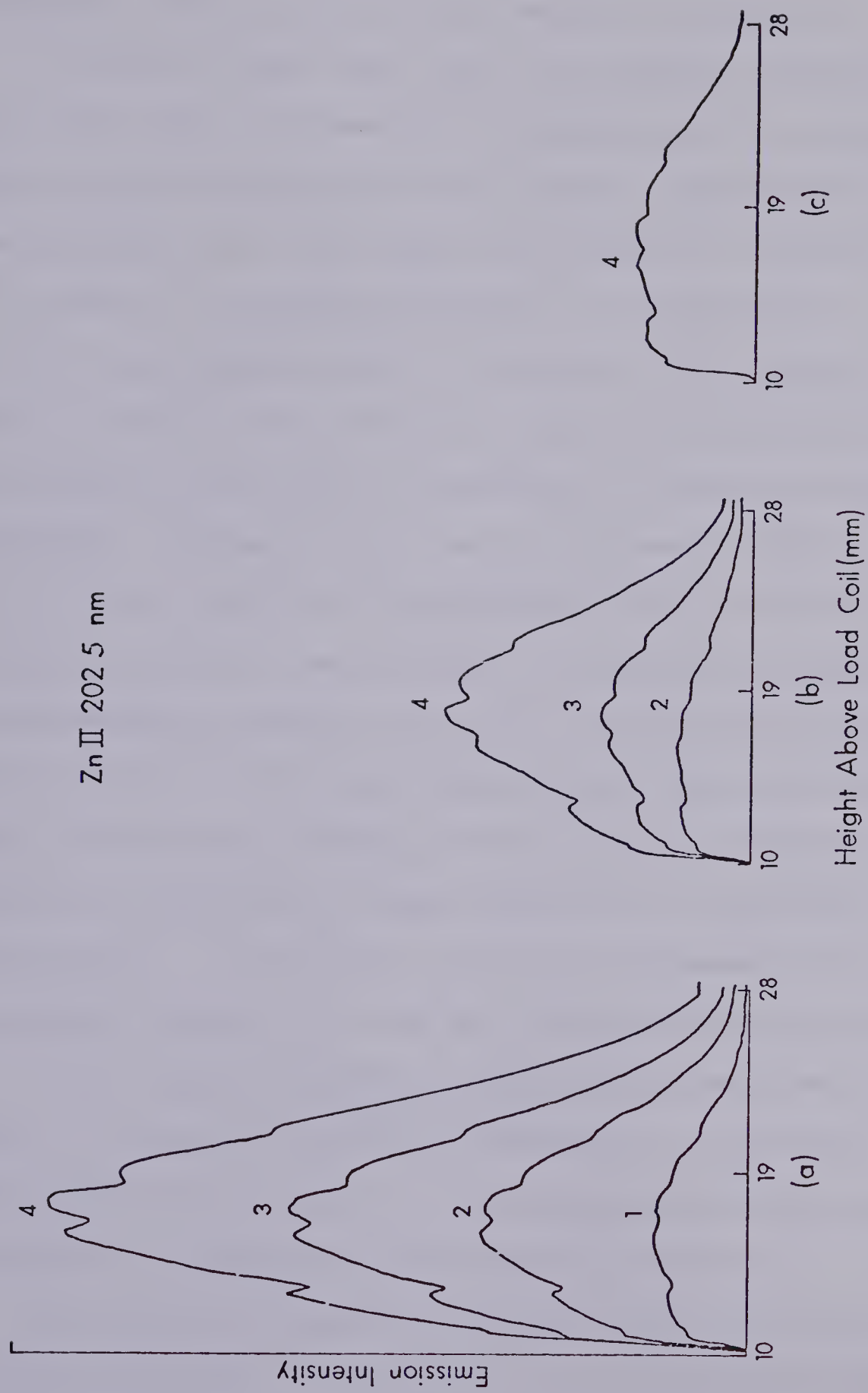


Figure 19. Vertical spatial profiles for ZnII 202.5 nm. Aerosol flow rates; (a) 0.9 lpm, (b) 1.0 lpm, and (c) 1.1 lpm. RF power; (1) 1.25 kw, (2) 1.50 kw, (3) 1.75 kw, (4) 2.0 kw, and (5) 2.25 kw.



taniously reducing the overall emission intensity.

It may be noted that while the emission intensity for hard type lines is expected to increase with an increase in applied power regardless of the spatial observation zone, the behaviour for soft lines is not quite so predictable. For example, the spatial profiles of NaI 588.9 nm, a soft line, are provided in Figure 20. The aerosol flow rate is 0.8 lpm for curve (a), and 0.9 lpm for curve (b). The format of the plots is analogous to those previously discussed. Curves 1, 2, 3, and 4 represent 1.25 kw, 1.5 kw, 1.75 kw, and 2.0 kw respectively. A plot of the net emission intensity versus power is provided in Figure 21 for observation heights of 13 mm, 19 mm, and 25 mm above the load coil. The figure demonstrates three different types of behaviour for the Na atom emission intensity in response to applied RF power depending on the height of observation. At 25 mm the intensity decreases with an increase in power, at 19 mm the intensity has a maximum at 1.5 kw, and at 13 mm the intensity increases with power. Clearly the spatial profile information is important in characterizing the nature of the response of emission intensity to changes in ICP operating parameters.

The vertical spatial profiles of the 418.2 nm Ar atom line are provided in Figure 22 in the region 10 to 28 mm above the load coil. The two frames (a) and (b) are for



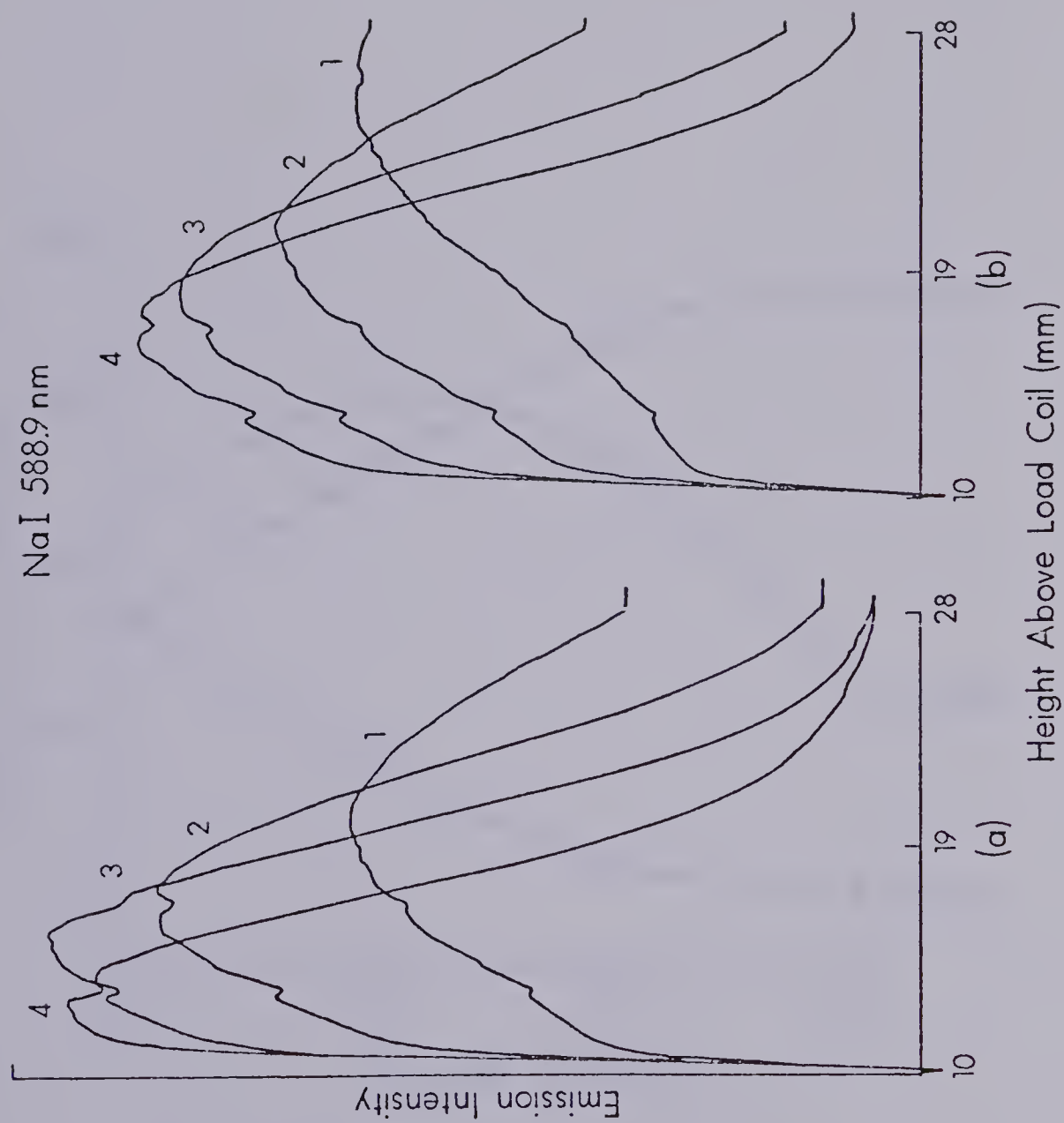


Figure 20. Vertical spatial profiles for NaI 588.9 nm. Aerosol flow rates; (a) 0.8 lpm, (b) 0.9 lpm. RF power; (1) 1.25 kw, (2) 1.50 kw, (3) 1.75 kw, and (4) 2.0 kw.



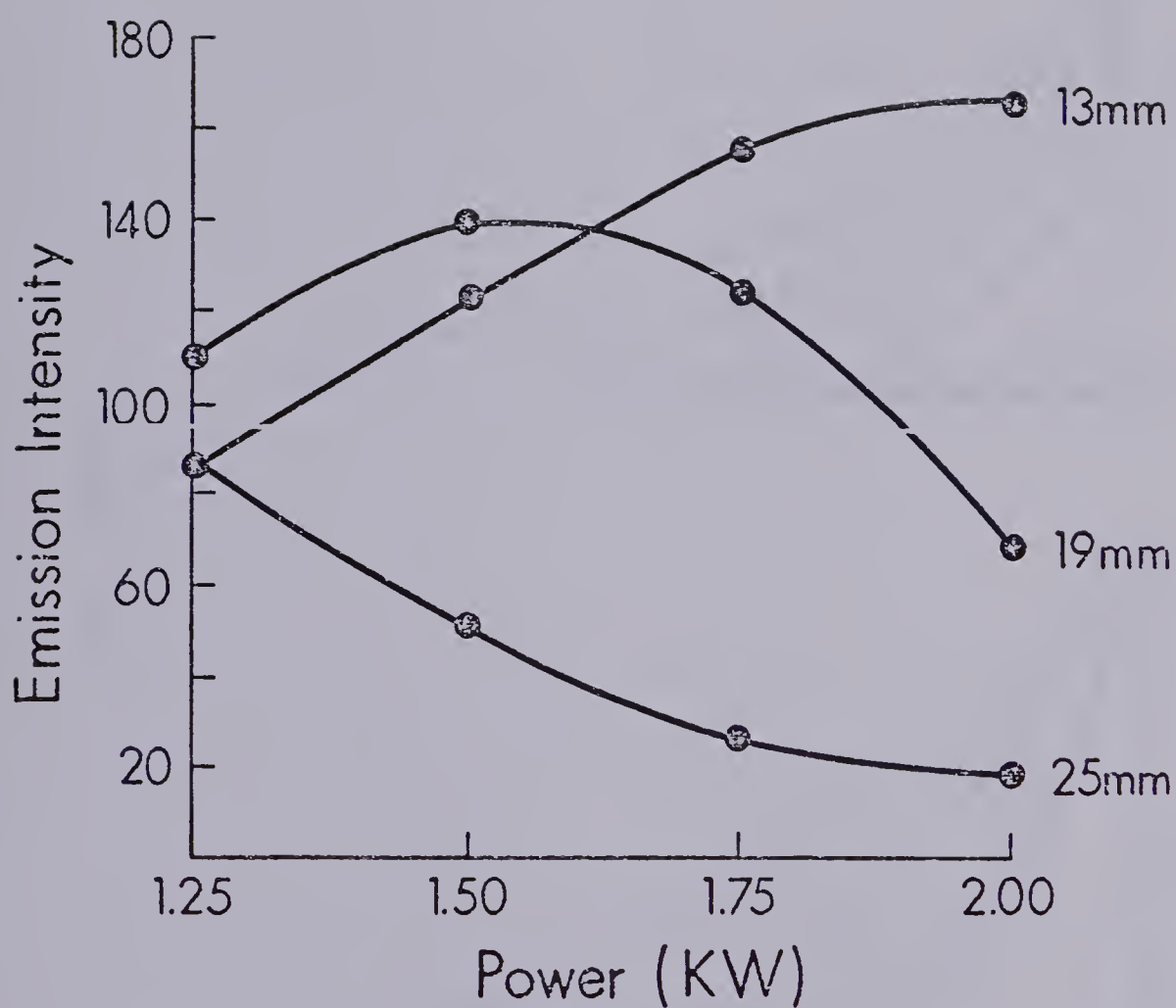


Figure 21. Emission intensity as a function of power for NaI 588.9 nm, at observation heights of 13 mm, 19 mm, and 25 mm above the load coil.





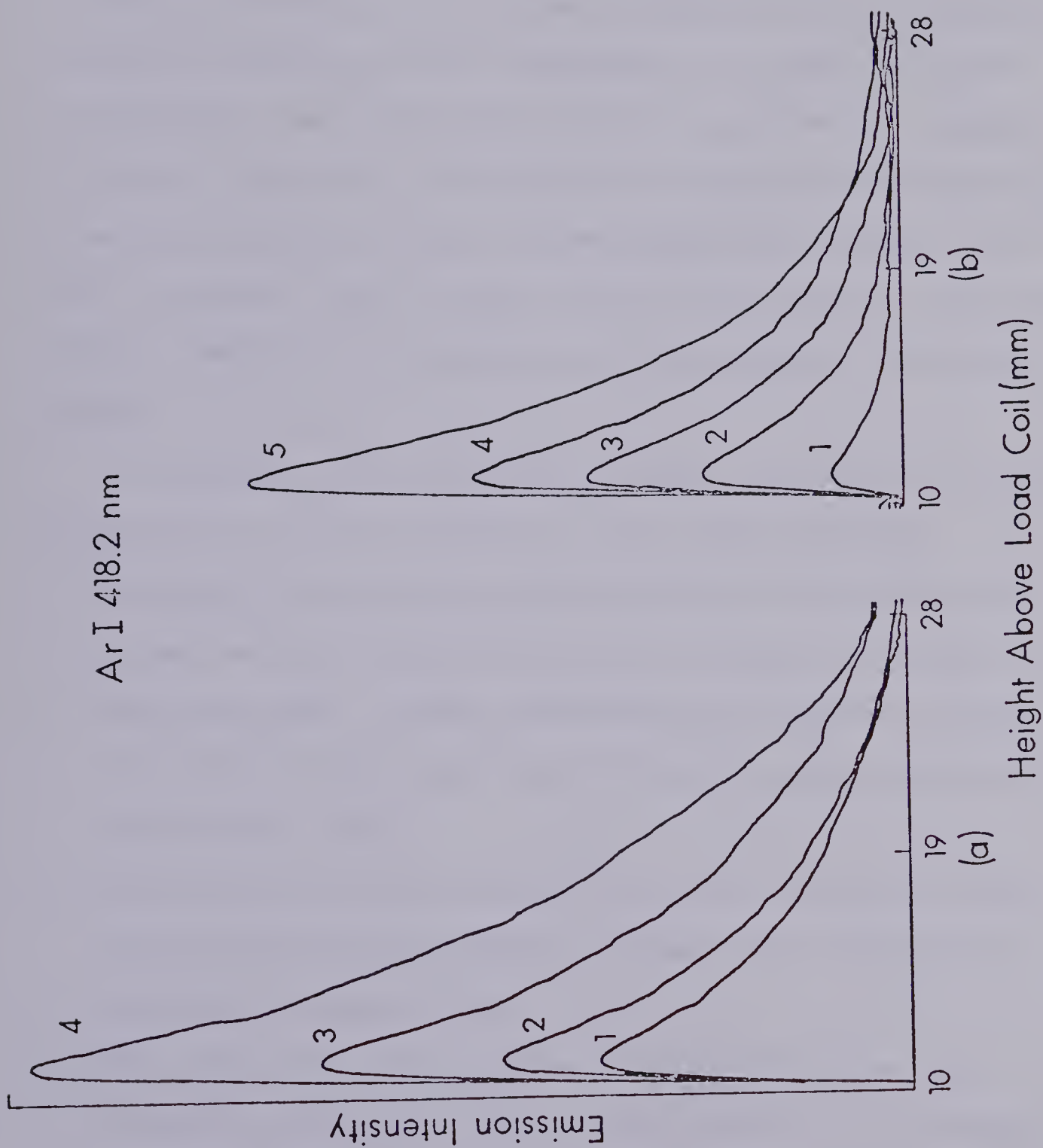


Figure 22. Vertical spatial profiles for Ar I 418.2 nm. Aerosol flow rate; (a) 0.9 lpm, (b) 1.0 lpm. RF power; (1) 1.0 kw, (2) 1.25 kw, (3) 1.50 kw, (4) 1.75 kw, and (5) 2.0 kw.



argon aerosol flow rates of 0.9 lpm and 1.0 lpm respectively. The plots from 1 to 5 represent applied powers of 1.0 to 2.0 kw in increments of 0.25 kw. The argon line intensity is seen to decrease with a decrease in RF power as would be expected, and shows little spatial response to changes in aerosol flow rate. The emission intensity decreases by a factor of about 0.75 at its maximum as the aerosol flow rate increases. This is the result of cooling of the aerosol channel leading to a decrease in argon emission from this region.

In summary, the following features characterize spatial behaviour of analyte species in the analyte channel:

- (1) Emission lines may be subdivided into two categories based on their spatial profile response to changes in applied power. These two categories have been given the names "soft" and "hard" following the terminology of Boumans [94].
- (2) The vertical spatial profiles of soft lines are much more sensitive to changes in power than the spatial profiles of hard lines.
- (3) For soft lines an increase in RF power causes the emission intensity peak to shift lower in the plasma. For hard lines an increase in RF power causes very little shift in the position of maximum emission.



- (4) In all cases ion lines have demonstrated hard line behaviour. Atom lines may display hard or soft line behaviour, depending upon the species being observed.
- (5) Hard lines are observed to peak at positions higher above the load coil than soft lines. This is in agreement with the observations of Edmonds and Horlick [69], Kawaguchi et al. [71], and Savage and Hieftje [96].

The question which arises is: "What is the cause for the two different types of spatial behaviour for analyte species in the ICP?" Edmonds and Horlick have roughly correlated the spatial position of maximum intensity with the excitation potential of the line being observed. This, however, cannot be the only criterion for determining spatial behaviour since CaI (422.7 nm) and CaII (393.3 nm) have similar excitation potentials (2.9 eV and 3.1 eV respectively). The process of ionization of atom species must play an important role in determining spatial behaviour since it will define the relative population of atom and ion species in the ICP. If the excitation and ionization characteristics of the line being observed are important in determining the spatial position of the atom and ion lines, how can we use these characteristics to predict spatial behaviour? These questions are addressed in the next chapter of this thesis.

In a more practical vein; what use can be made of the spatial information presented in this chapter? The use of



internal standards in emission spectroscopy is well known. Internal standards are chosen such that they will, as closely as possible, mimic analyte emission behaviour in response to changes in various parameters which will affect the emission intensity of the analyte. The theoretical aspects of choosing internal standards have been discussed by Barnett et al. [95]. In the ICP the use of the internal standard principle can improve precision [97,98]. The spatial behaviour of various analyte species in response to applied power has been discussed in this chapter, and it has been shown that different species can behave quite differently. This spatial behaviour should certainly be taken into account in choosing an appropriate internal standard. For example, a soft line should not be chosen as a ratio partner with a hard line. Of course, the choice of an internal standard with similar excitation characteristics as the analyte will probably assure similar spatial behaviour.

In a simultaneous multielement analysis situation, information such as that presented in this chapter should be considered carefully. The procedure of parameter optimization could be considerably simplified with the aid of this spatial information.





## CHAPTER IV

### SPATIAL BEHAVIOUR AND ANALYTE EXCITATION CHARACTERISTICS

#### Introduction

In the previous chapter it was pointed out that the spatial behaviour of analyte emission may be strongly species dependent. A trend emerged in which the response of the spatial profile to changes in applied RF power divided into two classes; hard or soft, depending on the analyte species being observed. The purpose of this chapter is to investigate the manner in which analyte ionization and excitation characteristics determine spatial behaviour of analyte emission in the ICP.

#### Soft Lines

Edmonds and Horlick [69] demonstrated a rough correlation between the position of the intensity maximum in the vertical spatial profile and analyte excitation characteristics for atom lines (soft lines) in the region 12 mm to 24 mm above the load coil. Atom lines with low excitation potential tended to peak lower in the analyte channel and those with higher excitation potential tended to peak higher up. In an effort to more clearly define the nature of this spatial structure a similar study was carried out on a set of atom lines with excitation potentials



ranging from 1.6 ev to 4.4 ev. The spatial emission profiles for the various lines in the region 4 to 18 mm above the load coil are provided in Figure 23, which plots "emission intensity" versus "height above the load coil" for these lines. Some of the profiles have been truncated and offset in the vertical direction for clarity. The conditions chosen for the study were 1.4 kw RF power, 0.85 lpm aerosol flow rate, 15 lpm plasma gas flow rate, and less than 1 lpm of auxiliary gas. These conditions are close to those normally used for quantitative multielement analysis. The analyte lines studied are listed in Table III along with their respective excitation potentials and observed position of peak maximum. The latter was measured by locating the position where the emission intensity is greatest. The position of maximum intensity is plotted against excitation potential in Figure 24. The plot indicates a crude correlation between excitation potential and position of peak maximum, however there are two features of the plot which indicate that excitation potential is not the sole criterion for determining the peak position. The first of these is the fact that Na, K, and Li (670.8 nm) form one straight line, and Ca, Cr, and Mg form another of differing slope. Secondly, the Li line at 610.4 nm does not fall on either



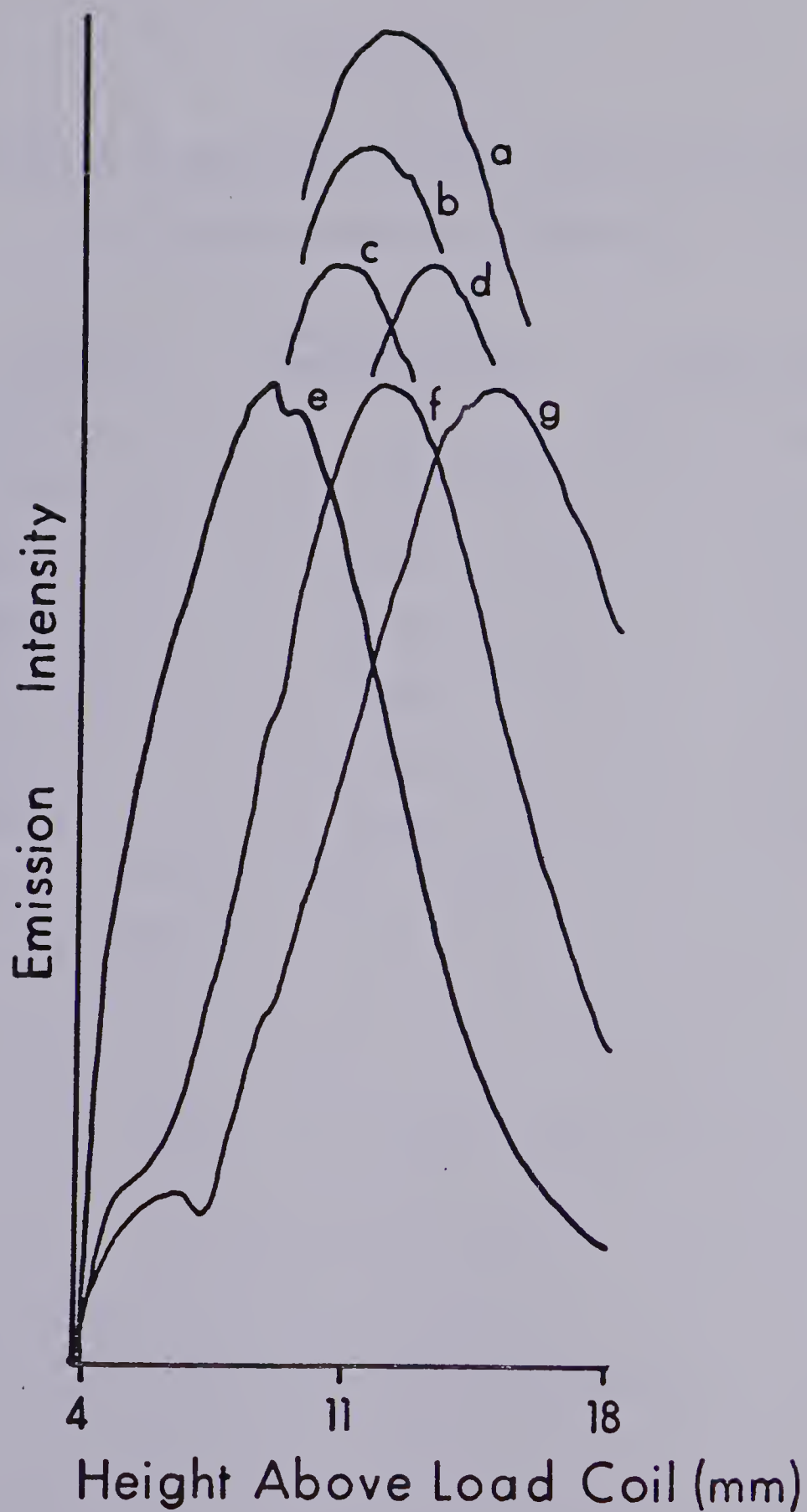


Figure 23. Vertical spatial emission profiles for; (a) NaI 588.9 nm, (b) LiI 610.4 nm, (c) LiI 670.8 nm, (d) CrI 357.8 nm, (e) KI 766.5 nm, (f) CaI 422.7 nm, (5) MgI 285.3 nm.



TABLE III

EXCITATION POTENTIALS AND PEAK MAXIMUM POSITION  
FOR ANALYTE LINES IN FIGURE 23

<u>Element Line (nm)</u>		<u>Excitation Potential (ev)</u>	<u>Peak Position<sup>*</sup></u>
KI	766.5	1.62	8.9
LiI	570.8	1.85	10.5
LiI	610.4	3.87	11.3
NaI	588.9	2.11	11.8
CaI	422.7	2.93	11.8
CrI	357.8	3.46	12.7
MgI	285.2	4.34	14.4

---

<sup>\*</sup> mm above load coil





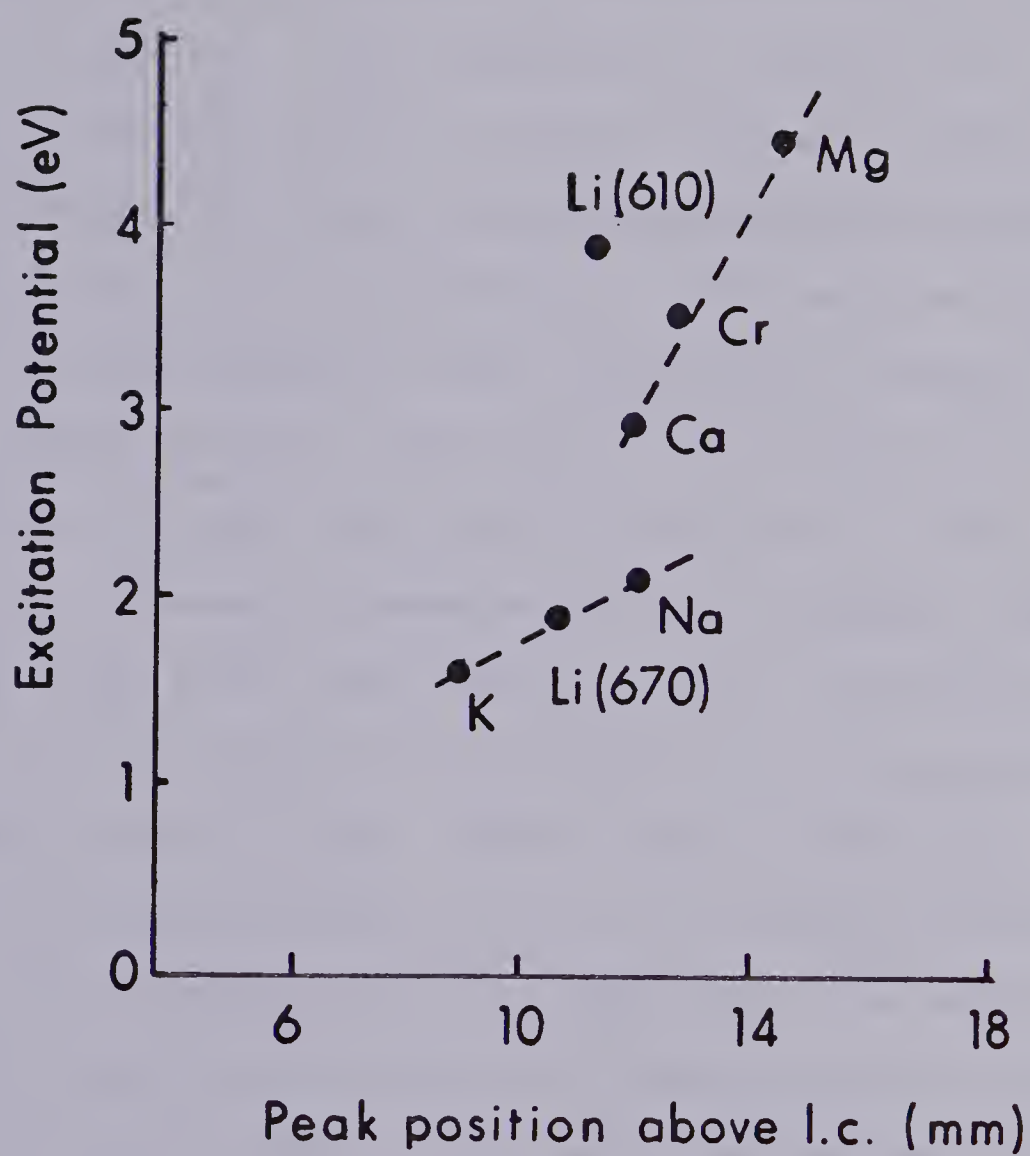


Figure 24. Position of peak maximum for lines listed in Table III, as a function of excitation potential of the line.



line but, rather, appears as an isolated data point.

In order to more accurately determine which analyte and plasma characteristics are important in determining peak position the problem will be approached from a theoretical standpoint. This theoretical approach will include analyte parameters such as analyte excitation potential and ionization potential, as well as ambient channel "temperature", a plasma parameter. The basis of the approach is the assumption that temperature increases as one moves from a position just above the load coil up through the analyte channel away from the load coil. This assumption has not been based on measured values of spatial temperature distributions which have appeared in the literature but rather on an intuitive feeling that the analyte spatial structure suggests this. Atomic species which are easily excited consistently peak lower in the analyte channel than those which are more difficult to excite. In addition all ion lines observed thus far have peaked high in the analyte channel; this in spite of the fact that ionization-excitation for these species is a very energetic process. It is acknowledged that some of these observations may be the result of "non-thermal" processes (such as Penning ionization), however, for the sake of simplicity this has not been considered in the following treatment. This point will be returned to in the discussion at the end of this chapter.



### Theoretical Treatment of Analyte Emission Intensity

The processes of desolvation, vaporization, and dissociation of the analyte in the region of the load coil result in ground state atomic species traveling up the analyte channel. The temperature increase experienced by the ground state atom will influence the emission intensity observed from the atomic species in two opposing ways. As the atom experiences a steadily increasing temperature the emission intensity will increase as the excited state population increases according to the Boltzmann distribution. Opposing this is a decrease in population of atom species due to increased ionization as described by the Saha equation. This will tend to decrease emission intensity of atom species. At some point in the analyte's progress, the effects of ionization will overtake the effects of increased excited state population and the emission intensity will reach a peak and begin to decrease, forming an emission intensity maximum at some position above the load coil. The temperature at which this maximum occurs has been called the "normal temperature" [94].

This process may be quantitatively described in the following way. The observed emission intensity of an atomic species,  $a$ , in excited state  $l$  is given by:

$$I_{a_l} = h\nu_{a_l} A_{a_l} N_{a_l} \quad (24)$$



where  $h$  is Planck's constant,  $\nu_{a_1}$  is the frequency of the transition,  $A_{a_1}$  is the transition probability and  $N_{a_1}$  is the number of atoms in the excited state. The number of atoms in the excited state can be described by the Boltzmann distribution:

$$N_{a_1} = \frac{N_a g_{a_1}}{Q_a(T_a)} \exp(-E_{a_1}/kT_a) \quad (25)$$

where  $N_a$  is the total number of atomic species,  $g_{a_1}$  is the statistical weight of the excited state,  $Q_a(T_a)$  is the electronic partition function,  $E_{a_1}$  is the excitation potential of the excited state,  $k$  is the Boltzmann constant, and  $T_a$  is the atomic excitation temperature. The total number of atoms,  $N_a$ , is given by:

$$N_a = N_t(1-\chi) \quad (26)$$

where  $N_t$  is the total number of analyte species present in all forms, ionic and atomic, and  $\chi$  is the degree of ionization. Substituting the expression given in Equations 25 and 26 into Equation 24 yields:

$$I_{a_1} = h\nu_{a_1} N_t(1-\chi) \frac{g_{a_1} A_{a_1}}{Q_a(T_a)} \exp(-E_{a_1}/kT_a) \quad (27)$$

This expression gives the emission intensity in terms of the degree of ionization of the analyte, its excitation





potential, and the temperature experienced by the atom such that:

$$I_{a_1} \propto \frac{(1-\chi)}{Q_a(T_a)} \exp(-E_{a_1}/kT_a) \quad (28)$$

if the total number of atoms  $N_t$  is constant.

The ionization can be expressed in terms of electron pressure,  $p_e$ , and the Saha equilibrium constant,  $S_p$ , by [56]:

$$(1-\chi) = \frac{p_e}{p_e + S_p} \quad (29)$$

where:

$$S_p = 6.58 \times 10^{-7} T_i^{5/2} \frac{Q_i(T_i)}{Q_a(T_a)} \exp(-V_i/kT_i) \quad (30)$$

and  $T_i$  is the ion temperature,  $Q_i(T_i)$  is the ion partition function, and  $V_i$  is the ionization potential of the atom. The partial pressure of electrons is related to electron density ( $n_e$ ) by:

$$p_e = 1.36 \times 10^{-22} n_e T \quad (31)$$

For the sake of simplicity, it is assumed that LTE exists, that is, the temperature defining the populations of excited states and the temperature defining the relative distribution of atom and ion species is the same. Under this condition the relative emission intensity of atom a



from excited state 1 can be expressed as:

$$I_{a_1} \propto \left( \frac{p_e}{p_e + S_p} \right) \frac{1}{Q_a(T)} \exp(-E_{a_1}/kT) \quad (32)$$

where T is the LTE temperature.

Equation 32 may be solved to yield relative emission intensity for an atom line at various values of temperature. The logarithm of the partition functions  $Q_a(T)$  and  $Q_i(T)$  are assumed to vary linearly with temperature [56]; according to the formula;

$$\log Q = \log Q' - \left( \frac{5040}{T} \right) \xi \quad (33)$$

where  $Q'$  and  $\xi$  are constants for a particular atom or ion and  $Q$  is the partition function at temperature  $T$ . The values of  $Q'$  and  $\xi$  for the set of atom lines studied are listed in Table IV for atom (subscript a) and ion (subscript i). These values have been extracted from Boumans [56].

The procedure employed was to solve Equations 30, 31, and 33 for a series of temperature values and inserting the solutions into Equation 32 to arrive at relative emission intensities for these temperatures. A plot of emission intensity as a function of temperature will yield a result such as that provided in Figure 25 for KI (766.5 nm) and MgI (285.3 nm) for an electron density of  $10^{13.5} \text{ cm}^{-3}$ . The overall shape and relative position of these curves are re-



TABLE IV

## ATOM AND ION PARTITION FUNCTION CONSTANTS

<u>Element</u>	<u>Q'<sub>a</sub></u>	<u>Q'<sub>i</sub></u>	<u>ε<sub>a</sub></u>	<u>ε<sub>i</sub></u>
K	4.374	1.0	0.30	0.0
Li	2.636	1.0	0.10	0.0
Ba	22.946	9.463	0.95	0.35
Na	2.586	1.0	0.10	0.0
Sr	4.951	3.0595	0.6	0.15
Ca	3.325	3.516	0.45	0.20
Cr	32.873	17.966	0.50	0.40
Mn	10.181	12.249	0.20	0.20
Al	5.9	1.0	0.0	0.30
Mg	1.146	2.0	0.05	0.0
Cd	1.0	2.0	0.0	0.0
Co	67.211	59.387	0.30	0.30



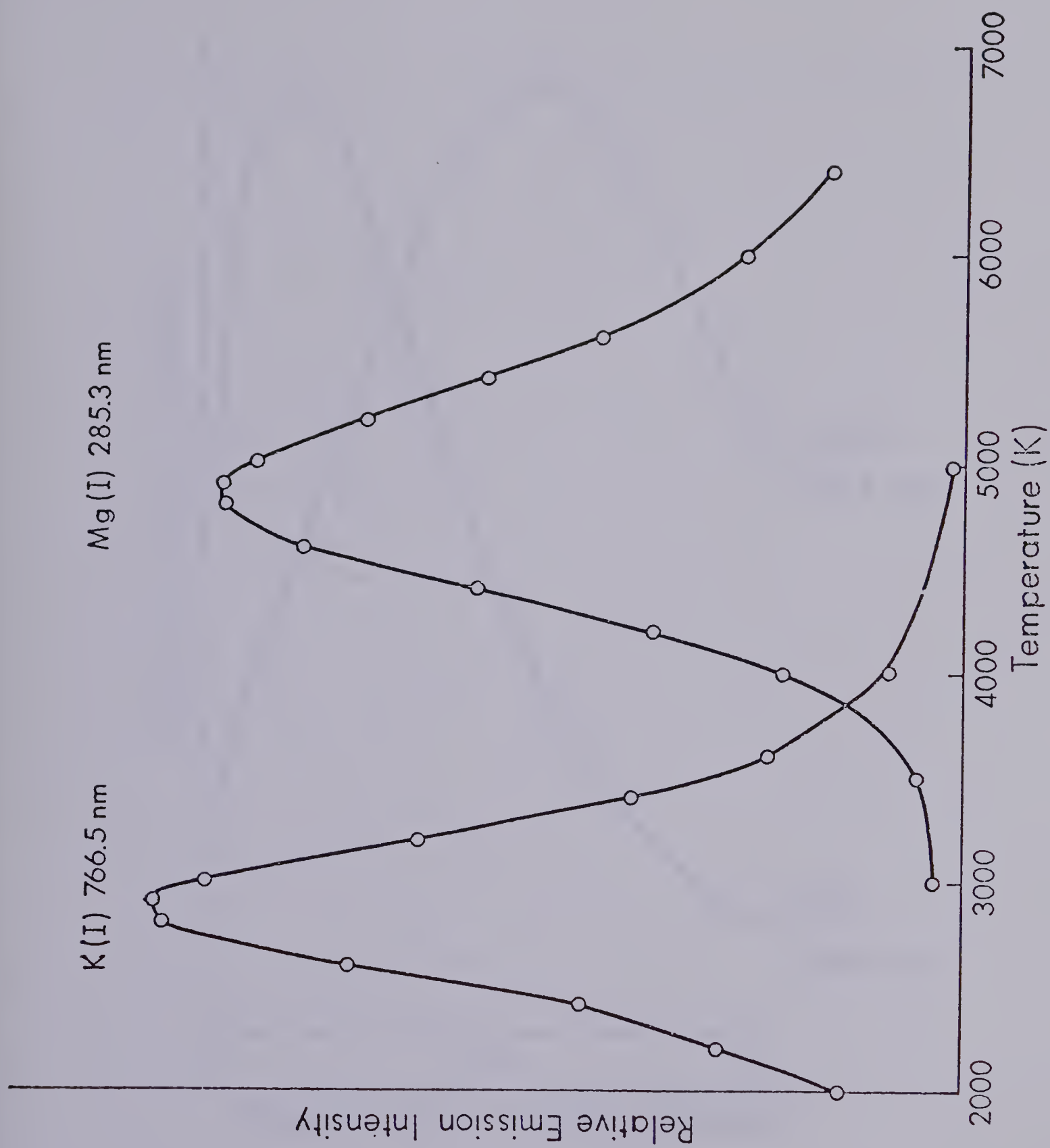


Figure 25.

Theoretically generated profiles of emission intensity as a function of height above the load coil for MgI 285.3 nm and KI 766.5 nm.





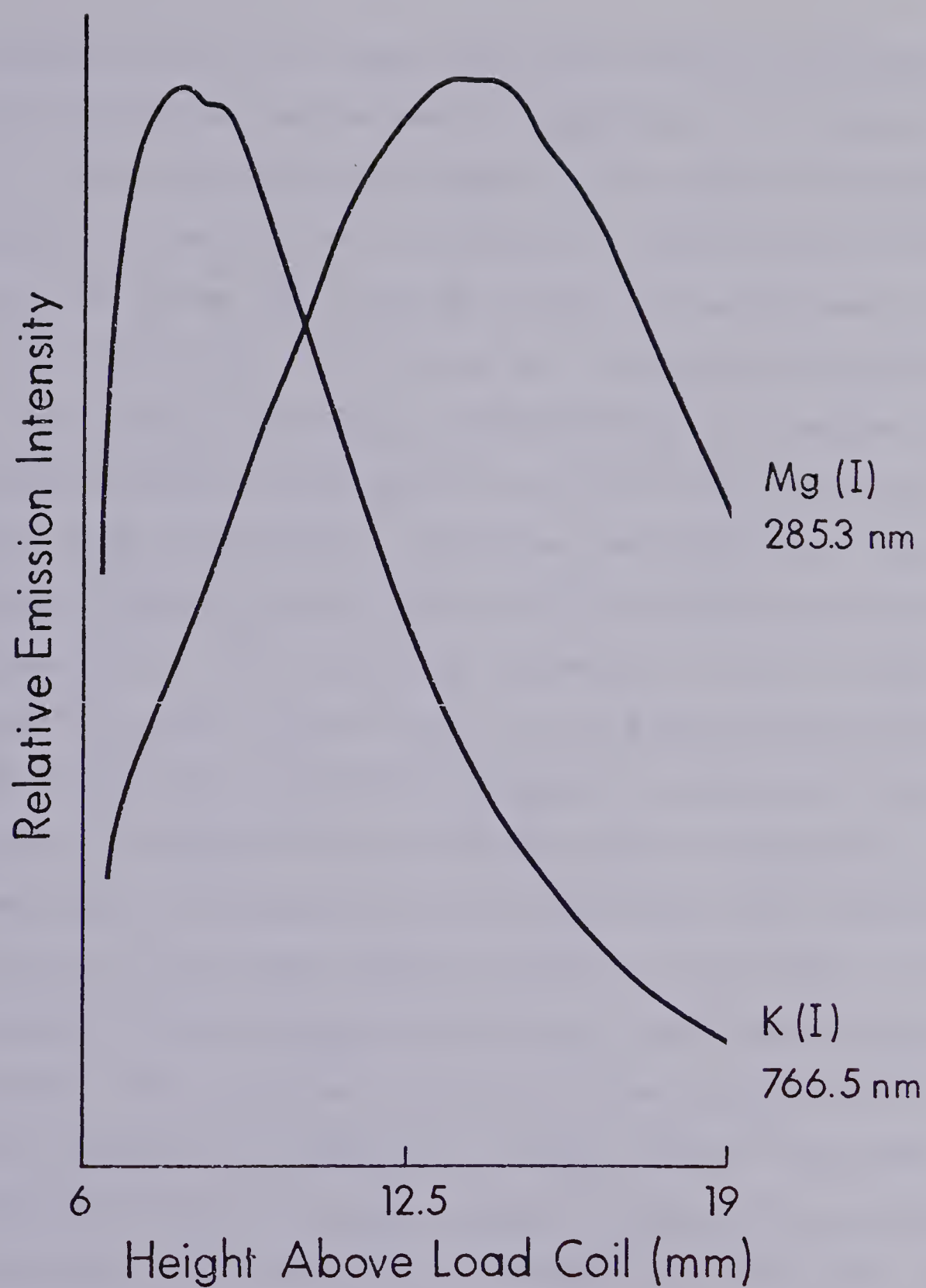


Figure 26. Vertical spatial profiles for MgI 285.3 nm and KI 766.5 nm.



markably similar to those which are obtained experimentally from the ICP as can be seen by comparison of Figures 25 and 26. The curves shown in Figure 26 are plots of relative emission intensity as a function of height above the load coil for these same K and Mg lines, for an RF power of 1.4 kw, aerosol flow rate of 0.8 lpm, and plasma gas flow rate of 15 lpm. This indicates a strong correlation between the temperature axis in Figure 25 and the height above the load coil axis in Figure 26. Both the position of the peak maximum and the profile width are in theory dependent on temperature, and in practice dependent on the vertical position above the load coil. As was mentioned previously, the temperature at which the maximum in emission intensity occurs in Figure 25 is called the normal temperature. The comparison of Figures 25 and 26 indicates that the spatial position of the peak maximum observed in the ICP is probably related to the normal temperature of the element being observed. This proposal is further substantiated by the plot provided in Figure 27. In this figure the normal temperature for the lines listed in Table III are plotted as a function of the excitation potential of the line. The electron density assumed is  $10^{13.5} \text{ cm}^{-3}$ . This plot is analogous to that provided in Figure 24. It is clear from these two plots that normal temperature and peak position are strongly related to each other.



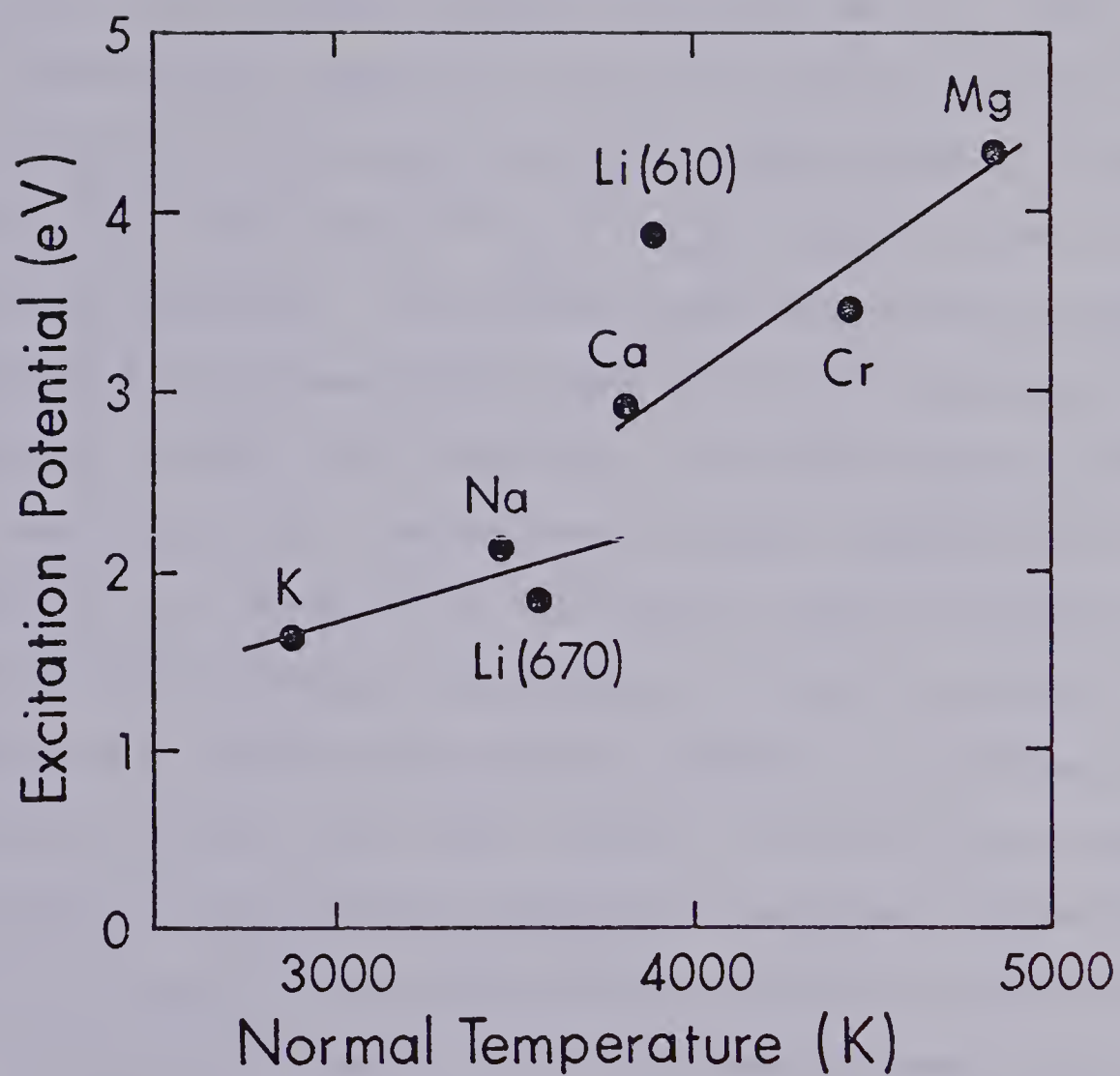


Figure 27. Plot of normal temperature versus excitation potential for lines listed in Table III.



In order to verify this correlation of peak position and calculated normal temperature, the normal temperature was calculated for a set of 16 atom lines of varying excitation and ionization potentials. These are listed in Table V. The electron density was taken as  $10^{13.5} \text{ cm}^{-3}$  for this calculation. Kalnicky et al. [36] have recently measured the electron density using the Saha equation to be between  $10^{12} \text{ cm}^{-3}$  and  $10^{14} \text{ cm}^{-3}$  in the region 15 mm to 25 mm above the load coil. The channel electron density demonstrated a height dependence decreasing with increasing observation height. For simplicity a uniform value of  $10^{13.5} \text{ cm}^{-3}$  was adopted for the values of normal temperature calculated. The effect of an increase in electron density is to increase the normal temperature. A plot of normal temperature as a function of electron density is provided in Figure 28 for MgI, CrI, BaI, and KI. It can be seen that regardless of the electron density, the normal temperature for the lines will be proportionally related to each other.

The plot provided in Figure 29 demonstrates that the emission peaks observed in the ICP are strongly related to the normal temperature of the line being observed. In this figure the peak position, a value obtained from experiment is plotted as a function of the calculated normal temperature for the lines tabulated in Table V. The spatial position is plotted with a bar to represent the finite width of the





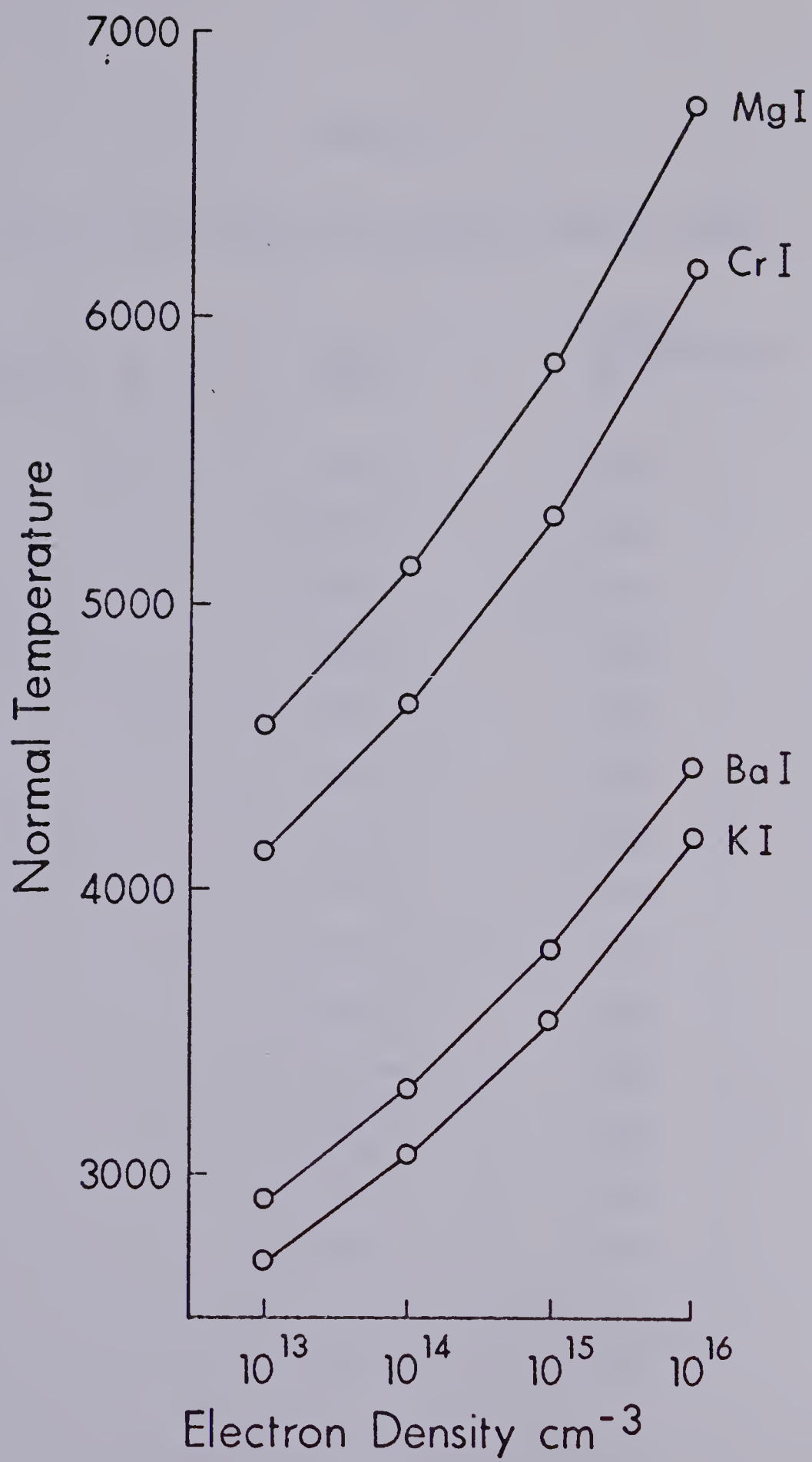


Figure 28. Normal temperature for MgI 285.3 nm, CrI 425.4 nm, BaI 553.4 nm, and KI 766.5 nm, as a function of electron density.



TABLE V

## NORMAL TEMPERATURE FOR SEVERAL ANALYTE LINES

<u>Species</u>	<u>Line (nm)</u>	<u>Normal Temperature (K)</u>
K	766.5	2870
Li	670.1	3578
Ba	553.4	3100
Li	610.3	3878
Na	588.9	3470
Sr	460.7	3510
Ca	422.7	3801
Cr	425.4	4372
Mn	403.0	4671
Al	396.2	4465
Cr	357.8	4448
Co	345.8	5078
Mg	383.8	5048
Mg	285.3	4837
Mn	279.4	4838
Cd	228.8	5655



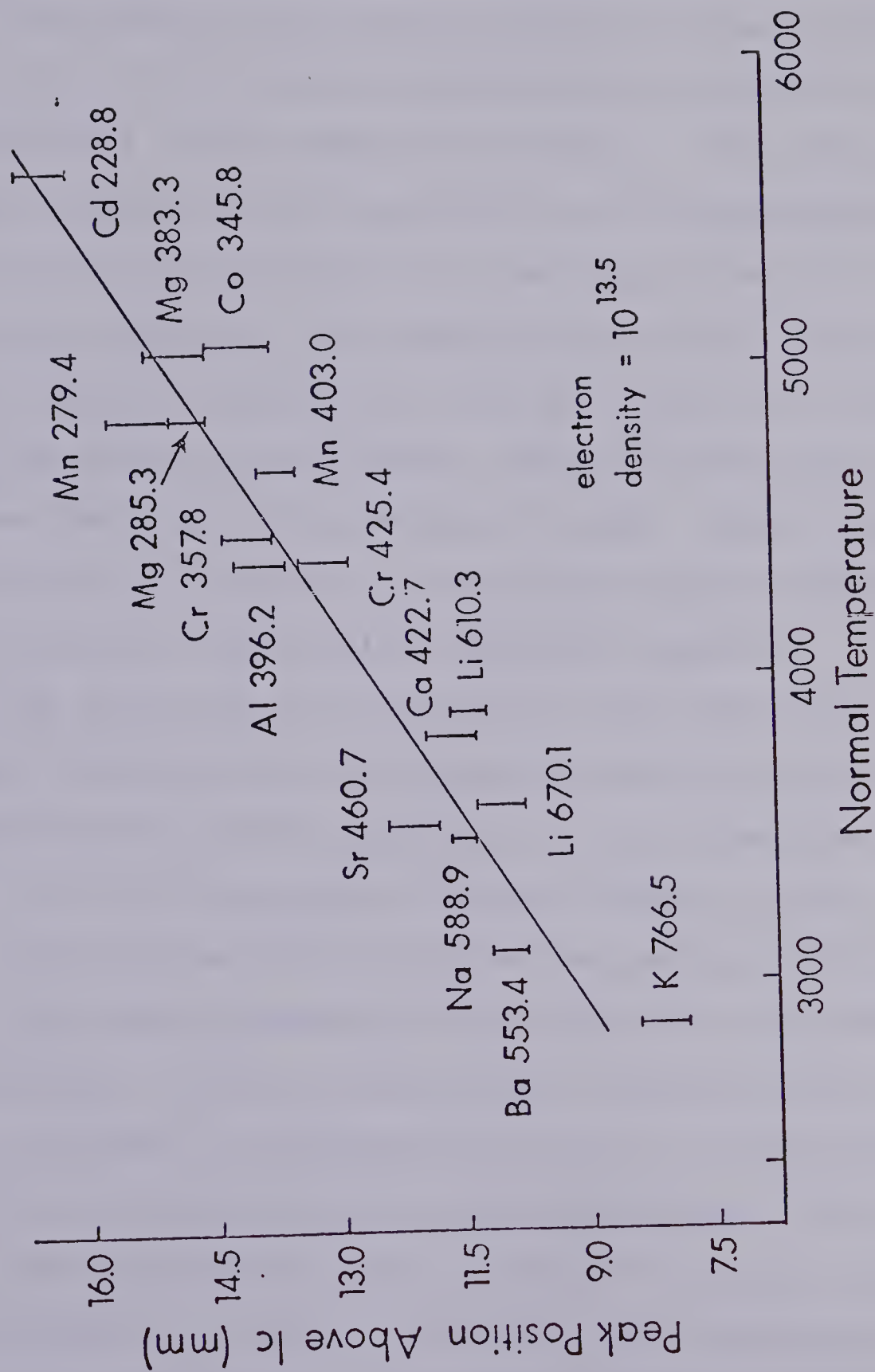


Figure 29. Position of vertical profile peak as a function of normal temperature (in K).



spatial profile at its peak. This plot confirms the notion that the peaks in the spatial profiles of these lines are the result of the excitation-ionization competition which results in a normal temperature maximum. The plot is a rather indirect way of arriving at an LTE temperature profile of the aerosol channel in the region 7 mm to 16 mm above the load coil. The temperatures in this region are seen to range from 3000 K to 6000 K. These are consistent with the values of temperature which have been measured in our own lab and by other workers [36,38]. Decker [100] has used a similar treatment to rationalize spatial behaviour in a D.C. plasma, with equally successful results.

The usefulness of the formulae which have been presented in this chapter is that they may be used to predict much of the observed spatial behaviour of many atom lines in the ICP. It is not universally useful, however, since it has been observed that above 16-18 mm the spatial profiles for many lines peak regardless of the value for the normal temperature. In fact, the position occupied by Cd on the plot in Figure 29 represents the point at which spatial position no longer follows normal temperature. This suggests that above this region the spatial position of the peak is independent of analyte excitation and ionization characteristics. In addition, it would be useful to know how these analyte parameters affect the spatial profiles of ion





lines which are not "covered" by the normal temperature calculation. These points are addressed in the next section.

### Hard Lines

The spatial profiles of ZnI (213.8 nm) and ZnII (202.5 nm) provided in Figure 30 typify the type of behaviour observed for hard type lines in response to changes in applied power. These plots are similar to those which have been discussed in Chapter III. The numbers refer to the applied RF power: (1) 2.0 kw, (2) 1.75 kw, (3) 1.5 kw, and (4) 1.25 kw. The position of maximum intensity for these two lines is seen to appear in approximately the same place in spite of the fact that the energy requirements for the two are quite different. This type of behaviour is also exhibited for CdI (228.8 nm) and CdII (214.4 nm) as is shown in Figure 31. The numbers on these plots are analogous to those in Figure 30. CdI and CdII clearly behave very similarly in response to changes in RF power. In fact the maximum in emission intensity is the same for both lines under the same conditions as can be seen in Figure 32. The spatial profile peaks higher in this figure than that in Figure 29 because the aerosol flow rate is higher, and the power in this case is 2.0 kw. This close coincidence is puzzling since the two lines have widely differing energy requirements to reach the excited state. These are sum-



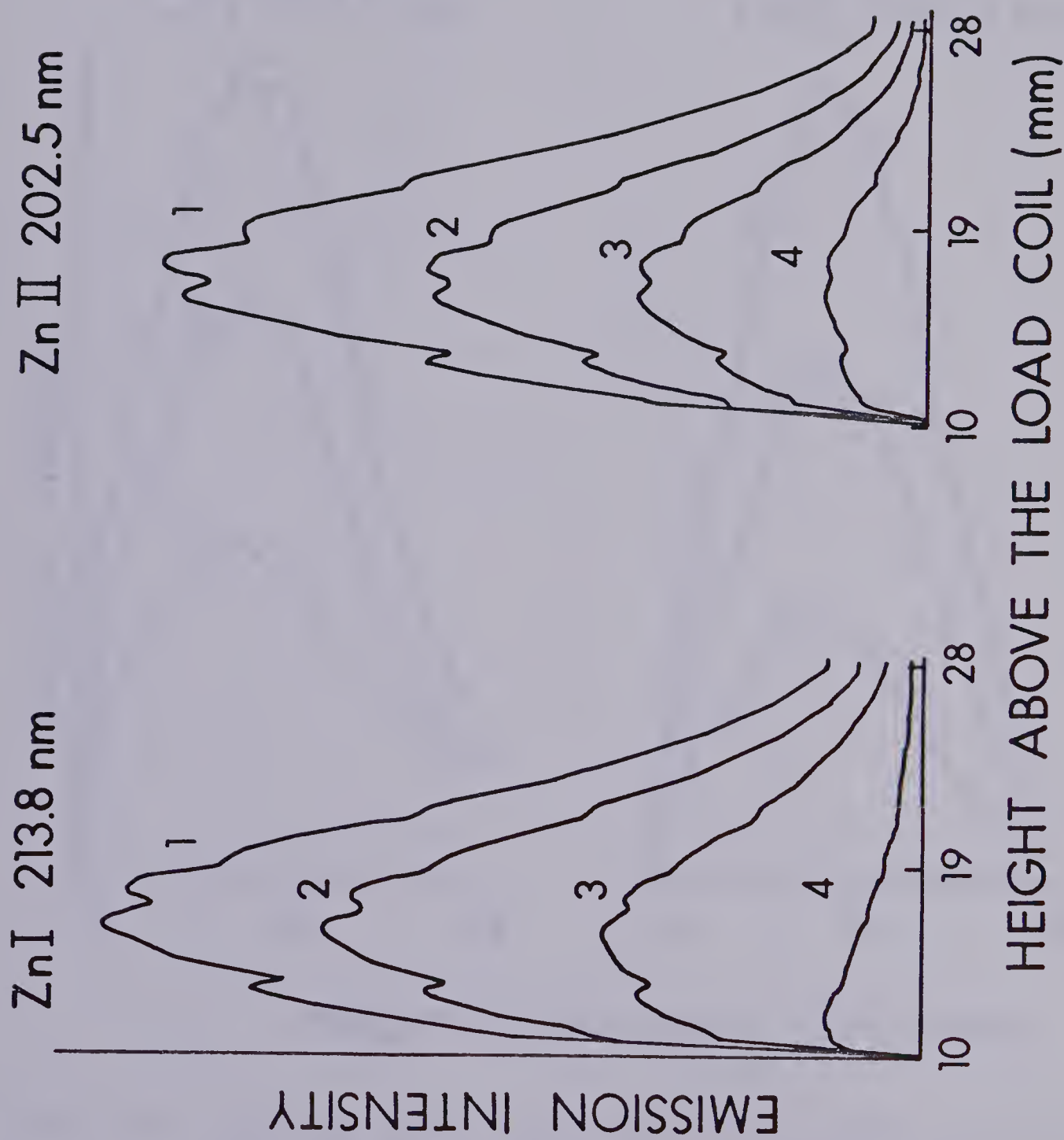


Figure 30. Vertical spatial profiles for ZnI 213.8 nm and ZnII 202.5 nm. RF power; (1) 2.0 kw, (2) 1.75 kw, (3) 1.5 kw, (4) 1.25 kw.



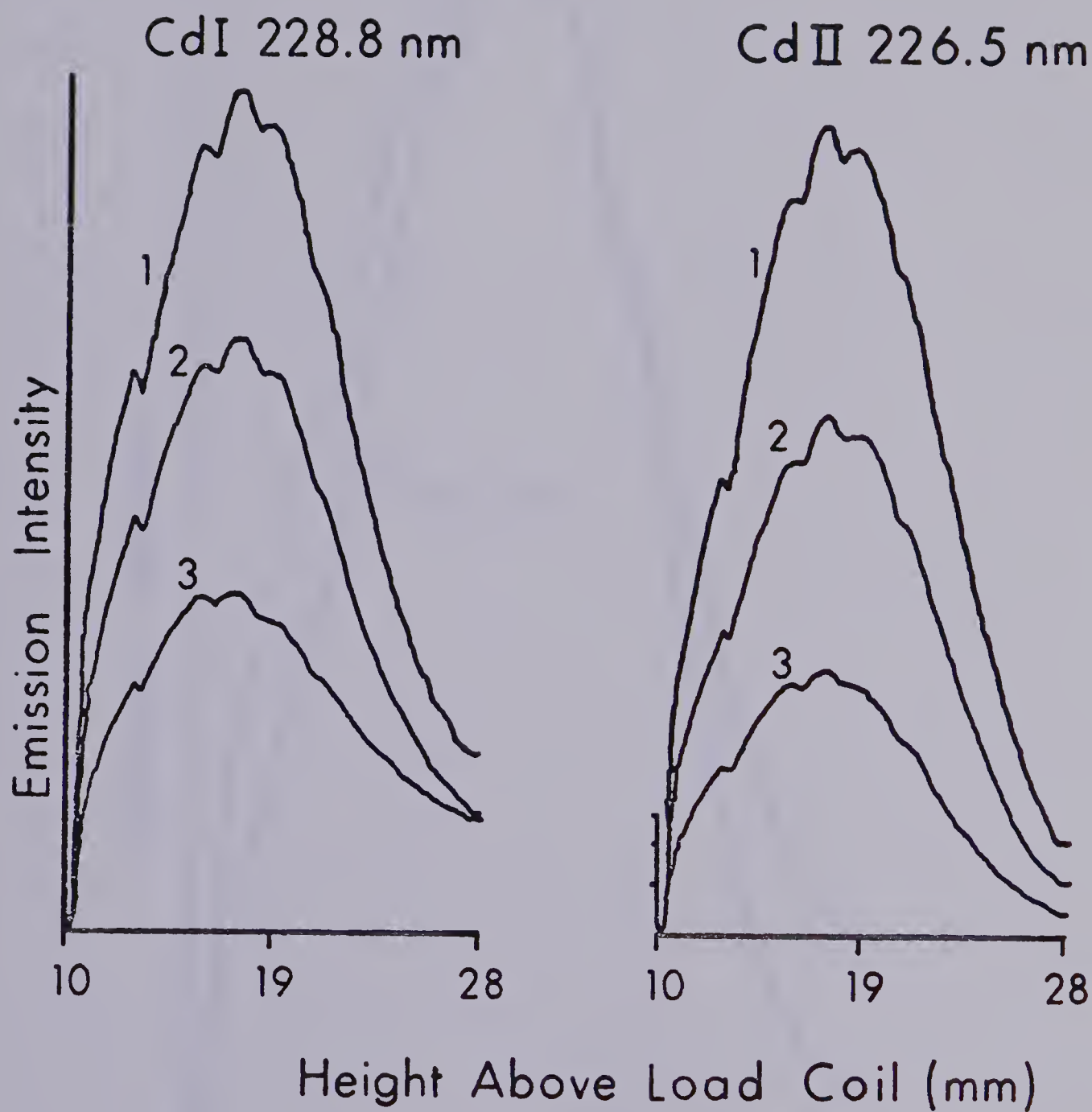


Figure 31. Vertical spatial profiles for CdI 228.8 nm and CdII 226.5 nm. RF power; (1) 2.0 kw, (2) 1.75 kw, (3) 1.5 kw, (4) 1.25 kw.



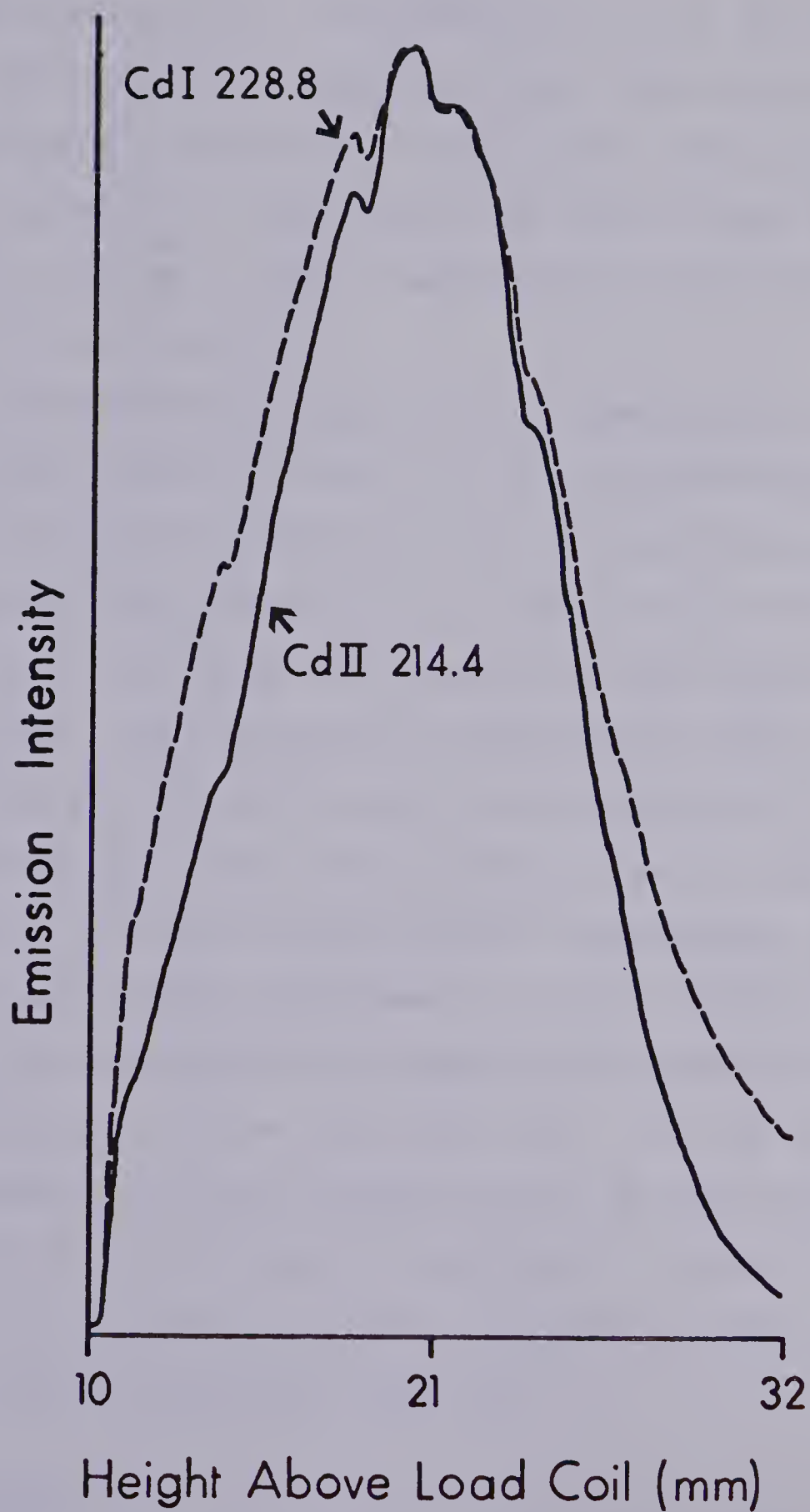


Figure 32. Superimposed vertical spatial profiles of CdI and CdII, at 2.0 kw RF power.





marized in Table VI. CdI requires 5.41 ev and CdII, 14.77 ev. This information suggests that there may be a wide range of energies available at this position above the load coil. This position also represents the region where we cannot use the "thermal" normal temperature calculation to predict spatial behaviour.

The relative insensitivity of the spatial profile to excitation characteristics is further demonstrated in Figure 33. The spatial profiles of five Ba ion lines with ionization-excitation sums between 7.72 ev and 11.21 ev are plotted. Table VII summarizes the energies of the various lines involved. The experimental conditions for this set of profiles are 1.5 kw RF power, 0.9 lpm aerosol flow rate, 15 lpm plasma gas flow, and less than 1 lpm auxiliary gas flow. These plots confirm that relative independence of spatial position on energy requirements of the different lines, since the 493.4 BaII line peaks at the same position above the load coil as the 233.5 BaII line. Ca ion lines are seen to behave in a similar manner as can be seen in Figure 34. In this case the ionization-excitation sums are (a) 9.26 ev, (b) 12.6 ev, and (c) 13.2 ev. The three lines peak at the same position above the load coil.

### Discussion

The examples discussed in the previous sections lead one



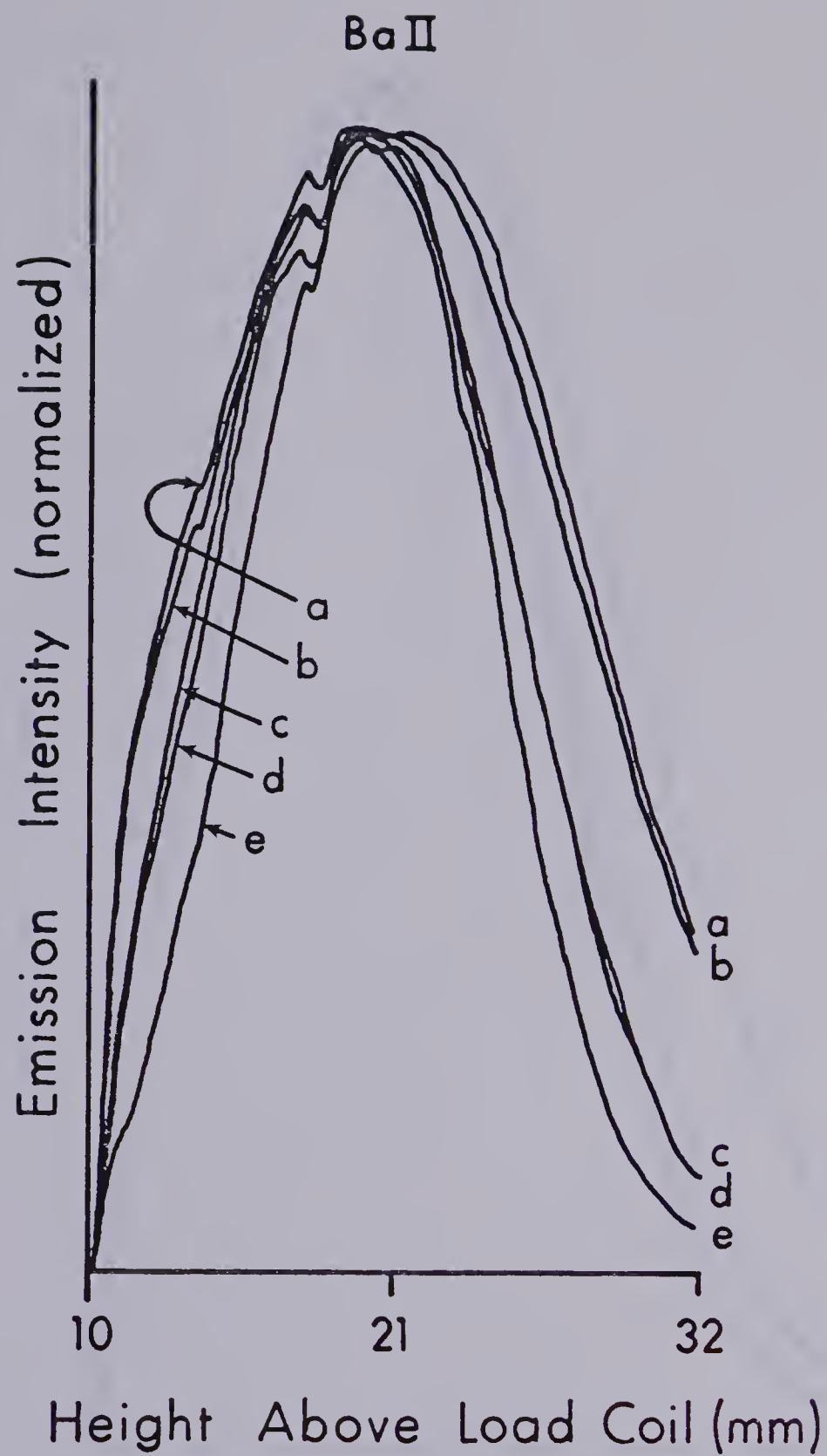


Figure 33. Vertical spatial profiles for BaII lines; (a) 455.4 nm, (b) 493.4 nm, (c) 413.1 nm, (d) 489.2 nm, and (e) 233.5 nm.



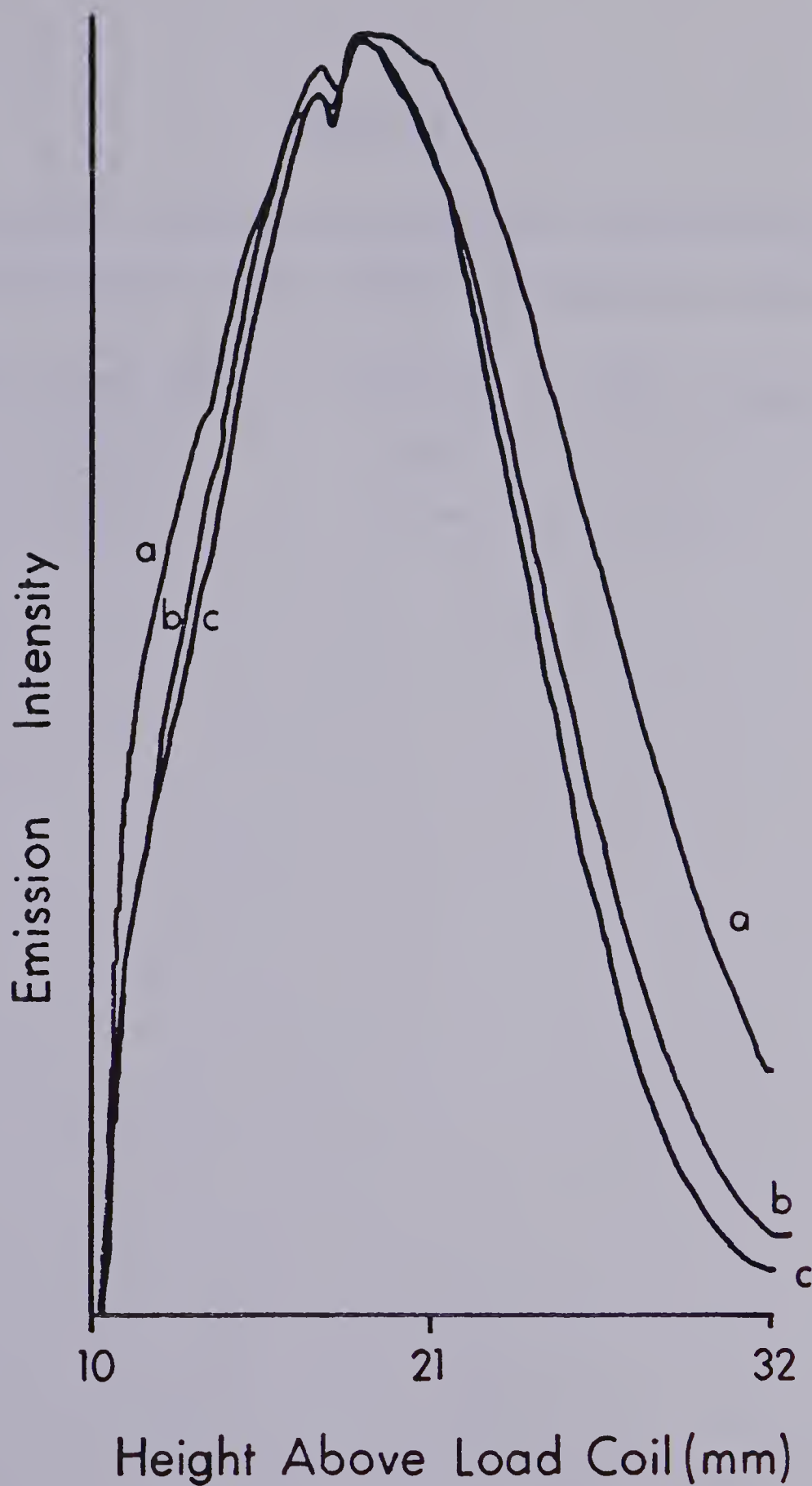


Figure 34. Vertical spatial profiles for CaII lines; (a) 39.3 nm, (b) 373.6 nm, and (c) 315.9 nm.



TABLE VI

WAVELENGTHS, EXCITATION POTENTIALS, AND SUM OF EXCITATION POTENTIAL AND IONIZATION POTENTIAL FOR Cd

<u>Species</u>	<u>Line (nm)</u>	<u>EP (ev)</u>	<u>EP + IP (ev)</u>
CdI	228.8	5.41	———
CdII	214.4	5.78	14.77





TABLE VII

WAVELENGTHS, EXCITATION POTENTIALS AND SUM OF  
EXCITATION POTENTIALS AND  
IONIZATION POTENTIALS FOR BaII

<u>Line (nm)</u>	<u>EP (ev)</u>	<u>EP + IP (ev)</u>
493.4	2.51	7.72
455.4	2.72	7.93
489.2	5.69	10.9
413.1	5.69	10.9
233.5	6.00	11.21



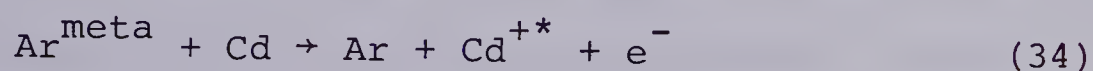
to believe that the aerosol channel may be divided into two regions. The first is a "thermal" region where soft line behaviour is observed, and spatial structure may be predicted on the basis of a normal temperature calculation. This is predominantly an atom line emission region and extends from just above the load coil to about 15 mm above the load coil at 1.5 kw. In this region it is probable that the soft line species are excited predominantly by collisions of the first kind between analyte atoms and electrons. The effect of an increase in power is to shift this zone toward the load coil and to increase the energy of the electrons slightly leading to a downward spatial profile shift and an increase in the overall emission intensity. The temperature in this region appears to increase as one moves up the central channel. This is in all likelihood the result of the diffusion of hot argon gas from the annular region toward and into the channel region. "Cold" argon gas injected into the bottom of the plasma moves up the aerosol channel becoming hotter as it mixes with "hot" annular argon gas. An increase in aerosol flow rate delays this process leading to the observed upward shift in the spatial emission profile of the analyte.

A "non-thermal" region where hard lines peak, and spatial behaviour is insensitive to analyte excitation parameters, characterizes the upper region of the analyte channel. By the time the analyte reaches this region, which extends from about 15 mm to 25 mm above the load coil, annular and aerosol

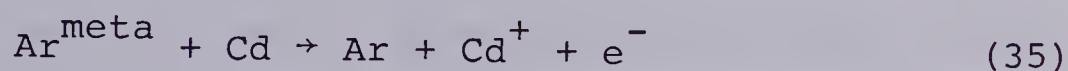


gas should be thoroughly mixed. The species responsible for excitation in this region appears capable of providing the high energy required to ionize and excite species such as Cd, Zn, Ba, and Ca. Since this region is well away from the load coils it is unlikely that electrons would possess sufficient energy to excite these species. Ion lines emitting in this region are often the most sensitive lines for analytical determinations in the ICP. This ion line advantage has been attributed to an excitation process involving argon metastable species as mentioned in Chapter I. It has been suggested that these metastable species may have lifetimes sufficiently long to exist in this region [101].

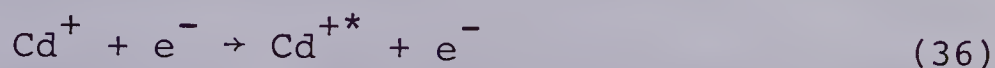
In the case of emission from Cd ion the value of 14.77 ev for ionization plus excitation precludes the direct Penning reaction,



since the metastable species have energies of 11.55 ev and 11.71 ev. However the Penning process,



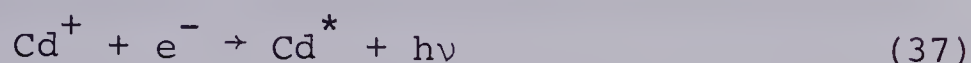
followed by a collision of the first kind with an electron of the proper energy,



is possible. The close correspondence of the spatial profiles for CdI and CdII also suggests that the mode of ex-



citation of these two species is related. CdI may be significantly populated by the ion-electron recombination reaction [5],



such that Penning produced  $\text{Cd}^+$  may act as a reservoir for both CdI and CdII emission.

In the case of Ba the energies involved make the excitation reaction



possible for all of the energy levels which were observed. This could be used to explain the close correspondence in spatial behaviour for these lines.

The division between these two regions is not a distinct one. The regions probably overlap significantly. There is also the possibility that ionization in the lower channel region is partially the result of a Penning ionization process such as that outlined in Equation 35. If this is the case it is difficult to assess the degree to which it will affect the spatial structure in the lower channel. The density of argon metastable species is undoubtedly closely related to the temperature. Thus, the correlation of the spatial structure of soft lines with a thermal ionization-excitation treatment only, might be misleading, even though





it is quite successful. Further experiments are required to unravel the problem. A detailed spatial map of argon metastable densities would be very useful. The effects of a metastable quencher should also be extensively investigated.



## CHAPTER V

### IMPLEMENTING ABEL INVERSIONS USING A PHOTODIODE ARRAY MEASUREMENT SYSTEM

#### Introduction

Up to this point the discussion of analyte spatial behaviour has been limited to observations on a vertical spatial zone up the centre of the plasma. Using 2:1 imaging this means that there is only a 50  $\mu\text{m}$  wide spatial observation window. The analyte channel is much wider than this, however, and it would be useful to measure emission intensity across the entire width of the channel. In addition, since the ICP is viewed from the side, the emission intensity observed is the result of contributions from all depths within the source, and is not solely limited to axial information. From a fundamental point of view it would be useful to be able to measure the emission from the ICP with radial resolution, that is, such that one can separately observe emission from varying depths within the source without contributions from other depths within the optical path.

The most common way of solving this problem has been to acquire a number of data points at right angles to the source axis, or "laterally". These points may subsequently be operated on using a mathematical process known as an



"Abel Inversion" [78]. This process converts measured, spatially integrated lateral information, and converts it to spatially resolved radial information. The measurement of radial emission intensities from the ICP using this Procedure is not new. Kornblum and deGalan designed a measurement system to measure radial spatial distributions of emission intensity in the ICP [3], and used it to calculate temperature, and electron densities [35], as well as to study matrix effects [76]. Kalnicky, et al. [36], Jarosz, et al. [37], and Alder, et al. [38] have all used this technique to measure emission intensities for the purpose of calculating radially resolved temperatures and electron densities.

The generation of a useful radial intensity distribution from a lateral intensity distribution imposes several requirements on the quality of the measured lateral data. These requirements have been discussed previously [3]. One of these requirements is that the lateral data be as detailed as possible; the greater number of data points, the more accurate will be the generated radial distribution. The acquisition of detailed spatial emission data from a spectrochemical source such as the ICP requires a very large number of measurements if complete information is to be obtained. Often the tedium of such measurements limits the range of conditions and number of analyte species which



can be studied in a reasonable amount of time. This problem has been circumvented in this study by using the photodiode array-based measurement system. The purposes of this chapter are to detail modifications to the previously described profiling system such that it can be used to acquire lateral emission intensities, and to outline how this data is converted into radial emission intensity information. Portions of this chapter have been previously published [83].

### Experimental

The monochromator/diode array measurement system has been previously described in Chapter II. In order to obtain complete detailed maps of analyte emission throughout the ICP this system has been modified so that a series of horizontal emission profiles can be acquired. In order to obtain horizontal emission profiles the monochromator was simply rotated  $90^\circ$  so that the entrance slit was horizontal rather than vertical. This was implemented by constructing a monochromator mount from aluminium schematically outlined in Figure 35. This mount holds the monochromator securely in place and mates with the optical rail bed. In order to measure horizontal slices of the plasma at different vertical heights the monochromator and lens were mounted on a 3 point screw adjustable kinematic mount which could be raised or lowered with a precision of 0.01 mm measured using





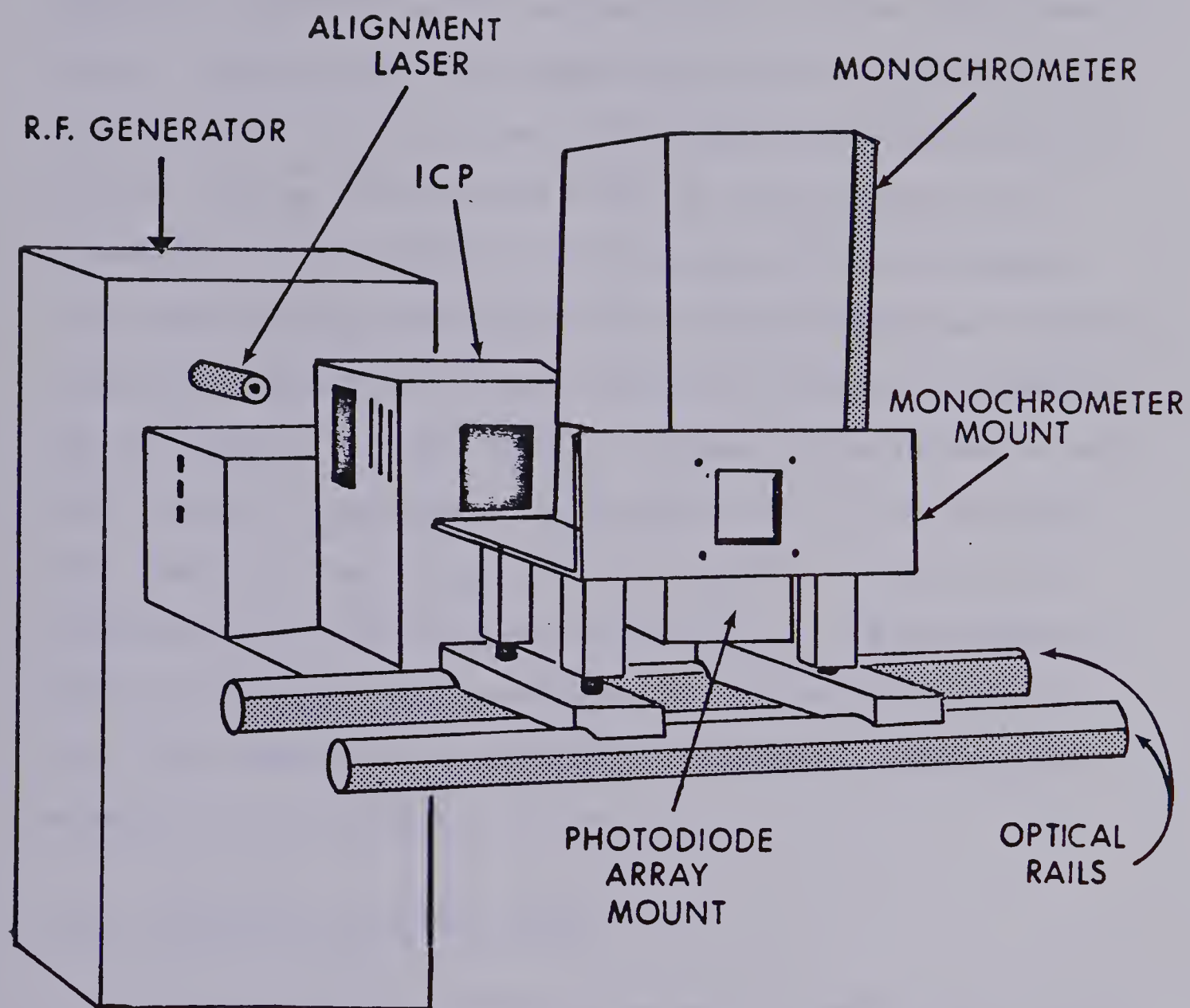


Figure 35. Horizontal profiling system.



a precision dial guage (Mitutoyo No. 3052, Japan). The plasma is imaged onto the entrance slit of the monochromator using a single spherical lens with 10 cm focal length and a magnification of 1/2. Since the individual diodes are on 25.4 mm centres and 25.4 mm wide the array samples the emission from the plasma in 256 separate 50.8  $\mu\text{m}$  steps. This measurement capability of the diode array-based system results in high quality input data for the Abel inversion. The acquisition of 256 separate lateral intensities at such fine spacing by horizontal translation of a conventional measurement system would indeed be tedious. Using this system and the Abel inversion technique it is possible to obtain horizontal profiles from 0 to 30 mm above the load coil, and thus build a complete 3-dimensional picture of emission in the plasma.

#### Abel Inversion of Lateral Data

The process of calculating a set of radial data points from a corresponding set of lateral data points is known as the Abel inversion. The application of this technique to spectroscopic data is well known [78] and good discussions of the technique as applied to spark sources [1,2,81], and ICP [7,35-37] are available and will not be repeated in this thesis. A short discussion, however, is warranted.

The relationship between the measured lateral intensities  $I_n(x)$  as measured with the diode array and the



desired radial intensities  $i_k(r)$  calculated by the Abel inversion is shown schematically in Figure 36. The diode number index is  $n$  and the radial index is  $k$ . We use a 256 element diode array centered on the plasma; thus the actual maximum value of  $N$  is 128.

Following the method of Nestor and Olsen [79] the radial intensity  $i_k(r)$  may be expressed in terms of the measured lateral intensity  $I_n(x)$  by the summation [78]:

$$i_k(r) = - \frac{2}{\pi a} \sum_{n=k}^{N-1} I_n(x) B_{k,n} \quad (39)$$

where  $k$  and  $n$  are integer position indicies for the radial and lateral intensities, and  $a$  is the width of the slice sampled by a single photodiode. The coefficient  $B_{k,n}$  can be evaluated by using the expressions

$$B_{k,n} = -A_{k,k} \text{ for } n = k \quad (40)$$

$$\text{and } B_{k,n} = A_{k,n-1} - A_{k,n} \text{ for } n \geq k + 1 \quad (41)$$

where

$$A_{k,n} = \frac{[n^2 - (k-1)^2]^{1/2} - [(n-1)^2 - (k-1)^2]^{1/2}}{2n-1} \quad (42)$$

To test the accuracy of the inversion calculation a set of radial test data was generated using the polynomial expression shown in Equations (43) and (44) [78].



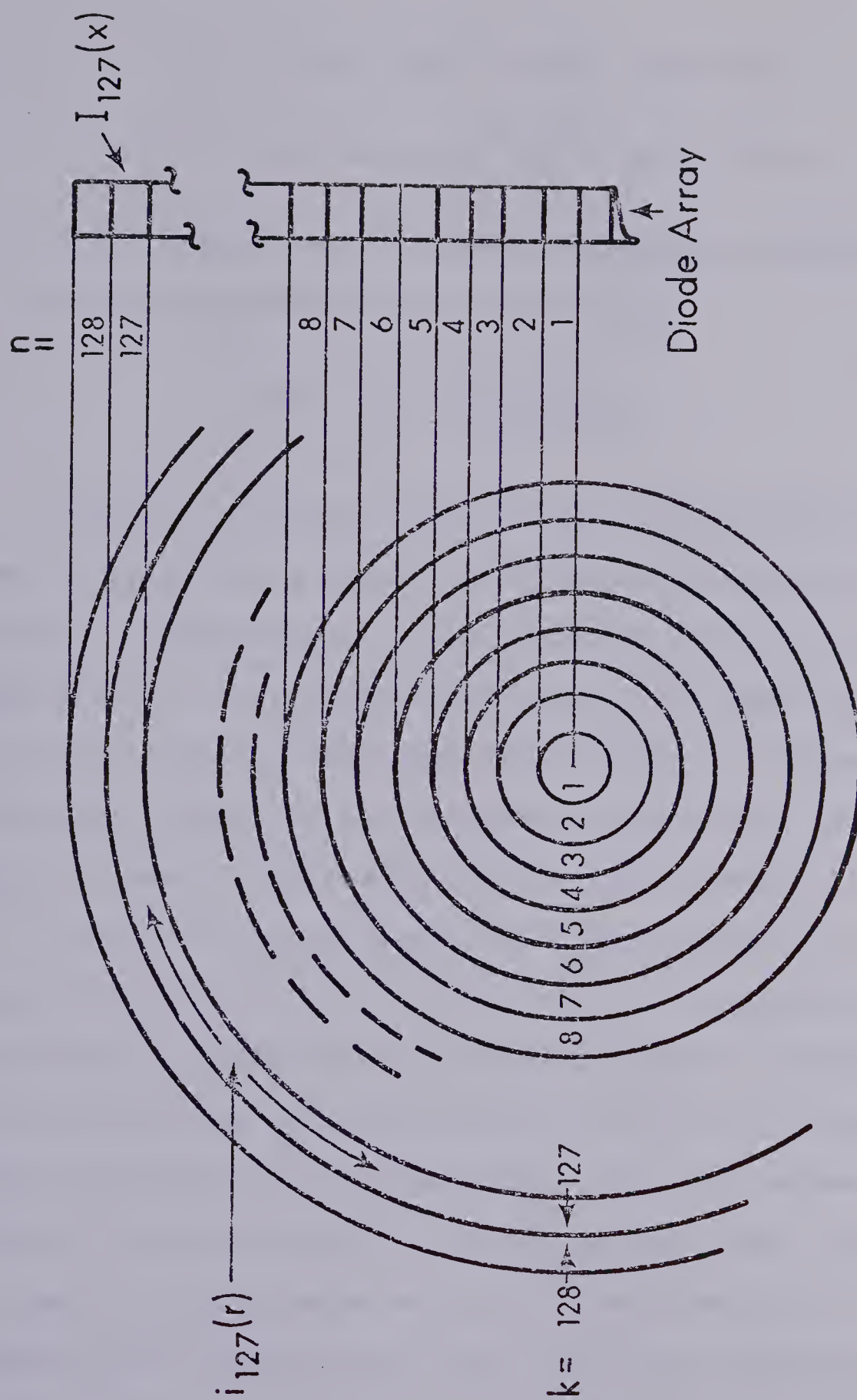


Figure 36. Schematic representation of the lateral and radial variables involved with Abel inversion.







$$i(r) = 0.75 + 12r^2 - 32r^3 \quad 0 \leq r \leq 0.25 \quad (43)$$

$$i(r) = 16/27(1+6r-15r^2+8r^3) \quad 0.25 < r \leq 1.0 \quad (44)$$

The corresponding set of lateral intensities may be obtained by direct integration of the expression

$$I(x) = 2 \int_x^1 \frac{i(r) r dr}{(r^2 - x^2)^{1/2}} \quad (45)$$

The set of lateral data points thus generated were used to calculate a radial array using the Abel inversion program. This program runs on the PDP-8 and is listed in Appendix C. The procedure utilized is to read lateral data stored on magnetic tape into the computer, perform the Abel inversion, and store the resultant radial data back on magnetic tape. The result of the test is shown in Figure 37. Curve (a) is the radial test data generated using Equations (43) and (44). Curve (b) is the lateral test data which is calculated from the integral in Equation (45), and curve (c) is the radial profile which is calculated using our Abel inversion program. Curve (c) shows a small amount of scatter near the centre of the trace ( $r=0$ ) which is due to the recursive nature of the calculation but generally it compares very well with the theoretical profile of curve (a).

An example calculation using spatial data acquired from an ICP is shown in Figure 38 in order to illustrate the



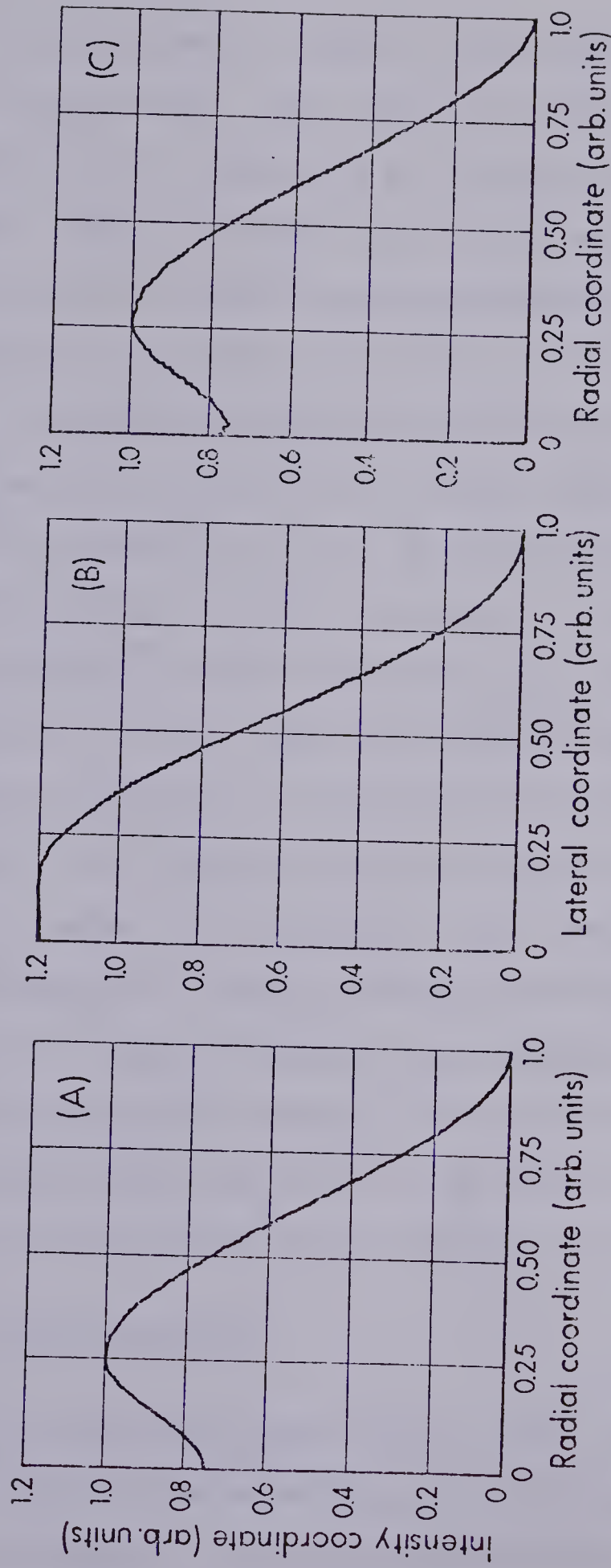


Figure 37. (A) Radial test data.

(B) Lateral intensities calculated from radial test data.

(C) Radial intensities calculated from lateral data via Abel inversion.



sequence of processing from raw horizontal data to calculated radial data. The spectral signal monitored was the MgII 279.5 nm line measured at a height of 12 mm above the load coil. The horizontal spatial emission profile as measured with the diode array measurement system is shown in Figure 38a. It takes only about 30 sec to acquire this signal. An average one-sided profile is then calculated by summing the intensities of diodes equidistant from the center and dividing by two. We found this step to be necessary because the Abel inversion is very sensitive to slight asymmetries and a discontinuity results at the center of the radial data for slightly asymmetric lateral data. The averaged one-sided lateral profile is shown in Figure 38b. The radial profile calculated from this lateral profile is shown in Figure 38c. Note the difference in shape of the lateral and radial emission profiles. The lateral profile of Figure 38b implies that emission peaks at the center of the analyte channel whereas, the radial profile in Figure 38c indicates that the emission in fact dips slightly at the center of the channel peaking just off axis.

### Results and Discussion

This system has been used to study analyte emission from the ICP, by constructing 3-dimensional "maps" of radial emission intensity. This is carried out by acquiring



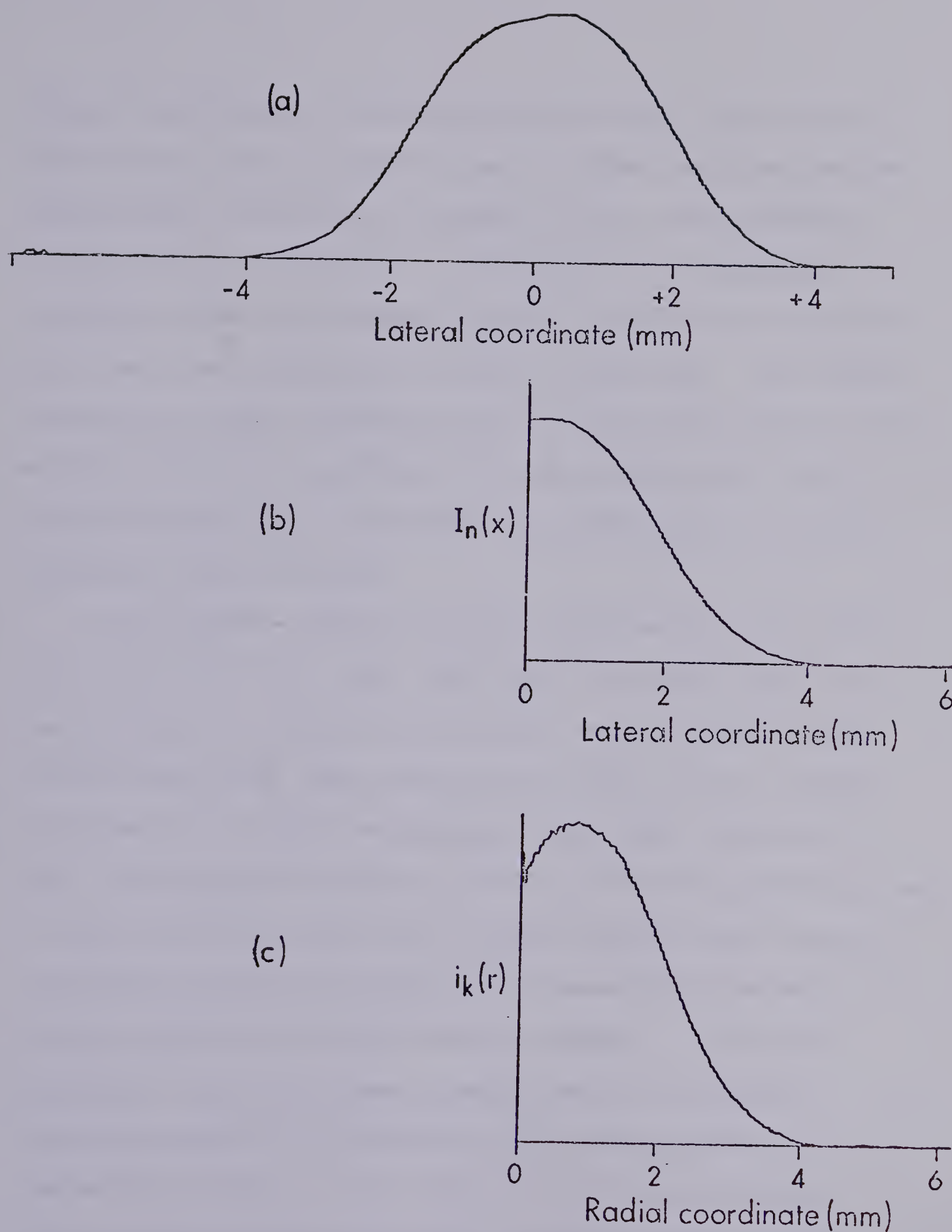


Figure 38. (A) Lateral intensity data measured for MgII 279.5 nm.  
 (B) Average one-sided lateral data.  
 (C) Calculated radial intensities





lateral profiles at different heights above the load coil and storing them on magnetic tape. These profiles may be subsequently inverted and plotted in the manner shown in Figures 39, 40, 41 and 42. In these figures emission intensity from the observed analyte is plotted on the vertical axis as a function of radial coordinate. The radial coordinate is the distance in mm out from the centre of the aerosol channel. A series of these are plotted at different heights above the load coil resulting in the 3-dimensional plots provided.

The complete radial emission profiles for CaI (422.7 nm), CaII (393.3 nm), MgI (285.3 nm), and MgII (279.5 nm) are provided in Figures 39, 40, 41, and 42 respectively. The ICP operating conditions are RF power 1.5 kw, plasma gas flow rate 15 lpm, coolant gas flow rate, less than 1 lpm, and aerosol flow rate, 0.8 lpm for the Mg profiles, and 0.9 lpm for the Ca profiles. These profiles show several interesting spatial features which seem characteristic of analyte emission from the analyte channel. Low in the plasma all four lines have similar spatial structure. Emission peaks up off axis with the peak emission corresponding roughly to the edge of the analyte channel. This is good evidence that the excitation lower in the channel is related to contact with hot argon gas originating from the annular region of the plasma. It is also



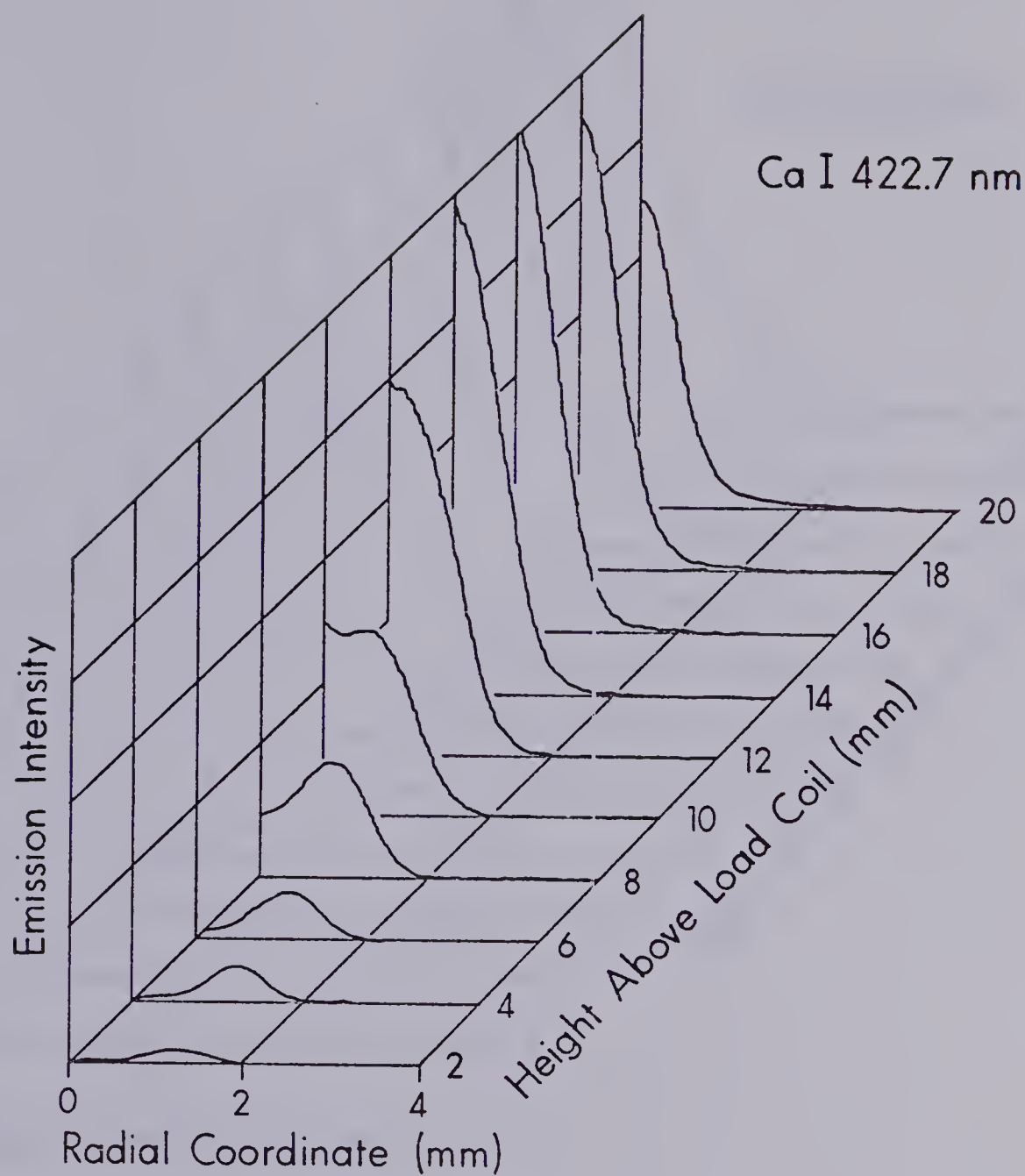


Figure 39. Complete radial emission map of the ICP discharge for CaI 422.7 nm.



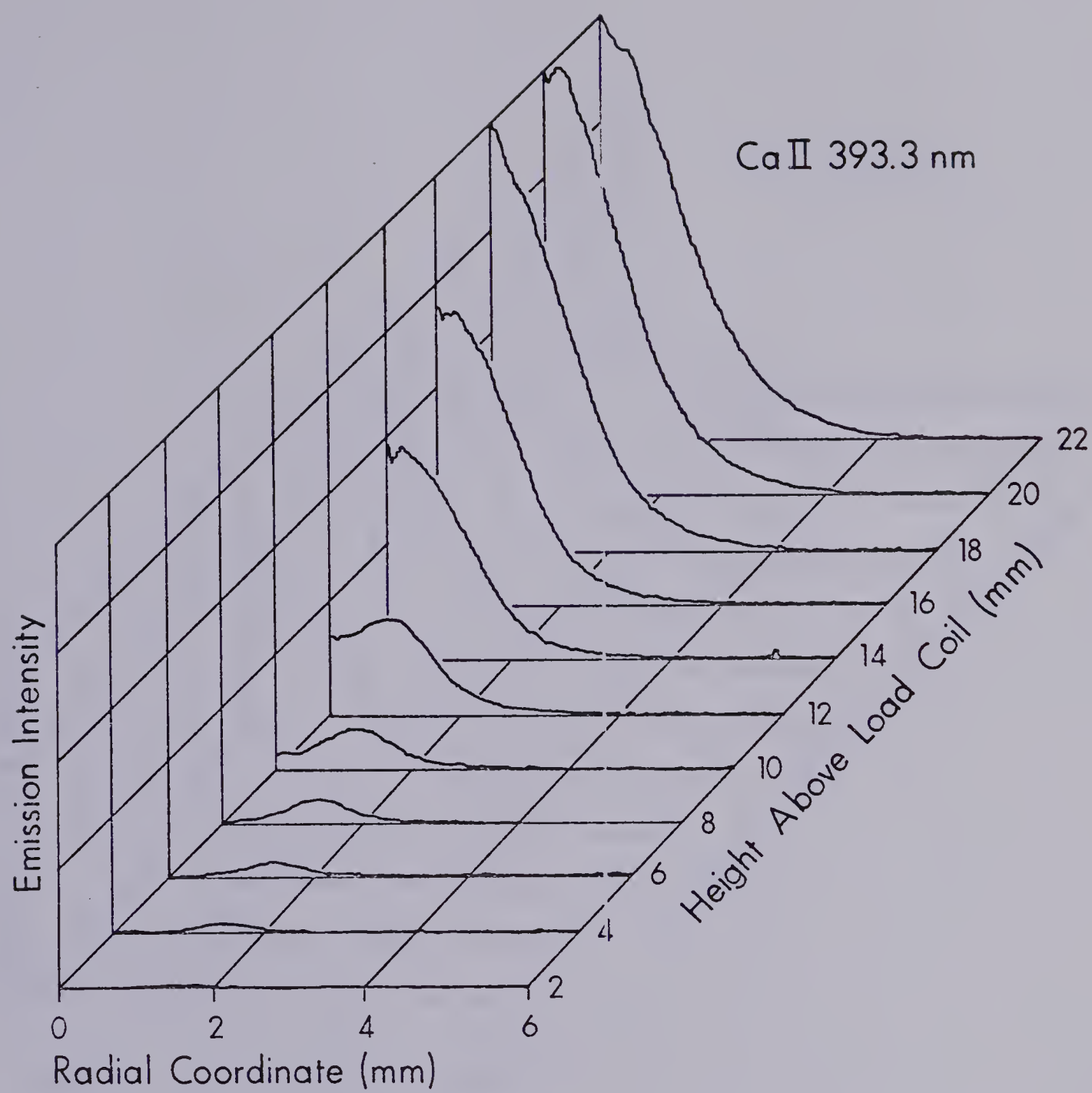


Figure 40. Complete radial emission map of the ICP discharge for CaII 393.3 nm.



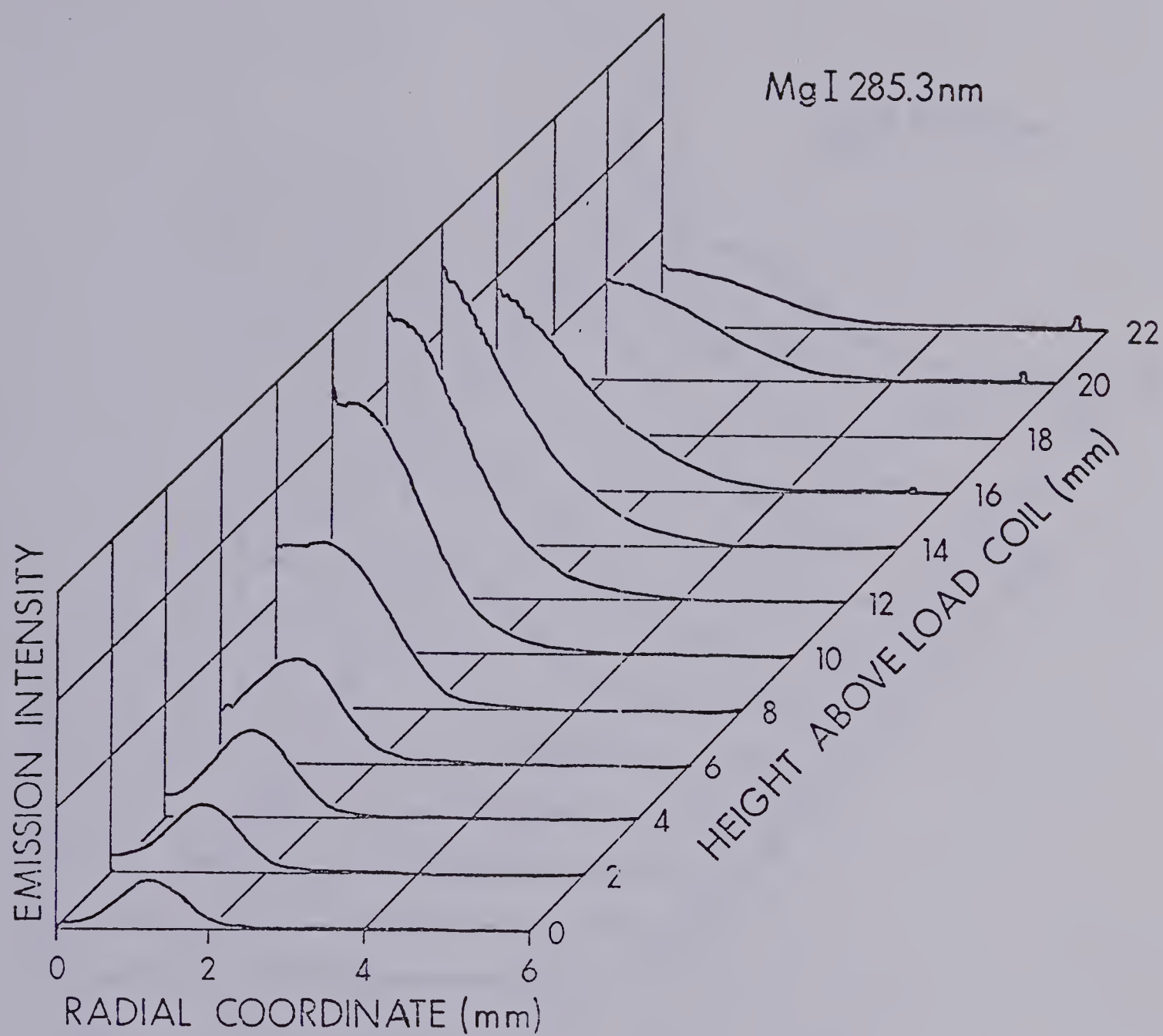


Figure 41. Complete radial emission map of the ICP discharge for MgI 285.3 nm.





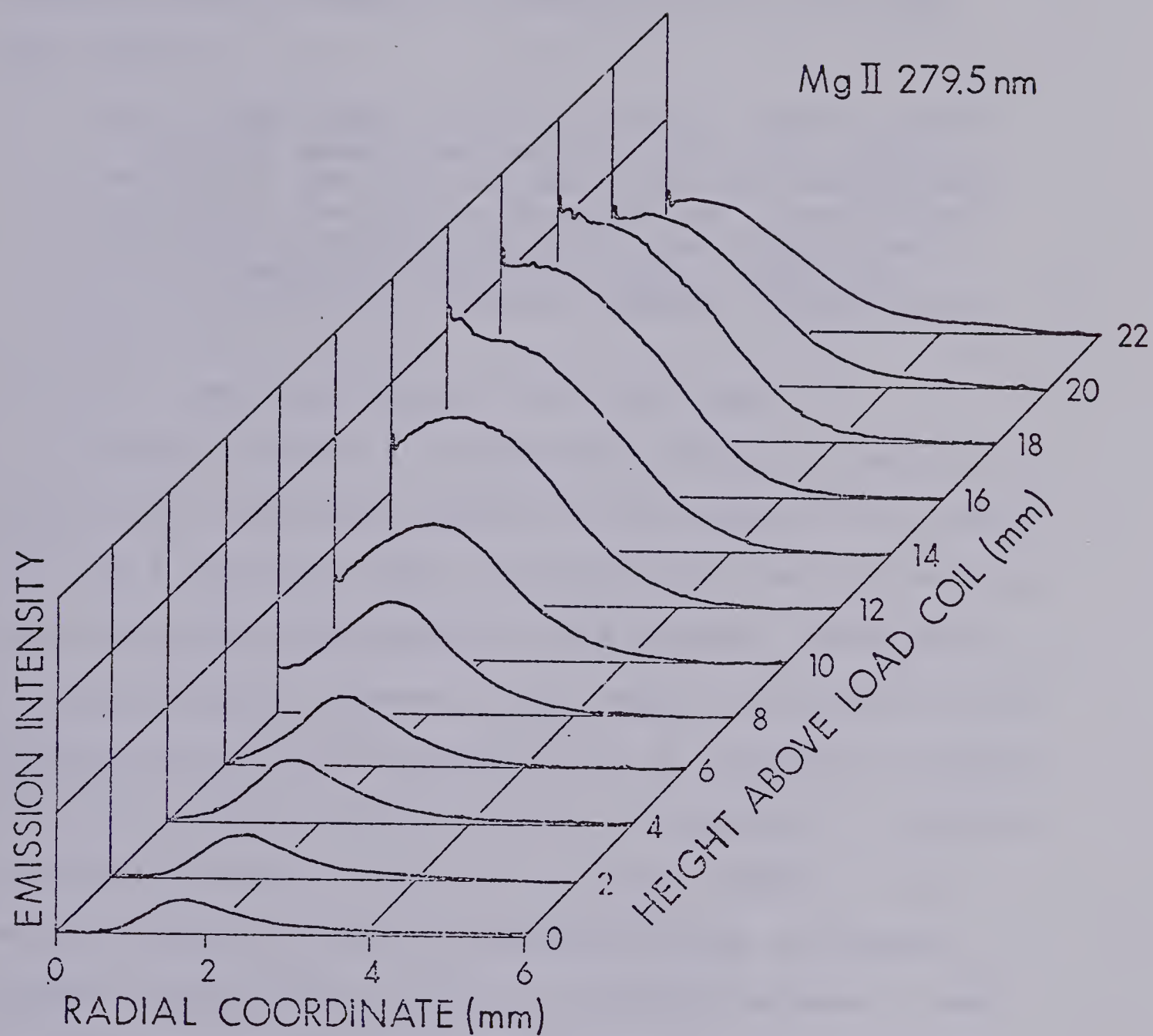


Figure 42. Complete radial emission map of the ICP discharge for MgII 279.5 nm.



verification of an assumption made by Human and Scott [43] in explaining the shapes of spectral lines in the ICP.

They noted:

"Low in the plasma (at 10 mm height) self-reversal of spectral lines does not occur for high concentrations of analyte, but the lines are considerably broadened. The unusual shape of the lines can be explained by assuming that the core of the plasma is a predominantly absorbing region, while the emission originates from the annular region around the core."

It can be seen that this is indeed the case.

With an increase in observation height the position of the off axis peak moves closer to the centre of the channel until at a height of about 12-14 mm above the load coil the emission peaks in the center of the channel. This can be interpreted as an increase in the amount of mixing of cold channel gas and hot annular gas with an increase in height, such that complete mixing occurs at this height. Emission continues to peak at higher observation heights. The emission from ion lines is characterized by a somewhat broader analyte emission plume at heights between 14 and 22 mm above the load coil, when compared to emission from atom lines. This might be the result of ambipolar diffusion of ion species. This phenomenon will be discussed in detail in Chapter VI of this thesis. Also, in agreement with the data presented in previous chapters the neutral atom lines are observed to peak lower in the analyte channel.



In general the analyte channel is characterized by a structure which starts out low in the plasma somewhat like a hollow bullet and, then higher in the plasma, in the region normally observed for analytical purposes, becomes a solid emitting plume. This structure suggests that the temperature of the channel is hotter near the edges low in the channel and hotter in the middle at higher observation heights. To test this, radially resolved excitation temperatures have been measured.

#### Spatial Distribution of Excitation Temperatures

Excitation temperature has been measured using the "two line" ratio method [55,56,102-105]. The method involves the measurement of emission intensity for two lines of the same species, and calculating the temperature from the ratio of these two lines, according to the formula:

$$\ln I_p/I_g = \ln \left[ \left( \frac{g_p A_p}{\lambda_p} \right) / \left( \frac{g_g A_g}{\lambda_g} \right) \right] + (E_g - E_p)/kT \quad (46)$$

where

$I_p$  = emission intensity from excited state p

$I_g$  = emission intensity from excited state g

$g_p A_p$  = transition probability of p

$g_g A_g$  = transition probability of g

$\lambda_p$  = wavelength of p transition



$\lambda_g$  = wavelength of g transition

$E_g$  = excitation energy of state g

$E_p$  = excitation energy of state p

k = Boltzmann's constant

T = excitation temperature

The two lines used for this measurement were PbI 280.1 nm and PbI 283.3 nm. Transition probabilities were taken from Moore [106]. The wavelength, transition probabilities and excitation potentials for these two lines are listed in Table VIII. Radial profiles for these two lines were acquired at various heights above the load coil and the ratio calculated to provide the temperature profiles given in Figure 43. The conditions used for this study were: 1.5 kw RF power, 15 lpm plasma gas flow rate, less than 1 lpm auxiliary flow rate, and 0.8 lpm aerosol flow rate. In Figure 43 temperature is plotted as a function of radial distance from the centre of the plasma from 0 to 3 mm, at the different heights noted on the figure. Temperatures ranged from 3500 K to 4900 K depending on spatial position. Errors in these values have not been included, so they should be taken as approximate only; however, the relative magnitudes may be compared. At low observation heights between 4 mm and 8 mm there may be inaccuracies in the Abel inversion as the result of off axis peaks, so these values near the analyte channel may not be representative.







TABLE VIII

WAVELENGTHS, TRANSITION PROBABILITIES, AND EX-  
CITATION ENERGIES FOR PbI USED  
TEMPERATURE DETERMINATION

		<u><math>\lambda</math> (Å°)</u>	<u><math>gA</math> (sec<sup>-1</sup>)</u>	<u><math>E</math> (ev)</u>
PbI	p	2801.99	$43 \times 10^8$	5.7439
PbI	g	2833.06	$1.8 \times 10^8$	4.37492



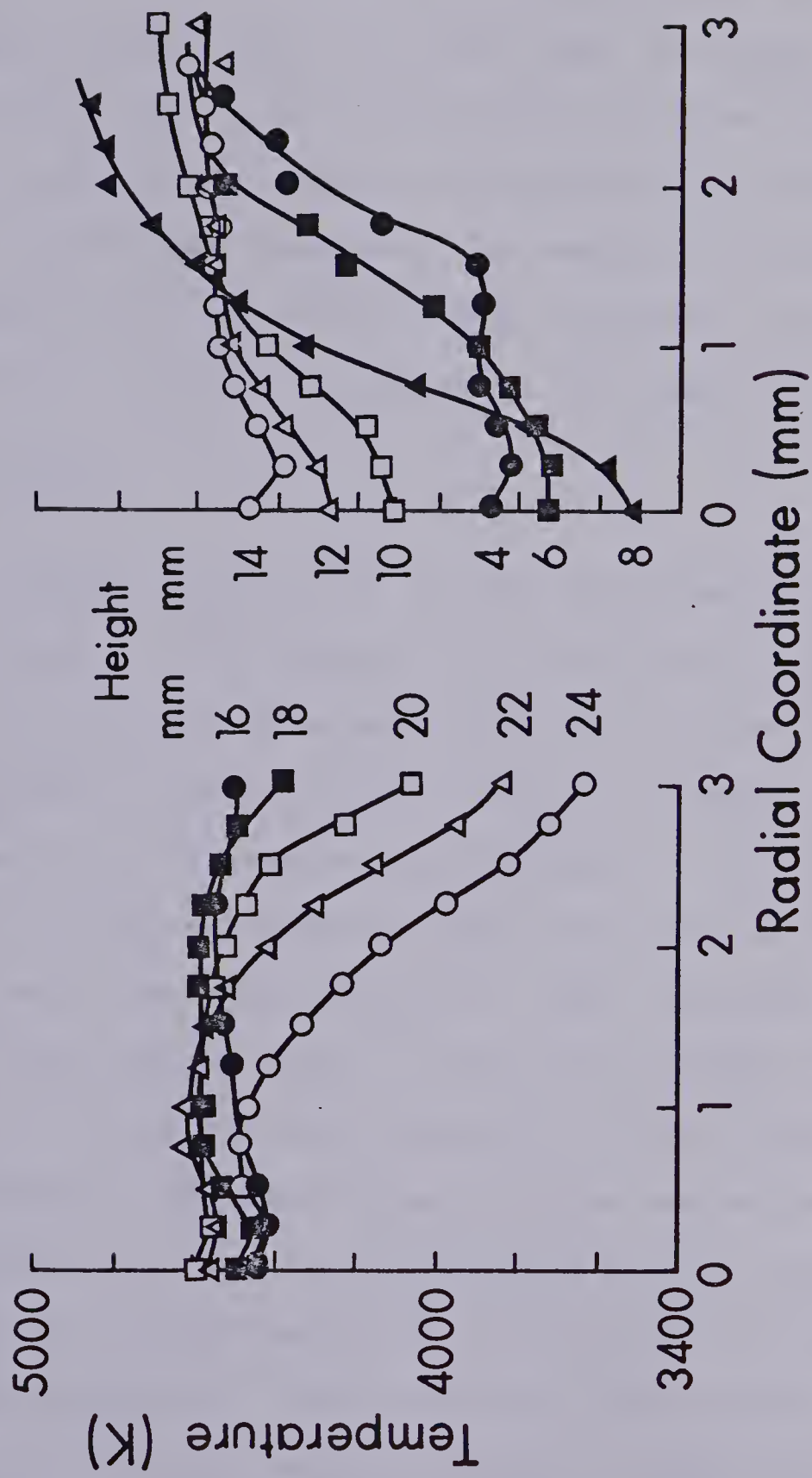


Figure 43. Radial temperature profiles for the ICP discharge.



The results confirm, however, that low in the analyte channel, temperature is higher near the edges as can be seen in the plots for 4 to 12 mm above the load coil. At higher observation heights this trend is reversed and temperatures peak near the centre of the analyte channel dropping with increasing radial distance, as can be seen in the plots for 18 to 24 mm above the load coil.

### Conclusion

Clearly the ability to make the kind of measurements described in this chapter has added greatly in the spatial characterization of analyte emission in the ICP. The ease and speed of acquisition of spatial information from the plasma can be tremendously increased using the photodiode array. High resolution lateral data are simultaneously acquired in an ideal format for Abel inversion. Thus the sometimes tedious task of collecting a large number of lateral points to ensure accuracy of the inversion is eliminated. The ease of acquisition means that complete 3-dimensional pictures of emission may be quickly built up which can provide detailed, quantitative information about analyte emission. These pictures have proved invaluable in unraveling the complex problem of the effect of easily ionizable elements on analyte emission intensity. This is discussed in the next chapter.



## CHAPTER VI

### INTERFERENCE FROM EASILY IONIZABLE ELEMENT MATRICES

#### Introduction

A literature survey of the effects of an excess of an easily ionizable element (EIE) such as Na, K, or Cs as a concomitant on analyte emission intensity in ICP's is a study in confusion. Virtually every ICP spectroscopist has studied the effect of this type of matrix, and the literature abounds with tables and graphs on the magnitude and characteristics of the effect. The driving force for these studies is the fact that EIE's, especially Na and K, turn up in a variety of natural matrices for which emission spectroscopy is used as an analytical probe. These include animal and plant materials, blood, seawater, and geological samples.

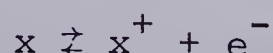
The sources of much of this confusion are twofold. First, much of the data which has appeared has not been consistent, some investigators observing analyte emission "enhancements", some observing "depressions", and some "no effect". Secondly, there is still no satisfactory explanation for the observed effects at a fundamental level. To clarify some of these observations and offer rational arguments on the nature of the effect a spatial study of the effect has been undertaken and forms the basis of this chapter. Some preliminary results have been published [77].



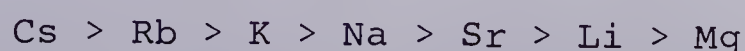


### Survey of the EIE Effect in Plasmas

The effect of EIE's in analytical flame spectroscopy has been well characterized. Enhancements in emission intensity from atom lines is observed when signals with and without the presence of an EIE are compared [107,108]. These observations have been rationalized on the basis of a shift in the ionization equilibrium for analyte atom (x), ion ( $x^+$ ) and electrons ( $e^-$ ).



The addition of the EIE has the effect of increasing the electron density in flames such that the equilibrium shifts toward the neutral atom species causing enhancement of neutral atom line emission [107,109]. The magnitude of the effect has been shown to be related to the ionization potential (IP) of the added EIE, being larger for those of lower IP and reducing in magnitude as the IP of the added element increases [110]. Thus, in terms of the effect, the sequence,



is observed. Quite a different situation is observed in an arc discharge. The addition of an EIE to the arc increases the electrical conductivity of the arc but leaves the thermal conductivity essentially unchanged [56]. The arc responds to this by a lowering in temperature such that the power supplied to the arc is once again balanced by energy loss due



to thermal conduction. Thus analyte emission intensities are observed to decrease due to the presence of EIE's.

The situation is not quite so well defined in the ICP, partially because of the variability in plasma operating conditions between investigators, and partially because the influence of EIE's has been observed to be complex in nature. Hoare and Mostyn [28] observed that 1000  $\mu\text{g/ml}$  Na did not affect the emission intensity of B and that 10,000  $\mu\text{g/ml}$  produced slight enhancements for atomic lines and slight depressions for ionic lines. Similarly Kirkbright et al. [39,40] reported that the emission intensities of S, P, As, I, Se, and Hg were not affected by the addition of K or Na in 50 fold weight excess representing 0.05 to 0.5% by weight salt. In the first detailed study, Larson et al. [48] investigated the effects of up to a 600 to 1 molar ratio excess of Na on the emission intensity of Ca, Cd, and Cr. The ion lines were all observed to be depressed by the addition of Na at heights above 15 mm, the magnitude of the depression increasing with increasing Na concentration. The magnitude of the depression was for the most part independent of the observation height between 15 to 25 mm above the load coil, at low aerosol flow rates (1.0 lpm). An increase in RF power from 1025 watts to 1250 watts likewise had little effect on the magnitude of the depression. At 1025 watts and 1.3 lpm flow rate, however, ion emission was enhanced between 15 and



17 mm above the load coil and depressed thereafter. This was an indication that there may be complex spatial features associated with the effect. The emission behaviour of the atom lines was more complex. Ca atom emission was in general enhanced, the magnitude increasing with increasing molar ratios of Na to Ca. The enhancement increased with increasing height above the load coil. An increase in power increased the magnitude of the effect as did an increase in the aerosol flow rate. Cr atom emission on the other hand was depressed at lower observation heights and enhanced at higher observation heights. An increase in both power and aerosol flow rate increased the effect. Cd atom emission was depressed at all heights, insensitive to power changes, but changed to enhancements at higher aerosol flow rates. They concluded that there was some evidence to suggest an ionization suppression mechanism, but they also commented that other factors must play a role since some of the data conflicted with this interpretation.

Abdallah et al. [45] carried out a similar study in which the emission intensities of  $\text{PI}$ ,  $\text{CaI}$ ,  $\text{CaII}$ ,  $\text{CdI}$ ,  $\text{CdII}$ ,  $\text{CrI}$ , and  $\text{CrII}$  were observed with additions of Na up to 0.1%, at observation heights of 5, 15, and 25 mm above the load coil.  $\text{CaI}$  was enhanced and  $\text{CaII}$  depressed only slightly in agreement with the observations of Larson et al.  $\text{CdI}$  and  $\text{CdII}$  were both observed to be depressed slightly at all heights.





CrI was relatively insensitive to Na addition, whereas CrII showed slight enhancement and then a larger depression as Na concentration was increased. The effect became less pronounced at higher observation heights. Emission from atomic phosphorus was enhanced significantly at 5 mm above the load coil, and slightly at 25 mm above the load coil. The variation of aerosol flow rate was found to cause complex changes in the nature of the effect. An increase in applied power was found to reduce the effect on CaI and CaII until at 2 Kw no effect could be observed. By measuring the ratio of the MgI (285.2 nm) and MgII (279.6 nm) emission lines, and the ratio of two TiII lines (322.2 and 322.4 nm) the effects of added Na on electron density and temperature were found to be negligible. It was also observed that Na exerted the same influence on emission and absorption signals which led them to believe that the effect of Na was largely due to a volatilization interference. Veillon and Margoshes [113] also performed an emission/absorption measurement on CaI and CaII and found no change in the absorbance signal for CaI in the presence of Na even though the emission signal increased by a factor of 2.7. The plasma studied, however, was a tear drop shape, rather than an annular plasma. Boumans and DeBoer [46] investigated the effects of K on analyte emission intensity as part of the optimization procedure for simultaneous multielement analysis using ICP. For LiI a fivefold en-





enhancement dropped to a 20% depression as the aerosol flow rate was decreased from 1.7 lpm to 1.1 lpm. Similar results were observed for MnI and BaII. The effect decreased sharply with an increase in power from 0.4 Kw to 1.0 Kw, such that at 1.0 Kw the effect was very small. Under the optimum conditions for multielement analysis, 0.7 Kw power input, 1.3 lpm aerosol flow rate and 15 mm observation height, the effects were found to be minimal, +20% for LiI, + 15% for SrI, -3% for AlI, -2% for MnI, 0% for CdI, and -6% for SrII and LaII, for 0.1% K as interferent. Similar magnitudes were found for Cs as an interferent.

In a subsequent publication [47] using ultrasonic nebulization, Boumans and DeBoer separated out nebulizer/desolvation effects and plasma effects. In general enhancements of 3% to 36% were observed for atom line emission, the exception being Mn where a depression of 14% was observed. Ion lines were depressed from 2% to 22% for all the elements studied. Nebulizer/desolution effects were found to be significant in only 3 of the 9 elements studied, the effect being in the range 4% to 7% compared with 21% to 29% for the analogous plasma effect. The magnitude of the effect correlated with the ionization potentials of the elements Ba, Sr, V, Mn, Fe, decreasing with increasing ionization potential. The results for Pd, Zn, and Cd did not follow this trend however. The effect of K on BaI was found to be related to molar con-



centration of K rather than the molar ratio of K to Ba. They suggested that ionization effects are partially the cause of the effect of K, but pointed to a possible volatilization effect as the result of water "included" in desolvated particles; or retarded volatilization due to the matrix causing "lateral diffusion effects".

Watson and Steele [111] studied the effects of up to 3% added Na on the emission intensities from several elements in an ICP operating at 5.5 kw, 2.0 lpm aerosol flow rate with nitrogen as the coolant gas. FeII, CaII, BI, SaI, AlI, CdII, and CrII all showed enhancements at 10 mm above the load coil, and depressions at 15 mm above the load coil. The magnitude of the interference was found to increase with increasing Na concentration, except for BI which showed a sharp initial enhancement of 8% which decreased to about 2% at a Na concentration of 30 g/l. The magnitude of the depressions at 15 mm above the load coil were much larger than the analogous enhancements at 10 mm above the load coil. For the most part an increase in power was found to decrease the matrix effect. No explanations were offered for the observations.

Clearly the exact nature of the effect of easily ionizable elements on analyte emission is complex. The picture is further clouded by the variety of operating conditions chosen by different investigators. Nevertheless, we would not expect the physical interactions among EIE, analyte and



plasma gas to be substantially different from system to system and some postulate which can unify the observations is required. Boumans and DeBoer [47] noted that, "Fundamental studies using spatial resolution will have to clear up the picture of plasma interferences...."

Kornblum and deGalan [76] undertook the first detailed spatial study of the effects of EIE's on analyte behaviour in the ICP. They used spatially resolved emission and absorption measurements to investigate the effect of Cs on ground state population and emission from excited states of Ca and Mg atom and ion species. They made the point that since high aerosol flow rates have been observed to magnify the effect, they would use this condition such that the effect could be more easily studied. The observations could then be extrapolated to analytical conditions, hopefully with no changes in the basic underlying mechanism. A horizontal profiling system was used which provided radial distributions, after Abel inversion, from the channel centre to 5 to 6 mm off axis. These radial profiles were collected at three different observation heights: 7.5 mm, 15 mm, and 30 mm above the load coil.

For CaI (422.7 nm), emission enhancements were observed at 7.5 and 15 mm, but changed to a depression at 30 mm. The analogous absorption measurements showed that ground state atom number densities decreased at all observation





heights. A similar depression was observed for ground state ion (CaII 393.3 nm) populations at all observation heights. Ion emission was enhanced at 15 mm but depressed at both 7.5 mm and 30 mm above the load coil. Kornblum and deGalan observed that this data indicated that there were probably three major contributions to the effect of EIE's. Radial data showed that the effect of Cs was to shift the off axis absorption maximum outward from the central channel. They interpreted this as a volatilization effect, the presence of excess matrix resulting in a slower release of analyte atoms. It is unclear whether this was the result of larger particle size or the formation of more stable molecular species. The other postulates were an increase in the excitation temperature due to the presence of Cs resulting in increased excitation, and a shift in ionization equilibrium, enhancing CaI emission and depressing CaII emission. The complex interaction of these three effects lead to the observed behaviour. The fact that high aerosol flow rates were used for these studies may make some of the conclusions suspect, for extrapolation to "normal" operating conditions. This must be considered especially in light of observations by Kalnicky et al. [136] which indicated that; "The surprisingly small changes in  $n_e$  and temperature profiles at 15 and 20 mm upon addition of Na as an EIE suggest that changes in the total composition of the sample do not





effect the radial excitation temperature nor degree of ionization of analyte species in a dominant manner". Clearly more spatial studies under normal operating conditions are required.

There is considerable variability in the observations of workers who have studied the effect of EIE's on analyte emission. In part these are probably due to a considerable variability in operating conditions under which these studies have been made. The observations by Boumans and DeBoer [46,47], and Larson et al. [48], indicate that the magnitude of the effect is a function of power. In addition Boumans and DeBoer demonstrated that a change in aerosol flow rate could change the effect from enhancement to depression. Couple these observations with those of Kornblum and deGalan [76], who observed a vertical spatial dependence whereby enhancements changed to depressions with increasing height, and at least part of the problem is clear. It seems that by the appropriate choice of operating and observation conditions any matrix effect desired can be generated. Of course this would not be done on purpose but it points out that care should be exercised in interpreting the cause of the effect using a single set of conditions for the investigation. Also, the observation that under optimum analytical conditions the matrix effect is negligible is not necessarily true. It may not be



"observed", but instruments which measure spatially integrated emission intensities can cloud the reality of the situation [77].

### Possible Mechanisms of EIE Interference

Several possible mechanisms have been postulated for the interference effect of EIE's on analyte emission which has been surveyed in the previous section. These mechanisms manifest themselves at different states in the analytes' progress from nebulization to emission of radiation. A brief discussion of each of these is warranted as a basis for a discussion of the data presented in this chapter.

(1) Shifts in ionization equilibrium. The nature of this interference has already been discussed in the previous section. If ionization equilibrium shifts were a dominant mechanism in the ICP we would expect to observe the same type of behaviour as that exhibited in flames. An increase in the electron density of the plasma would shift equilibrium toward neutral atom species resulting in enhancement of atomic emission and depression in ionic emission. The degree to which this mechanism will influence emission intensities in the plasma will depend upon how much the electron number density in the plasma is changed by introduction of the EIE. It has been calculated [112] and measured [36] that the electron density does not change



significantly when Na is introduced. However, the measurement of electron density extended only from 15 mm to 25 mm above the load coil. An extrapolation of the plot of electron density as a function of observation height to lower regions indicates that this may not be the case between 0 mm and 15 mm above the load coil. More measurements in this region are warranted before generalizations can be made.

(2) Enhanced Collisional Excitation. Vellion and Margoshes [113] suggested enhancements in emission intensity may be due to increased collision rate due to an increase in electron density. They evoked this mechanism to explain increases in emission intensity due to added Na, which did not cause corresponding increases in the ground state population of the analyte species. Franklin et al. [85] suggested that this could be used to explain simultaneous enhancements in the emission intensity from both Ca atom and ion lines in an ICP. If this is the case, then the effects of increased collision rate due to increased electron density must outweigh the effects of an ionization equilibrium shift. Presumably this would depend upon the relative velocity of the electrons. The greater the kinetic energy of the electron, the more likely an ion-electron collision will result in excitation rather than recombination. The outcome of an increase in the channel electron density, then, will depend on relative kinetic energies of the electrons.





Kitagawa and Takeuchi [122,144] suggested that the degree of ionization of analyte may also be enhanced by increased collision rate due to added EIE in a microwave plasma torch. In the same vein, they stated that the degree of ionization could also be depressed by charge transfer reactions between concomitant atom (c) and analyte ions ( $X^+$ ) in the following manner,



It should be noted that energy balance requires that the ionization potentials of the two species closely match each other for this process to take place.

(3) Voltailization effects. Boumans and DeBoer [47], and Kornblum and deGalan [76] discussed the possibility of volatilization effects in the ICP as a mechanism to explain the effects observed due to EIE's. In this mechanism, analyte atoms are "included" in a desolvated particle matrix which may take longer to volatilize than analyte particles alone. This may either be the result of larger particles, or particles with atomic bonds which are more difficult to break. The net effect is a delay in the release of the analyte atoms, when compared to the situation without matrix. This delayed volatilization can result in shifts in the spatial behaviour of analyte emission. "Lateral diffusion effects" are based on this mechanism, and have been





observed in flame spectroscopy [114,115], and discussed by L'vov et al. [116]. In the ICP a lateral diffusion effect would most likely result in a depression of emission in the central zone of the plasma, and an enhancement nearer the edges of a radial analyte distribution, in lower regions of the analyte channel. One should also observe vertical spatial effects as a result of volatilization effects. These should manifest themselves as a depression of emission in the lower analyte channel. Shifts in radial emission profiles [48], and absorption profiles [76] in the ICP have been explained as due to volatilization effects.

(4) Ambipolar diffusion. Boumans and DeBoer [47] have mentioned ambipolar diffusion as a possible source of emission intensity modification in the ICP. Ambipolar diffusion is interpreted as the diffusion of charged particles under the influence of an electric field [117]. In a gas which contains an appreciable quantity of ions and electrons, electrons tend to diffuse faster than ions which is related to their smaller mass. The resultant separation of charge produces an electric field which exerts its force in such a way to increase the drift velocity of the ion species and retard the drift velocity of electrons. Neutral particles are not affected to any significant degree by this process. The diffusion is in the direction from higher to lower electron densities. Murayama and his colleagues [72,73]



have interpreted the enhancement of emission from rare earth elements in a microwave discharge as the result of ambipolar diffusion.

(5) Nebulizer effects. The process of nebulization although simple in concept, can provide several different mechanisms through which an EIE might ultimately affect the emission from analyte species. The most straightforward of these are solution viscosity effects. An increase in the molar concentration of a dissolved salt can cause increases in the viscosity of the solution, which in turn will decrease the rate of transport of analyte solution to the nebulizing tip. This would have the overall result of decreasing the amount of analyte reaching the plasma and would tend to increasingly depress emission signals as the quantity of salt increased. In the present study solution uptake was depressed by 3% at NaCl concentrations of 2%, and the changes from this source are not considered significant.

In a recent study, Borowiec et al. [118] discussed the phenomenon of "Aerosol Ionic Redistribution (AIR)", as a mechanism for interference due to concomitants in atomic spectroscopy. They have shown that in systems involving cation pairs, the nebulized droplets demonstrate an enrichment in the minor component as a result of the presence of high concentrations of the major component. In a system involving 1% Mg and Na in a 200:1 weight ratio, enrichments



as high as 220% were found for Na in the aerosol droplets. The enrichment is generated in the droplet formation stage and the degree of enrichment is related to the droplet size. The enrichment is related to both the major cation concentration and the major to minor cation ratio becoming negligible at ratios less than 50:1. It is difficult to assess to what degree this effect will influence observations of the effect of EIE's in the plasma; since the magnitude of the AIR effect is related to droplet size, it will depend on the nebulizer type, and operating conditions. The effect is most pronounced in very small droplet sizes which usually form a low percentage of the overall droplet distribution. Dual nebulizer experiments by Boumans and DeBoer [47] provide some evidence that AIR may be operative; however on a relative basis the contribution to the EIE effect from the nebulizer was small compared to that from the plasma. Johnson et al. [75] found that the effect of added EIE in a DC plasma was the same when analyte and concomitant were nebulized from separate nebulizers or from the same nebulizer, indicating an absence of AIR.

Skogerboe and Olsen [119] investigated aerosol transport effects due to the presence of high concentrations of Na in a microwave induced plasma system with and without a desolvation chamber attached. They found that less Pb was





delivered to the plasma when Pb was nebulized in the presence of Na than when Pb was nebulized alone when the desolvation chamber was used. They attributed the decrease to the aerodynamic properties of aerosol particles, the transport efficiency being affected mainly by gravitational settling and inertial impingement losses. The transfer efficiencies for wet aerosol systems were found to be independent of Na concentration. This observation was supported in a subsequent study of the interference of high Na concentrations in a DC plasma system [75]. These studies indicate that care should be taken in comparing results from systems employing desolvation and those that do not. The present study did not involve the use of a desolvation chamber, so it is expected that transport effects do not play a significant role in causing the effects observed.

Although there may be other mechanisms which may contribute to the EIE effect, those which have been mentioned are those which have most frequently appeared in the literature, and as such are considered the prime candidates. It is entirely possible that no single mechanism is dominant, but rather the observations of many researchers are the result of a complex interaction of several of them. This could be particularly confusing since the effects of one mechanism may tend to oppose the effects of another.

Different mechanisms are most likely to manifest them-





selves in different spatial regions of the plasma. It has already been shown that different spatial regions in the plasma display different types of emission behaviour. This spatial inhomogeneity could result in different spatial regions having matrix effects due to different mechanisms. The results of Kornblum and deGalan suggest this may be the case [76]. Thus a detailed spatial study of different analytes and interferents under various operating conditions has been undertaken. The purpose of the study presented in the following pages is to clarify many of the observations on the effect of EIE's and to present data which will, hopefully, lead to a "universal" interpretation of this effect.

### Experimental

The elements chosen for study were the effects of Li, Na, and K as interferents on Ca, Mg, Cd, and Cr. In all cases the molar concentrations of Ca, Mg, Cd, and Cr were 1.25 mmolar corresponding to 50, 30, 140, and 65 ppm respectively. Solutions containing these elements and the interferent in the form of a chloride salt in molar ratios of 10, 30, 100, and 300 to 1 were made up using distilled water. These represent salt concentrations (by weight) in the range of 0.053 to 1.59% for Li, 0.073 to 2.19% for Na, and 0.077 to 2.8% for K. Corresponding blank solutions



were made up which contained the interfering salt only, at the same concentrations, for the purpose of background subtraction.

### Effect of EIE's on Vertical Profiles

Vertical spatial profiles have been acquired in the same manner as those presented in Chapter III in the region 7 to 24 mm above the load coil for Ca, Mg, and Cd with Na as the concomitant. These are provided in Figures 44, 45, and 46. The numbers on each set of figures refer to the molar ratio of Na to analyte; these are: (1) 0:1, (2) 10:1, (3) 30:1, (4) 100:1, and (5) 300:1. Curve sets a and b refer to emission from the atom and ion line of the analyte species respectively. The operating conditions chosen for the study were, 1.5 kw RF power, 0.85 lpm aerosol flow rate, 15 lpm plasma gas flow, and less than 1 lpm auxiliary gas flow. These conditions are close to those normally used for analytical determinations using the ICP.

Figures 44a and 44b provide the vertical spatial profiles for CaI (422.7 nm) and CaII (393.3 nm) respectively. It can be seen that the effect of Na is to generally enhance the emission of the atom and ion lines in the lower regions of the aerosol channel, and to depress emission in regions higher above the load coil. The magnitude of this enhancement or depression is dependent on either the molar ratio of Na to Ca, or the total concentration of Na present. A



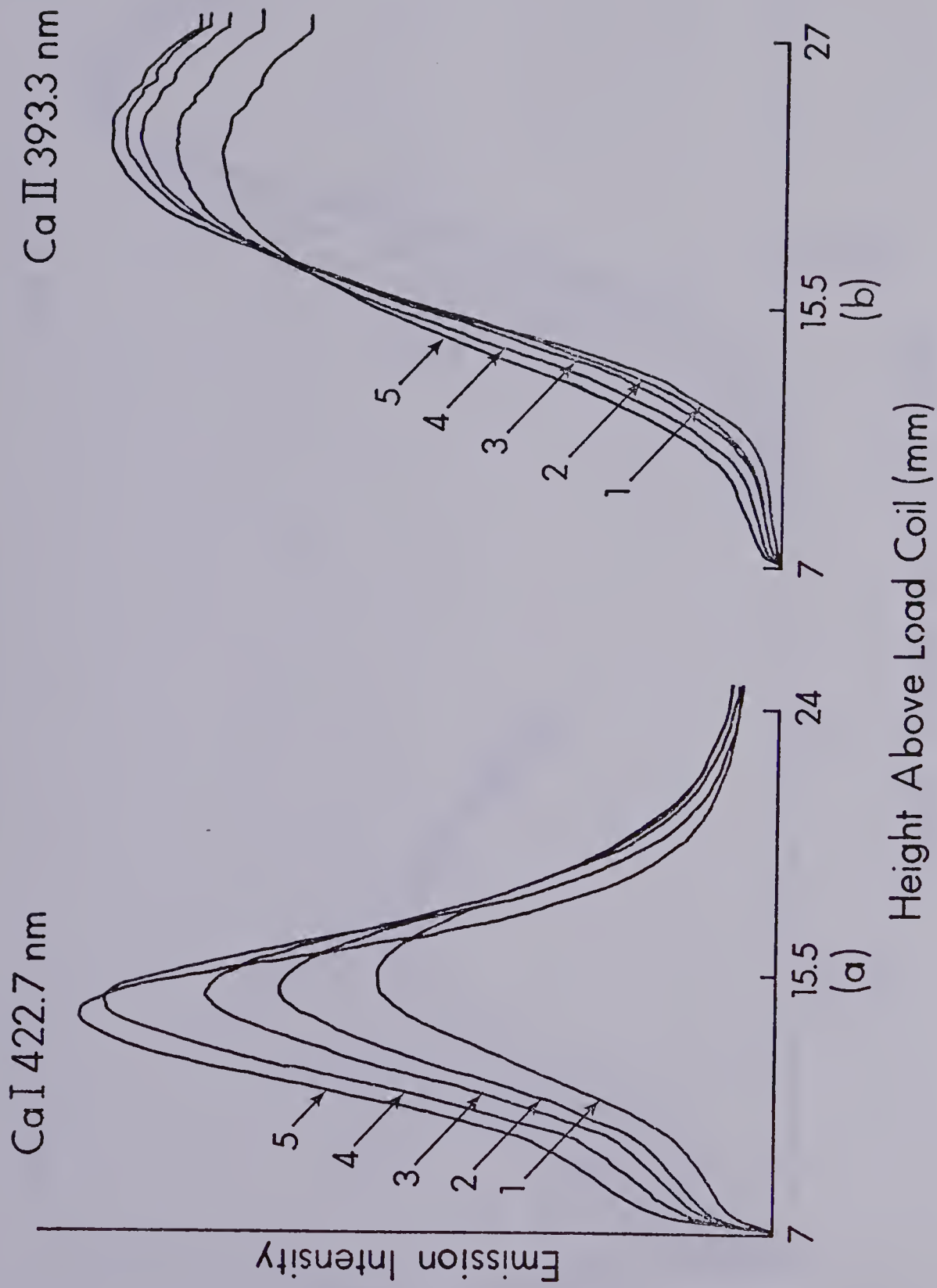


Figure 44. Vertical spatial profiles for Ca; (a)  $\text{CaI } 422.7 \text{ nm}$ , (b)  $\text{CaII } 393.3 \text{ nm}$ . Molar ratio of Na to Ca; (1) 0:1, (2) 10:1, (3) 30:1, (4) 100:1, (5) 300:1.



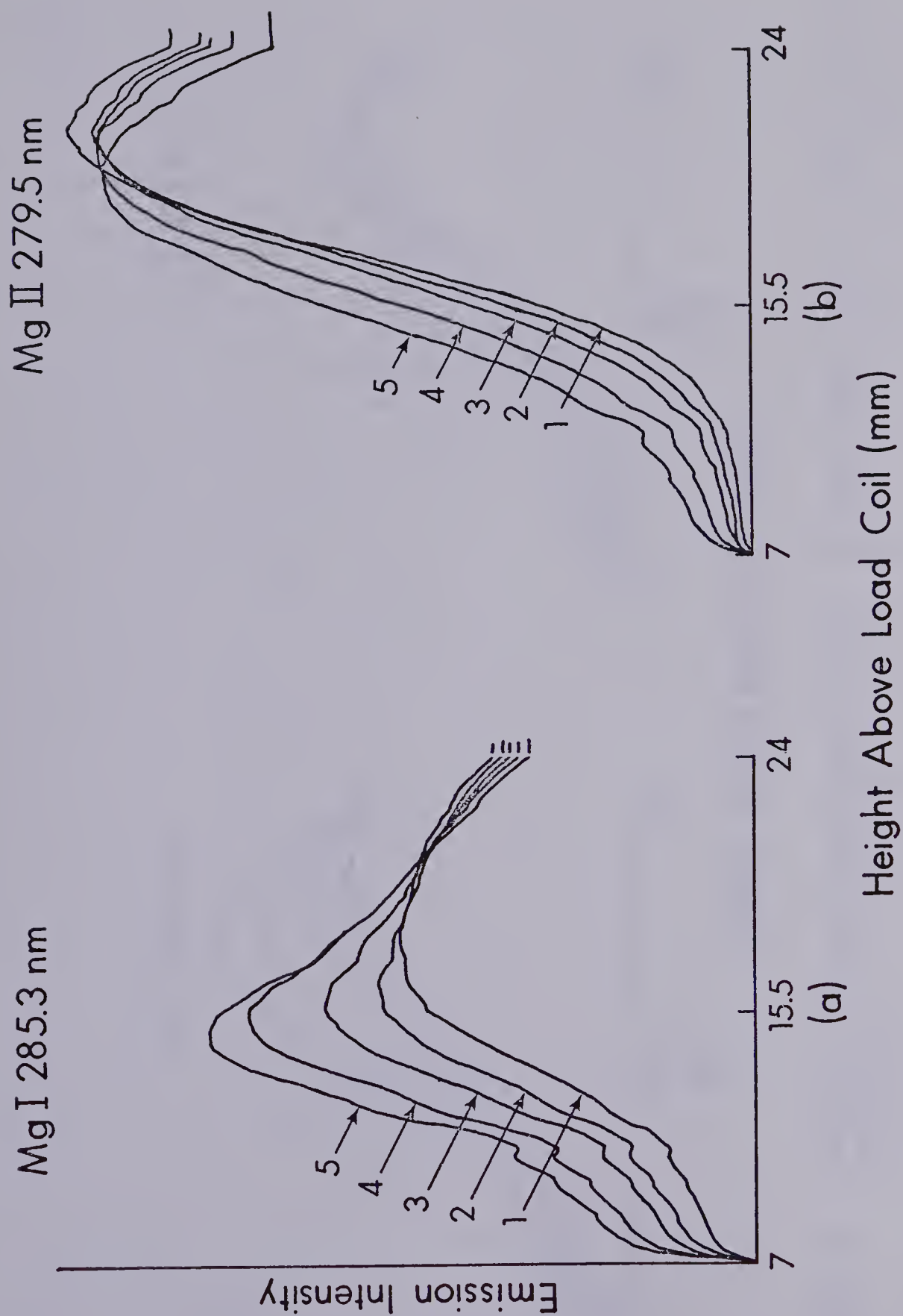


Figure 45. Vertical spatial profiles for Mg; (a) Mg I 285.3 nm, (b) Mg II 279.5 nm. Molar ratio of Na to Mg; (1) 0:1, (2) 10:1, (3) 30:1, (4) 100:1, (5) 300:1.





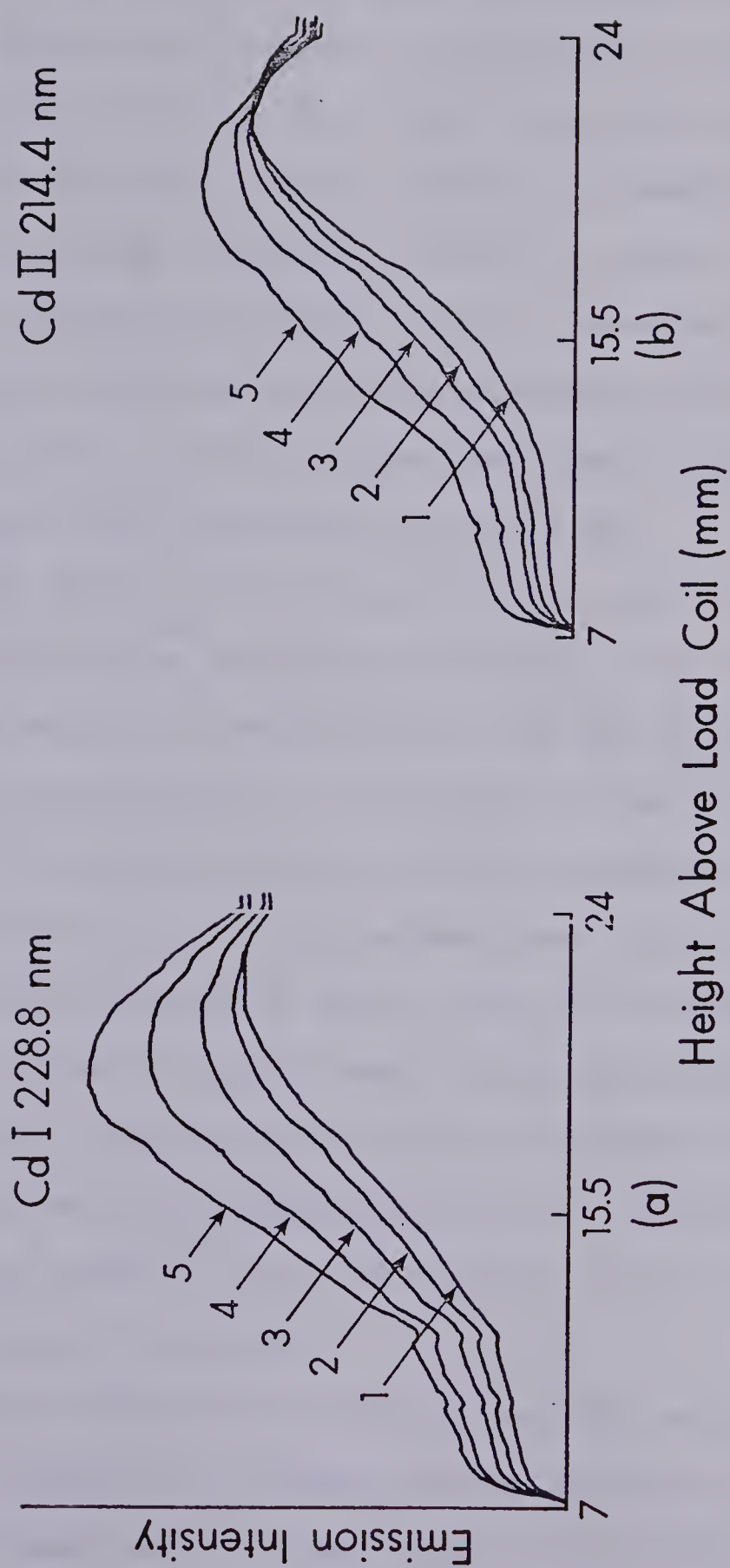


Figure 46. Vertical spatial profiles for Cd; (a) Cd( 228.8 nm, (b) CdII 214.4 nm. Molar ratio of Na to Cd; (1) 0:1, (2) 10:1, (3) 30:1, (4) 100:1, (5) 300:1.



plot of the magnitude of the matrix effect as a function of height above the load coil is provided in Figure 47 for a molar ratio of 100:1 Na to Ca. The matrix effect is defined as the ratio of the emission intensity with Na added to the emission intensity without Na added. It can be seen that the magnitude of the effect is greatest at a height of 7 mm above the load coil and decreases with an increase in height, until at about 16 mm the signal begins to show a depression which continues up to 24 mm.

Even though CaI and CaII behave quite similarly at a particular height above the load coil, the response at the optimum height for emission for the two is quite different. For CaI, enhancements are observed at the emission intensity peak. Overall the profile shifts slightly in the direction of the load coil. On the other hand, CaII is depressed at the emission intensity peak, the profile appearing to pivot about a crossover point where there is no effect due to excess Na. The position of this crossover point is independent of the concentration of Na. This behaviour appears to be the result of the two lines peaking in different spatial regions in the ICP.

Using Figure 47 it can be seen why variable results might be reported in observing the effect of Na on Ca using an instrument with a fixed observation height, particularly one with a relatively small slit height. In this case



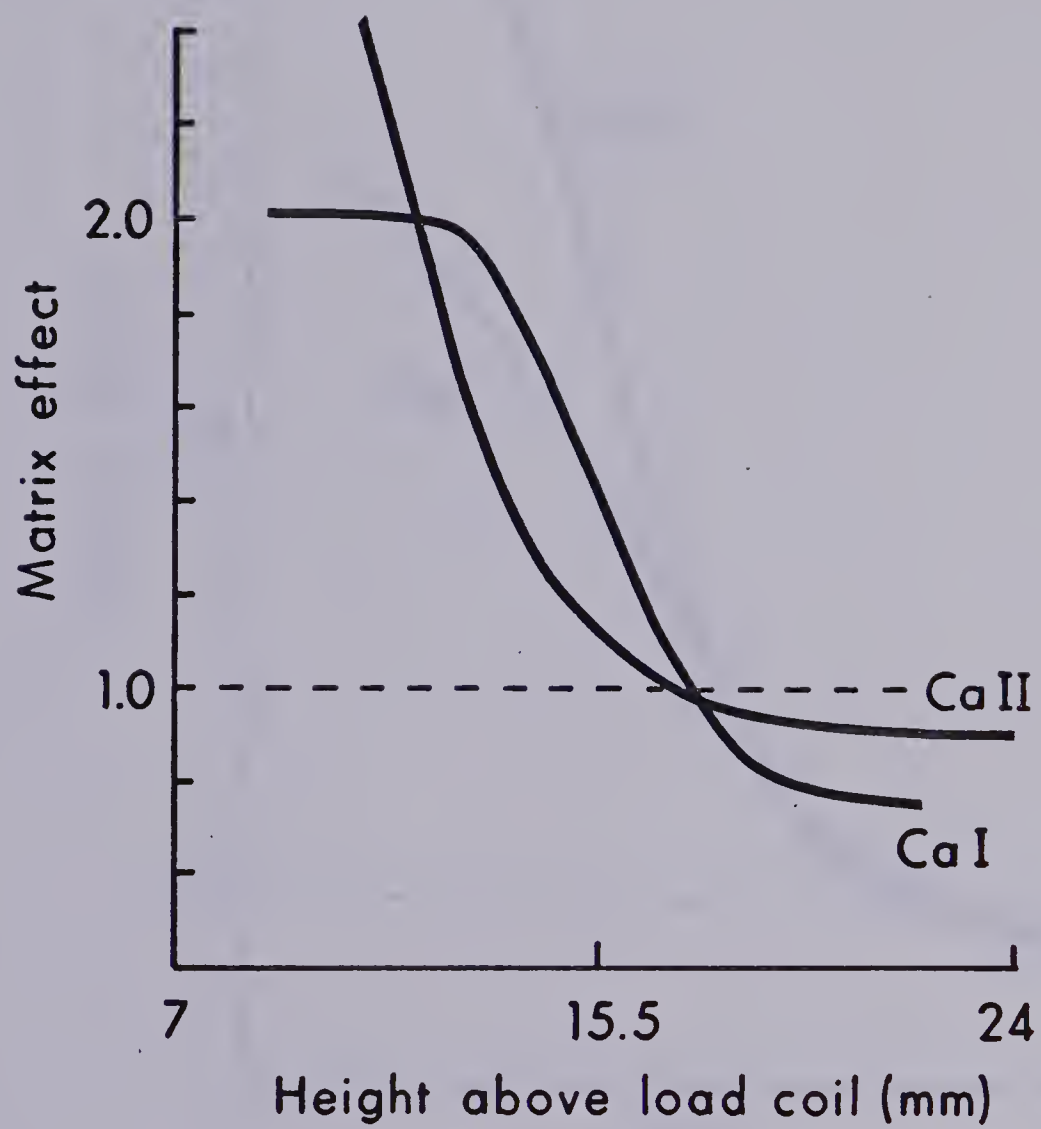


Figure 47. Matrix effect of 100:1 molar ratio Na to Ca as, a function of height above the load coil.



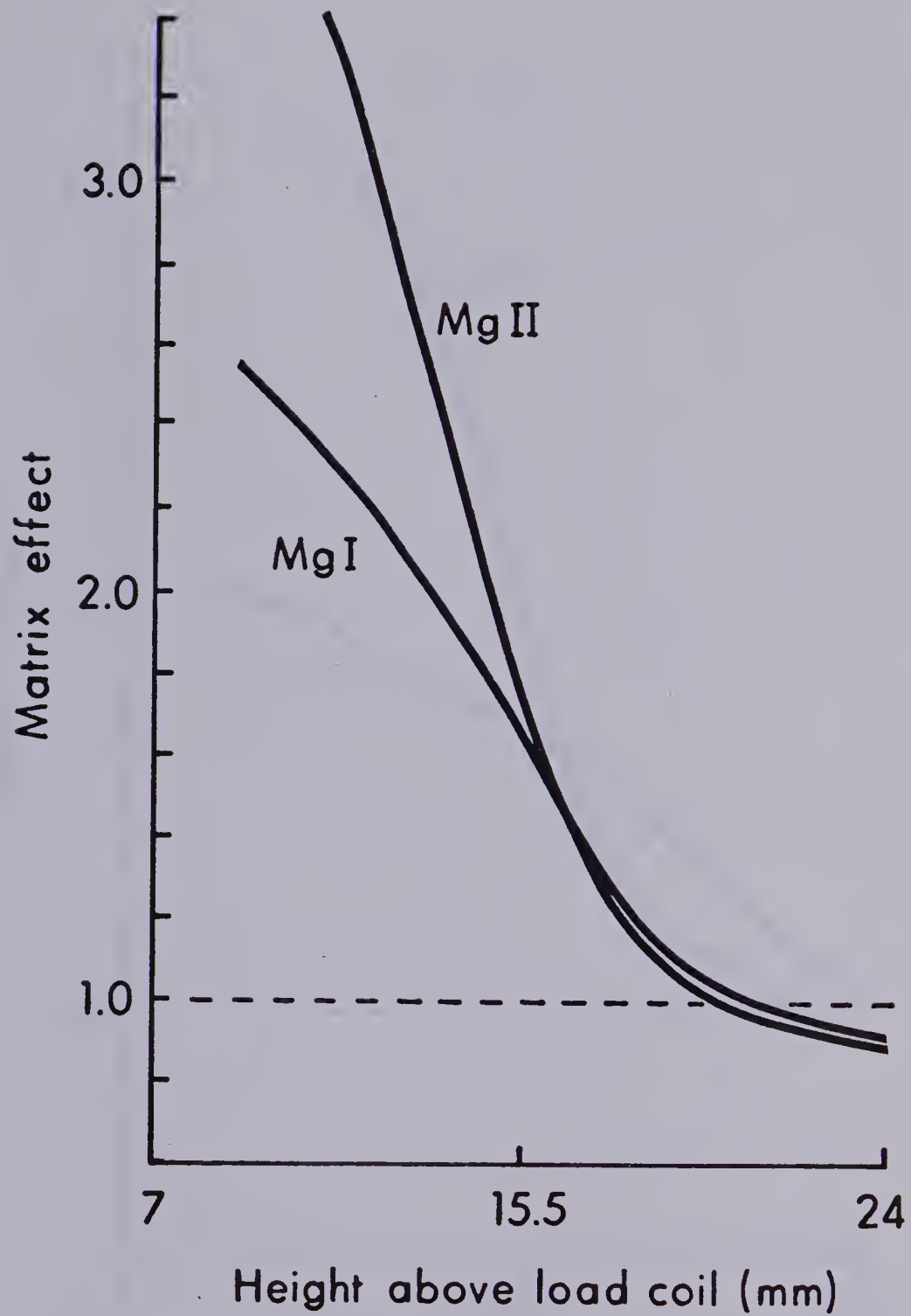


Figure 48. Matrix effect of 100:1 molar ratio Na to Mg as a function of height above the load coil.





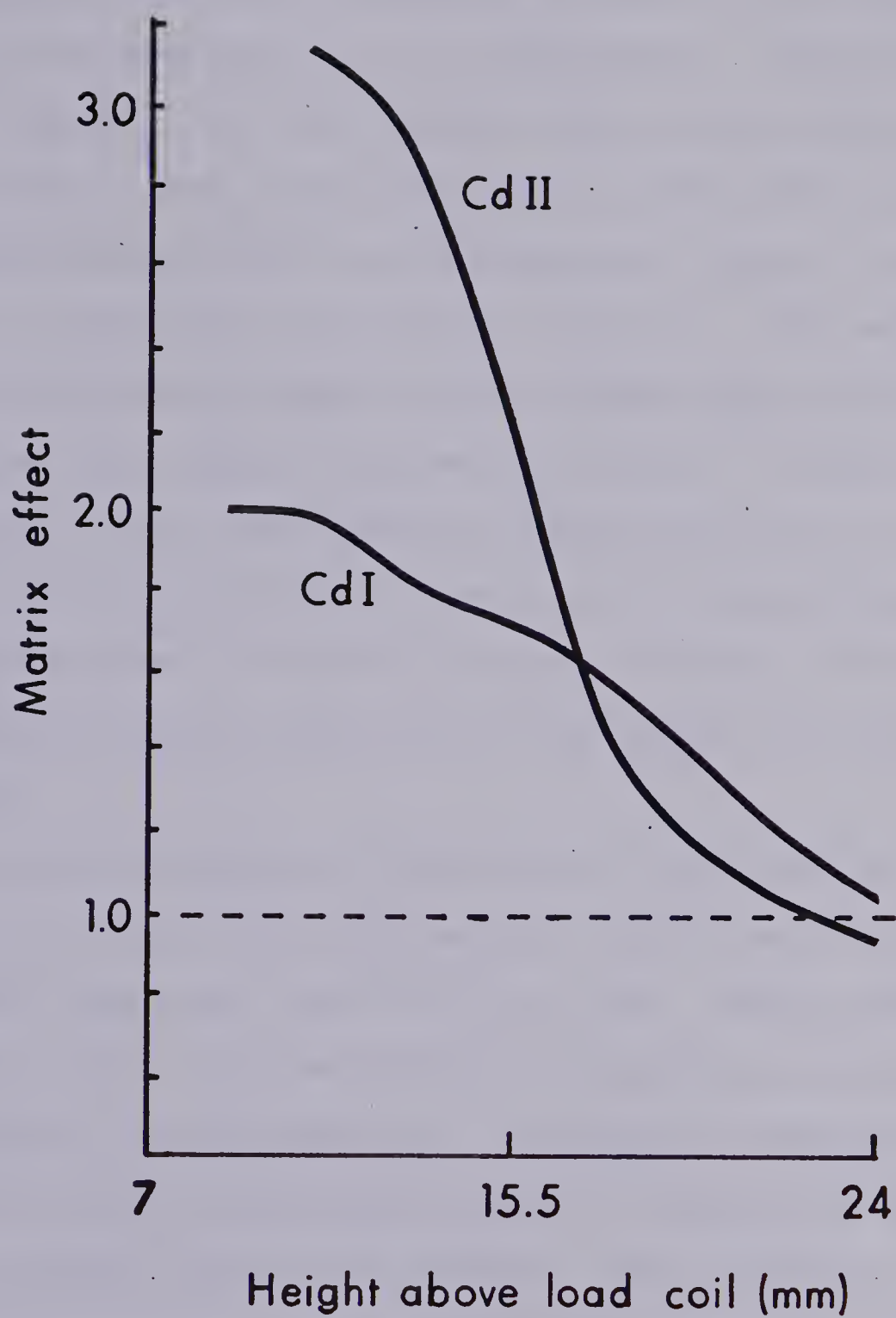


Figure 49. Matrix effect of 100:1 molar ratio Na to Cd as a function of height above the load coil.



measurements made low in the plasma (below 17 mm) would result in the observation of an enhancement. Measurements centered about 17 mm would likely result in an observation of "no effect", due to the enhancement effect being offset by the depression effect, and measurements above 17 mm would indicate a depression in emission intensity. The magnitude of the effect would depend on the relative size and positioning of the spatial observation window. It should be noted, also, that a broad spatial window (10-15 mm) centered around 18-20 mm would likely result in the observation that there is no effect of easily ionizable elements, which might be satisfying analytically, but is certainly not "true" in this case.

Profiles analogous to those for Ca are provided in Figure 45 for MgI (285.3 nm) and MgII (279.5 nm), and Figure 46 for CdI (228.6 nm) and CdII (214.4 nm). We can observe an overall trend in these profile sets which is similar to that observed for CaI and CaII. In general, enhancements are observed at lower observation heights, changing to depressions at higher observation heights. Atom lines and ion lines show the same general trends, as can be seen in Figures 48 for Mg and 49 for Cd. These are plots of matrix effect as a function of height above the load coil analogous to Figure 47, for a molar ratio of 100:1 of Na to analyte. These plots have features similar to those for Ca. A



depression is not observed for CdI below 24 mm above the load coil, but the trends of the profiles provided in Figure 46 indicate that they are likely to be encountered at higher observation heights. The case for Mg is similar to that for Ca. The atom line is enhanced at its peak of emission intensity and the peak position shifts slightly toward the load coil. The ion line is depressed at its peak in emission intensity and also exhibits a downward profile shift. The crossover point for MgII occurs at a higher height than that for CaII. This trend continues for CdI and CdII.

There are several features of the data presented in Figures 44 to 49 which warrant consideration in an interpretation of the matrix effect. A major point is the fact that emission from both atom and ion lines is enhanced at lower observation heights. Even though the overall effect on the spatial profile is different between these two, at a fixed height above the load coil the magnitude of the effect is very similar for atom and ion lines. At very low heights, ion lines tend to be enhanced more than atom lines of the same species. Also at some height, the matrix effect changes from being an enhancement to a depression of the analyte emission intensity. The plot provided in Figure 50 demonstrates that the height at which this happens for ion lines can be correlated with the ionization potential of the



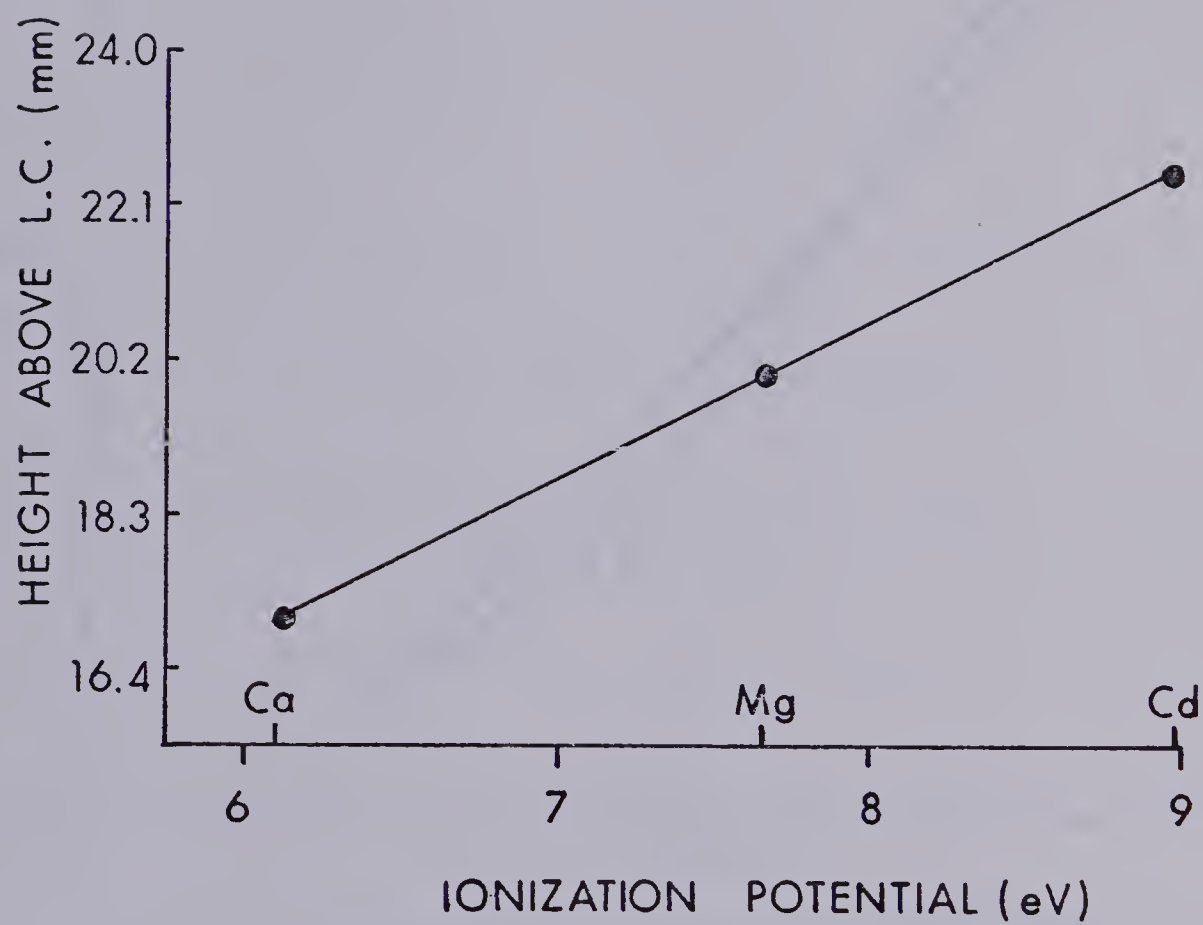


Figure 50. Spatial position where enhancements change to depressions as a function of ionization potential for Ca, Mg, and Cd.





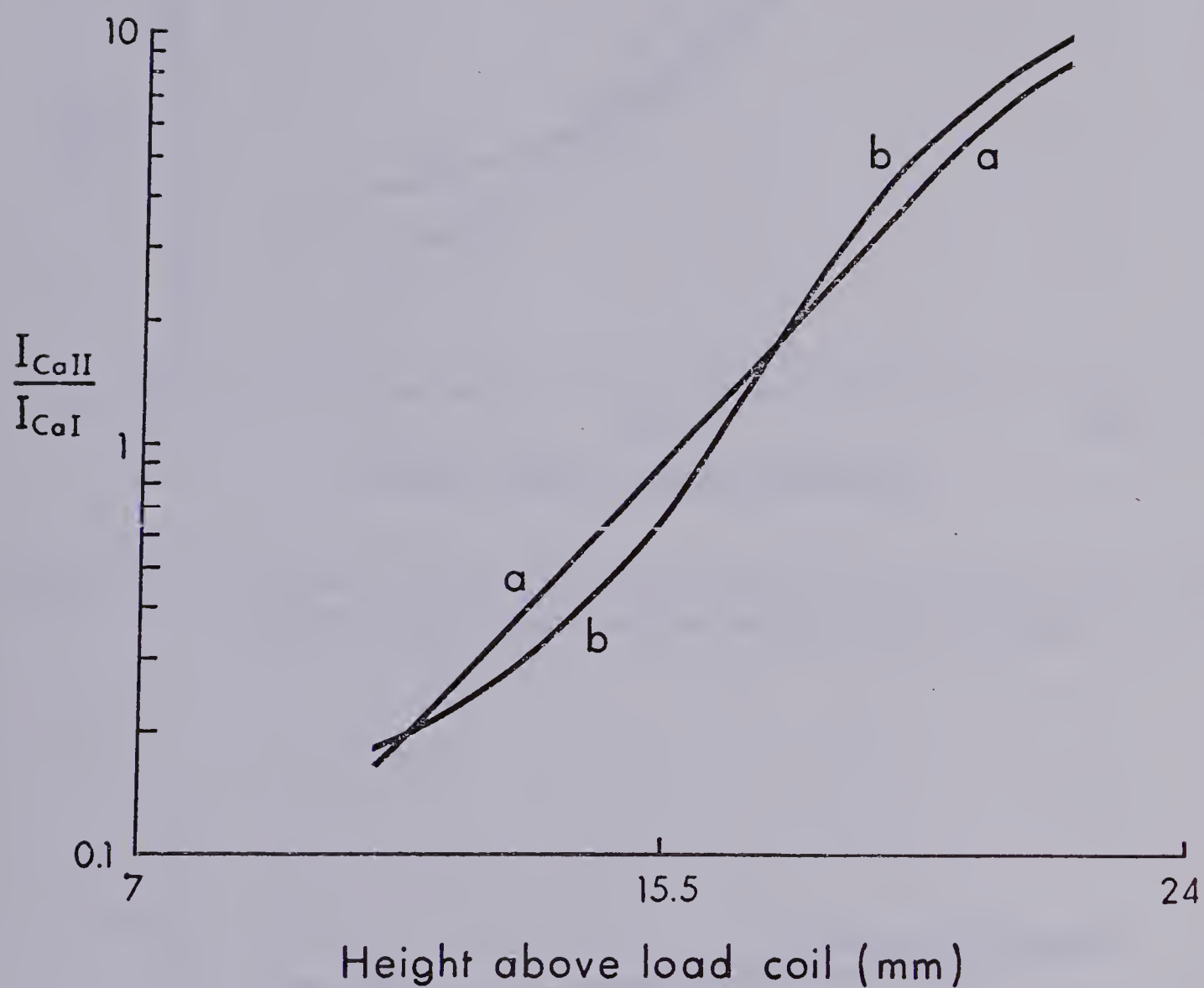


Figure 51. Ratio of emission intensities (I) for CaII 393.3 nm and CaI 422.7 nm. Molar ratio of Na to Ca; (a) 0:1, (b) 100:1.



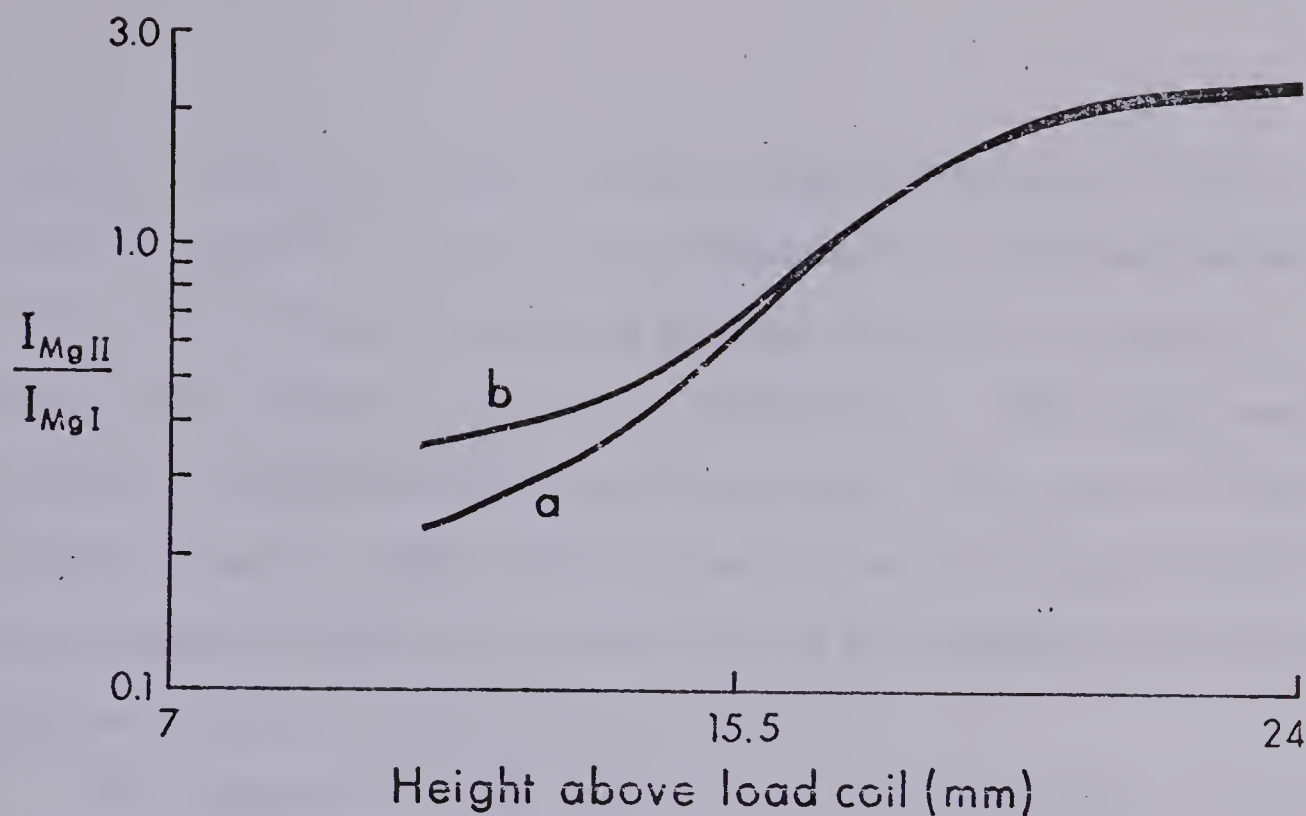


Figure 52. Ratio of emission intensities ( $I$ ) for MgII 279.5 nm and MgI 285.3 nm. Molar ratio of Na to Mg; (a) 0:1, (b) 100:1.

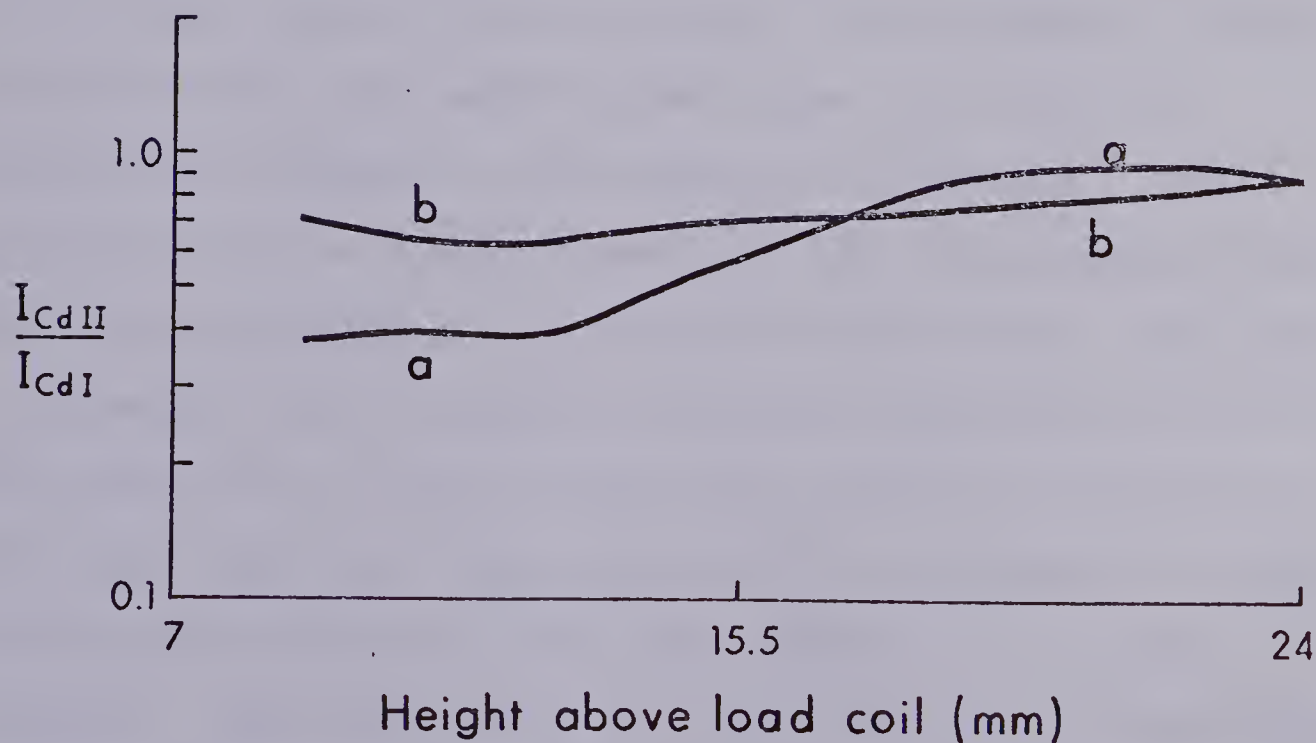


Figure 53. Ratio of emission intensities ( $I$ ) for CdII 214.4 nm and CdI 228.8 nm. Molar ratio of Na to Cd; (a) 0:1, (b) 100:1.



element. This is a plot of the spatial position of the crossover point of ion line enhancement to depression as a function of the ionization potential of the element. Atom lines closely follow this behaviour. More data are required to confirm the correlation but the trend is certainly present. The independence of spatial position of the crossover point as a function of Na concentration is a curious feature (Figures 44 to 46).

The effect of Na on the ratio of ion emission to atom emission is plotted in Figures 51, 52, and 53 for Ca, Mg, and Cd respectively. The data for these plots have been extracted from Figures 44 to 46. Curve (a) corresponds to a 0:1 molar ratio of Na to analyte, and curve (b), to a 100:1 molar ratio of Na to analyte. The increase in the value of this ratio with height above the load coil signals an increase in the degree of ionization. The magnitude of the slope in each plot is proportional to the ionization potential of the respective analyte. The slope is greatest for Ca with an ionization potential of 6.11 ev, and least for Cd with an ionization potential of 8.99 ev. For the case of Ca, the addition of Na depresses the ratio at heights less than 17 mm, and enhances it at higher heights. This depression in the lower region of the channel might be the result of some small amount of ionization suppression. It has already been noted, however, that overall,



enhancement in ion emission at these heights is observed. Therefore, even if ionization equilibrium shifts are taking place, they are not a dominating mechanism.

In contrast to the slight depression observed for the ratio of intensities for Ca up to 17 mm, the ratio is enhanced for Cd and Mg at heights below 17 mm due to excess Na. It seems ionization suppression does not even play a minor role for these two elements. The shift indicates either an increase in the degree of ionization, or increased excitation of the ion line over the atom line. Above the level of 17 mm, the ratio is not appreciably affected by the addition of excess Na.

The data presented in this section certainly do not support an interpretation of the matrix effect in terms of an ionization suppression mechanism. The observations for Ca indicate that some small degree of this must be taking place lower in the channel, but its effect is dominated by some other process which seems to affect Ca, Mg, and Cd in a similar manner for both atom and ion emission. The fact that enhancements in emission are observed lower in the channel, and depressions are observed in the upper region, points to at least two different mechanisms, or one mechanism which redistributes the spatial structure of analyte emission. The point of crossover where signal enhancements convert to depressions is more dependent on analyte ionization





parameters than the concentration of Na present, even though the electron density at this point should increase with increasing Na concentration. This might indicate that it is the velocity distribution of electrons which is more important than the actual number density, velocity being a function of distance from the load coil. Elements with different ionization potentials might be affected in a way which is proportional to this velocity distribution.

The data presented thus far have all been for the interference effect of Na on analyte emission intensity. Figures 54, 55, and 56 demonstrate that similar results are obtained for the matrix effect of Li on Ca and Cr emission. These figures are analogous to Figures 44, 45, and 46 for the spatial region 4 to 18 mm above the load coil. Figure 54 provides the effect of Li on CaI (422.7 nm), Figure 55, the effect of Li on CaII (393.3 nm), and Figure 56, the effect of Li on CrI (357.8 nm) and CrII (283.5 nm). These figures show the same general features as those already presented. To investigate any subtle changes which might ensue when the EIE is changed, a study of the effect of Li, K, and Na on Ca, Mg and Cd has been carried out.

#### Effect of Varying Interferent

To assess the effect of different EIE's on the magnitude and spatial features of the matrix effect, the same



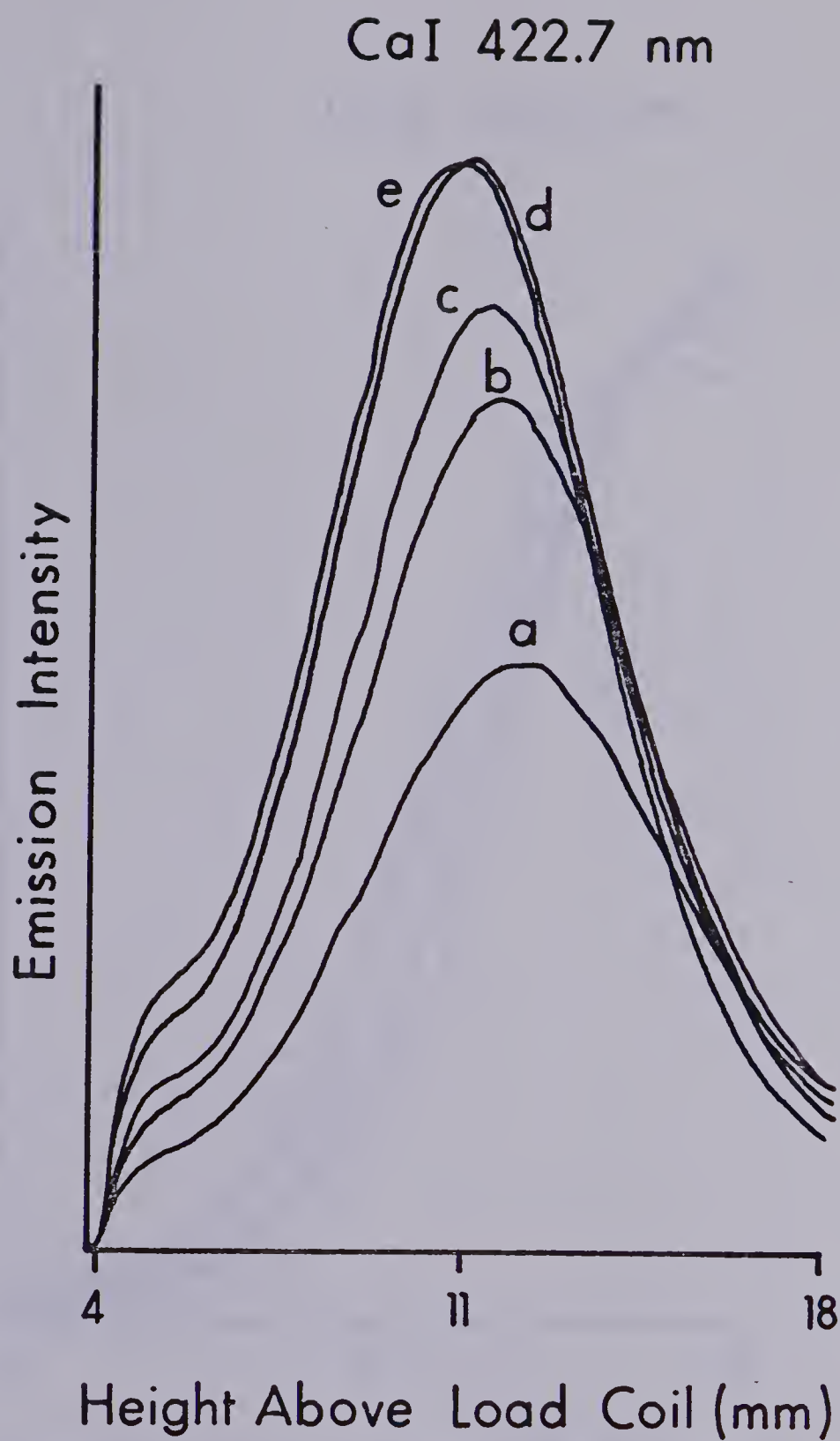


Figure 54. Vertical spatial profiles for CaI 422.7 nm. Molar ratio of Li to Ca; (a) 0:1, (b) 10:1, (c) 30:1, (d) 100:1, (e) 300:1.



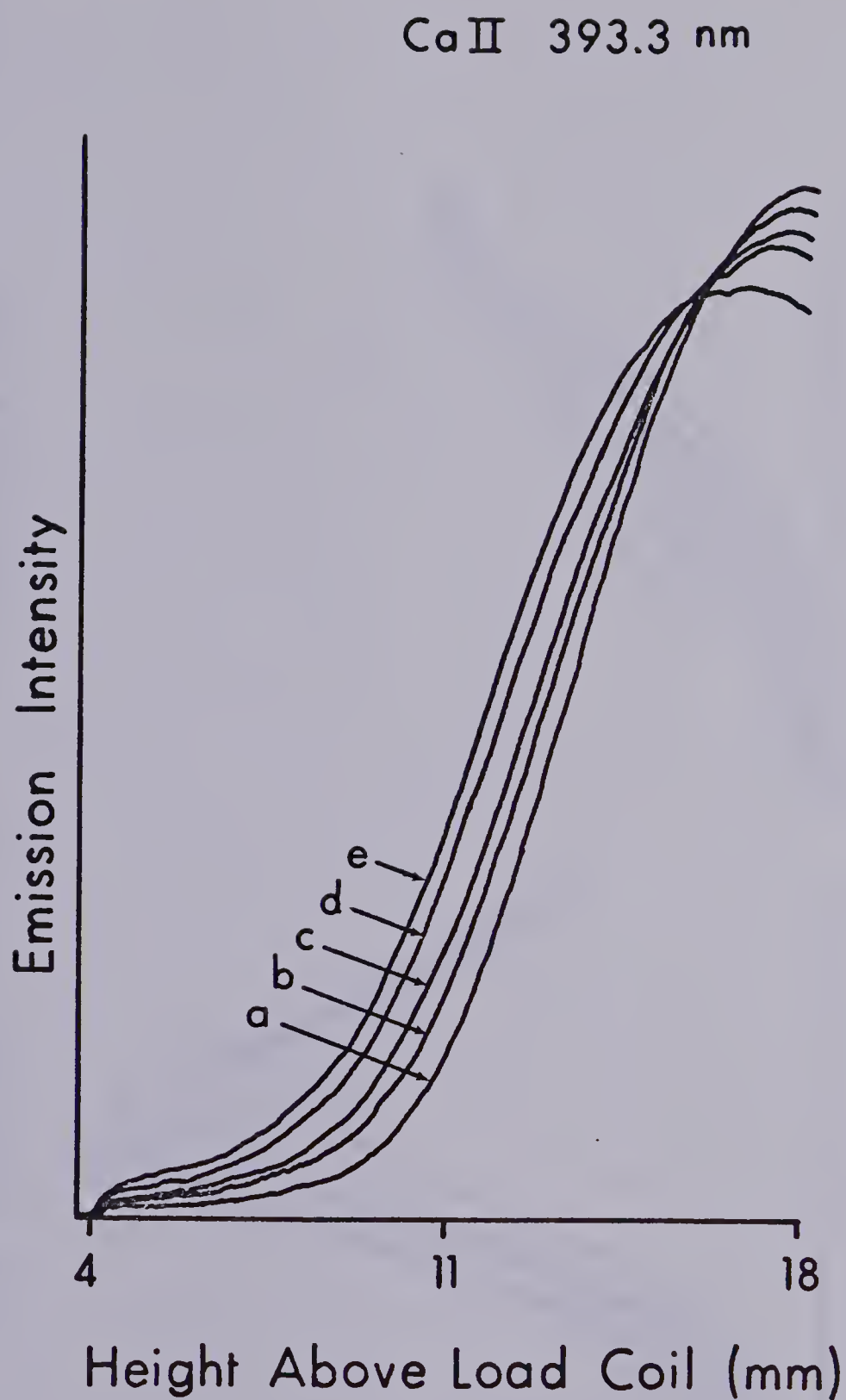


Figure 55. Vertical spatial profiles for CaII 393.3 nm. Molar ratio of Li to Ca; (a) 0:1, (b) 10:1, (c) 30:1, (d) 100:1, (e) 300:1.



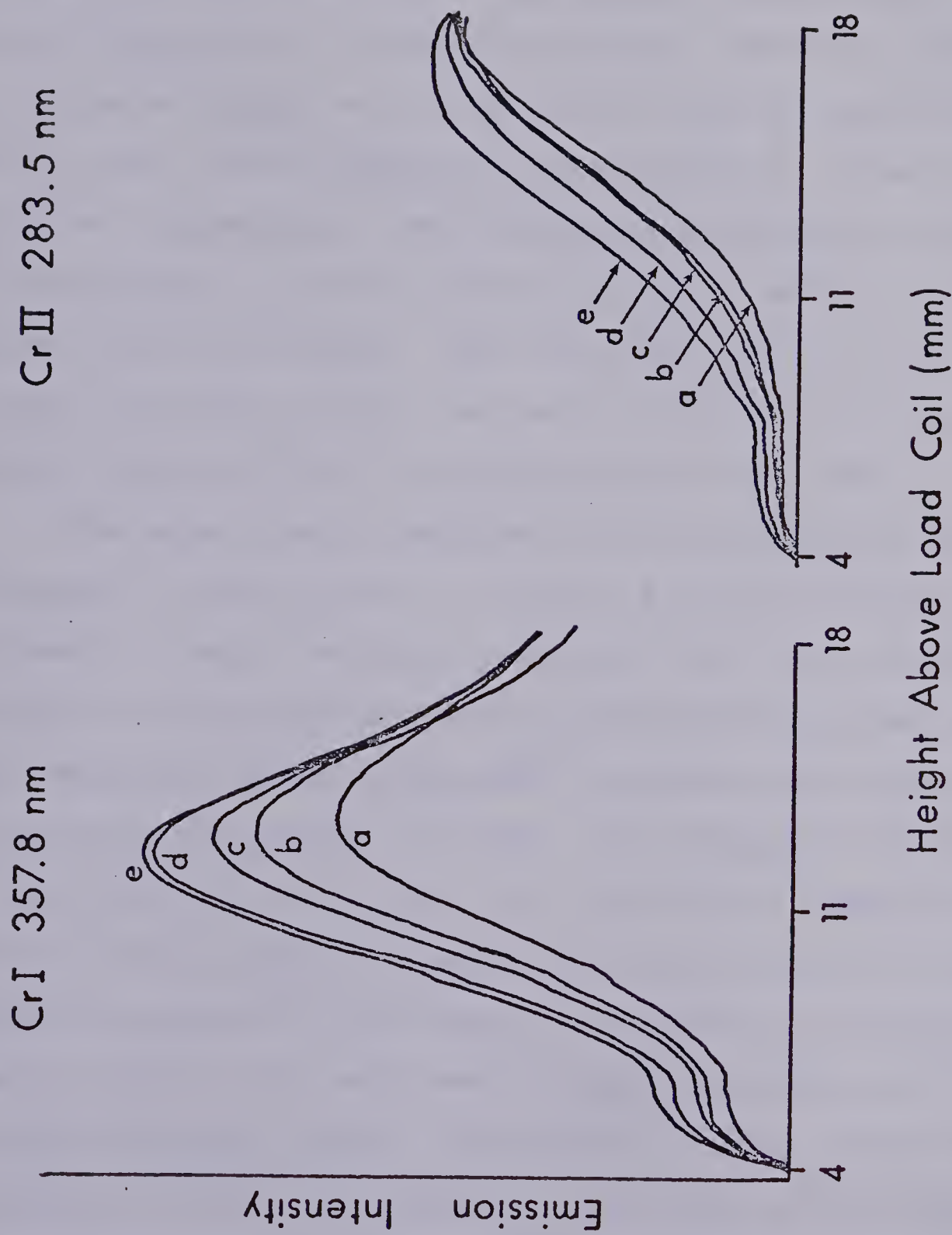


Figure 56. Vertical spatial profiles for CrI 357.8 nm and CrII 283.5 nm. Molar ratio of Li to Cr; (a) 0:1, (b) 10:1, (c) 30:1, (d) 100:1, (e) 300:1.





Ca, Mg, and Cd atom and ion lines discussed in the previous section were studied. Spatial profiles in the region 7 to 24 mm above the load coil were acquired using a 100:1 molar ratio of Li, Na and K to analyte. These are presented in Figures 57, 58, and 59 for Ca, Mg, and Cd respectively. Curve sets 1 and 2 represent the atom and ion of each analyte species respectively. The curves are labelled in the following manner: (a) no interferent, (b) Li added, (c) Na added, and (d) K added. The conditions are 1.5 Kw RF power, 0.85 lpm aerosol flow rate, 15 lpm coolant gas flow rate, and less than 1 lpm auxiliary gas flow rate.

The same general features of the matrix effect are apparent in going from Li to Na to K as the interfering element. Analyte emission intensity tends to be enhanced lower in the aerosol channel and depressed at higher heights. The magnitude of the enhancement increases with decreasing ionization potential of the EIE. The ionization potentials of Li, Na, and K are 5.39, 5.14, and 4.34 eV respectively. This evidence tends to support the notion that it is some species produced as the result of ionization of the EIE which produces the enhancements observed, either electrons or the EIE ion. However, the effect of these is more significant in the lower regions of the plasma, even though the EIE should be more fully ionized as one moves up the analyte channel. Either the relative contribution of electrons from



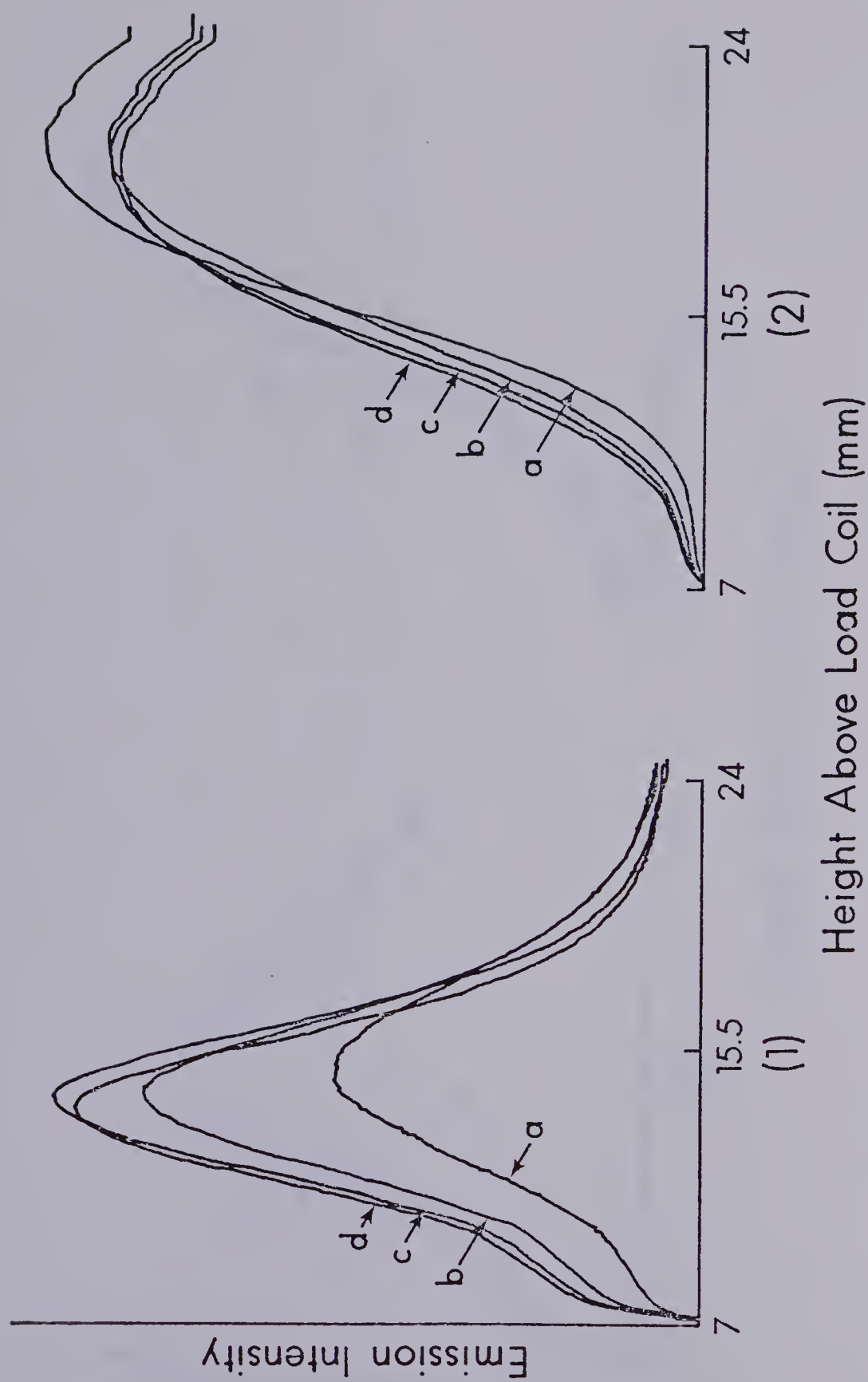


Figure 57. Vertical spatial profiles for; (1) CaI 422.7 nm, and (2) CaII 393.3 nm. Concomitant present in 100:1 molar ratio; (a) none, (b) Li, (c) Na, (d) K.



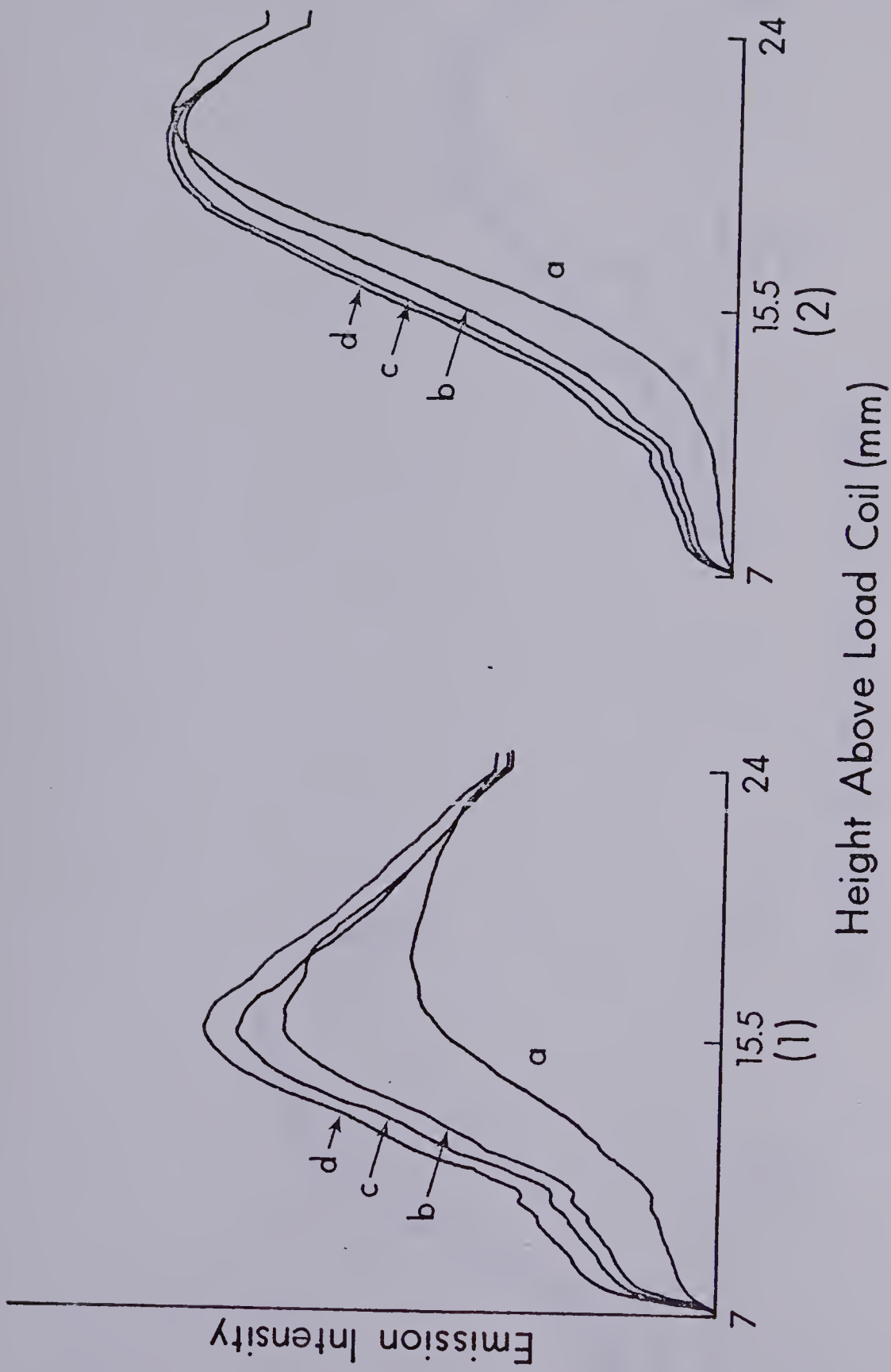


Figure 58. Vertical spatial profiles for; (1) MgI 285.3 nm, and (2) MgII 279.5 nm. Concomitant present in 100:1 molar ratio; (a) none, (b) Li, (c) Na, (d) K.



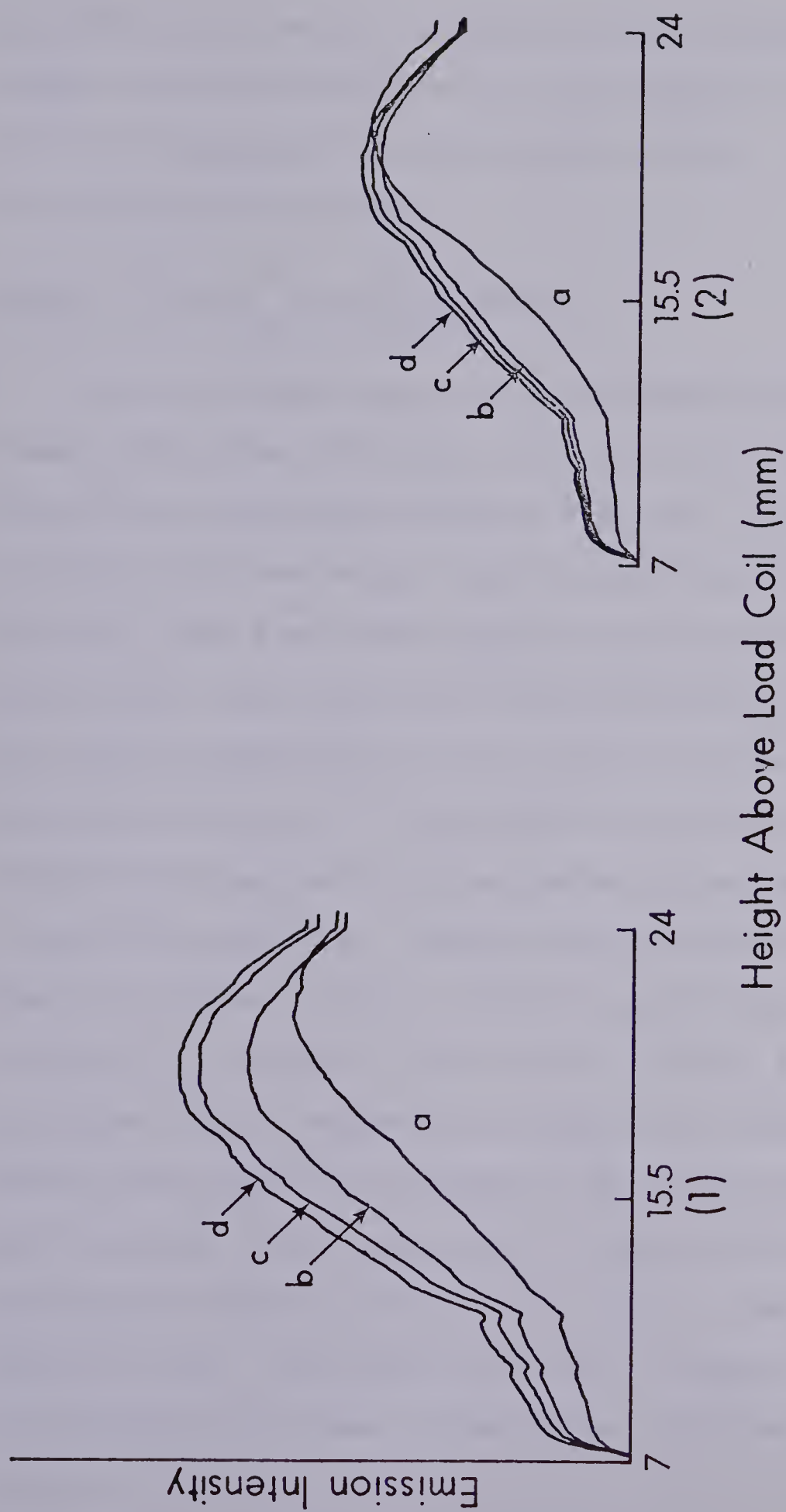


Figure 59. Vertical spatial profiles for; (1) CdI 228.8 nm, and (2) CdII 214.4 nm. Concomitant present in 100:1 molar ratio; (a) none, (b) Li, (c) Na, (d) K.





the EIE to the overall electron density decreases with height, or the strength of the interaction of electron and RF field decreases with increasing height. Both of these are probably important.

#### Effect of Power on Matrix Effect

It was pointed out in the introduction that several researchers have found that the effect of increasing the power was to decrease the matrix effect. In order to clarify this observation spatial profiles of CaI (422.7 nm) and CaII (393.3 nm) were acquired with the presence of a 100:1 molar ratio Na to Ca, and without the presence of Na. The spatial observation region extends from 7 to 24 mm above the load coil. The conditions used for this study were 0.85 lpm aerosol, 15 lpm coolant flow and less than 1 lpm auxiliary flow. Figures 60(i) and 61(ii) provide the spatial profiles for CaI, at RF powers of (a) 2.0 kw, (b) 1.75 kw, (c) 1.50 kw, (d) 1.25 kw, and (e) 1.0 kw. The profiles 1 and 2 represent the emission intensity of Ca without and with the presence of Na respectively. All profiles are on the same scale. Figures 61(i) and 61(ii) provide the spatial profiles for CaII in the same format as those for CaI. The plots in 61(ii), frame e, are on a scale which is 4 times as sensitive as those in frames a to d.



The basic nature of the interference effect does not appear to change as the power is changed from 1.0 kw to 2.0 kw. Figures 62 and 63 plot the magnitude of the interference effect as a function of applied power for CaI and CaII respectively. The data for these figures have been taken from Figures 60 and 61. Curves a, b, c, and d refer to observation heights of 12, 14.5, 16.5, and 21 mm above the load coil respectively. It can be seen that, indeed, the effect of an increase in power is to decrease the magnitude of the matrix effect. The effect, however, does not go away. It is still apparent at all power levels. A significant observation with respect to an interpretation of the decrease in matrix effect with increasing power is the variation in the spatial position of the crossover point where enhancements change to depressions. As power is increased from 1.0 kw to 2.0 kw the crossover point demonstrates a downward shift toward the load coil. If one were to use an instrument with a fixed observation height and relatively small entrance slit height to perform an analogous experiment the results could be misinterpreted. For example, if the observation window were centred at 15 mm, the enhancement would decrease as RF power was increased in a manner similar to the curves provided in Figure 62. At 2.0 kw, it could be observed that the matrix effect has "disappeared". In fact this is not the case. At this height the



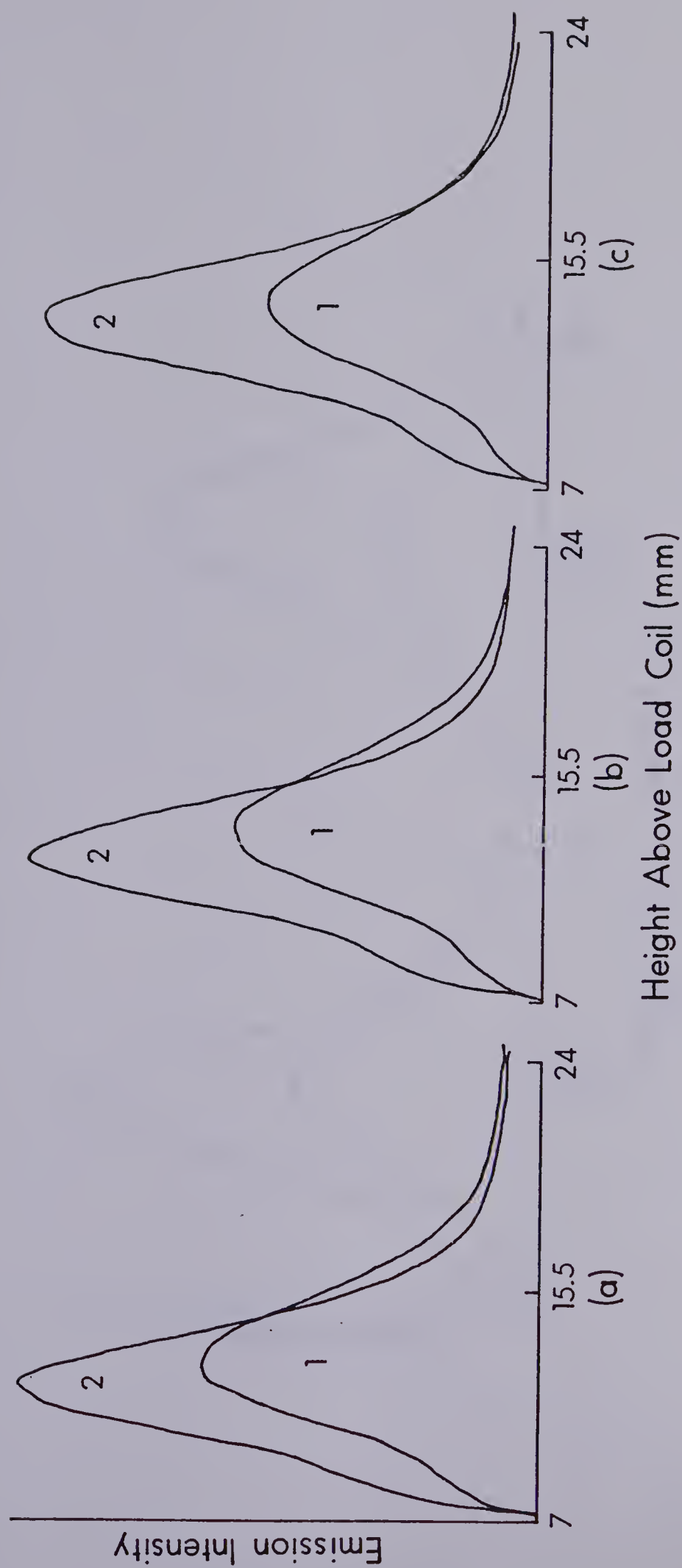


Figure 60(i). Vertical spatial profiles for CaI 422.7 nm. RF power; (a) 2.0 kw, (b) 1.75 kw, (c) 1.50 kw. (1) no Na, (2) 100:1 molar ratio of Na to Ca.



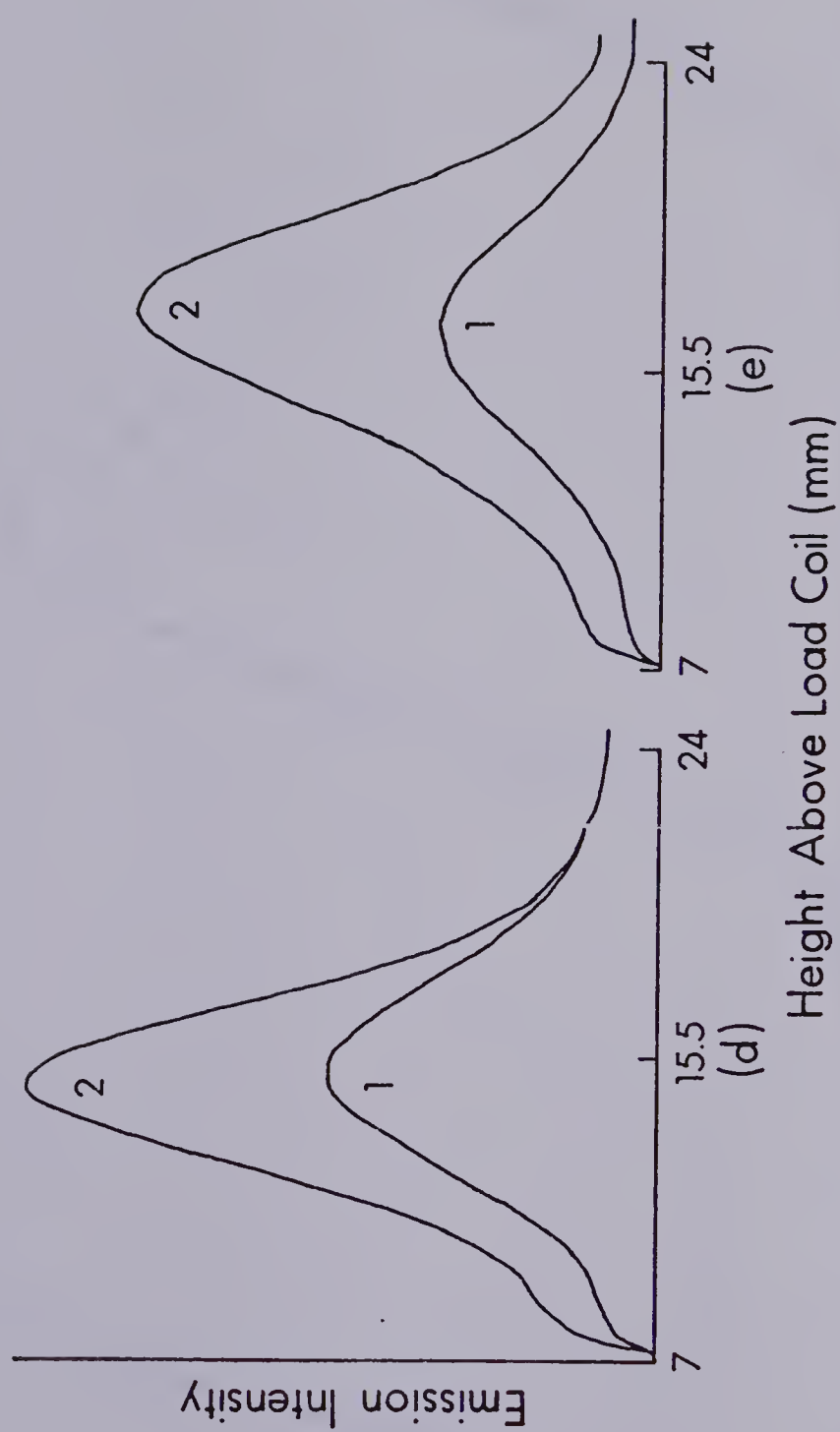


Figure 60(ii). Vertical spatial profiles for CaII 393.3 nm. RF power; (d) 1.25 kw, (e) 1.0 kw. (1) No Na, (2) 100:1 molar ratio of Na to Ca.





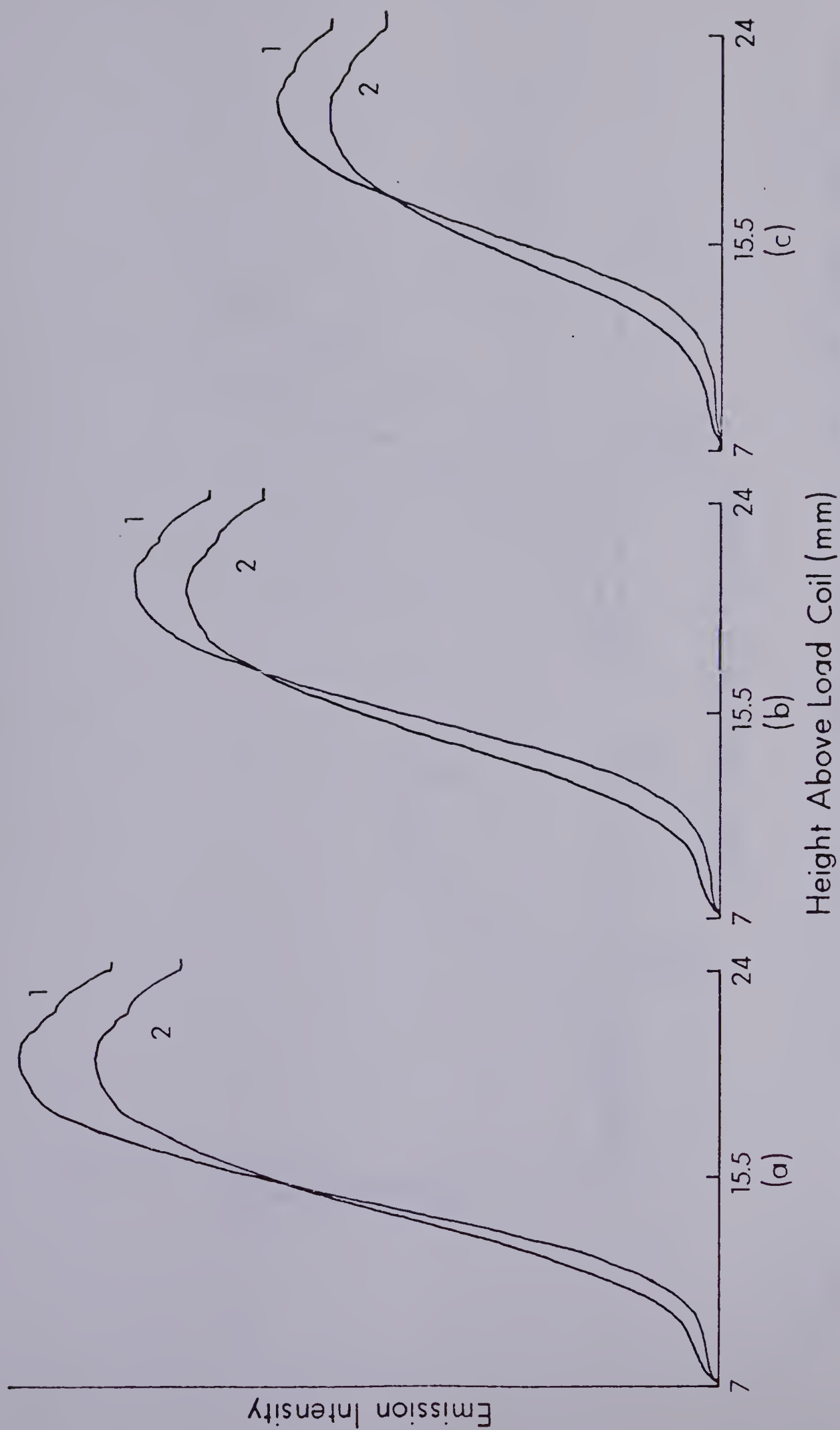


Figure 61(i). Vertical spatial profiles for CaII 393.3 nm. RF power; (a) 2.0 kw, (b) 1.75 kw, (c) 1.50 kw. (1) No Na, (2) 100:1 molar ratio of Na to Ca.



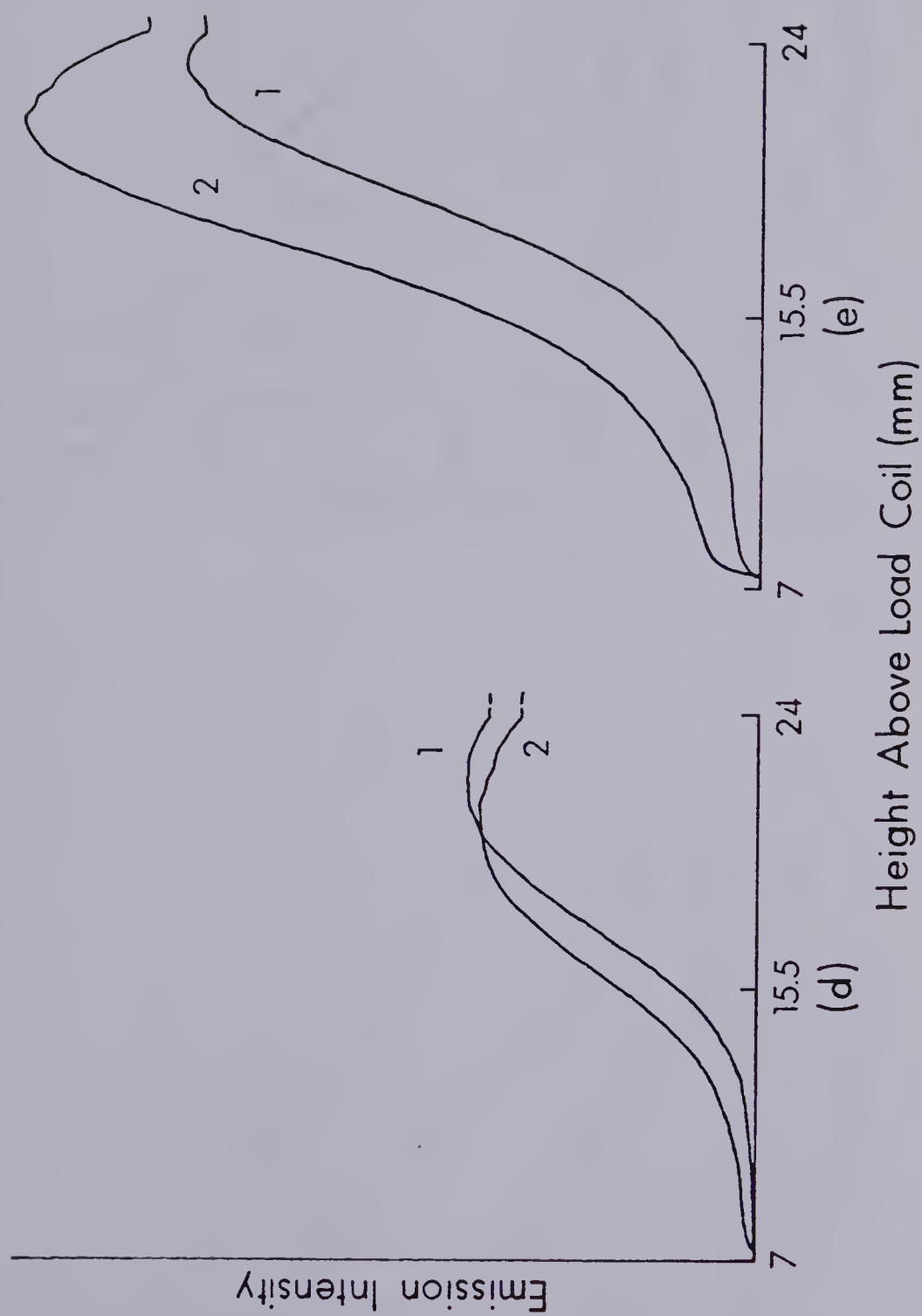


Figure 61(ii). Vertical spatial profiles for CaII 393.3 nm. RF power; (d) 1.25 kw, (e) 1.0 kw. (1) No Na, (2) 100:1 molar ratio of Na to Ca.



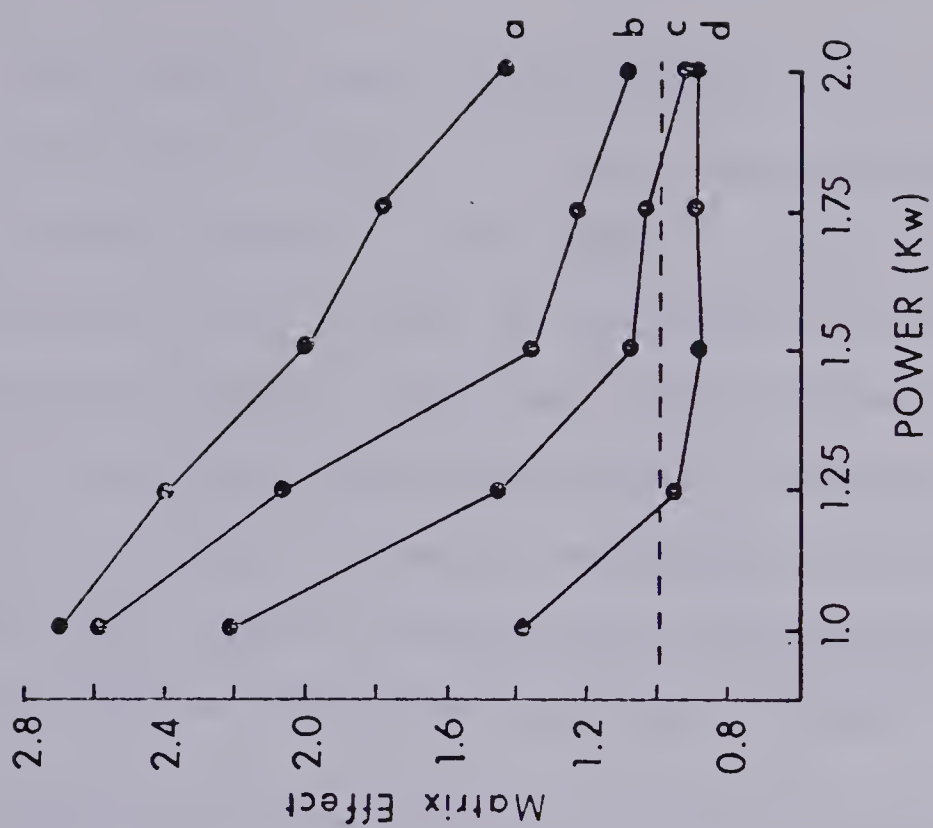


Figure 63. Matrix effect as a function of RF power input at (a) 12 mm, (b) 14.5 mm, (c) 16.5 mm and (d) 21 mm above the load coil for CaII 393.3 nm.

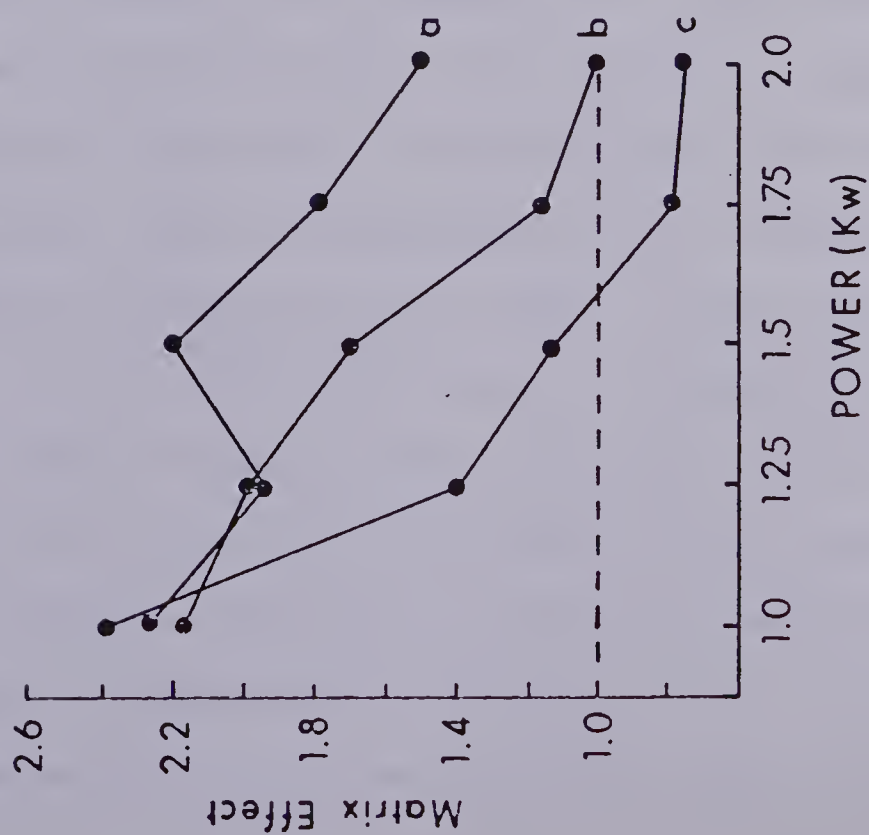


Figure 62. Matrix effects as a function of RF power input at (a) 12 mm, (b) 14.5 mm, and (c) 16.5 mm above the load coil for CaI 422.7 nm.



the enhancements lower in the channel coil would be offset by depressions higher up to give the impression that there is no matrix effect at this power. For CaI these observations could further be compounded by the overall shift in spatial profile, which has been discussed in Chapter III. It is this shift which produces the increase in effect between 1.25 and 1.5 kw for an observation height of 12 mm. Clearly the spatial information is required for a complete interpretation of analyte behaviour in the ICP.

#### Horizontal Spatial Profiles of the Matrix Effect

To assess any possible radial spatial effects of the presence of excess EIE on analyte emission, horizontal profiles of Ca atom and ion emission have been acquired with and without the presence of a 100:1 molar ratio of Na. These were acquired using the profiling system described in Chapter V from 0 to 22 mm above the load coil, in 2 mm increments. The corresponding radial emission profiles are Presented in Figures 64, 65, 66, 67, 68, and 69 for CaI (422.7 nm) and CaII (393.3 nm). In each figure curve (a) is the spatial emission profile of Ca without the presence of Na, and curve (b) is the profile with addition of Na. In each figure, curve (a) is given an amplitude of 1.0 and curve (b) scaled relative to this.

The spatial profiles for Ca at 0 mm, 2 mm, 4 mm, and 6 mm





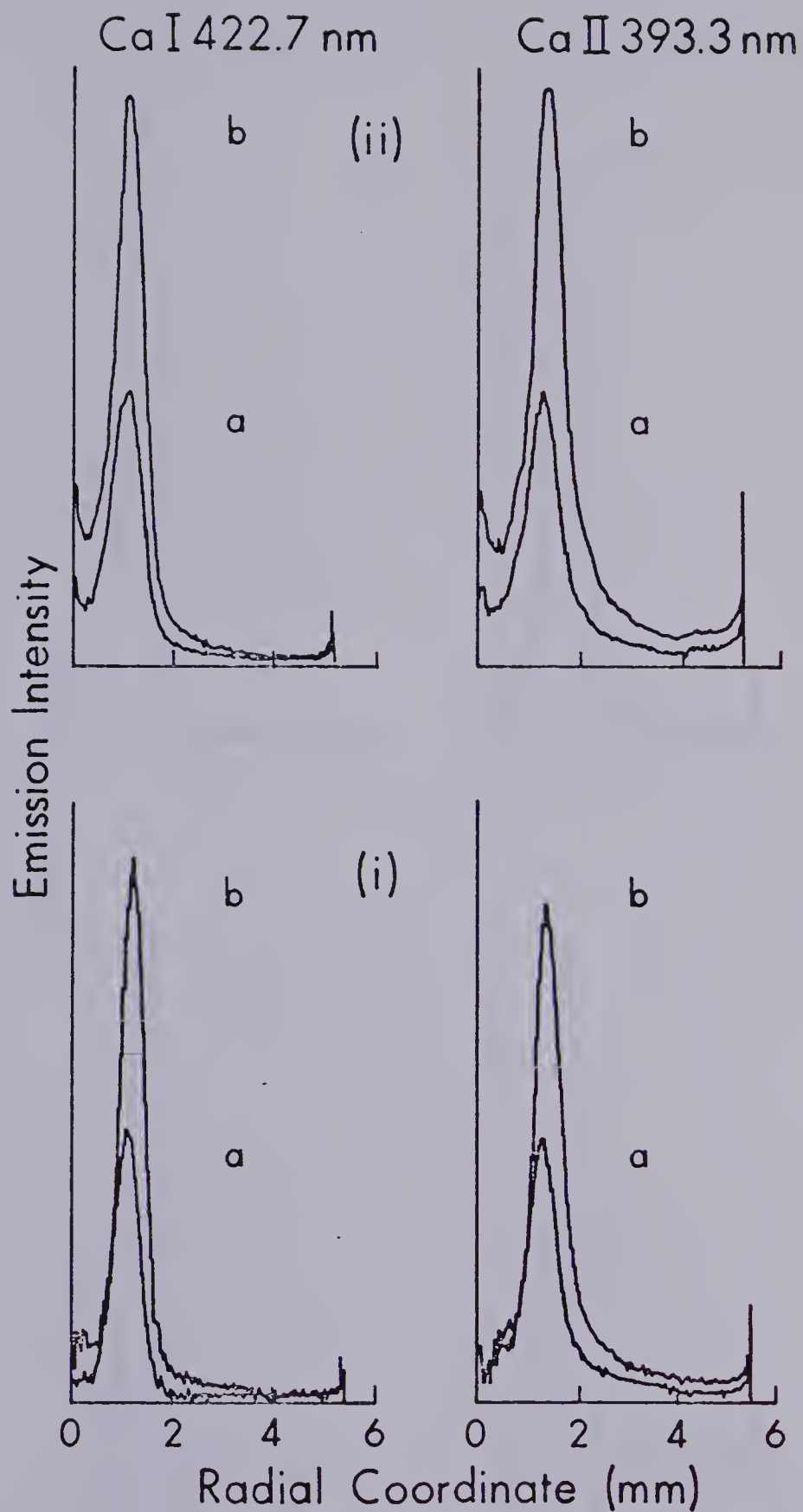


Figure 64. Radial spatial profiles of Ca emission at, (i) 0 mm, and (ii) 2 mm above the load coil. (a) no Na added, (b) 100:1 molar ratio of Na to Ca.



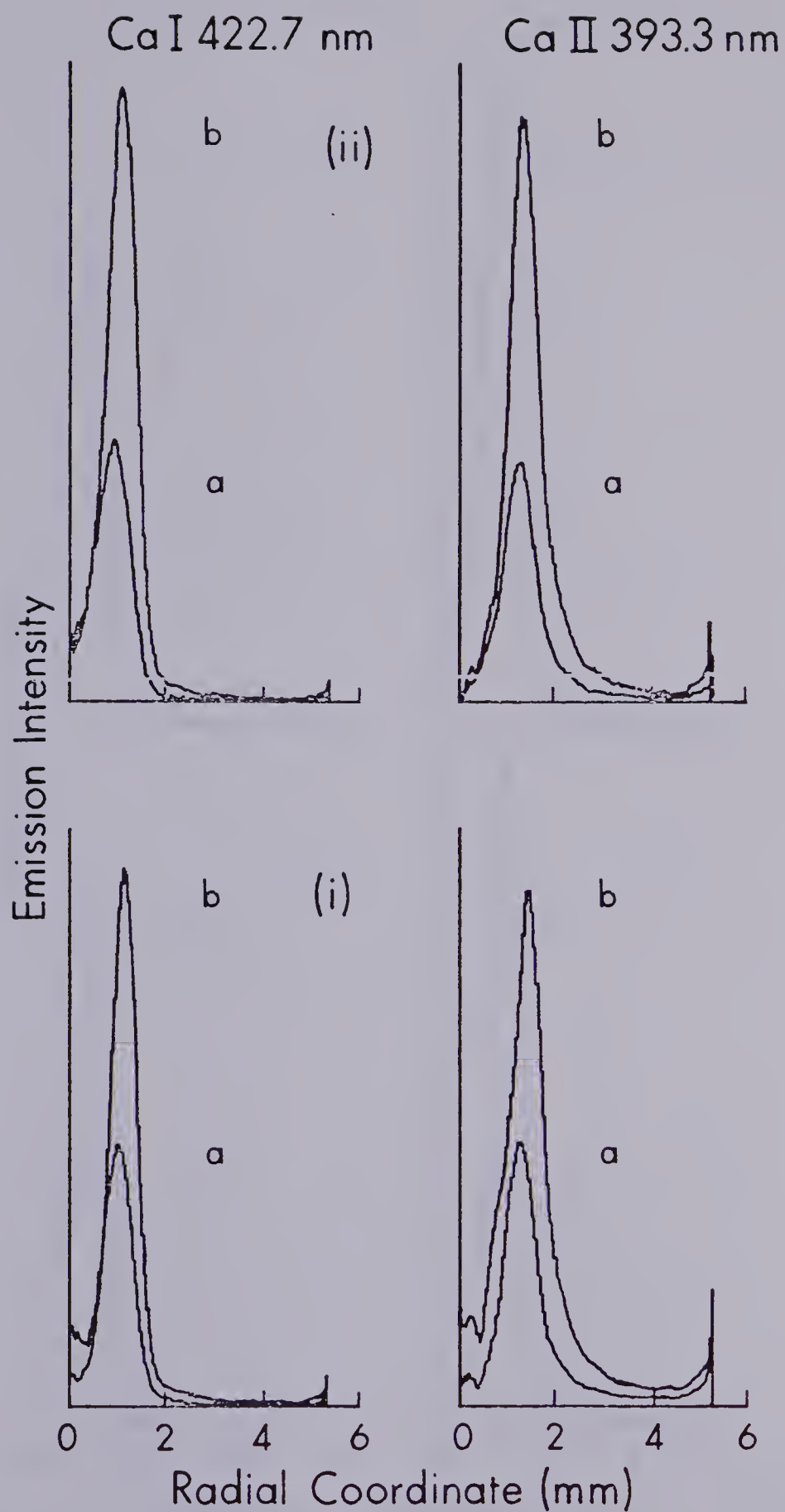


Figure 65. Radial spatial profiles of Ca emission at, (i) 4 mm and (ii) 6 mm above the load coil. (a) no Na added, (b) 100:1 molar ratio of Na to Ca.



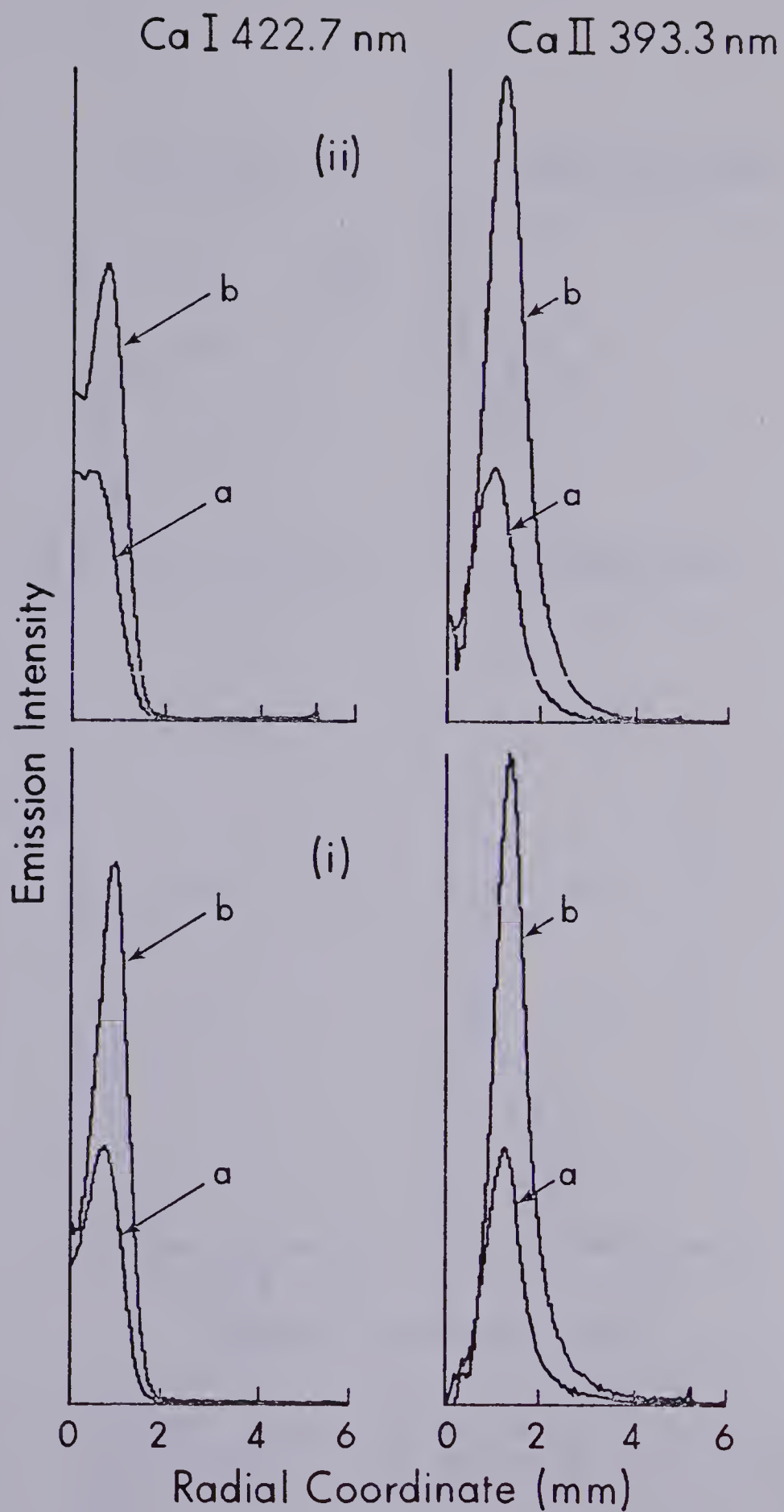


Figure 66. Radial spatial profiles of Ca emission at (i) 8 mm and (ii) 10 mm above the load coil. (a) No Na added, (b) 100:1 molar ratio of Na to Ca.



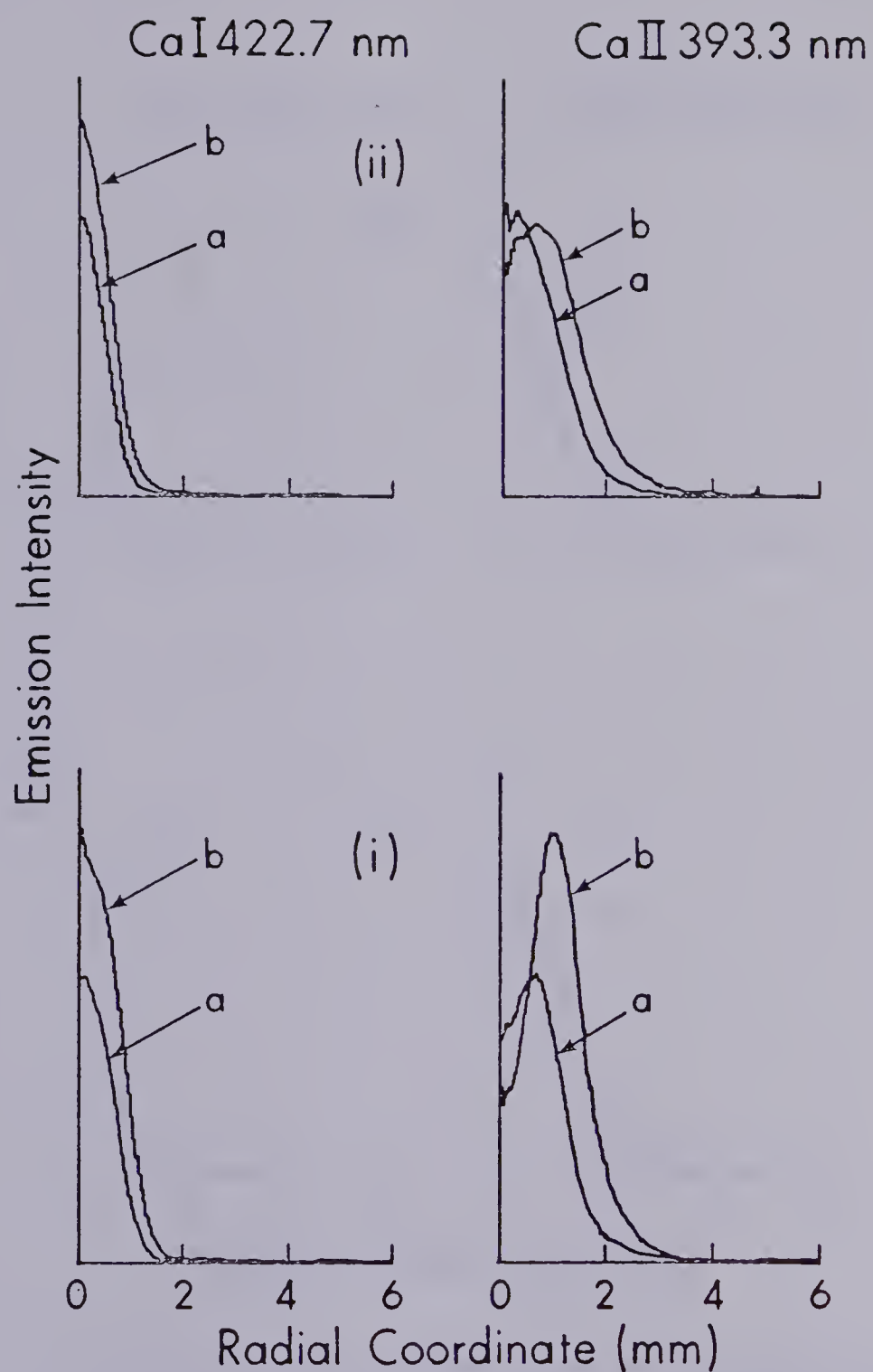


Figure 67. Radial spatial profiles of Ca emission at, (i) 12 mm and (ii) 14 mm above the load coil. (a) No Na added, (b) 100:1 molar ratio of Na to Ca.





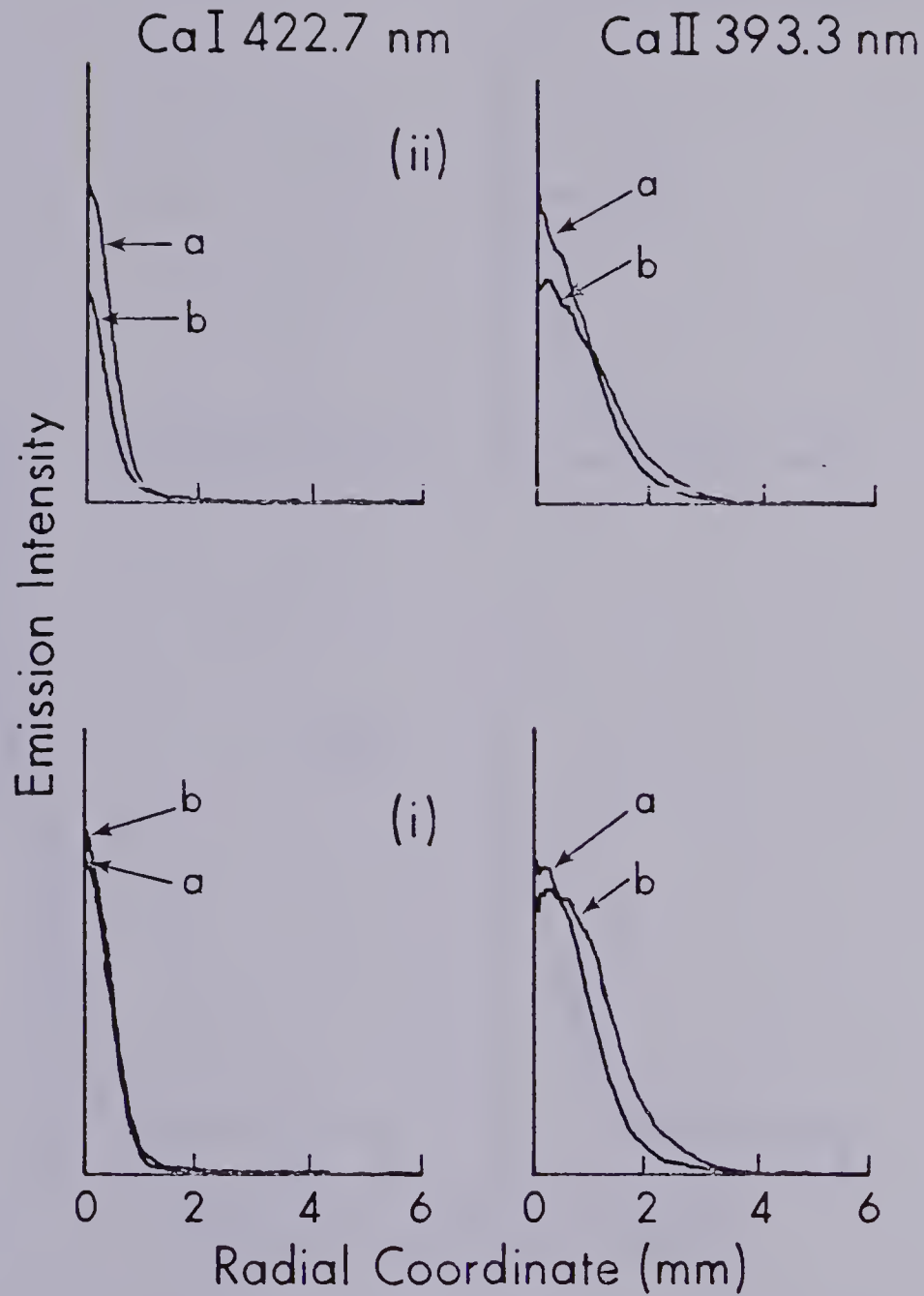


Figure 68. Radial spatial profiles of Ca emission at, (i) 16 mm and (ii) 18 mm above the load coil. (a) No Na added, (b) 100:1 molar ratio of Na to Ca.



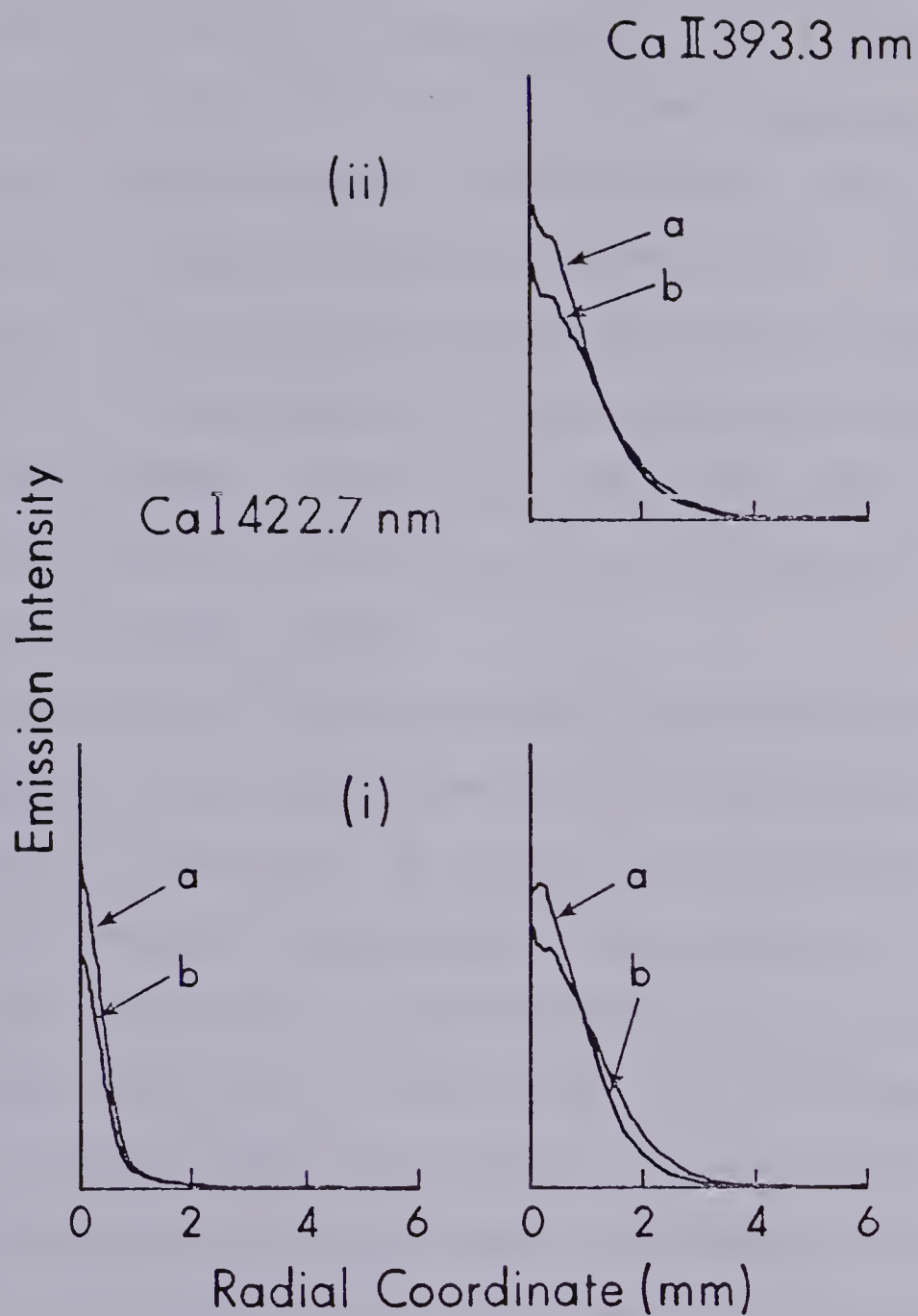


Figure 69. Radial spatial profiles of Ca emission at, (i) 20 mm and (ii) 22 mm above the load coil. (a) No Na added, (b) 100:1 molar ratio of Na to Ca.



above the load coil are provided in Figures 64(i), 64(ii), and 65(i), and 65(ii) respectively. The behaviour of Ca atom and Ca ion in this region is very similar. An off axis emission intensity peak is exhibited for both CaI and CaII at about 1 to 1.5 mm from the channel axis. At these heights, the presence of excess Na enhances emission intensity, but does not substantially alter the spatial position of the peak maximum. This is an indication that the lateral diffusion effect from delayed volatilization is probably not important in this region.

The similar behaviour of CaI and CaII in this region suggests that the enhancement is probably due to either an increase in the amount of analyte transferred to the plasma, or, increased excitation due to the presence of Na. A dual nebulizer experiment in which analyte and concomitant were nebulized separately, then mixed, and introduced into the plasma demonstrated that similar enhancements are observed. This leads one to believe that increased collisional excitation is the root cause of the signal enhancements observed in this region of the plasma. The spatial profiles for Ca at 8 mm and 10 mm above the load coil are provided in Figures 66(i) and 66(ii) respectively. Analogous enhancements to those observed in the lower region are observed in this region for both CaI and CaII. Similar off axis behaviour is observed for both CaI and CaII and there is no evidence to



suggest that the mechanism causing the enhancement in this region is any different from that in the lower region.

In the region 12 mm to 22 mm above the load coil some interesting differences begin to appear between the behaviour of CaI and CaII emission, when Na is present. At a height of 12 mm above the load coil (Figure 67(i)), CaI no longer displays the off axis peak whether or not Na is present. CaII however retains the peak at this height, and the presence of Na shifts the position of maximum intensity more toward the edge of the analyte channel. Whereas at this height an enhancement is observed for CaI across the entire profile, the emission for CaII is depressed near the centre of the analyte channel, and enhanced at distances greater than about 1 mm from the centre. Similar behaviour is observed at 14 mm (Figure 67(ii)) and 16 mm (Figure 68(i)) above the load coil, although the off axis peak becomes less pronounced for CaII at these heights. This seems to indicate that at a height of 12 mm above the load coil an additional interference mechanism begins to make itself evident which selectively affects CaII and not CaI. The enhancements for CaII at the channel edge become less pronounced as the height of observation increases from 12 to 16 mm above the load coil. The difference in spatial behaviour between CaI and CaII continues at heights of 18 mm (Figure 68(ii)) and 20 mm (Figure 69(i)) above the load





coil. At these heights the emission from CaI is depressed at all radial distances, but CaII still demonstrates depressions at the channel centre and enhancements near the edges. The spatial profile for CaI at 22 mm above the load coil is not available but clearly the trend is established.

These observations suggest that at observation heights greater than 12 mm, ambipolar diffusion may be important as a matrix effect mechanism. At this height the electron density in the channel from ionization of Na may be significant compared to the electron density at the channel edges due to argon atom ionization. Under this condition electrons will diffuse toward the channel edge setting up an electric field which will "drag" ions along with them. This reduces the overall ion population at the channel center and increases it at the channel edges, resulting in a reduction in emission intensity in the centre and an enhancement at the edge. The field will not affect neutral atom populations to any significant degree so the profile should remain relatively unchanged. The data presented in Figures 67, 68, and 69 support this interpretation.

Significant enhancements of emission intensity at 12 mm, 14 mm, and 16 mm above the load coil indicate that the effects of increased excitation may still be important, but decrease progressively with increasing height. At 18 mm, 20 mm, and 22 mm above the load coil, ambipolar diffusion



appears to be the dominant mechanism. The depression in CaI emission intensity at these heights is probably related more to an excitation effect than a direct diffusion effect. Certainly CaI does not demonstrate the spatial redistribution of emission intensity that is observed for CaII. The depression may be the result of an enhancement in ionization. As CaII ion diffuses outward the ionization equilibrium will shift to produce more ions in order to re-establish equilibrium. This will reduce the overall number density of Ca atom. The relative ratio of ion to neutral atom populations in this spatial region is such that even a 1% increase in the degree of ionization could radically reduce the Ca population, without "significantly" adding to the ion population.

### Nebulizer Effects

To investigate the possibility of aerosol ionic redistribution as a mechanism for producing the enhancements observed, an experiment was performed in which Mg analyte and Na concomitant were independently nebulized. Mg was nebulized using an ultrasonic nebulizer and Na was nebulized through the crossflow nebulizer used in the previous studies. The aerosol streams were mixed and introduced into the plasma concurrently, such that the molar ratio of Na to Mg entering the plasma was 222 to 1. At the same overall flow rate



the mixed solution was introduced through the same setup using only the crossflow nebulizer at molar ratios of 100:1 and 300:1, and the emission intensity for MgI was interpolated to a molar ratio of 222:1. The results of this experiment showed an enhancement of 1.87 for the dual nebulizer system, and 2.3 for the single nebulizer system, at a height of 10 mm above the load coil. These results indicate that under these conditions 23% of the observed enhancement could be due to an AIR effect. This is significant but is still not sufficient to completely explain the observed enhancements, and is certainly not the dominant interference mechanism.

#### Ionization Equilibrium Shifts

There is very little indication that any of the effects observed result from a shift in the ionization equilibrium of the analyte species. This has been confirmed by performing an atomic absorption experiment on MgI under plasma operating conditions and in a spatial region where large signal enhancements are observed due to the presence of Na. The measurement was made by monitoring the 285.3 nm MgI line from a hollow cathode lamp focussed on the analyte channel. Measurements were performed using a photomultiplier tube coupled to the data acquisition system described in



Appendix A. Various molar ratios of Na to Mg were introduced and the emission and absorption signals measured. The results are summarized in Table IX. It can be seen that while the emission signal increases with increasing Na concentration, the absorption signal shows only a slight change indicating an increase in excited state population but no corresponding increase in ground state population of the Mg atom. This data supports an interpretation of the effect in terms of increased collisional excitation, and discounts any mechanism which increases overall atom populations.

#### Summary and Conclusions

Clearly the spatial study of the effect of EIE's on analyte emission intensity has clarified the observations of many workers in the field, and has provided data to support a rational interpretation of the nature of the effect. This type of spatial information is indispensable in a description of the matrix effect. It has been demonstrated that the magnitude and net result of the presence of excess EIE is spatially dependent. This spatial dependence has been used to satisfactorily explain the variability in observations by several investigators on the same analyte-concomitant system. The matrix effect does not disappear under an appropriate choice of operating and







TABLE IX

EMISSION INTENSITY AND ABSORBANCE OF  
MgI 285.3 nm FOR VARIOUS MOLAR RATIOS OF Na to Mg

<u>Solution</u>		<u>Emission Intensity</u>	<u>Absorbance</u>
0:1	Na:Mg	27.14	0.2805
10:1	Na:Mg	38.63	0.3129
30:1	Na:Mg	49.95	0.3132
100:1	Na:Mg	69.52	0.3170
300:1	Na:Mg	95.51	0.2929



observation conditions. The spatial redistribution of analyte emission can make this appear to be the case; however, it is simply not an "exact" description of the situation.

In general, the addition of excess EIE enhances emission in the lower regions of the analyte channel for both atom and ion lines. In the upper regions of the analyte channel, emission intensity is depressed for both atom and ion species. The spatial position at which enhancements switch over to depressions is not a function of Na concentration but rather seems correlated to the ionization potential of the analyte species. Thus it is felt that the addition of Na defines the excitation environment, and different analyte species respond in slightly different ways to this environment. The cause of the crossover seems to be the result of a switch in the mechanism of interference. In the lower regions of the channel, the mechanism causing an enhancement appears to be the result of increased collisional excitation, as a result of an increase in the number of electrons with the appropriate energy to cause excitation of atom or ion levels. The energy of these electrons will be a function of distance from the load coil. Thus, the decrease in overall enhancement with increasing height above the load coil. This interpretation also correlates well with the observation that the enhancement increases slightly as the ionization



potential of the concomitant decreases. The effect of increasing collisional excitation appear to outweigh any effects of a shift in ionization equilibrium which could take place with an increase in electron density. The evidence from the AA experiment on MgI, confirms the relative absence of any such ionization shift mechanism at heights where emission enhancements occur. As the effects of increased excitation decrease with height, the influence of ambipolar diffusion begin to exert an influence on the spatial distribution of analyte species. This eventually leads to the observed depressions in the analyte emission. There is not enough data to interpret the plot provided in Figure 50, which indicates the position of the switchover as related to ionization potential of the analyte. This may be related to the relative width of the radial profiles of Ca, Mg, and Cd at the various heights. Certainly a detailed radial spatial study of a variety of analyte species and concomitants is warranted to further clarify this point.

The important message of this chapter is that workers should take care in investigating, reporting, and interpreting this complex system. Much confusion could have been avoided if early investigators had more carefully studied the spatial dependence of the matrix effect. Different observations by different workers gave the impression that the nature of the effect varied from plasma to plasma. As



has been stated previously, it is the author's opinion that the interaction of argon plasma gas, analyte, and concomitant is basically the same in all argon ICP's, regardless of RF power, aerosol flow rate, etc.





## CHAPTER VII

### CONCLUSIONS

The ease and speed with which spatial information may be acquired using a photodiode array detector has facilitated a detailed study of ICP spatial structure. This structure is a complex function of instrumental operating parameters, and analyte excitation and ionization characteristics. The emission lines studied divide into two categories, based on response of the spatial profile to changes in applied power. The first of these is one in which the position of maximum emission intensity is highly dependent on RF power. These are predominantly atom lines whose emission peaks in the spatial region below 15-17 mm above the load coil (at 1.5 kw power and 0.8 to 0.9 lpm aerosol flow rate). The vertical position at which these lines peak in the analyte channel can be correlated with their normal temperature. The normal temperature can be easily calculated using a set of equations if LTE is assumed. The ability to predict spatial structure based on an LTE calculation, suggests that in this spatial region LTE may exist. This region is not normally observed in analytical applications. Thus it has not been studied in as much detail as the region between 15 and 25 mm by workers using temperature and electron density measurements as probes to test for LTE. This lower region should be further studied



since it is fundamentally very interesting. Such studies would confirm or deny the existence of LTE. Lines whose emission peaks between 17 and 25 mm above the load coil form the other category. The spatial structure of these lines is not as highly dependent on ICP operating parameters or analyte excitation characteristics. It has been stated that LTE does not exist in this region and the spatial structure seems to support this.

The upper and lower regions are characterized by two different types of structure for radial emission profiles as well. In the lower region, between 0 and 12 to 15 mm above the load coil, analyte lines show off axis peaks. These peaks roughly mark the edge of the aerosol channel. Excitation in this region seems mainly the result of contact with hot argon gas originating from near the channel edge. Higher up, this structure collapses and emission peaks in the centre of the channel. It is likely that at these heights there is complete mixing between analyte and hot argon gas originating from annular regions of the plasma. The width of the radial profiles for ion lines is greater than those for atom lines. This may be the result of ambipolar diffusion of ion species. The relationship between profile width and analyte species (ion or atom) and excitation characteristics should be investigated. It may be that the degree of ionization increases as radial distance increases. This would also broaden the ion



line relative to the neutral atom line. A detailed study of ion and atom ground state populations would certainly aid in an overall understanding of this spatial structure. In fact, three dimensional spatial maps of ground state populations analogous to those for emission presented in Chapter V would be invaluable in characterizing ICP phenomena. Included in these should be a map of argon metastable densities. To this point spatial studies of the aerosol channel have suggested that these species reach maximum density at heights between 18 and 22 mm above the load coil. A spatially resolved absorption experiment would confirm or deny this suggestion.

The dependence of emission intensity on excess EIE has certainly been clarified by the spatial study. It has been demonstrated that many of the conflicting statements which have appeared on the nature of the effect can be rationalized on the basis of changes in the spatial structure of analyte emission. Several suggestions have been offered on the reasons for these changes in spatial structure. The enhancements in emission observed in the lower regions of the analyte channel appear to be the result of an increase in the channel electron temperature. Measurement of electron temperature from the absolute continuum emission intensity, with and without the presence of EIE, would clarify this suggestion. Depressions in emission intensity appear to be the result of





ambipolar diffusion. The dependence of the position where enhancements convert to depression on analyte ionization characteristics is significant and should be further investigated. This may be related to radial profile width, atom and ion mobilities, or complex electric field effects.

There are several areas which warrant spatial investigation which have not been undertaken as part of this thesis. The spatial distribution of species introduced as part of the sample aerosol is one of these. The dissociation products of water such as OH, H, and oxygen radical may be important in excitation and/or de-excitation processes and should be studied in detail. This should be combined with a study of any spatial redistribution of analyte emission which may result from the use of a desolvation chamber. In addition, it is curious that as ion emission drops off in the area between 20 and 35 mm above the load coil, atom emission does not correspondingly increase. This may be the result of oxide formation. A spatial study of analyte oxides would be helpful in deciding if these species are important in the removal of atom and ion species.

Finally, as has been illustrated a number of times throughout this thesis, a detailed knowledge of analyte spatial behaviour has clarified observations which have been made by researchers using instruments which measure spatially integrated emission intensities. It has been pointed out that care should





be exercised in interpreting plasma phenomena based on measurements of this type alone. The confusion on the nature of the matrix effect is a good example of this. Spatially resolved measurements are the key element in the investigation and understanding of a complex source like the ICP. The use of a linear photodiode array is a rapid, detailed, and quantitative method for making these measurements.



## BIBLIOGRAPHY

1. A. Scheeline and J.P. Walters, *Anal. Chim. Acta*, 95, 59 (1977).
2. A. Scheeline and J.P. Walters, *Anal. Chem.*, 48, 1519 (1976).
3. G.R. Kornblum and L. deGalan, *Spectrochim. Acta*, 29B, 249 (1974).
4. Martin A. Uman, "Introduction to Plasma Physics", McGraw Hill, Inc., N.Y., 1964).
5. H.N. Olsen, *J.Q.S.R.T.*, 3, 59 (1963).
6. L.P.P. Butler, H.G.C. Human, and R.H. Scott, "Hand-book of Spectroscopy", Chapt. XIV.
7. G.I. Babat, *J. Inst. Elec. Engrs. (London)*, 94, 27 (1947).
8. T.B. Reed, *J. Appl. Phys.*, 32, 821 (1961).
9. S. Greenfield, I. Ll. Jones, and C.T. Berry, *Analyst*, 89, 713 (1964).
10. R.H. Wendt and V.A. Fassel, *Anal. Chem.*, 37, 920 (1965).
11. V.A. Fassel and R.N. Kniseley, *Anal. Chem.*, 46, 1155A (1974).
12. V.A. Fassel and R.N. Kniseley, *Anal. Chem.*, 46, 1110A (1974).
13. I.C.P. Info. Newsletter, R. Barnes (ed.).
14. R.H. Scott, A. Strasheim, and M.L. Kokot, *Anal. Chim. Acta*, 82, 67 (1976).



15. R.H. Scott and M.L. Kokot, *Anal. Chem. Acta*, 75, 257 (1976).
16. R.L. Dahlquist and J.W. Knoll, *Appl. Spectrosc.*, 32, 1 (1978).
17. R. Diemiaszonek, J.L. Mouton, and C. Trassy, *Analisis*, 7, 96 (1979).
18. R.H. Scott and A. Strasheim, *Anal. Chim. Acta*, 76, 71 (1975).
19. R.K. Winge, V.A. Fassel, R.N. Kniseley, E. DeKalb, and W.J. Haas, *Spectrochim. Acta*, 32B, 329 (1977).
20. J. Locke, *Anal. Chim. Acta*, 113, 3 (1980).
21. R.N. Merryfield and R.C. Loyd, *Anal. Chem.*, 51, 1965 (1979).
22. D.L. Winsor and M.B. Denton, *Appl. Spectrosc.*, 32, 366 (1978).
23. S. Greenfield, H. McD. McGreachin, and P.B. Smith, *Talanta*, 22, 1 (1975).
24. S. Greenfield, H. McD. McGreachin, and P.B. Smith, *Talanta*, 22, 553 (1975).
25. S. Greenfield, H. McD. McGreachin, and P.B. Smith, *Talanta*, 23, 1 (1976).
26. R.M. Barnes, "C.R.C. Critical Reviews in Analytical Chemistry", Sept. 1978.
27. R.M. Dagnell, D.J. Smith, T.S. West, and S. Greenfield, *Anal. Chim. Acta*, 54, 397 (1971).



28. H.C. Hoare and R.A. Mostyn, *Anal. Chem.*, 39, 1153 (1967).
29. E.D. Salin and Gary Horlick, *Anal. Chem.* 51, 2284 (1979).
30. J. Carr, M.Sc. Thesis, University of Alberta, 1980.
31. H.G.C. Human, R.H. Scott, A.R. Oakes, and C.D. West, *Analyst*, 101, 265 (1976).
32. H.N. Olsen, *Phys. Rev.*, 124, 1703 (1961).
33. G. Horlick, *Ind. Res./Dev.*, 20, 70 (1978).
34. N. Furuta, "Research Report from the National Institute for Environmental Studies - No. 12", Yatabe, Japan (1980).
35. G.R. Kornblum and L. DeGalan, *Spectrochim. Acta*, 32B, 71 (1977).
36. D.J. Kalnicky, V.A. Fassel, and R.N. Kniseley, *Appl. Spectrosc.*, 31, 139 (1977).
37. J. Jarosz, J.M. Mermet, and J.P. Robin, *Spectrochim. Acta*, 35B, 163 (1980).
38. J.F. Alder, R.M. Bombelka, and G.F. Kirkbright, *Spectrochim. Acta*, 35B, 163 (1980).
39. G.F. Kirkbright, A.F. Ward, and T.S. West, *Anal. Chim. Acta*, 62, 241 (1972).
40. G.F. Kirkbright, A.F. Ward, and T.S. West, *Anal. Chim. Acta*, 64, 353 (1973).
41. S.S. Berman and J.W. McLaren, CIC Conference, Ottawa, Ontario, paper # AN-35, June, 1980.
42. P.W.J.M. Boumans and F.J. DeBoer, *Spectrochim. Acta*, 32B, 365 (1977).





43. H.G.C. Human and R.H. Scott, *Spectrochim. Acta*, 31B, 459 (1976).
44. G.F. Kirkbright and A.F. Ward, *Talanta*, 21, 1145 (1974).
45. M.H. Abdallah, J.M. Mermet, and C. Trassy, *Anal. Chim. Acta*, 87, 329 (1976).
46. P.W.J.M. Boumans and F.J. DeBoer, *Spectrochim. Acta*, 30B, 309 (1975).
47. P.W.J.M. Boumans and F.J. DeBoer, *Spectrochim. Acta*, 31B, 355 (1975).
48. G.F. Larson, V.A. Fassel, R.H. Scott, and R.N. Kniseley, *Anal. Chem.*, 47, 238 (1975).
49. J.M. Mermet, *Spectrochim. Acta*, 30B, 383 (1975).
50. J. Jarosz and J.M. Mermet, *J.Q.S.R.T.*, 17, 237 (1977).
51. J.F. Alder and J.M. Mermet, *Spectrochim. Acta*, 28B, 421 (1973).
52. I. Reif, V.A. Fassel, and R.N. Kniseley, *Spectrochim. Acta*, 28B, 105 (1973).
53. I. Reif, V.A. Fassel, and R.N. Kniseley, *Spectrochim. Acta*, 29B, 79 (1974).
54. I. Reif, V.A. Fassel, and R.N. Kniseley, *Spectrochim. Acta*, 30B, 163 (1975).
55. I. Reif, V.A. Fassel, and R.N. Kniseley, *Spectrochim. Acta*, 31B, 377 (1976).
56. P.W.J.M. Boumans, "Theory of Spectrochemical Excitation", Plenum Press, N.Y., (1966).



57. E.E. Muschlitz, *Science*, 159, 599 (1968).
58. J. Mika and T. Török, "Analytical Emission Spectroscopy - Fundamentals", Butterworths, London (1974).
59. R.S. Berry, *Rad. Res.*, 59, 367 (1974).
60. H. Hotop, *Rad. Res.*, 59, 379 (1974).
61. M.J. Shaw, *Contemp. Phys.*, 15, 445 (1974).
62. J.A.C. Broekaert, F. Leis, and K. Laguna, *Spectrochim. Acta*, 32B, 173 (1977).
63. C.I.M. Beenakker, *Spectrochim. Acta*, 32B, 173 (1977).
64. J.M. Mermet, CIC Conference, Ottawa, Ontario, paper #AN-9, June 1980.
65. T.G. Cowley, V.A. Fassel, and R.N. Kniseley, *Spectrochim. Acta*, 23B, 771 (1968).
66. J.P. Walters, *Science*, 198, 787 (1977).
67. J. Jarosz, J.M. Mermet, and J. Robin, *Comptes Rendus Academie des Sciences, Paris, Series B*, 278, 884 (1974).
68. G. Dubé and M.I. Boulos, *Can. Jour. Spectrosc.*, 22, 68 (1977).
69. T. Edmonds and G. Horlick, *Appl. Spectrosc.*, 31, 536 (1977).
70. R.M. Barnes and R.G. Schleicher, *Spectrochim. Acta*, 30B, 109 (1975).
71. H. Kawaguchi, T. Ito, K. Ota, and A. Mizuike, *Spectrochim Acta*, 35B, 199 (1980).
72. S. Murayama, H. Matsuno, and M. Yamamoto, *Spectrochim. Acta*, 23B, 513 (1968).



73. S. Murayama, *Spectrochim. Acta*, 25B, 191 (1970).
74. Kitagawa and T. Takeuchi, *Anal. Chim. Acta*, 60, 309 (1971).
75. G.W. Johnson, H.E. Taylor and R.K. Skogerboe, *Appl. Spectrosc.*, 34, 19 (1980).
76. G.R. Kornblum and L. deGalan, *Spectrochim. Acta*, 32B, 455 (1977).
77. G. Horlick and M. Blades, *Appl. Spectrosc.*, 34, 229 (1980).
78. C.J. Creamers and R.C. Birkebak, *Appl. Optics*, 5, 1057 (1966).
79. O.N. Nestor and H.N. Olsen, *S.I.A.M. Rev.*, 2, 200 (1960).
80. C.D. Maldonado, A.P. Caron, and H.N. Olsen, *Jour. Opt. Soc. Amer.*, 55, 1247 (1965).
81. R.D. Sacks and J.P. Walters, *Anal. Chem.*, 42, 61 (1970).
82. T.J. Olscheske and J.P. Walters, *Appl. Spectrosc.*, 6, 600 (1979).
83. M.W. Blades and G. Horlick, accepted for publication *Appl. Spectrosc.*, 34 (1980).
84. R.N. Kniseley, H. Amenson, C.C. Butler, and V.A. Fassel, *Appl. Spectrosc.*, 28, 285 (1974).
85. M. Franklin, C. Baber, and S.R. Koirtyohann, *Spectrochim. Acta*, 31B, 489 (1976).
86. J.E. Meinhard and Associates Catalogue (1976), Tustin, Cal., 92680.



87. Gary Horlick, *Appl. Spectrosc.*, 30, 113 (1976).
88. Gary Horlick and E.G. Coddling, *Anal. Chem.*, 45, 1490 (1973).
89. Gary Horlick and E.G. Coddling, "Contemporary Topics in Analytical and Clinical Chemistry, Vol. I, D.M. Hercules and G.M. Hieftje, Eds., Plenum Press, N.Y. (1977).
90. D.M. Coleman and J.P. Walters, *Spectrochim. Acta*, 33B, 127 (1978).
91. J.P. Walters, "A Synergic Approach to Graduate Research in Spectroscopy and Spectrochemical Analysis" in "Contemporary Topics in Analytical and Clinical Chemistry", edited by D.M. Hercules, G.M. Hieftje, L.R. Snyder and M.A. Evenson, Plenum Press, N.U. (1978), p. 91.
92. P.W.J.M. Boumans and F.J. DeBoer, *Spectrochim. Acta*, 27B, 391 (1972).
93. S. Berman and J.W. McLaren, *Appl. Spectrosc.*, 32, 372 (1978).
94. I.C.P. Info. Newsletter, 4, 89 (1978).
95. W.B. Barnett, V.A. Fassel, and R.N. Kniseley, *Spectrochim. Acta*, 23B, 643 (1968).
96. R.N. Savage and G.M. Hieftje, *Anal. Chem.* 52, 1267 (1980).





97. R.L. Watters, Jr., and J.A. Norris, "Applications of ICP to Emission Spectroscopy", R. Barnes, Ed., Franklin Institute, 1979.
98. E.D. Salin and Gary Horlick, accepted for publication, Anal. Chem. (1980).
99. K.W. Busch and T.J. Vickers, Spectrochim. Acta, 28B, 84 (1973).
100. R.J. Decker, Spectrochim. Acta, 35B, 19 (1980).
101. I.C.P. Info. Newsletter, 4, 147 (1978).
102. D.J. Kalnicky, R.N. Kniseley, and V.A. Fassel, Spectrochim. Acta, 30B, 511 (1975).
103. G.F. Kirkbright, M. Sargent, and S. Vetter, Spectrochim. Acta, 25B, 465 (1970).
104. G.F. Kirkbright, M.K. Peters, M. Sargent, and T.S. West, Spectrochim. Acta, 663 (1968).
105. K. Visser, F.M. Hamm, and P.B. Zeeman, Appl. Spectrosc., 30, 34 (1976).
106. C.E. Moore, "Experimental Transition Probabilities for Spectral Lines of Seventy Elements", NBS Monograph #53. U.S. Dept. Commerce (1962).
107. R. Herrman and C.T.J. Alkemade, "Chemical Analysis by Flame Photometry", 2nd ed., Interscience Pub., London (1963).
108. S.R. Koirtyohann and E.E. Pickett, Spectrochim. Acta, 28B, 139 (1968).



109. G.R. Kornblum and L. deGalan, *Spectrochim. Acta*, 28B, 139 (1973).
110. T. Maruta, T. Takouchi, and M. Suzuki, *Anal. Chim. Acta*, 58, 452 (1972).
111. A.E. Watson and T.W. Steele, *I.C.P. Info. Newsletter*, 5, 553 (1980).
112. J.M. Mermet and J. Robin, *Anal. Chim. Acta*, 70, 271 (1975).
113. C. Veillon and M. Margoshes, *Spectrochim. Acta*, 23B, 503 (1968).
114. A.C. West, V.A. Fassel, and R.N. Kniseley, *Anal. Chem.*, 45, 1586 (1973).
115. A.C. West, V.A. Fassel and R.N. Kniseley, *Anal. Chem.*, 45, 2420 (1973).
116. B.V. L'vov, D.A. Katsov, P.L. Kruglikova, and L.K. Polzik, *Spectrochim. Acta*, 31B, 49 (1976).
117. M. Howatson, "Introduction to Gas Discharges", Pergamon Press, 2nd ed., N.Y. (1976).
118. J.A. Borowiec, A.W. Boorn, J.H. Pillard, M.S. Cresser, and R.F. Browner, *Anal. Chem.*, 52, 1054 (1980).
119. R.K. Skogerboe and K.W. Olsen, *Appl. Spectrosc.*, 32, 181 (1978).
120. "8080 Microcomputer Peripherals User's Manual", Intel Corp., 3065 Bowers Ave., Santa Clara, CA 95051.



121. H.V. Malmstadt, C.G. Enke, S.R. Crouch, and Gary Horlick, "Optimization of Electronic Measurements", W.A. Benjamin, Menlo Park, CA, 1974 p. 124.
122. Intel Corp., User's Library, 3065 Bowers Ave., Santa Clara, CA 95051.
123. R. Findley, "Scelbi '8080' Software Gourmet Guide and Cook Book", Scelbi Computer Consulting Inc., 1322 Rear-Boston Post Road, Milford, CT 06460.
124. A.F. Ward, American Laboratory, 10(11), 79 (1978).



## APPENDIX A

The photomultiplier tube is the most widely used detector for spectrochemical measurements in the ultraviolet and visible spectral regions. Although many diverse experimental situations exist, a rather large number of applications have very similar basic measurement requirements. In our own laboratory we had a need for a general purpose wide dynamic range integrating readout system. One of the main applications for this system was the acquisition of basic signal to noise ratio data on spectrochemical sources such as the inductively coupled plasma. For this application background subtraction capability was required in order that a blank (i.e. plasma spectral background) and/or photomultiplier tube dark current signal could be automatically subtracted from an analyte emission reading. In addition, to facilitate the signal to noise ratio studies, automatic acquisition of replicate integrated measurements was required along with subsequent calculation of standard deviations and signal to noise ratios. Finally it was desirable to have all data logged in a systematic fashion to a hardcopy readout device.

These basic requirements essentially dictated the development of a microprocessor based readout system. In fact we developed two types of wide dynamic range integrating readout systems both of which operate under microprocessor control. In both systems the output current signal from the





PM tube is first converted to a voltage with an operational amplifier. Then, in the first measurement system (Figure 70) this voltage is converted to a frequency with a wide dynamic range (6 orders of magnitude) voltage-to-frequency converter. The voltage-to-frequency converter was interfaced to an 8080 based single board microcomputer, the Intel SDK-80. The key subsystem in this interface is the 8253 programmable interval timer chip of Intel. Utilizing two of those chips in conjunction with the SDK-80 microcomputer one has, in a sense, a very flexible software programmable frequency meter for the measurement of v-to-f converter output. In the second system (Figure 70) a monolithic 10 bit successive approximation ADC was interfaced to the SDK-80. Wide dynamic range integrating measurement capability was achieved by summing a large number of conversions.

In both systems the microprocessor controls the acquisition of replicate integrated measurements and software is included for background subtraction, the calculation of standard deviations of the replicate values and signal to noise ratios. Development of this software capability in a small system was greatly facilitated by use of the AM9511 Arithmetic Processing Unit of Advanced Micro Devices. This chip (24 pin package) is capable of performing fixed point single and double precision (16 or 32 bit) arithmetic and floating point single precision (24 bit mantissa, 7 bit ex-



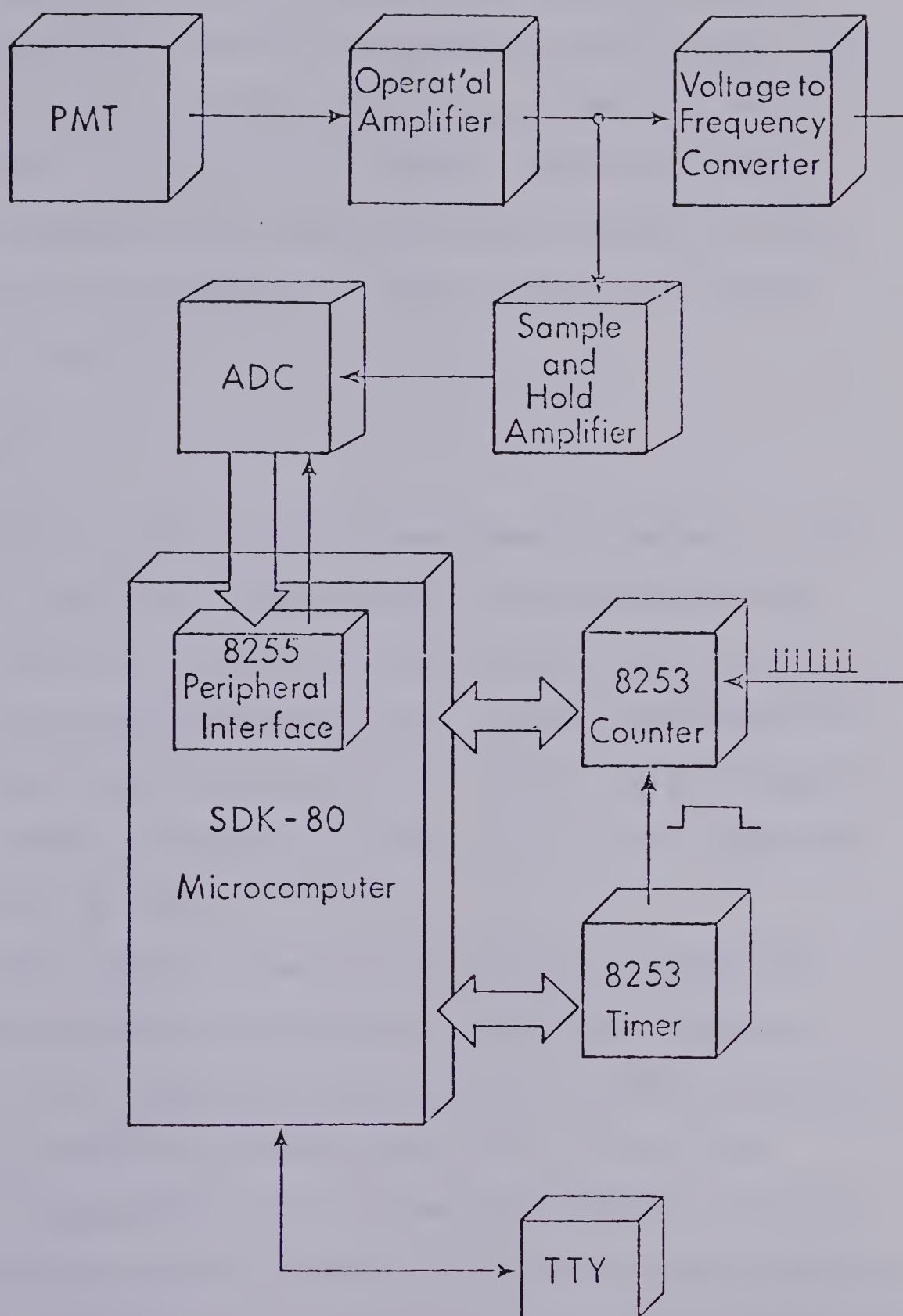


Figure 70. Block diagram of the voltage-to-frequency converter and analog-to-digital converter based measurement systems.



ponent) arithmetic. Operations performed include add, subtract, multiply, divide, trigonometric and inverse trigonometric functions, square roots, logarithms and exponentiation. The use of this chip greatly expedited overall software development and execution time compared to software floating point packages. Both systems will now be described in detail.

### Experimental

Components common to both measurement systems are the operational amplifier and the SDK-80 single board microcomputer. The OA is Model 52K (Analog Devices), a low noise, low drift, precision FET amplifier. It was operated with a 10 M $\Omega$  feedback resistor in parallel with a 450 pf capacitor. Thus the output voltage was 1 V for a  $10^{-7}$  amp input current from the PM tube.

The heart of both measurement systems is the Intel SDK-80 single board microcomputer. The basic hardware features of this board include an 8080 A central processing unit, 1 k of read/write memory (8111's), 4 k of 2708 erasable programmable read only memory (EPROM), an 8251 programmable peripheral interface chip providing 48 digital I/O lines. In addition a small but very useful breadboarding area is provided on the board. All additional circuitry for both applications was placed in this breadboard area,



except for the voltage-to-frequency converter and operational amplifier, which were located near the PMT.

### Voltage-to-Frequency Converter Based System

The voltage-to-frequency converter used was Model 460 k (Analog Devices), a high accuracy unit with a six decade (1 Hz to 1 MHz) dynamic range.

The key subsystem of this measurement system is the Intel 8253 programmable interval timer. A block diagram of this 24 pin integrated circuit is shown in Figure 71. It consists of three independent 16 bit pre-settable down counters, read/write logic, a control word register and a data bus buffer. The read/write logic controls the overall device operation such as loading and reading of the various counters as well as loading of the control word register. The counters can be software programmed to act as either binary or BCD counters and each counter can be independently programmed to operate in any of six different modes. The basic operation of each mode is illustrated schematically in Figure 72.

Mode 0 is a software triggered interrupt in which an interrupt signal, a rising edge at the output terminal, is generated N clock pulses after software loading the counter with N. In Mode 1 (programmable one shot or monostable) an external trigger (rising edge) applied to the gate input





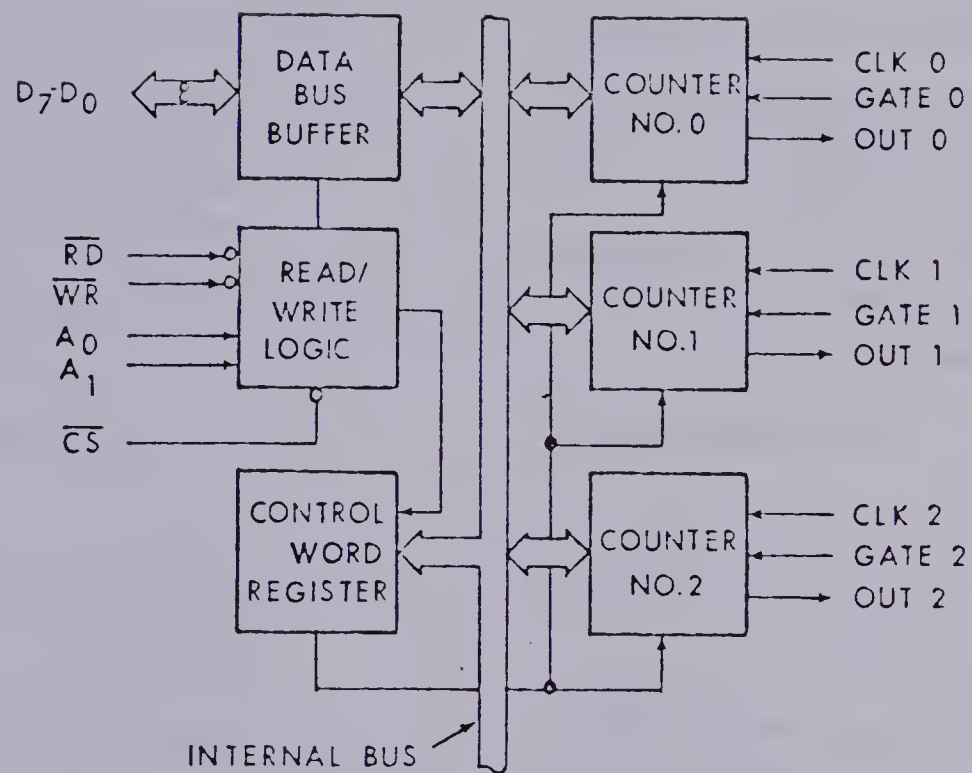


Figure 71. Block diagram of the 8253 programmable interval timer.



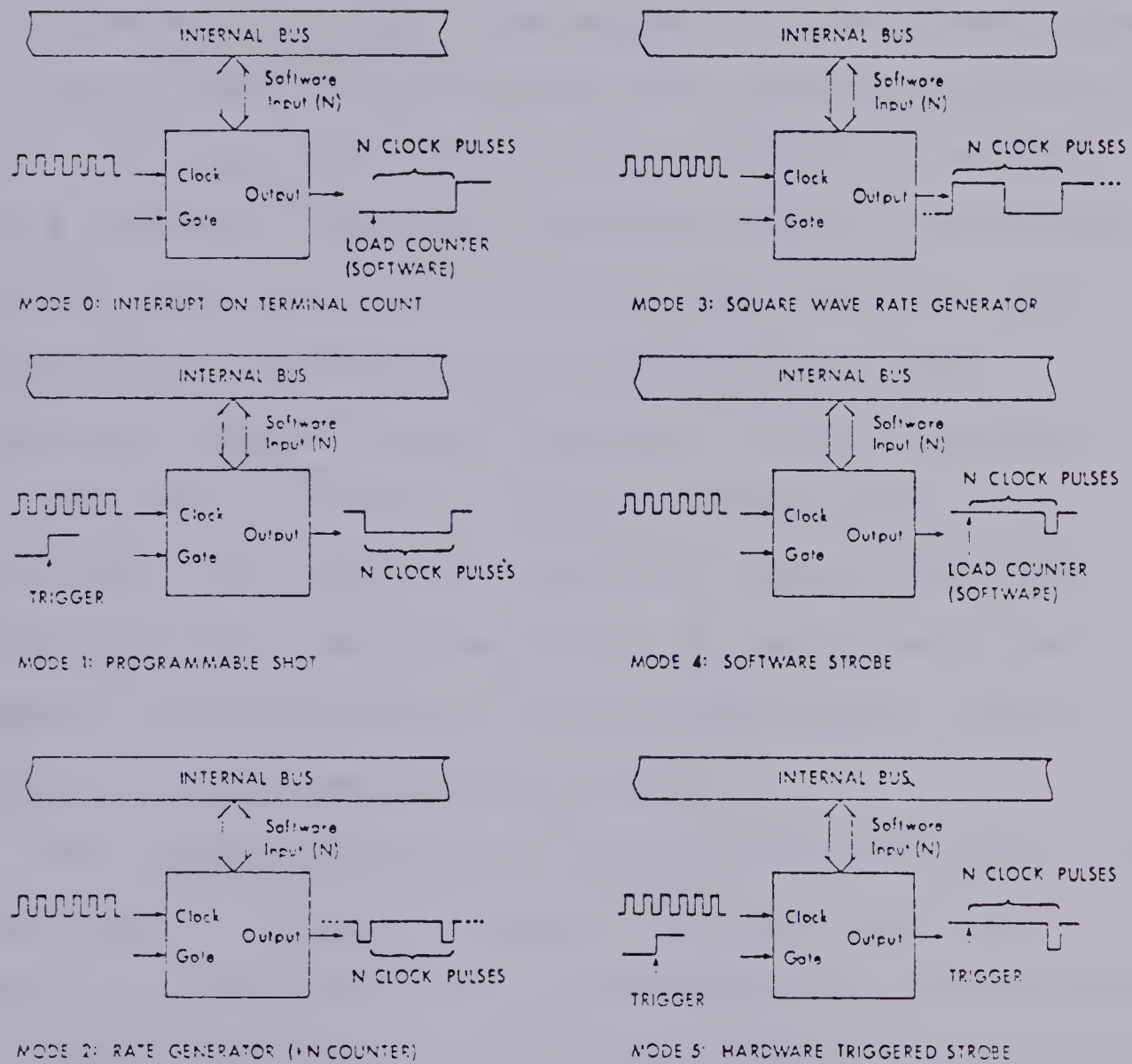


Figure 72. Schematic representations of the 8253 modes.



generates a zero level pulse at the output. The duration of the pulse is  $N$  clock pulses where  $N$  is again a software loaded value. Mode 2 and Mode 3 both divide by  $N$  counter modes. In Mode 2 the output is a zero level pulse, one clock pulse in duration, every  $N$ th clock pulse while in Mode 3 the output is a symmetrical divided by  $N$  waveform. Mode 4 provides a software triggered strobe, a zero level pulse of one clock period duration that occurs  $N$  clock pulses after a software load of the counter. Mode 5 (hardware triggered strobe) provides a similar operation but requires an external trigger, a rising edge at the gate input. The above discussion and Figure 72 provide only a brief and basic description of the operation and capabilities of the 8253. For complete details Intel's literature should be consulted [120].

The complete schematic of the way the 8253's are connected to the SDK-80 is shown in Figure 73. One of the 8253's functions as the counter for the measurement of the voltage-to-frequency converter output and the second 8253 generates the counter time base (integration time) for the first 8253. Simplified diagrams of the integration timer and counter are shown in Figure 74.

The integration time is derived from the 2.048 MHz clock of the microprocessor. Counter 0 on the timer 8253 is operated in Mode 2, binary (divide by  $N$  counter) by



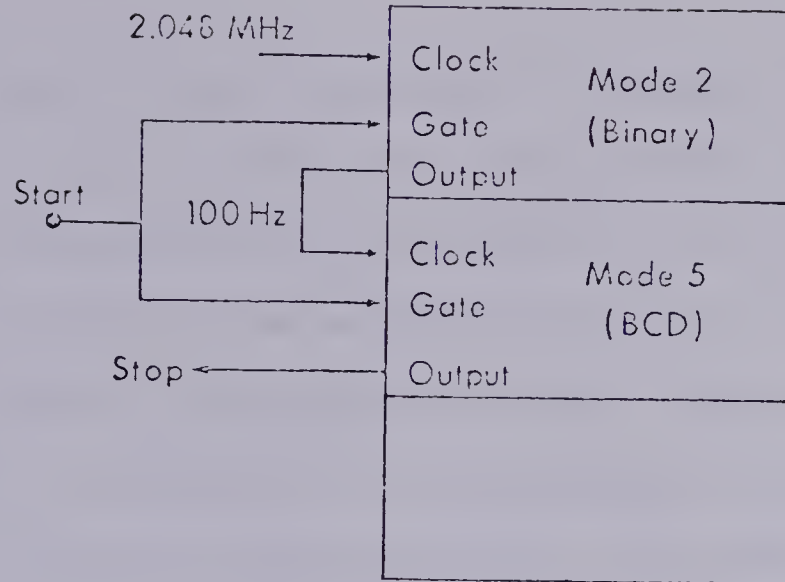


Figure 73. Circuit diagram of the complete programmable frequency meter as interfaced to the SDK-80.





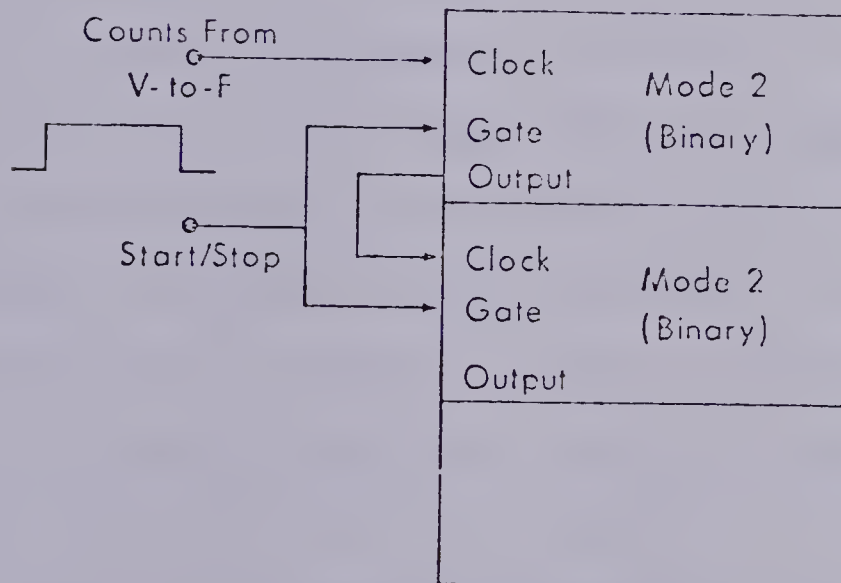
## INTEGRATION TIMER



Mode 2: Rate Generator ( $\div N$  Counter)

Mode 5: Hardware Triggered Strobe

## COUNTER



Mode 2: Rate Generator ( $\div N$  Counter)

Figure 74. Simplified block diagrams of the integration timer and the counter.



loading HEX 3C into the control register. This counter is then preset to HEX 5004 which divides the 2.048 MHz system clock down to 100 Hz which is available at the output pin of counter 0. This 100 Hz signal is connected to the clock input of the second counter. Counter 1 (the second counter) on the same IC is programmed to operate in Mode 5 BCD (hardware triggered strobe) by loading the control register with HEX BB, and is present with a BCD number input from the teletype. For example, presetting this counter with 0100 results in a 1 second integration time. Thus integration times from 0.01 to 99.99 sec in 0.01 sec intervals can be set by TTY input.

The other 8253 is used to count the pulses produced by the voltage to frequency converter for the integration time generated by the timer 8253. In order to obtain the desired resolution two counters on this second chip are cascaded, providing 32 bit resolution. Both 16 bit counters are set to operate in Mode 2, binary by loading the control register with HEX BC and 7C. The counters are preset with HEX FF for full count.

An 8255 programmable peripheral interface chip that is a standard feature of the SDK-80 board is used to aid sequencing of the measurement. A measurement is initiated by outputting a logic 0 followed by a logic 1 at one bit of Port B. This sets the flip-flop ( $Q = 1$ ) which enables



the gates of both the timer and counter 8253's. Note that both 8253's have NAND gates on the cascade line from output to the succeeding input of each IC. This is necessary because we found that the 8253's do not count the first pulse which is used to set up the counter. For this reason a charge delay monostable is used to set up the counters at the start of the measurement. The charge delay monostable is triggered by the falling edge at  $\bar{Q}$  of the flip-flop.

When the timer 8253 reaches its full count its output undergoes a  $1 \rightarrow 0$  transition which toggles the flip-flop setting  $Q$  to "0" thus disabling all gates and terminating the count measurement. During counting the status of the flip-flop is continuously monitored by inputting  $\bar{Q}$  of the flip-flop to bit 0 of Port A on the 8255. When counting is completed ( $\bar{Q} = "1"$ ) the microcomputer enters a routine that reads and stores the binary numbers in the counter 8253 in memory.

### Successive Approximation ADC Based System

The complete schematic of the successive approximation ADC based system is shown in Figure 75. An Analog Devices AD571 was chosen as the ADC. It is a 10 bit unit with a specified conversion time of 25  $\mu$ sec. The ADC was front ended with an Analog Devices AD582 sample-and-hold amplifier.



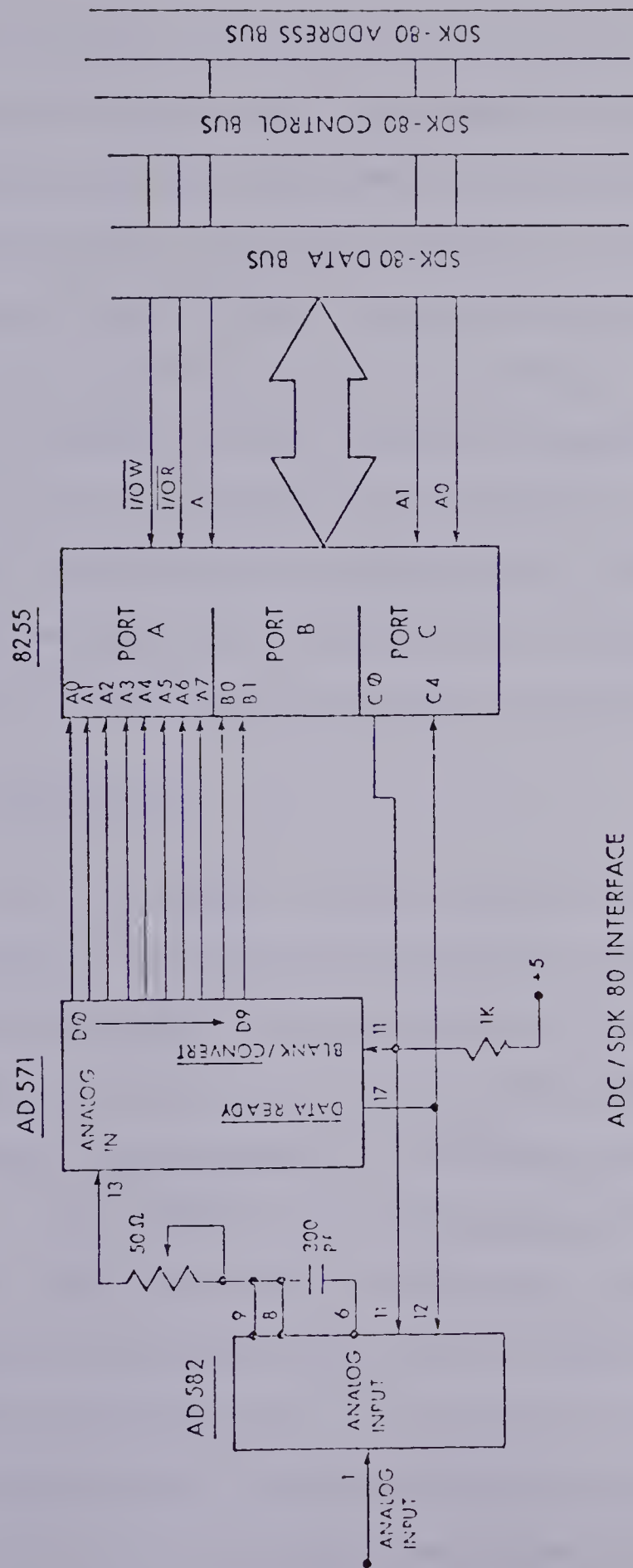


Figure 75. Circuit diagram of the analog-to-digital converter based system as interfaced to the SKK-80.





The sample-and-hold amplifier-ADC subsystem was interfaced to the SDK-80 via the 8255 programmable peripheral interface chip. Acquisition of a data point was initiated by a pulse from pin C0 of Port C and upon receipt of the DATA READY signal the converted 10 bit value is read into the microprocessor using Ports A and B of the 8255. Integration is achieved by summing a large number of converted values. For example a 1 sec integration is achieved by summing 10,923 conversions. Even though we are using a 10 bit converter the integrated value has a resolution of about 16-17 bits as a result of the summation (signal averaging) step [121].

### Software Development

The key, of course, to the versatility and power of a microprocessor based system is software control. The SDK-80 single board microcomputer has room for 1 k of read/write memory (RAM) and 4 k of ROM (i.e. 4 2708 EPROM's). One EPROM contains the standard 1 k MONITOR provided with the SDK-80 kit. The MONITOR provides software to communicate with a TTY, enter and edit user programs, examine, list or change memory locations, and initiate execution of programs with breakpoint capability. In addition to providing general system control, several MONITOR routines are called and utilized by other programs developed for this application. Utility programs were required for reading and



writing paper tapes on the TTY. Unfortunately Intel did not provide these programs in the SDK-80 MONITOR. Paper tape input/output programs were obtained from the Insite [122] user library.

In order to carry out mathematical operations on a microprocessor beyond the simplest binary additions and subtractions a set of so-called floating point routines is required. We initially adapted a floating point package from Findly [123] to use on our system. However it soon became both too time and memory space consuming to set up a complete floating point package on this small a microprocessor system beyond routines for floating point normalization, addition, subtraction, multiplication, division and TTY output.

Full floating point capability is now provided on our system using the AM9511 Arithmetic Processing Unit of Advanced Micro Devices. The chip is essentially a complete hardware floating point package. The AM9511 contains an internal stack onto which operands are loaded from the 8080 CPU over the system data bus. The appropriate execution command is sent to the AM9511 and the result of the operation is left on the stack. A command summary for the AM9511 is shown in Table X and schematic for the hardware interface to the SDK-80 is shown in Figure 76. It is difficult to overemphasize the extent to which the use of this chip expedited overall software development for this



## TABLE X

## AM9511 COMAND SUMMARY

1. FIXED POINT.... 16 or 32 BIT

ADD	MULTIPLY
SUBTRACT	DIVIDE

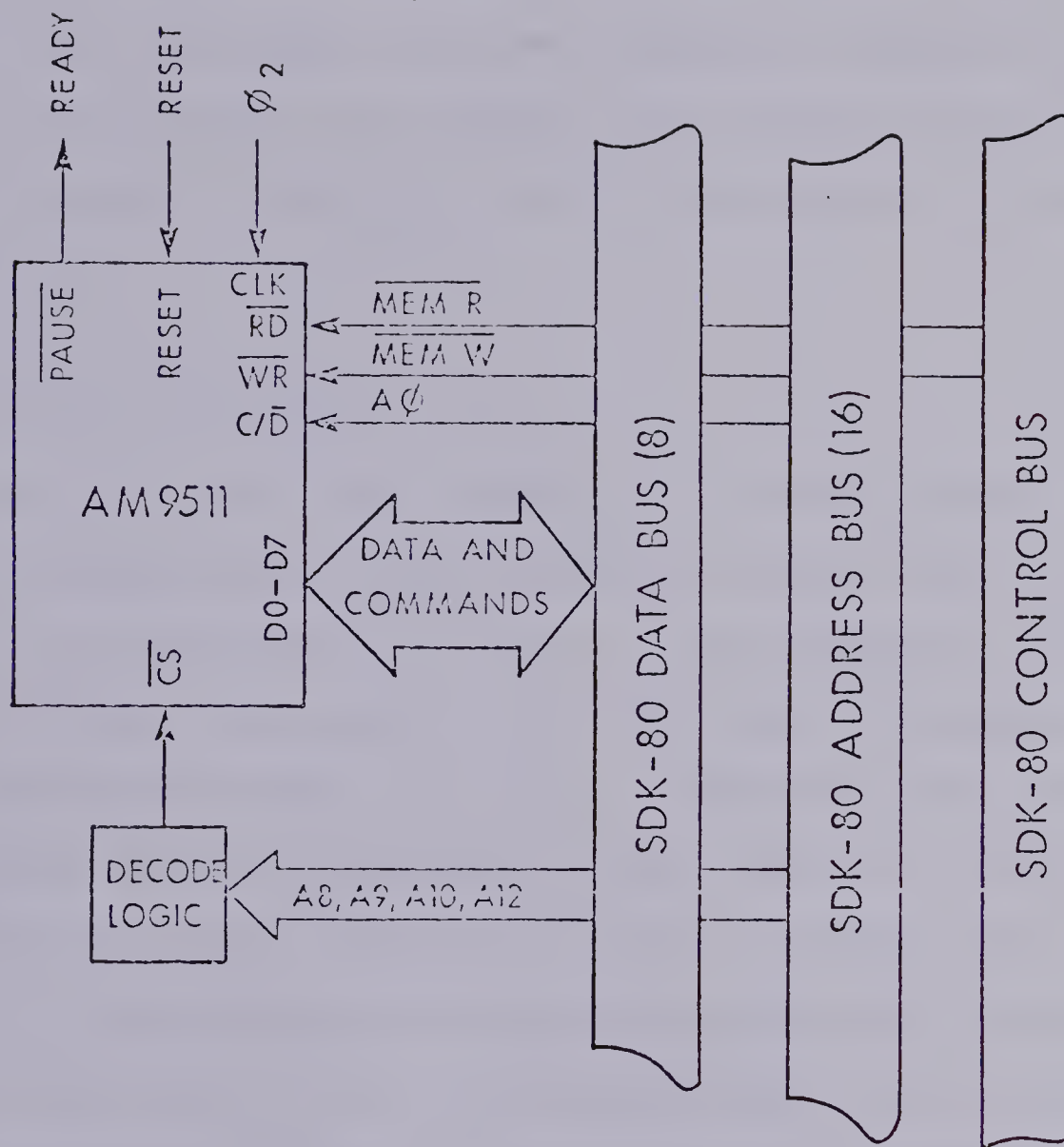
2. FLOATING POINT.... 25 BIT MANTISSA, 7 BIT EXPONENT

ADD	MULTIPLY
SUBTRACT	DIVIDE
SQUARE ROOT	SIN
COS	TAN
ASIN	ACOS
ATAN	LOG
LN	LOG
X TO POWER Y	EXP

3. DATA MANIPULATION

FLOATING POINT TO FIXED POINT	16 and
FIXED POINT TO FLOATING POINT	32 BIT
CHANGE SIGN	
READ/LOAD STACK	





AM9511 MATH CHIP MEMORY MAPPED

Figure 76. Interface circuit for the AM9511 to the SDK-80.





system.

All programs were placed in EPROM (2708's). The 2708's were programmed using the PROMPT-80 system of Intel. Program development and assembly were carried out using a cross-assembler running on a PDP-11 minicomputer in our laboratory.

### Results and Discussion

The TTY output for a typical run (v-to-f system) for the measurement of an analyte emission signal from an ICP source is illustrated in Figure 77. The operator types in the desired integration time (1.00 sec) and number of replicate measurements ( $16 \equiv 10_{16}$ ). Note that the number of repeats must be designated in HEX. This is a typical concession that one often has to make in dealing with a minimum configuration microprocessor system such as the single board SDK-80. In our case it simply was not worth the programming time and in particular the programming space to include a conversion routine. The integration time could be input in decimal format because the second counter on the timer 8253 was being operated in a BCD mode. Finally the operator indicates whether this is a background or sample (analyte) run and types a sample identification code. The measurements are then carried out, in this case 16 consecutive 1 sec integrations, the meas-



```
INT TIM? 0100
# REPTS? 10
BACK(B)/SAMP(S)? S
ID? 1
```

```
+0.2526000E+04
+0.2543000E+04
+0.2530000E+04
+0.2534000E+04
+0.2536000E+04
+0.2534000E+04
+0.2539000E+04
+0.2549000E+04
+0.2534000E+04
+0.2535000E+04
+0.2539000E+04
+0.2538000E+04
+0.2545000E+04
+0.2534000E+04
+0.2537000E+04
+0.2551000E+04
```

```
SUM: +0.4060400E+05
AVE: +0.2537750E+04
BSB: +0.2461750E+04
STD: +0.6587867E+01
S/N: +0.3736793E+03
```

Figure 77. Typical TTY dialogue and output for a run with the v-to-f converter based measurement system.



urements are summed, averaged, background is subtracted, standard deviation and signal to noise ratio are calculated, and all data are logged to the TTY. The background subtracted is that measured in a previously acquired and so designated run, and would represent, for example, the output signal while running a blank solution.

The TTY dialogue for the ADC based integrating system is essentially identical except that the integration time is chosen by indicating the number of ADC conversions to be summed. A 1 sec integration is equivalent to 10,923 conversions. Based on signal to noise ratios ( $1/\text{relative standard deviation when } n = 32$ ) for several analyte signals the performance of the v-to-f and ADC based systems as integrating measurement systems was essentially identical, i.e. equivalent signal to noise ratios were obtained for the same signal and integration times for both systems. However practical differences do exist between these two systems with respect to factors such as cost, set-up time and expansion to multichannel measurements.

While costs are admittedly hard to pin down these days, the ADC with its attendant sample-and-hold amplifier was a little more expensive than the V-to-f converter and 8253 counter/timer chips but no great difference occurs here. In terms of setup time (i.e. interfacing to the SDK-80) the ADC based system was simpler, as it was carried



out using the standard on-board chips while with the v-to-f system, the 8253 based programmable frequency meter had to be developed and interfaced. With respect to expansion to simultaneous multichannel measurements (i.e. for a direct reading spectrometer containing several photomultiplier tubes) the v-to-f based system is, perhaps, more effective. A proposed approach is illustrated in Figure 78. Each channel requires an operational amplifier, a v-to-f converter and a 12 bit counter (i.e. 2/3 of an 8253). A single microprocessor could easily control the complete system as once the counters are set up for the measurement they need not be read until the integration is complete and the integrated values, i.e. the total count, can be held indefinitely, it being a digital signal. No software intervention is necessary during integration and in general software overhead for such a system would be minimal. Of course, multichannel ADC systems could also be set up and in fact the readout systems for one current direct reading spectrometers [124] is based on analog integration at each channel with subsequent multiplexing to a single ADC. In particular, the software overhead of this system is more complex than that proposed in Figure 78, in part because of dynamic range limitations associated with analog integration. However, our goal here is not to pick a "best" system, but simply to indicate that the v-to-f based system





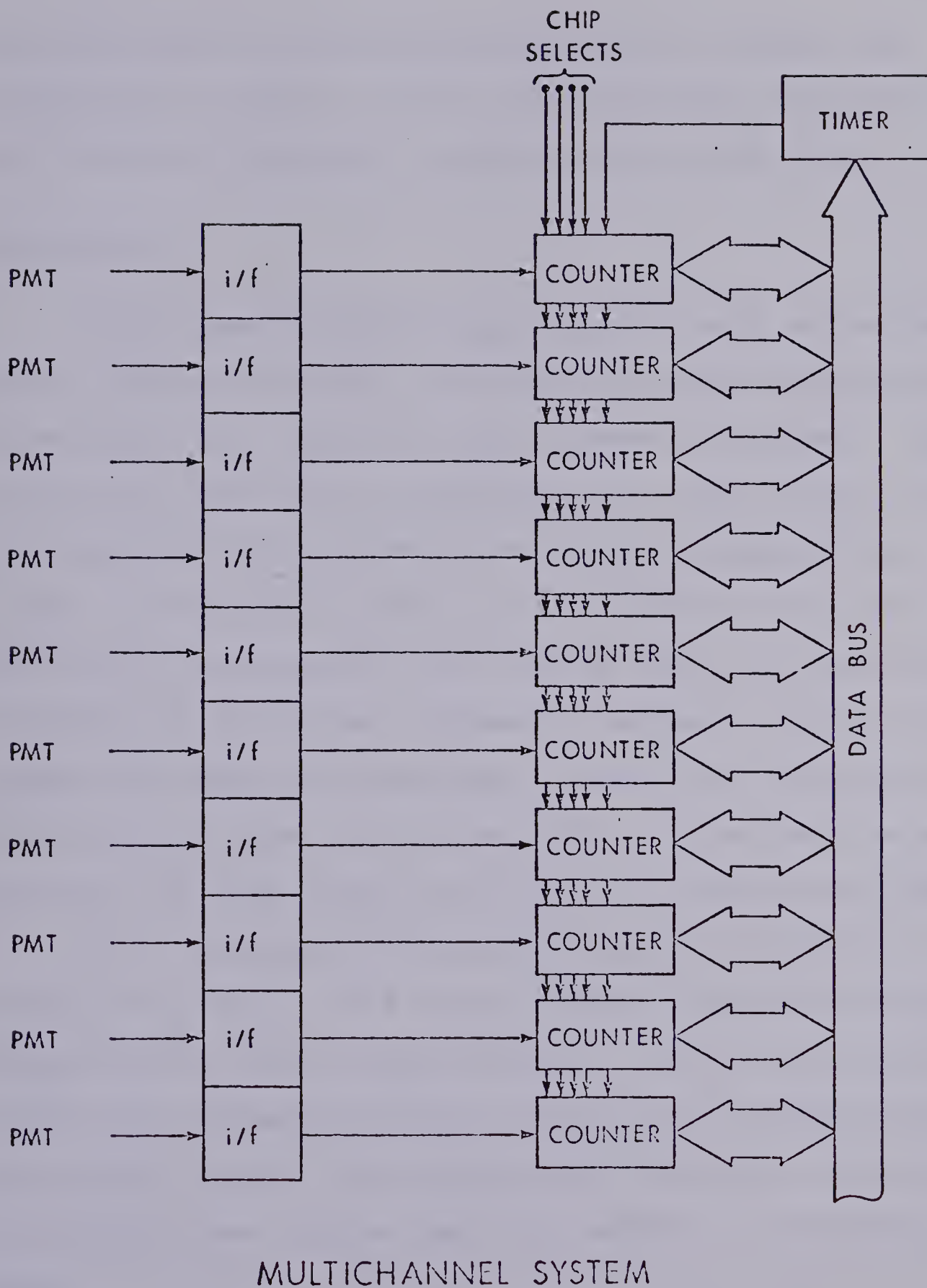


Figure 78. Proposed approach for a multichannel measurement system based on the v-to-f converter-counter integration system.



when developed with software programmable counters can potentially provide a powerful microprocessor controlled multichannel integrating readout system for PM tubes.

### Conclusions

Single board microprocessor systems, such as the one used in this application, can easily provide the basis for intelligent data acquisition and processing systems. The system described here is applicable to a wide variety of spectrochemical measurements involving photomultiplier tubes. Versatility is built in as a result of the capability of programmable chips such as the 8253 counter/timer chip and, in particular, because of software control of the system via EPROM based routines. Indeed, the complete single board microprocessor system can easily be dedicated to an entirely new task simply by inserting an appropriate EPROM.

In our laboratory this system has been used for acquisition of data from a single channel inductively coupled plasma atomic emission spectrometer. It has been particularly useful for fundamental signal to noise ratio measurements and studies where it has relieved the tedium of collecting, calculating, and logging the large amounts of statistical data.



## APPENDIX B

This program is used to collect data from the photo-diode array. The program runs on a DECTAPE based PDP8/e minicomputer with an OS/8 operating system. It is written in FORTRAN II and SABR. Originally written by E.G. Coddington, it has been modified by E.D. Salin and the author.



```

COMMON FU,ICHE
DIMENSION J(1027),FU(1024)
SOPDEF KCF      6503
SOPDEF DBSK     6502
SOPDEF DBCI     6503
SOPDEF DBRI     6504
SOPDEF DBCU     6505
SOPDEF DBSU     6506
SOPDEF SUDF     6531
SOPDEF SCCC     6535
SOPDEF RBCF     6536
ICHE=0
3      WRITE(1,711)
711    FORMAT('STORED SPECTRUM TO BE READ? Y OR N.')
      READ(1,507)LYN
      IF(LYN-1632)963,730,963
730    WRITE(1,731)
731    FORMAT('ENTER DEV., FILE NAME, NO. OF POINTS, 2A6I4')
      READ(1,732)F1,F2,NP
732    FORMAT(2A6,I4)
      N=1
      CALL IOPEJ(F1,F2)
      READ(4,505)(J(I),I=1,NP)
      WRITE(1,809)
809    FORMAT('INPUT SCALING FACTOR')
      READ(1,311)SS
811    FORMAT(F12.4)
      DO 990 I=1,NP
990    FU(I)=(FLDAT(J(I)))/SS
      GO TO 29
963    WRITE(1,502)
502    FORMAT('BACKGROUND SUBTRACTION, Y OR N')
      READ(1,507)JBKD
      WRITE(1,500)
500    FORMAT('ENTER NO OF SCANS AND POINTS, 2I4')
      READ(1,501)N,NP
501    FORMAT(2I4)
S      CLA
S      TAD      N      /ENTER NO. OF SCANS
S      CIA      /NEGATE N
S      DCA      SCAN   /STORE IN SCAN
S      TAD      NP     /ENTER NO. OF POINTS
S      CIA      /NEGATE NP
S      DCA      POINT  /STORE IN POINT
39     CONTINUE
S      CLA CLL      /REPEAT CYCLE STARTS AT 39
      K=0
      DO 1      I=1,NP
1      FU(I)=0

```





```

        JB=JBKD
        READ(1,507)JC
SSCAN5, TAD      SCAN      /GET NO. OF SCANS
S        DCA      12        /SET THE SCAN COUNTER
SCJ,     TAD      POINT     /GET THE NO. OF POINTS
S        DCA      10        /SET THE POINT COUNTER
S        TAD      K0177     /GET THE STARTING ADDRESS
S        DCA      11        /SET THE STORAGE ADDRESS
S        CLA
S        DBCI
S        CLA
SSTART, DBCI
S        JMP      START     /CHECK FOR START FLAG
S        DBRI
S        DBCI             /CLEAR INPUT BUFFER
S        SPA
S        JMP      START
S        CLA CLL
S        SCGC
SCLOCK, SODF
S        JMP      CLOCK
S        SCGC
S        RBCF
S        CLL PAR
S        DCA  I  11        /STORE DATA POINT
S        ISZ      10        /CHECK POINT COUNTER, SKIP IF ZERO
S        JMP      CLOCK
S        CLA CLL
        IF(K)41,40,41
40       DO 5      I=1,NP
5        FJ(I)=FLOAT(J(I))+FJ(I)
S        JMP      CHECK
41       DO 42     I=1,NP
42       FJ(I)=FJ(I)-FLOAT(J(I))
SCHECK, ISZ      12        /CHECK SCAN COUNTER, SKIP IF ZERO
S        JMP      60
S        CLA CLL
        IF(K)29,30,29
30       IF(JB-1332)29,33,29
29       R=FLOAT(J)
        K=1
        DO 34     I=1,NP
34       FJ(I)=FJ(I)/R
33       AMAX=FJ(1)
        DO 17     I=2,NP
        IF(FJ(I)-AMAX)17,17,13
13       AMAX=FJ(I)
17       CONTINUE
        AMIN=FJ(1)
        DO 19     I=2,NP

```



```

      IF(FJ(1)-AMIN)20,19,19
20    AMIN=FJ(1)
19    CONTINUE
      S=1000./(AMAX-AMIN)
      IF(K)35,36,35
35    WRITE(1,514)S
514    FORMAT('SCALING FACTOR=',F12.4)
      DO 231 I=1,NP
231    FJ(I)=FJ(I)-AMIN
330    DO 282 I=1,NP
232    J(I)=FJ(I)*S
      GO TO 16
36    DO 23 I=1,NP
23    J(I)=(FJ(I)-AMIN)*S
16    WRITE(1,503)
503    FORMAT(' ')
      READ(1,509)NO
509    FORMAT(I3)
      IF(NO)16,16,37
37    IF(8-NO)16,38,38
38    CONTINUE
      GO TO (21,22,23,24,25,26,39,700)NO
25    IF(JB-1632)3,13,3
13    READ(1,507)JG
      JB=0
      K=1
S      JMP      SCANS
21    WRITE(1,701)
701    FORMAT('ENTER FIRST AND LAST DIODES 214. ')
      READ(1,702)JF,NL
702    FORMAT(2I4)
      WRITE(1,505)(J(I),I=JF,NL)
505    FORMAT(10(I5,1X))
      WRITE(1,703)
703    FORMAT('FINISHED? Y OR N. ')
      READ (1,507) JYN
      IF(JYN-1632)21,13,21
22    WRITE(1,510)
510    FORMAT('ENTER FILE NAME, A6')
      READ(1,511)FILE
511    FORMAT(A6)
      CALL ODPEN('DTA1',FILE)
      WRITE(4,505)(J(I),I=1,NP)
      CALL OCLOSE
      GO TO 16
26    WRITE(1,516)
516    FORMAT('ENTER THE THRESHOLD, I4')
      READ(1,501)JO
      WRITE(1,517)
517    FORMAT('POINT NO .      AMPLITUDE   SCALED AMP      SUM ')
      JZ=NP-3

```



```

DO 63 I=3,NZ
IF(J(I)-J(I-1))63,63,64
64 IF(J(I+1)-J(I))65,65,63
65 IF(J(I)-J(I-1))63,63,66
66 SJ=FJ(I)
IS=I-7
IE=I+7
SUM=0.0
DO 67 L=IS,IE
67 SUM=SUM+FJ(L)
WRITE(1,518)I,J(I),SJ,SUM
513 FORMAT(1X,I4,9X,I4,8X,F6.2,4X,F6.0)
63 CONTINUE
GO TO 16
23 WRITE(1,520)
READ(1,507)JS
IF(JS-1632)70,71,70
71 IF(JB-1632)75,76,75
76 R=FLOAT(J)
DO 77 I=1,NP
77 J(I)=FJ(I)/R
GO TO 70
75 DO 72 I=1,NP
72 J(I)=FJ(I)
70 J(NP+1)=500
J(NP+2)=1023
J(NP+3)=500
JZ=NP+3
K=0
S CLA CLL
S TAD NJZ
S CIA
S DCA POIN
SSET, CLA
S TAD POIN /GET NO. OF POINTS
S DCA 10 /SET POINT COUNTER
S TAD K0177 /GET STARTING ADDRESS
S DCA 11 /SET STARTING ADDRESS
SPLOT, CLA CMA
S DBCO /CLEAR OUTPUT BUFFER
S CLA
S TAD I 11 /GET DATA POINT
S TAD K2000 /SET OUTPUT FLAG
S DBCO /SET OUTPUT BUFFER
S KCF /CHECK FOR STOP FROM KEYBOARD
S JNP CONT
S KCF /CLEAR KEYBOARD BUFFER
S CLA CLL

```



```

IF(JS-1632)73,74,73
74 IF(JB-1632)330,36,330
73 CONTINUE
S JMP N16 /EXIT
SCOUT, ISZ 10 /CHECK POINT COUNTER, SKIP IF ZERO
S JMP PLUT /GET NEXT POINT
S JMP SET /START OVER
24 WRITE(1,520)
520 FORMAT(/' SCALE PLOT? Y OR N')
READ(1,507)JS
IF(JS-1632)50,51,50
51 DO 52 I=1,JP
52 J(I)=FJ(I)/2.
50 CONTINUE
S CLA CLL
S TAD NJP
S CIA
S DCA POINT
S CLA CLL
S TAD POINT /GET NO. OF POINTS
S DCA 10 /SET POINT COUNTER
S TAD K0177 /GET STARTING ADDRESS
S DCA 11 /SET STARTING ADDRESS
31 DO 32 I=1,380
32 JG=1*1
S CLA CMA
S DBCO /CLEAR OUTPUT BUFFER
S CLA
S TAD I 11 /GET DATA POINT
S TAD K2000 /SET OUTPUT FLAG
S DBSD /SET OUTPUT BUFFER
S CLA
S ISZ 10 /CHECK POINT COUNTER, SKIP IF ZERO
S JMP N31
IF(JS-1632)16,74,16
SK0777, 0777
SK2000, 2000
SPOIN, 0000
SPOINT, 0000
SK0177, 0177
SSCAN, 0000
700 DO 999 I=1,JP
FJ(I)=FJ(I)*R
999 CONTINUE
CALL CAL1 (FJ,ICHE,S)
CONTINUE
GO TO 16
507 FORMAT(A1)
4 CALL EXIT
END

```





## APPENDIX C

This program is used to read 256 point lateral data from magnetic tape, perform an Abel inversion on the data, and store the radial data back on tape. Written in FORTRAN II it runs on a DECTAPE based PDP8/e under an OS/8 operating system. The program is written in two parts; a main program and an Abel inversion subroutine. It was written by the author.



```

C PROGRAM TO PERFORM ABEL INVERSION ON DATA FROM 256 ARRAY
COMMON FR,FL, JT,A
DIMENSION J(256),FJ(256),FR(256),FL(256)
A=1.0
C PROGRAM TO READ FROM DECTAPE
C
700 WRITE(1,731)
731 FORMAT('ENTER DEV., FILE NAME, NO. OF POINTS, (2A6I4) ')
READ(1,732) F1,F2,NP
732 FORMAT(2A6,I4)
J=1
CALL IOPEN(F1,F2)
READ(4,505)(J(I),I=1,NP)
505 FORMAT(10(I5,1X))
C
C PORTION TO SCALE THE SPECTRUM READ FROM TAPE
WRITE(1,733)
733 FORMAT('ENTER SCALING FACTOR(F6.3) ')
READ(1,734) S
734 FORMAT(F6.3)
DO 99 N=1,NP
99 FJ(N)=(FLOAT(J(N)))/S
DO 56 I=1,NP
56 FL(I)=FJ(I)
C
25 WRITE(1,60)
60 FORMAT('AVERAGE(1), STORE(2), ABEL(3), END(4), RESTART(5) ')
READ(1,61)J
61 FORMAT(I1)
GO TO(600,183,104,291,700)J
C ENTER CENTRE OF SYMMETRY OF AXIAL PLOT
600 WRITE(1,601)
601 FORMAT('ENTER STARTING DIODE')
READ(1,602)IMID
602 FORMAT(I3)
WRITE(1,603)
603 FORMAT('ENTER END DIODE,(0 OR 256) ')
READ(1,602) IEND
JT=IABS(IMID-IEND)
C AVERAGE BOTH SIDES OF AXIAL TO GIVE 128 ELEMENT AXIAL
DO 100 I=1,JT
J=IMID+1-I
K=IMID+I-1
100 FL(I)=(FJ(J)+FJ(K))/2.
C ZERO OUT THE END ELEMENTS
N=128-JT
DO 101 I=1,N
K=JT+I
101 FL(K)=0.

```



```

      DO 103 I=1,123
103    FJ(I)=FL(I)
      GO TO 25
104    NT=123
C      DO ABEL INVERSION OF LATERAL ARRAY (USING ABELSE)
      CALL ABEL
      DO 200 J=1,123
200    FJ(J)=FF(J)
      GO TO 25
C      SCALE ARRAY AND STORE ON MAG TAPE
133    NT=123
      AMAX=FJ(1)
      DO 17 I=2,NT
      IF(FJ(I)-AMAX) 17,17,13
18    AMAX=FJ(I)
17    CONTINUE
      AMIN=FJ(1)
      DO 19 I=2,NT
      IF(FJ(I)-AMIN) 20,19,19
20    AMIN=FJ(I)
19    CONTINUE
      S=1000./(AMAX-AMIN)
      WRITE(1,514) S
514    FORMAT('SCALING FACTOR=',F12.4)
      DO 231 I=1,NT
231    FJ(I)=FJ(I)-AMIN
      DO 202 I=1,NT
202    J(I)=FJ(I)*S
      WRITE(1,510)
510    FORMAT('ENTER FILE NAME,A6')
      READ(1,511) FILE
511    FORMAT(A6)
      CALL OPEN('DATA',FILE)
      WRITE(4,505)(J(I),I=1,NT)
      CALL CLOSE
      GO TO 25
291    STOP
      END

```



```

SUBROUTINE ABEL
COMMON FR,FL,JT,A
DIMENSION FR(256),FL(256)
C=-2./(3.15159*A)
JTT=JT-1
DO 10 K=1,JT
J=K
XJ=FLOAT(J)
XK=FLOAT(K)
XK2=(XK-1.)*(XK-1.)
A1=SQRT((XJ**2)-XK2)
A2=SQRT(((XJ-1.)*2)-XK2)
AKJ=(A1-A2)/((2.*XJ)-1.)
FR(K)=-C*FL(J)*AKJ
KK=K+1
DO 11 J=KK,JTT
XJ=FLOAT(J)
A1=SQRT((XJ*XJ)-XK2)
A2=SQRT(((XJ-1.)*(XJ-1.))-XK2)
XM=FLOAT(J-1)
A11=SQRT((XM*XM)-XK2)
A22=SQRT(((XM-1.)*(XM-1.))-XK2)
AKJ=(A1-A2)/((2.*XJ)-1.)
AKJM=(A11-A22)/((2.*XM)-1.)
FR(K)=FR(K)+(C*FL(J)*(AKJM-AKJ))
11 CONTINUE
FR(K)=FR(K)*FLOAT(JTT)
WRITE(1,88) K,FL(K),FR(K)
88 FORMAT(I5,2F12.4)
10 CONTINUE
RETURN
END

```













**B30306**